



HAL
open science

Adipose tissue senescence in the context of high-fat diet-induced obesity and aging: mechanisms associated with the initiation of cellular senescence

Zaineb Mezdari

► **To cite this version:**

Zaineb Mezdari. Adipose tissue senescence in the context of high-fat diet-induced obesity and aging: mechanisms associated with the initiation of cellular senescence. Health. Université Paris-Est, 2021. English. NNT: 2021PESC0042. tel-03667958

HAL Id: tel-03667958

<https://theses.hal.science/tel-03667958>

Submitted on 13 May 2022

HAL is a multi-disciplinary open access archive for the deposit and dissemination of scientific research documents, whether they are published or not. The documents may come from teaching and research institutions in France or abroad, or from public or private research centers.

L'archive ouverte pluridisciplinaire **HAL**, est destinée au dépôt et à la diffusion de documents scientifiques de niveau recherche, publiés ou non, émanant des établissements d'enseignement et de recherche français ou étrangers, des laboratoires publics ou privés.

DOCTORAL THESIS

Life and Health Sciences

By

Zaineb MEZDARI

January, the 8th 2021

Adipose Tissue Senescence in the Context of High-fat Diet-Induced Obesity and Aging: Mechanisms associated with the initiation of cellular senescence

Pr Geneviève DERUMEAUX

Thesis supervisor

Dr Daigo SAWAKI

Co-supervisor

Dr Carl MANN

Reporter

Dr Ramaroson ANDRIANTSITOHAINA

Reporter

Dr Bénédicte GABORIT

Reviewer

Dr Andrea LAZZATI

Reviewer

Dr Maria PINI

Reviewer

“The process of scientific discovery is, in effect, a continual flight from wonder”

--Albert Einstein

Acknowledgments/ Remerciements

بِسْمِ اللَّهِ، الْحَمْدُ لِلَّهِ، وَ الصَّلَاةُ وَ السَّلَامُ عَلَى رَسُولِ اللَّهِ

Cette thèse, est l'aboutissement d'un long travail qui n'a été possible que grâce au concours de plusieurs personnes à qui je souhaite témoigner toute ma reconnaissance.

Pour commencer je tiens à remercier les membres du jury pour avoir accepté de consacrer du temps à évaluer mes travaux de recherche malgré leurs emplois du temps très chargés. Merci au **Dr Carl MANN** et au **Dr Ramaroson ANDRIANTSITOHAINA** d'avoir accepté de rapporter mon travail, et merci au **Dr Andrea LAZZATI**, au **Dr Benedicte GABORIT**, au **Dr Daigo SAWAKI** et au **Dr Maria PINI** d'avoir accepté d'examiner mon travail.

Ensuite, je tiens à remercier tout particulièrement le **Pr Geneviève DERUMEAUX**, d'abord de m'avoir permis d'intégrer son équipe, pour avoir encadré et supervisé mon travail, mais surtout de m'avoir encouragée et soutenue, d'avoir été toujours bienveillante envers moi, d'avoir été compréhensive et patiente avec moi lors des moments difficiles, de m'avoir aidée et poussée à surmonter toutes les difficultés, de m'avoir tirée vers le haut pour me permettre de grandir sur le plan personnel et professionnel, en bref, d'avoir été une directrice de thèse exemplaire. Mille Mercis Geneviève!

The second ones that I would like to warmly thank for co-supervising my work are the **Dr Daigo SAWAKI** and **Dr Gabor CZIBIK**. In fact, thank you is far from being sufficient, Gabor, Daigo, whatever I say or I do, I will never be able to express my gratitude to both of you. Since I joined your team, you treated me as if I was your little sister, your « Padawan ». You taught me everything, you were always there when I needed, when I had difficulties you were there to help me and encourage me, when I was lost, you were there to guide me, when I was depressed you were there to support me, when I succeeded you were there to congratulate me and when I was happy you were there to share this happiness with me Thank you for being my Masters, thank you for being my friends, thank you for being my Big brothers... thank you for being you!!

Next, I want to express my profound gratitude to my best friends and colleagues **Suzain** and **Maïssa**. Girls! I don't know what would have been my daily life in the lab without you... Since that famous day when I « saved you from tumbing dans la m**de » Suzain and after you joined Maïssa, I thank God for all these good times we spent together, all these crazy laughter we shared, all these stressful moments we faced, all the support I got from you, your friendship is really priceless...thank you for being my sisters !

A **Nora** et **Julia**, vous êtes tout simplement géniales ! J'ai une chance inouïe de vous avoir auprès de moi, de pouvoir partager avec vous les bons et les mauvais moments, de bénéficier de vos conseils précieux et de votre aide inestimable, mais surtout de votre joie de vivre très contagieuse...Merci infiniment !

A **Maria** et **Yanyan**, je vous remercie pour votre aide et votre soutien, vos compétences et connaissances scientifiques m'ont été d'une aide précieuse le long de mon parcours.

Ensuite, je voudrais remercier le **Dr Anne PIZARD**, pour son aide, pour son soutien, pour ses précieux conseils, pour ses encouragements, mais aussi pour sa bonne humeur, son humour...et pour l'idée de la poule ! Merci Anne, tu es géniale ;)

Puis je tiens également à remercier le **Dr Costin RADU**, pour son aide, son soutien et ses conseils toujours bien avisés.

Je tiens également à remercier le **Pr Serge ADNOT** ainsi que le reste de mon équipe, **Hao, Thomas, Thaïs, Amal, Elisabeth, Shariq** et les autres...Merci à tous pour votre aide.

Ensuite, je remercie bien évidemment le directeur de l'IMRB : **Mr. Jorge BOCZKOWSKI** et le directeur de l'UPEC : **Mr. Jean-Luc DUBOIS-RANDÉ** ainsi que toutes les personnes qui contribuent quotidiennement au bon fonctionnement de l'institut et de l'université pour nous permettre de travailler dans un cadre propice à nos activités de recherche scientifique.

Je remercie particulièrement le personnel des plateformes, surtout les membres de l'EP3, en particulier **Adrien, Florine** et **Alice** et le personnel de la plateforme d'imagerie : **Xavier, Christelle** et **Wilfried**, Merci à tous pour votre gentillesse et votre professionnalisme.

Merci également à tous ceux que je n'ai pas cité mais qui m'ont aidé d'une manière ou d'une autre.

Pour finir, je tiens à remercier chaleureusement tous les membres de ma Famille :

A **mes chers parents**, à qui je dois tout, merci d'avoir toujours été là pour moi, merci pour votre soutien et votre amour inconditionnel

الله يتقبل منكم و يبارك فيكم و يجازيكم خيرا

A **mes frères**, merci pour votre aide et votre soutien, merci pour vos encouragements et merci d'être toujours là pour moi.

A **mes oncles**, merci pour votre soutien et vos encouragements, merci d'être toujours près de moi malgré les distances qui nous séparent.

A ma sœur **Yousra**, je ne pourrais jamais te remercier assez pour toute l'aide que tu m'as apportée, pour ton soutien et tes encouragements, pour m'avoir poussée à surmonter les difficultés et pour avoir été mon coach dans cette course de l'écriture du manuscrit : en comptant les pages écrites au fur et à mesure pour m'encourager, en exigeant des rapports détaillés de mon avancement, tout en prenant soin de contrôler mes heures de réveil et de coucher !! ce rythme militaire aura fini par payer, Merci Yousra, t'es un amour! Je te souhaite tout le bien que tu mérites.

A **mes cousines les « BenLag »**, qui n'ont jamais arrêté de m'encourager et de me soutenir tout au long de mes études et dont la compagnie me fait tellement de bien.

A **mes beaux-parents**, qui m'ont toujours encouragée, aidée, et poussée à aller toujours plus loin, merci à vous, merci pour tout.

A **mes chers enfants, Balkys et Oways**, que je remercie du fond du cœur de faire partie de ma vie, d'être ma source de motivation, d'être ma raison de me battre, d'être ma source de bonheur, de joie et d'amour...Merci pour votre patience et votre soutien.

Et pour finir... A Moi !! Parce que j'ai franchi des montagnes pour en arriver là...



*Because Hard
Work Always
Pays Off !!*

TABLE OF CONTENTS

List of abbreviations	7
Abstract	11
Résumé.....	12
INTRODUCTION.....	14
CONTEXT & LITERATURE REVIEW	16
Section 1: OBESITY.....	17
Chapter 1: Definition and Epidemiology	18
Chapter 2: Clinical research and limitations.....	19
Chapter 3: Animal models	22
Section 2: ADIPOSE TISSUE: PHYSIOLOGICAL STRUCTURE & FUNCTION.....	24
Chapter 1: Diversity of adipose tissue depots in humans and mice	25
Chapter 2: Adipose tissue cell types and their functions	26
I) Adipocytes	26
II) Adipose-derived stem cells (ADSCs) and preadipocytes	31
III) Endothelial cells and their progenitors	33
IV) Adipose tissue immune cells	33
Section 3: ADIPOSE TISSUE: PATHOPHYSIOLOGICAL STRUCTURE & FUNCTION.....	37
Introduction.....	38
Chapter 1: Obesity and insulin resistance	39
I) Insulin signaling pathway in adipocytes.....	39
II) Mecanism of insulin resistance in adipocytes.....	41
Chapter 2: Obesity and low-grade inflammation.....	42
Chapter 3: Obesity and adipose tissue fibrosis	47
Chapter 4: Obesity and adipose tissue senescence	50
I) Definition of cellular senescence	50
II) Replicative cellular senescence	51
III) Premature cellular senescence	52
IV) Biomarkers of senescence.....	53
V) Adipose tissue senescence in aging and obesity.....	57
VI) Adipose tissue cell-type specific senescence	58

VII) Adipose tissue senescence as a therapeutic target for the treatment of aging- and obesity-related metabolic disorders	60
Chapter 5: Conclusion	62
OBJECTIVES	64
METHODS	66
RESULTS	103
Study 1.....	105
Study 2.....	137
Study 3.....	184
Study 4.....	228
DISCUSSION	281
CONCLUSION & PERSPECTIVES	297
SUPPLEMENTAL TABLES	301
BIBLIOGRAPHY	311

List of abbreviations

AdPLA2	Adipose-specific phospholipase A2
ADSC	Adipose-derived stem cell
A-FABP	Adipocyte-fatty acid binding protein
AP-1	Activating protein
AP	Antigen-presenting cell
AT	Adipose tissue
ATGL	Adipose triglyceride lipase
ATM	Adipose tissue macrophage
ATM (kinase)	Ataxia telangiectasia mutated
ATR (kinase)	Ataxia telangiectasia and Rad3 related
BAT	Brown adipose tissue
BCR	B cell receptor
BH4	Tétrahydrobioptérine
BMI	Body mass index
BMP	Bone morphogenic protein
BW	Body-weight
CCL2	C-C motif chemokine ligand 2
CD	Chow diet
CDK	Cyclin dependent kinase
CHK	Checkpoint kinase
CLS	Crown-like structures
CM	Chylomicron
COX	Cyclooxygénase
CTGF	Connective tissue growth factor
CVD	Cardiovascular disease
CXCL1	C-X-C motif chemokine ligand 1

DAG	Diacylglycerol
DC	Dendritic cell
DDR	DNA damage response
DIO	diet induced obesity
ECM	Extracellular matrix
EC	Endothelial cell
ELISA	Enzyme Linked ImmunoSorbent Assay
EPC	Endothelial progenitor cell
EV	Extracellular vesicles
FA	Fatty acid
FACS	Fluorescence-activated cell sorting
FCS	Fetal-calf serum
FFA	Free FA
G3P	Glycerol-3-phosphate
GLUT	Glucose transporter
GTT	Glucose tolerance test
HFD	High fat diet
HIF-1α	Hypoxia-inducible factor 1 α
HP1	Heterochromatin protein 1
HRP	Horseradish peroxidase
HSP90	Heat shock protein 90
IDF	International Diabetes Federation
IL	Interleukin
INSR	Insulin receptor
IRS	Insulin Receptor Substrate
ITT	Insulin tolerance test

JNK	c-Jun N-terminal kinase
LPL	Lipoprotein lipase
MAG	Monoacylglycerol
MCP	Monocyte chemoattractant protein
MDM2	Murine double minute 2
MGL	MAG lipase
MHO	Metabolically healthy obesity
MMP	Matrix metalloproteinase
MSC	Mesenchymal stem cell
mTORC1	Mammalian target of rapamycin
NF-κB	Nuclear factor kappa B
NK	Natural Killer
OIS	Oncogene-induced senescence
OPN	Osteopontin
PAI-1	Plasminogen activator inhibitor-1
PAMP	Pathogen-associated molecular pattern
PBMC	Peripheral blood mononuclear cells
PBS	Phosphate-buffered saline
PDGF	Platelet-derived growth factor
Phe	Phenylalanine
PI3K	Phosphatidyl Inositol 3 Kinase
PKA	Protein kinase A
PKB	Protein kinase B
PPAR-γ	Peroxisome proliferator-activated receptor-γ
PTEN	Phosphatase and tensin homolog

qRT-PCR	Quantitative reverse transcriptase-polymerase chain reaction
RBP4	Retinol binding protein 4
ROI	Region of interest
ROS	Reactive oxygen species
SAHF	Senescence-associated heterochromatin foci
SASP	Senescent-associated secretory phenotype
SAT	Subcutaneous fat
SMA	Smooth muscle actin
SREBP1c	Sterol regulatory element-binding protein
SVF	Stromal vascular fraction
T2DM	Type 2 diabetes mellitus
TAG	Triacylglycerol
TCR	T-cell receptor
TGFβ	Transforming growth factor β
TIMP	Tissue inhibitors of metalloproteinases
TLR	Toll-like receptor
TNF	Tumor necrosis factor
TZD	Thiazolidinedione
UCP1	Uncoupling protein 1
VAT	Visceral adipose tissue
VEGF	Vascular endothelial growth factor
VLDL	Very low-density lipoproteins
WAT	White adipose tissue
WT	Wild-type
ZFR	Zucker fatty rats

Abstract

Obesity has dramatically increased worldwide and has become a major public health burden. Indeed, it increases the risk for death, mainly from cardiovascular disease. Physical inactivity and high energy in diet are known to promote oxidative stress and alter adipose tissue (AT) structure and function. In particular, our team has contributed to identify a critical role of visceral AT on cardiac fibrosis in addition to previous observations showing remote organ damage through a profibrotic and proinflammatory secretome of AT. Interestingly, these secreted factors are coincident with the accumulation of senescent cells in AT during both natural aging and obesity. Cellular senescence is associated with stable cell-cycle arrest induced by various stimuli such as telomere dysfunction and oxidative stress. Its functional implication is illustrated by observations that selective elimination of senescent cells prevents insulin resistance and delays the onset of age-related pathologies.

However, time course of AT senescence and mechanisms underlying its initiation are yet unclear, as well as the precise identity of the cells affected within the AT. Therefore, my Doctoral project aimed to:

- Establish the chronological order of events leading to visceral AT senescence in obesity
- Identify the AT cells mainly affected by cellular senescence
- Explore the role of senescent AT macrophages in the crosstalk between AT and heart.
- Compare different strategies in order to mitigate visceral AT senescence

We showed that AT senescence is an early and primary event that could orchestrate subsequent maladaptive changes in AT and heart function and remodeling. Besides, our results demonstrated the importance of early macrophage senescence in diet-induced and age-related cardiometabolic dysfunction and may shed new light on the search for developing better therapeutic options, including senolytic therapies, in the context of obesity in order to prevent cardiac and metabolic disorders

Résumé

L'obésité a augmenté de façon spectaculaire ces dernières années à travers le monde et ceci est devenu un problème majeur de santé publique. En effet, cela augmente le risque de décès, principalement des suites de maladies cardio-vasculaires. La sédentarité, ainsi qu'une alimentation riche en énergie, sont des facteurs connus pour favoriser le stress oxydatif et altérer la structure ainsi que la fonction du tissu adipeux (TA). Le TA viscéral, en particulier, a été identifié par notre équipe et par d'autres comme étant responsable des dommages causés aux organes distants par l'intermédiaire d'un sécrétome pro-fibrotique et pro-inflammatoire.

De façon intéressante, la sécrétion de ces facteurs coïncide avec l'accumulation de cellules sénescents au niveau du TA au cours du vieillissement naturel mais également dans le contexte de l'obésité. La sénescence cellulaire est définie par l'arrêt irréversible du cycle cellulaire et est déclenchée par différents facteurs parmi lesquels on retrouve le raccourcissement des télomères ou encore le stress oxydatif. Son impact au niveau fonctionnel est démontré par les observations selon lesquelles l'élimination sélective des cellules sénescents prévient l'insulino-résistance et retarde l'apparition des pathologies liées au vieillissement. Cependant, les mécanismes de l'initiation et de l'évolution de la sénescence au cours du temps dans le TA sont encore mal compris, de même que les cellules affectées et les principaux acteurs restent inconnus. Les principaux objectifs de mon projet de thèse consistaient donc à :

- Etablir l'ordre chronologique des événements conduisant à la sénescence prématurée du TA viscéral, et donc à son altération, dans le contexte de l'obésité,
- Identifier les principales cellules affectées par la sénescence,
- Explorer le rôle des macrophages sénescents du TA viscéral dans le dialogue entre TA et cœur,
- Comparer différentes stratégies visant à atténuer les altérations métaboliques et cardiaques liées à l'obésité.

Notre travail a démontré que la sénescence du TA est l'un des premiers événements apparaissant lors de l'obésité et que cette sénescence avait un rôle majeur dans les altérations métaboliques et cardiaques liées à cette pathologie. De plus, nos résultats ont mis en évidence

l'implication des macrophages du TA et leur rôle crucial dans les complications mentionnées, apportant ainsi de nouveaux horizons et de nouveaux éléments dans la recherche et le développement de nouvelles thérapies pour traiter l'obésité et ses comorbidités.

INTRODUCTION

Introduction

The world faces an obesity epidemic afflicting the entire cross-section of society, with increased risk for type 2 diabetes mellitus (T2DM), dyslipidaemia and cardiovascular disease. Physical inactivity and high energy content in diet are known to alter adipose tissue structure and function. Visceral adipose tissue (VAT) is considered paramount to obesity disease and our team has contributed to identify a key role of this organ in promoting cardiac alterations and remodeling through a profibrotic and proinflammatory secretome. Interestingly, these secreted factors were coincident with the accumulation of senescent cells in adipose tissue during both natural aging and obesity. Besides, some studies demonstrated that selective elimination of senescent cells prevents insulin resistance and delays the onset of age-related pathologies.

In the following section, we will summarize the current knowledge about obesity disease and clinical implications, before going more in depth by describing adipose tissue physiology and pathophysiology with a special focus on obesity-induced adipose tissue remodeling and dysfunction and finally give an overview of therapeutic approaches in obesity-associated metabolic complications.

CONTEXT

&

LITERATURE

REVIEW

SECTION 1

OBESITY

Chapter 1: Definition and Epidemiology

Obesity is the consequence of accumulation of fat mass following an imbalance between calorie intake and expenditure. In adult patients, body mass index (BMI) is commonly used to measure the severity of the overweightness. Although it provides no information about the percentage of fat mass in the body, BMI proved useful in clinical evaluation of patients with BMI ≥ 25 kg/m² considered overweight and patients with BMI ≥ 30 kg/m² defined as obese.

Over the past decades, the incidence of obesity has dramatically increased worldwide, especially in Western societies, and the developing world. The worldwide prevalence of obesity nearly tripled between 1975 and 2016 and obesity is now officially recognized as a chronic disease and global epidemic by the World Health Organization. Specifically, in 2016, more than 1.9 billion adults (39% of the world's adult population) were overweight, and 650 million (13% of the world's adult population) were obese.

Obesity is associated with increased risk for type 2 diabetes mellitus (T2DM), dyslipidemia, hypertension and cardiovascular disease and is associated with elevated all-cause mortality compared to normal weight.^{1,2} It was estimated that in 2015, approximately 1 in every 11 adults has T2DM globally, and about 75% of patients with diabetes mellitus live in developing countries³ (figure 1).

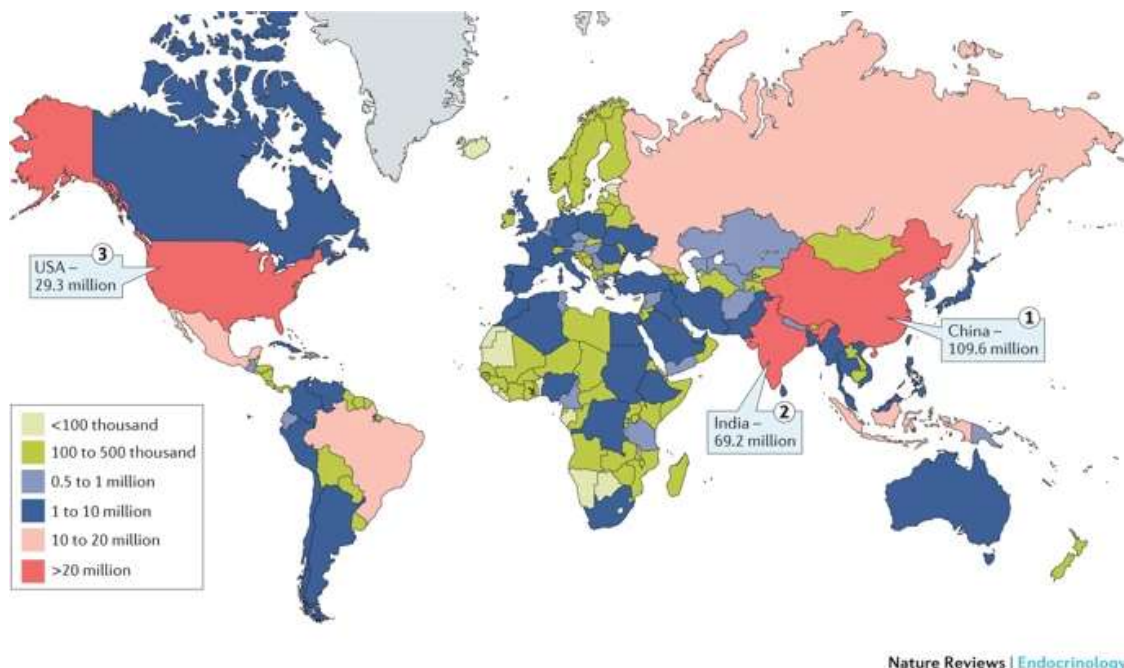


Figure 1: Estimated total number of adults (20–79 years) living with diabetes mellitus, highlighting the top three countries or territories for number of adults with diabetes mellitus (20–79 years) in 2015. (From Zheng & al., *Nat Rev Endocrinol* 2018)⁴

T2DM is characterized by an impairment in insulin action (particularly in insulin-sensitive tissues: liver, muscle and adipose tissue become insulin-resistant), which pancreatic β -cells are not able to compensate by increasing insulin secretion. This imbalance results in abnormal blood levels of glucose.⁵ Associated complications include but are not limited to macrovascular complications leading to cardiovascular disease (CVD) and microvascular complications affecting lower limb, kidney, retina and nervous system.⁴

Global Burden of Disease Study 2013 identified diabetes mellitus (all forms) as the ninth major cause of reduced life expectancy.⁵ In 2010, it was estimated that diabetes mellitus caused 3.96 million deaths in adults aged 20–79 years during that year (6.8% of global mortality).⁶ This estimate was raised to 5 million deaths due to diabetes mellitus and its complications during 2015 in an International Diabetes Federation (IDF) report.

From an economic perspective, about 12% of the global health expenditure was spent on treatment of T2DM and its related complications in 2015.³

Chapter 2: Clinical research and limitations

To address the dual epidemics of obesity and diabetes mellitus, many observational studies and randomized clinical trials showed the importance of prevention by maintaining a healthy body weight with a focus on maintaining energy balance through regular physical activity and healthy diet.^{7,8} Major clinical trials have demonstrated that intensive lifestyle interventions can lower the incidence of diabetes mellitus by 58% compared with control groups and are more effective than pharmacological approaches.⁹

Further studies indicated that not all adipose tissue pads are equal, but different anatomical depots show their own specific characteristics. The significance of varying body fat distribution is best illustrated by different clinical outcomes. Accumulation of visceral adipose tissue (VAT) corrodes health more than subcutaneous fat (SAT) does.^{1,10} Indeed the inability of subcutaneous adipose tissue to store surplus triglycerides may lead to the development of ectopic fat depots in different organs such as the liver, the heart, the muscle and the pancreas. This ectopic lipid deposition is of growing interest, since it is an important contributor to the development of obesity comorbidities¹¹ and may result from a dysfunctional subcutaneous adipose tissue not being able to appropriately store the lipid overload, which is redirected to cells of internal organs, leading to steatosis and organ dysfunction. Regional body-fat

distribution is one of the key variables that explains the metabolic heterogeneity of obesity and its associated cardiovascular risks. This differential repartition of adipose tissue accumulation is due to many factors including genetics, environment, gender and age,¹²⁻¹⁵ (figure 2)

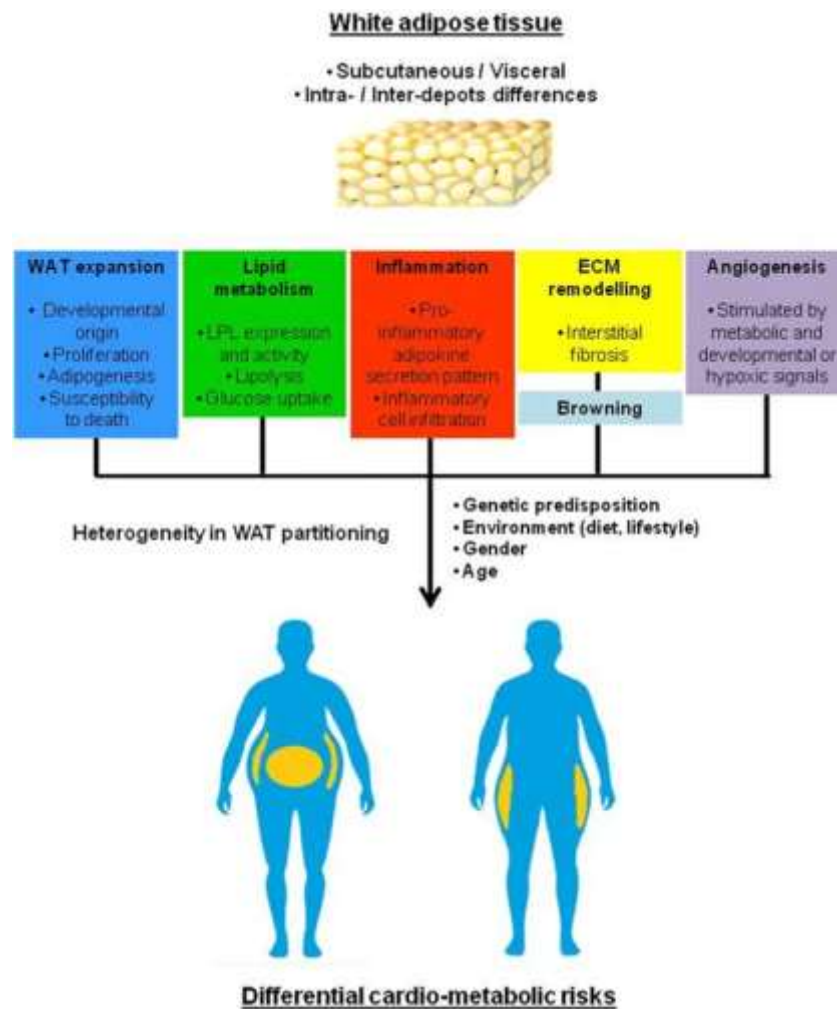


Figure 2: Heterogeneity in WAT repartition and factors involved. (From Guglielmi, V. & al., *Eat Weight Disord* 2018).¹⁰

Observations that a proportion of obese patients have a significantly lower risk for cardiometabolic abnormalities led to the concept of metabolically healthy obesity (MHO). This condition is characterized by lower amounts of ectopic fat (visceral and hepatic), together with normal glucose and lipid metabolism parameters, preserved insulin sensitivity and no hypertension compared to unhealthy obese patients.¹⁶

Such an observation raises therefore the crucial need to characterize the body fat distribution to evaluate the percentage of “ectopic adipose tissue” in the adiposity index. This can be

performed in routine clinic evaluation by different techniques of bioelectrical impedance analysis, or quantitative magnetic resonance for measuring total body water, fat, and lean tissue, as well as imaging techniques to further define ectopic fat depots.¹⁷ 1H-magnetic resonance spectroscopy (MRS) is a reliable noninvasive quantitative method to assess the pancreatic triglyceride content in vivo, which has been validated in rodents and in humans.^{18,19} Another important factor to be evaluated in obese patients is the remodeling of adipose tissue as progression toward obese state is often accompanied by pericellular collagen deposition resulting in decreased extracellular matrix (ECM) flexibility.²⁰ Fibrosis within the adipose tissue compartment is one of the factors that may influence the development of obesity-related comorbidities,²¹ and this parameter can also be measured using the techniques mentioned above. However, the metabolic dysfunction associated with fibrosis may also depend on which fat pads are affected.

Obesity and comorbidities were furthermore studied from an interesting and newly developed point of view which consists in visualizing the potential interrelationships among human diseases and set up a network in which connections are based on common genetic or functional origins. This aims to understand the complex intertwined factors that may be part of an individual disease in order to analyse all the disorders and diseases of an organism as a whole.²² According to this concept, a representation of obesity and T2DM “diseasome” was proposed,²³ (figure 3).

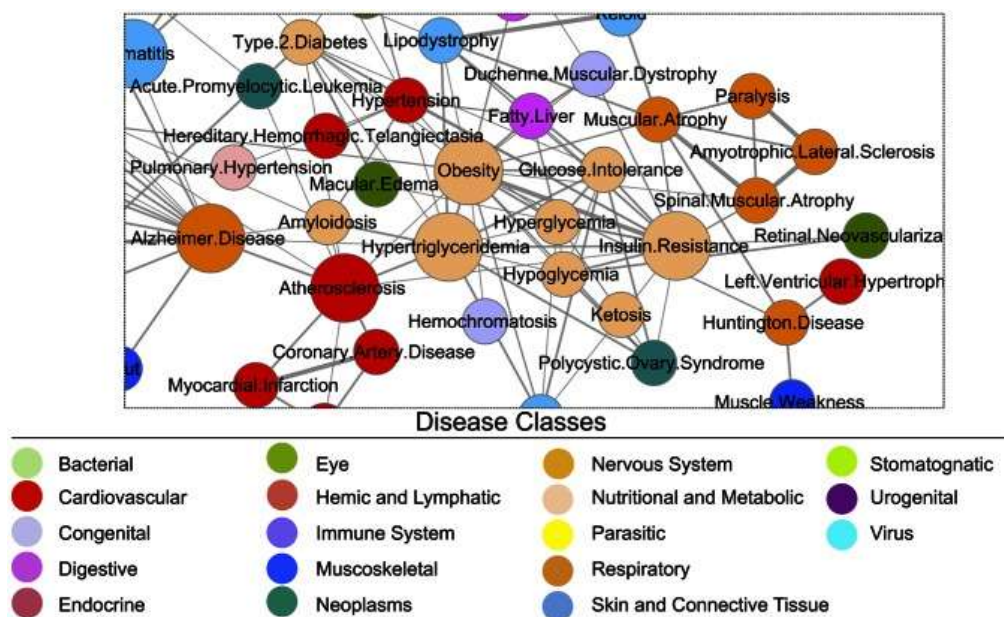


Figure 3: Type 2 diabetes related functional linkage network (T2DFN). (From Rende, D. & al., Plos One 2013)²³

Basic research is particularly helpful in deciphering mechanistic aspects underlying the dysregulation of metabolism, insulin resistance and inflammation that is often not possible through human observational studies. By contrast, suitable adaptations of human conditions to animal models allow intervention studies that can greatly facilitate mechanistic, hence drugable facets of pathology. For instance, basic research has extended our understanding about the pathophysiological role of adipose tissue in obesity-related cardiometabolic diseases. Further to the identification of epicardial adipose tissue as being profibrotic for the adjacent myocardium,²⁴ our group has uncovered the important role of remote visceral adipose tissue in promoting cardiac fibrosis in the context of obesity and aging in a mouse model.^{25,26}

Chapter 3: Animal models

The great degree of anatomical and physiological similarities in humans and mammals encouraged to investigate mechanisms and assess novel therapies in animal models before applying to humans. To further underscore the importance of *in vivo* models, assessment of physiological functions and systemic interactions between organs requires a whole organism that is not available via *in vitro* studies. Several human diseases affect also animal species such as allergies, cancer, epilepsy, myopathies, hypertension, and Type I diabetes. The mechanisms are also very similar in most of the cases and 90% of the veterinary drugs used to treat animals are identical or very similar to those used to treat humans.²⁷ Moreover, a number of major discoveries in basic science and medicine have been possible thanks to observations and testing on animals. A relevant example is the treatment of Type I diabetes by insulin that was established in the dog by Banting and McLeod, who received the Nobel Prize in 1921 for their discovery.²⁸

However, not all results obtained in animals are confirmed in humans. Several reasons were proposed to explain these failed translations. For example, some studies use inappropriate models or neglect the differences between the model used and humans when the percentage of homology is very high. Also, over 95% of genes are homologous between mice and humans,²⁹ yet, this does not exclude physiological discrepancies due to differences in the members of gene families, gene redundancies and nuanced interspecies differences in the regulation of expression. Accordingly, these aspects are increasingly better described and understood.²⁷

Several animal models are available for the study of obesity, which are classified into monogenic and polygenic models. The monogenic models are characterized by mutations in single genes having important roles in metabolism. For example, leptin gene in ob/ob (obese) mice, leptin receptor in db/db (diabetic) mice, tub (tubby) mice, Zucker fatty rats (ZFR), and carboxypeptidase E gene in fat/fat mice. The polygenetic models of obesity are lines of mice or other animals differing in body weight gain and fat deposition dynamic. One of the more intensively studied models of polygenic obesity is the C57BL/6J mice submitted to high fat diet (HFD), also known as model of diet-induced obesity (DIO).^{30,31}

SECTION 2

ADIPOSE TISSUE:

PHYSIOLOGICAL

STRUCTURE & FUNCTION

Chapter 1: Diversity of adipose tissue depots in humans and mice

Adipose tissue in humans and mice is divided into two major subtypes: white adipose tissue (WAT) and brown adipose tissue (BAT).

BAT is localized mostly within the supraclavicular region in humans³² and within the interscapular region in mice but also within the supraclavicular region like in humans.³³ Brown adipocytes contain multilocular lipid droplets and a high number of mitochondria expressing the mitochondrial uncoupling protein 1 (UCP1). Their primary function is to dissipate energy in the form of heat (instead of producing ATP),³⁴ a thermogenic function that may have a role in the regulation of energy balance.³⁵

WAT is the major adipose tissue in mammals and is mainly composed of large adipocytes with a single lipid droplet and much fewer mitochondria than brown adipocytes. However, inducible brown adipocytes, also known as beige adipocytes, can be found inside WAT. Beige adipocytes are phenotypically distinct from both white and brown adipocytes but functionally closer to brown type. Their accumulation in WAT is termed browning and is induced by cold exposure or exercise.³⁶ It has been suggested that browning process could have beneficial effects on metabolism. Hence, the potential therapeutic role of browning in obesity and aging has gained a lot of attention.^{37,38}

There are two anatomically and functionally distinct subtypes of WAT: visceral white adipose tissue (VAT) and subcutaneous white adipose tissue (SAT). VAT in humans consists in omental, mesenteric, retroperitoneal, gonadal and pericardial WAT³⁹ whilst SAT is located in upper (deep and superficial abdomen) and lower (gluteofemoral) body regions.⁴⁰ In mice, VAT is composed of perigonadal, perirenal and mesenteric WAT, and SAT is located all around leg muscles in the inguinal region (figure 4). On average, SAT represents more than 80% of total body fat in humans and act as a protective barrier against external mechanical stress, dermal inflammatory processes and heat dispersion.⁴⁰ Clinically, it has been found to have beneficial effects on metabolism.⁴¹ By contrast, VAT represents 10-20% of total body fat in men and 5-10% in women¹⁰ and is commonly associated with metabolic disorders, such as diabetes and cardiovascular disease.⁴²

In addition to major WAT pads, small tissue-associated or -infiltrating adipose tissue, also known as ectopic fat is distributed across the body,⁴³ (figure 4).

In subsequent sections, WAT will be in focus, and “adipose tissue” or “AT” refers to WAT.

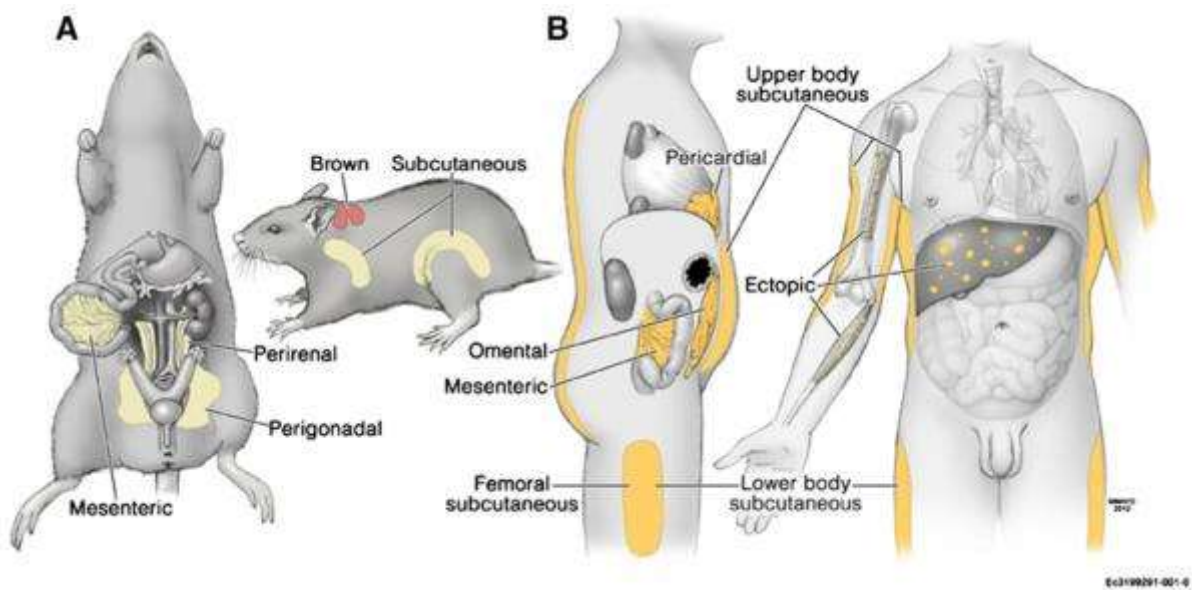


Figure 4: *Anatomy of major fat depots in rodents (A) and Humans (B), (From Tchkonina, T. & al., Cell Metabolism 2013)⁴⁴*

Chapter 2: Adipose tissue cell types and their functions

I) Adipocytes

Mature adipocytes are the parenchymal cells of adipose tissue. They have a key function in regulating lipid metabolism and maintaining normal energy homeostasis by controlling fatty acid (FA) turnover through lipogenesis and lipolysis. As such, mature adipocytes have an important role in the regulation of circulating levels of FA and glucose.

Circulating FAs are derived from the combination of dietary fat intake and endogenous *de novo* synthesis. Fatty acids serve as substrates for energy production and precursors for the synthesis of lipids involved in the membranes (triglycerides) and the cellular signaling (e.g. prostaglandines and leukotrienes). Despite the importance of FAs in physiological processes, their oversupply results in toxic cellular effects. This lipotoxicity is characterized by disruption of biological membrane integrity, alteration of cellular acid-base homeostasis and generation of harmful bioactive lipids. These adverse effects, in turn, induce endoplasmic reticulum stress, mitochondrial dysfunction, inflammation and cell death.^{45,46} To avoid toxicity of free

FAs (FFAs), adipocytes are able to detoxify non-esterified FAs by esterification with glycerol to produce inert triacylglycerols (TAGs), a process called lipogenesis.

1.1) Lipogenesis

The canonical stimulant of lipogenesis is insulin. Prior to lipogenesis *per se* insulin increases glucose uptake through glucose transporter GLUT4 into adipocytes and induces glycolysis. The combined action of glycolysis and pyruvate dehydrogenase activity provides glycerol-3-phosphate (the backbone of TAGs) and acetyl-CoA (the FFA precursor), respectively. FFAs, as previously mentioned, can also be derived from dietary fat intake. In that case, lipoprotein lipase (LPL), secreted by adipocytes and localized within capillaries lumen is a key enzyme that hydrolyzes TGs contained in chylomicrons and very low-density lipoproteins (VLDL) to provide FFAs,⁴⁷ (figure 5).

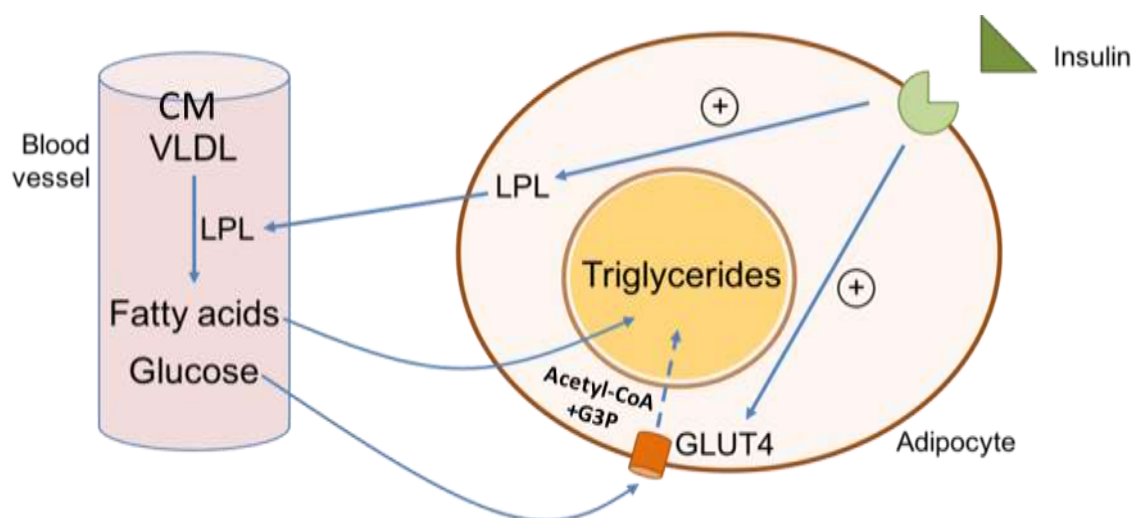


Figure 5: Regulation of lipogenesis within adipocytes. CM: chylomicron; VLDL: very low-density lipoproteins; LPL: Lipoprotein lipase; G3P: glycerol-3-phosphate. (modified from *exsymol.com*: <https://www.exsymol.com/en/dossier/lipogenese/>)

1.2) Lipolysis

During fasting or sympathetic activity, lipogenesis is inhibited, whilst lipolysis is induced. These states are typically characterized by low insulin concentrations as well as activation of the β -adrenoreceptor signaling by catecholamines released from sympathetic nerves stimulated by low blood glucose levels. Consequences of these upstream events are increased TAG

breakdown followed by the release of glycerol and FFA from adipocytes. At least three different enzymes are involved in this process:

- Adipose triglyceride lipase (ATGL) catalyzes the initial step of lipolysis by converting TAGs to diacylglycerols (DAGs).
- Hormone-sensitive lipase (HSL) is mainly responsible for the hydrolysis of DAGs to monoacylglycerols (MAGs) and finally,
- MAG lipase (MGL) hydrolyzes MAGs.

ATGL and HSL are responsible for more than 90% of TG hydrolysis subject to β -adrenergic stimulation, activation of adenylate cyclase and PKA,⁴⁷ (figure 6).

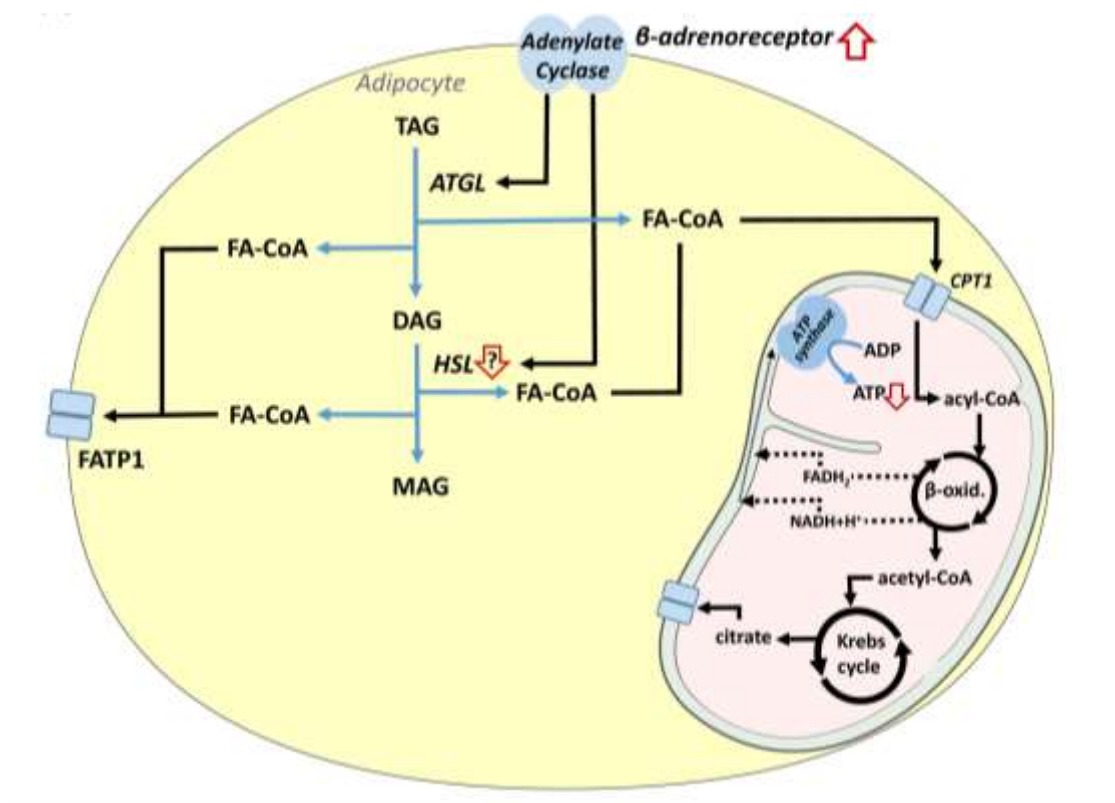


Figure 6: Regulation of lipolysis within adipocytes. Black arrows indicate pathways of biochemical substrates and products. Blue arrows indicate joined pathways of biochemical substrates resulting in the respective product. Open arrows in red show the direction of change in the insulin-resistant state (From Bódis, K. & al., Eur J Clin Invest. 2018)⁴⁷

Adipocytes express 4 types of adrenergic receptors: beta1, beta2, beta3 and alpha2. Beta receptors are mostly expressed in VAT, and catecholamine-induced lipolytic response is higher

in VAT. Alpha2-receptors (anti-lipolytic effect) are highly expressed in SAT. On the other hand, VAT is less sensitive to insulin as opposed to SAT so insulin-stimulated lipogenesis is preferentially occurring in the SAT.^{10,39,47} These characteristic differences may explain why SAT is a metabolically healthier fat pad compared to VAT.

1.3) Secretory activity

The discovery of leptin in 1994⁴⁸ and adiponectin one year later⁴⁹ led to a widespread recognition of adipose tissue as an endocrine organ. Other adipose tissue-secreted signaling mediators, known as adipokines, have been identified since then, and were involved in the communication linking adipose tissue with other organs of the body with a role in maintaining systemic homeostasis in physiological conditions or participating in organ remodeling or failure in pathological processes such as aging and obesity (see Section 3, chapter 4, part V). Leptin, a 16 kDa protein hormone, is an adipokine secreted by adipocytes, acting to regulate food intake and energy expenditure. This occurs by communicating information about the degree of adiposity to the brain. Specifically, increasing adiposity enhances plasma leptin levels, which then reduces food intake by inhibiting secretion of neuropeptide Y and Agouti-related protein in the hypothalamus, whilst simultaneously boosts energy expenditure.^{50,51} Much of our understanding about leptin's role in metabolic regulation comes from observations made in leptin deficient ob/ob mice and congenital leptin deficient humans. Importantly, both affected mice and humans show severe obesity, together with glucose intolerance and insulin resistance, whilst symptoms were reversed by leptin administration.^{52,53} Leptin exerts its effect on target tissues by binding to its receptor Ob-R. This receptor is found in the brain but has also been identified in peripheral tissues such as adipose tissue, skeletal muscle, liver, pancreatic beta cells, blood mononuclear cells, lymphocytes, and endothelial cells. Through its insulin-like effects on glucose metabolism leptin is considered as potential treatment to attenuate hyperglycemia in type 1 diabetes in mice, rats, and lipodystrophy syndromes in humans.⁵⁴⁻⁵⁶ Expression and secretion of leptin is subject to complex regulation with a plethora of factors involved. For example, leptin is upregulated by insulin, glucocorticoids, TNF α , estrogens, and CCAAT/enhancer-binding protein- α and downregulated by β 3-adrenergic activity, androgens, free fatty acids, growth hormone, and peroxisome proliferator-activated receptor- γ (PPAR- γ) agonists.⁵⁷

Leptin is not the only adipokine that adipocytes secrete. As a matter of fact, after the discovery of leptin, a number of other adipokines have been identified, the most important of which is adiponectin. As opposed to leptin levels, plasma levels of adiponectin are elevated in lean human subjects and reduced in with obesity and type 2 diabetes.^{58,59} Adiponectin secretion is upregulated via PPAR- γ agonists such as the anti-diabetic drugs thiazolidinediones (TZDs) and this contributes to improve insulin sensitivity as extensively demonstrated in animal and human subjects treated with TZDs.⁶⁰ Interestingly, adiponectin as much as leptin are predominantly produced in SAT rather than VAT.

Beyond adipokines, adipose tissue is a highly dynamic secretory organ that employs a plethora of lipids, metabolites, noncoding RNAs, and extracellular vesicles (EVs) to relay information to other organs of the body. EVs – encompassing microparticles, exosomes, and apoptotic bodies – are emerging as a novel mode of communication between cells and have been recently implicated in physiological and pathological processes.⁶¹ For instance in metabolic syndrome, they were shown to promote liver fibrosis by up-regulating tissue inhibitor of matrix metalloproteinase (TIMP)-1 and integrin $\alpha\beta$ -5, whilst downregulating some matrix metalloproteinases (MMP-7 and MMP-9).⁶² Furthermore, EV isolated from obese adipose tissue of mice induced an M1-like macrophage polarization with secretion of proinflammatory cytokines such as interleukin (IL)-6 and tumor necrosis factor (TNF)- α , and led to the development of insulin resistance when injected *in vivo* to WT mice.⁶³ (figure 7).

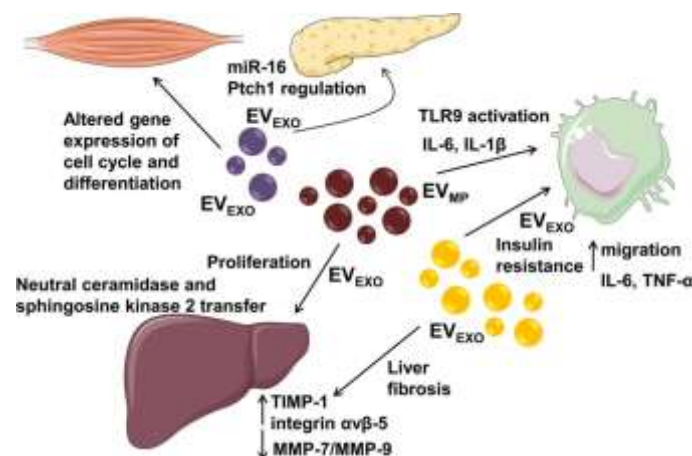


Figure 7: Effects of extracellular vesicles (EVs) from adipocytes, hepatocytes, and skeletal muscle. (From Martínez MC, Andriantsitohaina R. *Circ Res.* 2017)⁶¹

II) Adipose-derived stem cells (ADSCs) and preadipocytes

Adipocyte progenitors are mostly localized in perivascular areas where adipogenesis starts.^{64,65}

Adipogenesis is the process that results in the formation of mature adipocytes. It is divided into two major stages: the determination phase - or commitment - and terminal differentiation. The determination phase is the conversion of the ADSC into a preadipocyte without any change in morphology but with a loss of multipotency. A fundamental property of preadipocytes is their ability to constantly proliferate and differentiate into mature adipocytes, allowing adipose tissue to have plasticity and capacity for expansion.⁶⁵ Terminal differentiation refers to the mechanisms that a committed preadipocyte undergoes transformation into a mature adipocyte, starting with growth arrest, followed by mitotic clonal expansion before final differentiation.⁶⁴

Adipogenesis is mainly regulated by preadipocytes themselves. Underlying regulation involves several pathways in a complex organization and at different levels. WNT signaling pathway for example promotes adipogenesis through upregulation of WNT5B gene or inhibits it by upregulating WNT10 gene. Hedgehog signaling pathway suppresses preadipocyte differentiation by downregulating peroxisome proliferator-activated receptor gamma 2 (PPAR- γ 2) expression. Transforming growth factor β (TGF β) and preadipocyte factor-1 (Pref-1/ Dlk1) are other inhibitors of the adipogenic transformation of preadipocytes, whilst bone morphogenic proteins (BMPs) promote the commitment of pluripotent stem cells to the adipogenic lineage. This complex regulation ensures control of preadipocyte homeostasis within adipose tissue.^{64,66-71}

Moreover, several other parameters modulate adipogenesis such as extracellular matrix (ECM) composition and stiffness,⁷² the secretome of adipocytes and SVF cells,⁷³ epigenetics,⁷⁴ miRNAs,⁷⁵ androgenic hormones,⁷⁶ etc...

In addition to responsiveness to extrinsic factors, intrinsic cell properties are known to shape preadipocyte dynamics. Tchkonja & al. reported the existence of two different preadipocyte subtypes in humans, which differ in their capability for replication and differentiation.⁷⁷ Taken together, the differences observed between fat pads come down to inherent differences in a highly complex regulatory circuit.

During differentiation, as the cells progress from immature stem cells to committed preadipocytes and eventually to mature adipocytes, the cell surface markers change accordingly, with CD34 being the most frequently used preadipocyte cell marker.⁶⁵ However, a large variety of cell surface markers expressed in ADSCs and committed preadipocytes has been reported^{64,65,78,79} (Table 1).

Table 1 Surface marker expression in ADSCs and committed preadipocytes

Authors	Surface markers on ADSCs	Surface markers on committed preadipocytes
Cawthorn et al. 2012	Sca-1+, 3G5+, HLA-ABC, ABCG2+, NG2+, CD10+ CD13+, CD29+, CD34+ CD44+, CD49a+, CD49b+, CD49d+, CD49e+ CD55+, CD59+, CD71+ CD73+, CD90+, CD105+ CD120a+, CD124+, CD140a+, CD140b+, CD166+	Sca-1+, NG2+, CD24+, CD29+, CD34+, CD90+, CD140b+
Cristancho and Lazar 2011	N/A	CD24+, CD29+, CD34+, SCA1+
Zimmerlin et al. 2013	CD105+/CD44+/CD34+	CD146-/CD31-/CD34+/CD73+/CD105+/CD90+
Moreno-Navarrete and Fernandez-Real 2014	CD31-, CD34+, CD45-, CD90+, CD105+, D146-	CD24+, CD29+, CD34+, SCA-1+
Hausman and Dodson 2013	CD29+, CD31-, D34+, CD44+, CD45-, CD73+, CD90+, CD105+, CD146-	CD24+, CD29+ CD34+, SCA-1+
Bourin et al. 2013	CD13+, CD29+, CD44+, CD73+, CD 90+, CD105+ CD34+, CD31-, CD45- CD235a-	CD10+, CD26+, CD36+, CD49d+, CD49e+, CD3- CD11b-, CD49f-CD106-, PODXL-
Rosen and Spiegelman 2014	Lin-/CD34+/CD29+/SCA-1+	CD24+, CD29+, CD34+ SCA-1+
Ussar et al. 2014	N/A	CD34+/ SCA1+/Ter119-/CD45-Asc-1 also known as SLC7A10
Arimochi et al. 2016	N/A	CD45-/CD31-/CD29+/ CD34+/Sca-1+/ CD24+ and CD45-/CD31-/CD29+/ CD34+/Sca-1+/ CD24-
Chazenbalk et al. 2011, 2013	CD34+, CD105+, CD146+	CD34+, CD68+, DLK+
Walmsley et al. 2015	CD36 Low, CD40 Low	CD40 High, CD36 (class B scavenger receptor family member) High. CD36 expression promotes adipo- cyte differentiation and adipogenesis
Harhour et al. 2010	N/A	CD146
Buxser et al. 1985	N/A	CD271
Tchkonina et al. 2005, 2007, 2013	CD105+ (SH2), PDGFR- α + (CD140a), CD166, FGF2, FGF7, MMP2	CD34, ZFP423 LPL, MMP3

Table 1: Surface marker expression in ADSCs and committed preadipocytes (Modified from Sarantopoulos, C. N. & al., *Stem Cell Rev Rep* 2018)⁶⁴

The origin and fate of preadipocytes are not entirely clear; several lines of evidence support mesenchymal origin but hematopoietic origin is not altogether excluded.⁸⁰ Preadipocytes are mainly giving rise to mature adipocytes but when put in adequate environment they are able to differentiate into other cell types, like for example macrophages. This property was demonstrated in an elegant set of experiments by Charriere & al: when injected into the peritoneal cavity or co-cultured with macrophages, preadipocytes were rapidly and efficiently converted into macrophages.⁸¹ Other studies showed that macrophages also can transform into preadipocytes when co-cultured with ADSCs and mature adipocytes, further showing a significant plasticity between these cells.⁷³

III) Endothelial cells and their progenitors

Mature adipocytes are not the only cells found in adipose tissue, in normal state, they represent one-third of the cells in total ; the remainder is a combination of a heterogenous collection of cells known as the stromal vascular fraction (SVF), which includes mesenchymal stem cells (MSCs), preadipocytes, fibroblasts, endothelial cells along with their progenitors, and immune cells.⁸²⁻⁸⁶ Endothelial cells (ECs), pericytes and endothelial progenitor cells (EPCs) are found in the adipose tissue as a part of the SVF. ECs constitute the vessels and are surrounded by pericytes. EPCs are circulating and attracted by angiogenic factors produced by cells under hypoxic conditions. Adipose tissue expansion requires vessel remodeling and growth. The chain of events is as follows: tissue expansion creates a hypoxic microenvironment, which induces lactate production by adipocytes and preadipocytes, IL-8 secretion by macrophages and pro-angiogenic factors including VEGF, TGF- β , angiopoietins, leptin and others by adipocytes and other adipose tissue cells.⁸⁷ The combination of these factors facilitates EPCs recruitment and differentiation to form new vessels in a process called angiogenesis. ECs and EPCs are identified by their specific marker CD31 and studies showed that they may represent 25% of total SVF cells.^{88,89}

IV) Adipose tissue immune cells

Immune cells, also known as leucocytes, are normally found in adipose tissue, interspersed with adipocytes. They are the local sentinels of the immune system.

Leucocytes originate from bone marrow and/or lymphoid organs and found in blood/lymphatic circulation system, with some of them becoming tissue residents. They are divided into 3 subtypes: granulocytes, lymphocytes, and monocytes.

Granulocytes are composed of neutrophils, basophils, and eosinophils. In adipose tissue, they are very few but still important as they are the first cells to migrate to sites of acute infection and injury and start immune response by inducing recruitment of further immune cells.⁹⁰

Lymphocytes belong to one of three subpopulations: Natural Killer (NK) lymphocytes expressing CD16 cell surface marker (CD16+), B lymphocytes (CD19+) and T lymphocytes (CD3+). NK cells have two major functions. The first function is to eliminate tumours or infected cells through cytotoxic activity, whilst secondly NK cells additionally stimulate

immune response by modulating other immune cells via cytokine production. B lymphocytes are activated in later stage during immune response as they trigger the adaptive phase. Their main role is to produce antibodies after being activated either directly by the antigens or by T lymphocytes.⁹¹ The process starts when B-cell link an antigen through specific membrane receptors known as B cell receptors (BCRs). Then, in a process common to all antigen-presenting cells (APCs), they display the antigen complexed with MHC class II molecules on their surface and T-cells recognize these complexes thanks to their T-cell receptors (TCRs). As a result, T-cells get activated and produce cytokines including IL-2, IL-4 and IL-5, which will in turn activate B-cells and allow them to produce antibodies (figure 8). T lymphocytes are divided in 3 subpopulations: T cytotoxic lymphocytes (CD8+), T helper lymphocytes and regulatory T-cells (Treg) which are both CD4+. T cytotoxic lymphocytes have the same functions as NK cells except that they act in a more targeted way: they specifically kill cells with an antigen they recognized before. T helper lymphocytes participate in the elimination of target cells indirectly through modulation of other immune cells. Treg cells play an important role in modulating the immune response toward the end of it in order to make sure inflammation stops as soon as the danger is gone.⁹¹

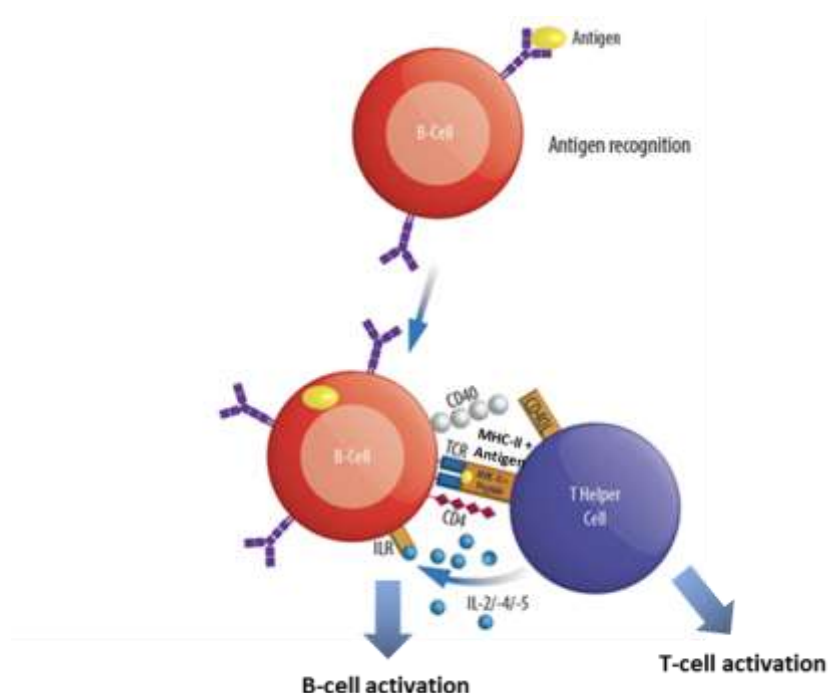


Figure 8: T-cell-dependant B-cell activation (Modified from preprotech.com: <https://www.preprotech.com/de/immunology-research-booklet-2>)

Monocytes are the largest type of leukocytes and are circulating cells with the ability to infiltrate a tissue and differentiate either into dendritic cells (DCs) or macrophages. Main functions of DCs and macrophages are phagocytosis, antigen presentation and, like all immune cells, cytokine production. They are special in the sense that they are a part of both innate and adaptive immune system, potentially displaying either pro- or anti-inflammatory properties. Adipose tissue macrophages (ATMs) have a key role in maintaining tissue integrity and homeostasis. DCs can cover a large surface of tissue thanks to their specific shape with branched projections also called dendrites – hence their name – that makes them particularly suited for antigen presentation. Although they functionally overlap with tissue macrophages, they are more involved in antigen presenting activity. ATMs can adopt a similar spreading shape, but this mostly occurs in inflammation, otherwise in normal condition they are small. Their main activity is phagocytosis, more specifically efferocytosis, which consist in clearance of cell debris and apoptotic cells. In adipose tissue, they participate in ensuring adipocyte turnover and keeping tissue health. ATMs are classically divided into several subpopulations according to their surface markers, which reflect different activation states. The most investigated macrophage states (also known as macrophage polarisation) are classically activated M1 inflammatory and alternatively activated M2 anti-inflammatory polarisations with M0 phenotype corresponding to the non-activated state. During the past few years, however, ATMs and their role in metabolic disease suggested that the canonical division of macrophage phenotypes inaccurately describes ATMs *in vivo*. This recognition led to the discovery of a wide range of intermediate phenotypes such as "metabolically activated" (MMe) or "oxidized" (Mox) macrophages, which are both associated with insulin resistance,⁹²⁻⁹⁶ (figure 9).

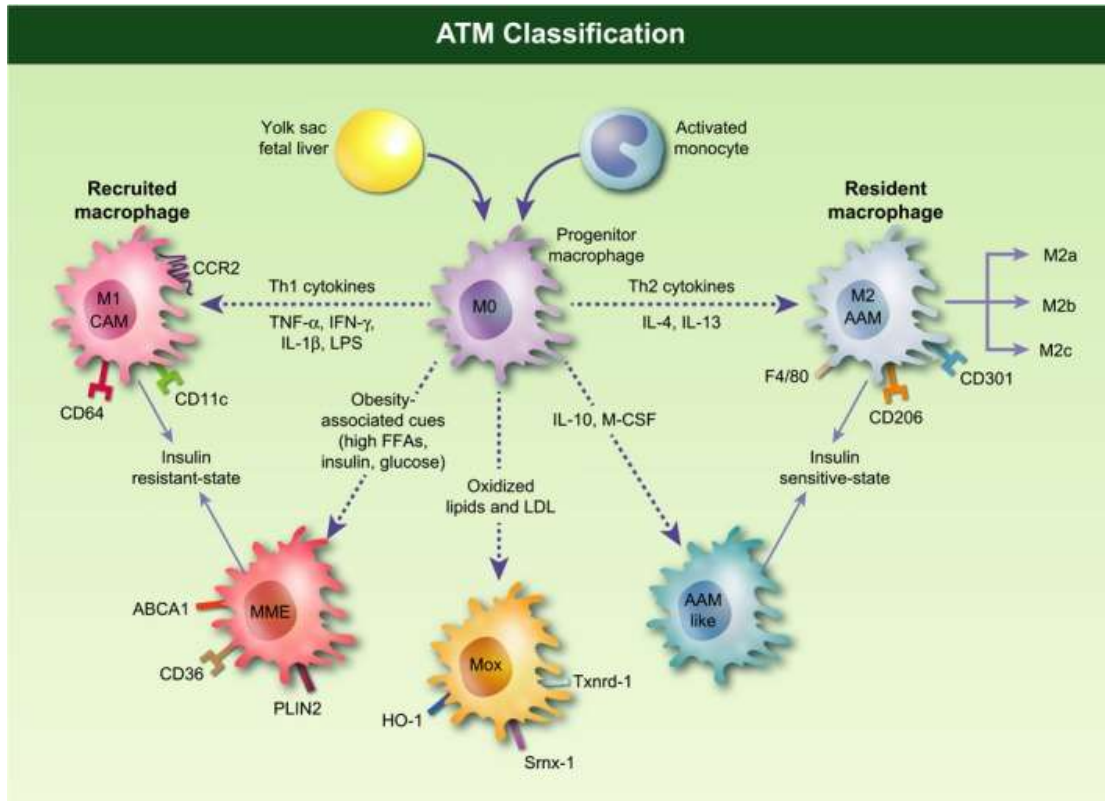


Figure 9: Adipose tissue macrophages (ATMs) classification. AAMs: alternatively activated macrophages; MME: metabolically activated macrophages; Mox: oxidized macrophages. (From Russo, L. & al., Immunology 2018)⁹²

SECTION 3

ADIPOSE TISSUE:

PATHOPHYSIOLOGICAL
STRUCTURE & FUNCTION

Introduction

During obesity, as a consequence of calorie overload, adipose tissue undergoes progressive expansion and remodeling leading to functional alterations with adverse effects on metabolism locally and systemically.⁹⁷

In physiological condition, hyperglycaemia following food intake stimulates insulin secretion in pancreatic β -cells. Insulin stimulates then glucose uptake and lipogenesis in adipocytes through PI3K/Akt signalling pathway and adipose tissue homeostasis is preserved.⁴⁷ In the context of calorie overload, adipose tissue maintains whole body energy homeostasis through hyperplasia (cell number increase ie. increased adipogenesis) and hypertrophy (cell size increase).⁹⁸ In obesity, excessive lipogenesis, together with impaired adipogenesis leads to adipocyte hypertrophy, lipotoxicity, cell dysfunction and death.^{47,99} Adipocyte death by necroptosis has been shown to dramatically increase in obese mice and humans.^{100,101} Adipocyte hypertrophy and death results in excessive leptin, cytokine and chemokine secretion leading to immune cell recruitment and formation of crown-like structures (CLS) – i.e. macrophages and other immune cells surrounding dead or dying adipocytes.¹⁰⁰ Unlike acute inflammation happening in physiological condition, inflammation in obese AT becomes persistent and systemic over the time, which is known as chronic low-grade inflammation.⁹¹

Chapter 1: Obesity and insulin resistance

I) Insulin signaling pathway in adipocytes

Insulin is an endocrine peptide hormone that binds intramembrane receptors in target cells to orchestrate an integrated anabolic response to disposable nutrients.

Although insulin receptors are expressed in many cell types, the role of insulin in glucose homeostasis is mainly characterized by insulin's direct effects on skeletal muscle, liver, and white adipocytes.¹⁰² In skeletal muscle, insulin increases glucose uptake and glycogen synthesis.^{103,104} In liver, it promotes glycogen synthesis, increases lipogenic and decreases gluconeogenic gene expression.¹⁰⁵⁻¹⁰⁸ In WAT, our focus here, insulin inhibits lipolysis, induces lipogenesis, and enhances glucose uptake.

Once insulin protein binds to the extracellular α subunits of the receptor, it induces phosphorylation of tyrosine residues in the intracytoplasmic β subunits. This leads to phosphorylation of Insulin Receptor Substrate (IRS-1) which, in adipocytes, induces Phosphatidylinositol 3 Kinase (PI3K) and protein kinase B (PKB/Akt) recruitment and activation,^{102,109} (figure 10).

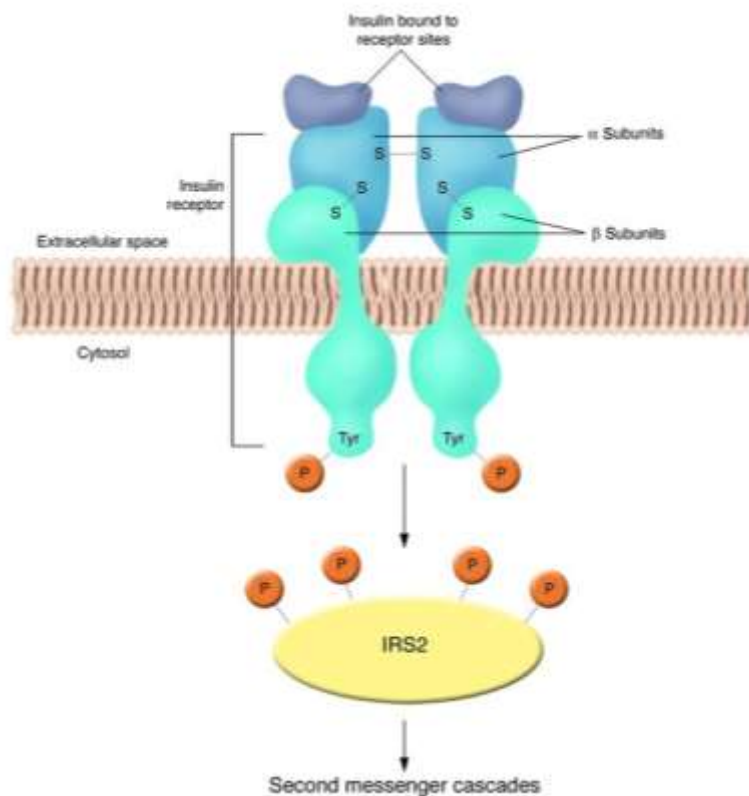


Figure 10: *Insulin receptor (INSR) activation and the associated signal transduction. (From Matthew J. Brady, J Clin Invest. 2004)¹⁰⁹*

The antilipolytic effect of insulin is mediated via insulin-dependent activation of adipose-specific phospholipase A2 (AdPLA2) which inhibits adenylate cyclase and also via Akt activated mammalian target of rapamycin (mTORC1) which inhibits β -adrenoreceptor-induced ATGL transcription.⁴⁷ On the other hand, mTORC1 induces lipogenesis through activation of sterol regulatory element-binding protein (SREBP1c),⁴⁷ (figure 11).

Insulin also promotes adipogenesis through the transcription factor peroxisome proliferator-activated receptor- γ (PPAR γ).¹¹⁰

Stimulation of glucose transport into adipocytes is another main function of insulin, despite the fact that it only accounts for a small fraction of whole-body glucose disposal.¹¹¹ This process is mediated by PKB/Akt which promotes Glucose transporter 4 (GLUT4) translocation into cell membrane, (figure 11). Internalized glucose provides a source of glycerol-3-phosphate to which fatty acids can be esterified, and insulin enhances lipoprotein lipase activity in adipose tissue endothelium.^{112,113}

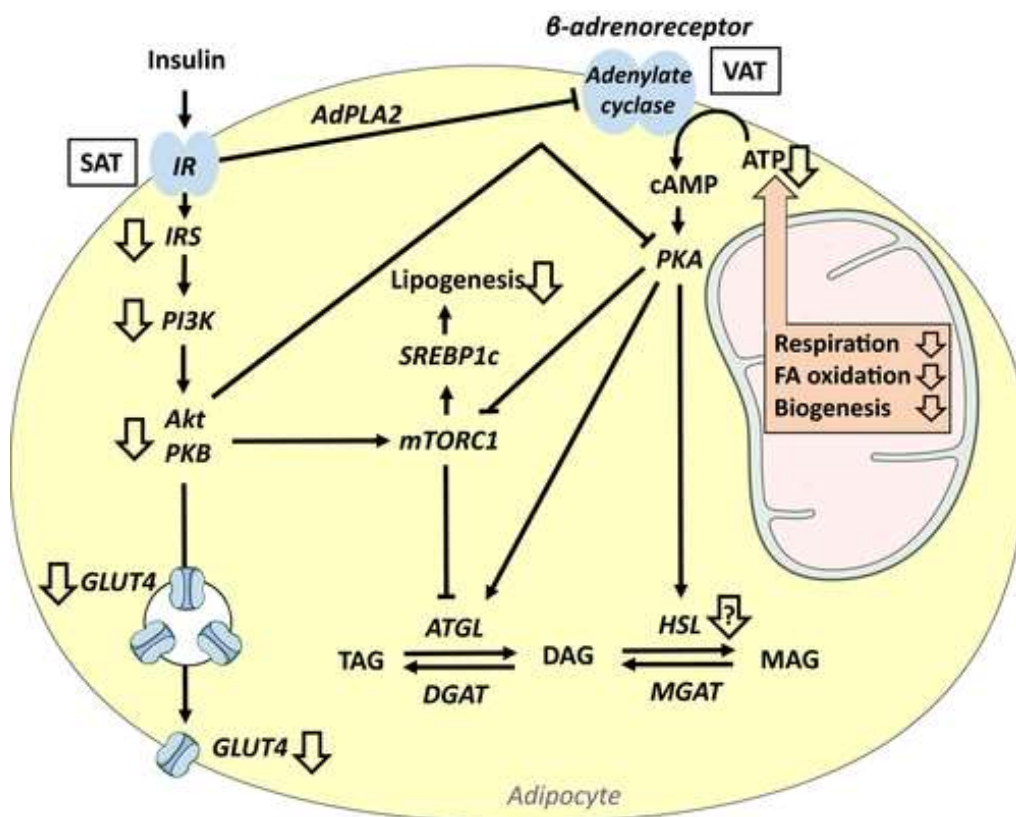


Figure 11: Insulin signaling pathway in adipocytes. Black arrows indicate pathways of biochemical substrates and products and unfilled thick arrows indicate the direction of change in insulin-resistant state. (From Bódis, K. & al., *Eur J Clin Invest.* 2018)⁴⁷

At the level of the whole organism, indirect effects of insulin via tissue cross-talk are also important and sometimes predominate over direct effects. Among several examples, a particularly well-studied one is the insulin-adipocyte-hepatocyte axis and its control of hepatic glucose production where insulin suppresses hepatic gluconeogenesis by inhibiting lipolysis in WAT.^{114,115}

II) Mechanism of insulin resistance in adipocytes

When higher circulating insulin levels are needed to achieve the integrated glucose-lowering response described above, we can talk of insulin resistance. Hyperglycemia and hyperinsulinemia are both features of insulin resistance as we can see in T2D patients.

Glucose and lipid overconsumption, usually seen in obesity create a toxic environment for organs and are responsible for the alterations in both insulin target tissues and pancreatic β -cells. The defective insulin action at target cells is due to receptor defects together with decreased surface insulin receptor (INSR) content, but also to post-receptor defects, i.e. impaired signal transduction. In adipocytes, as in muscle and liver, a decrease in tyrosine kinase activity in T2D patients was shown.^{116,117}

Glucose transport alterations in adipocytes resulting from INSR dysfunction aggravate the situation even though WAT is not a quantitatively significant site of insulin-stimulated glucose disposal, accounting for <5% of an oral glucose load in humans.^{118,119} Yet adipose-specific deletion of GLUT4 in mice resulted in liver and skeletal muscle insulin resistance without any change in body weight¹²⁰, highlighting once again the importance of indirect effect of insulin through cross-talk between organs and the role of adipokines such as, in this case, retinol binding protein 4 (RBP4) and nicotinamide N-methyltransferase,^{121,122} (figure 12).

The impact of adipocyte insulin resistance on lipid metabolism is of immense pathophysiological importance, considering that AT is the major source of plasma FFA, and that lipolysis is a critical and very fast regulator of hepatic gluconeogenesis which regulates fasting glycemia,¹²³⁻¹²⁵ (figure 12). However, whether insulin resistance to suppression of adipose lipolysis involves primarily increased lipolysis per se, decreased re-esterification of FA, or both is not clear, although some studies move toward lipid storage defects rather than lipolysis defects.^{126,127}

Interestingly, unlike liver and skeletal muscle, the specific molecular defects related to adipocyte insulin resistance are largely uncharacterized. Studies have mostly focused on autocrine and paracrine effects of inflammatory cytokines and their impact on insulin signalling,¹²⁸⁻¹³⁰ despite the fact that some studies have shown that insulin resistance was evident after few days of HFD feeding and before significant inflammation develops, suggesting that non-inflammatory mechanisms are probably responsible for the initial dysfunction leading to adipocyte insulin resistance.^{131,132}

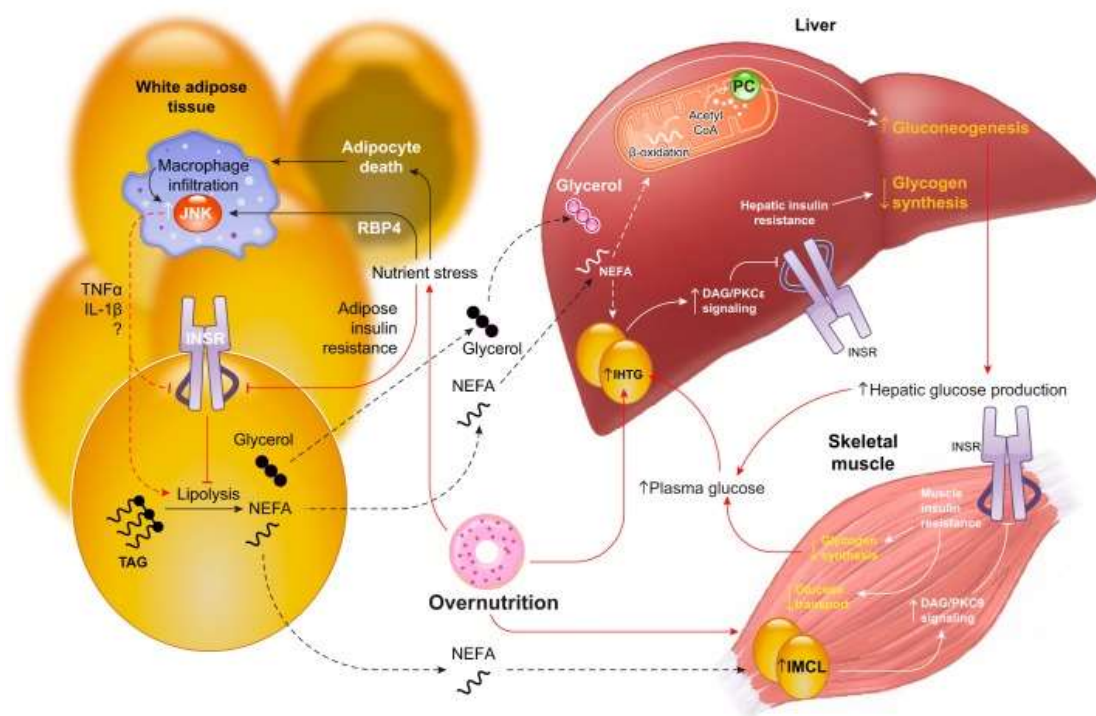


Figure 12: *Physiological impact of insulin resistance: an integrated perspective.* (From Petersen, M. C. & al., *Physiol Rev.* 2018)¹⁰²

Chapter 2: Obesity and low-grade inflammation

Inflammation can happen in response to microbial infection, which leads to the recruitment of inflammatory cells, especially innate immune cells, such as neutrophils, dendritic cells and macrophages. Their role is based on recognizing general aspects of molecules associated with pathogens (pathogen-associated molecular patterns, or PAMPs) through toll-like receptors (TLRs), a family of transmembrane proteins that play an important role in the innate immune system.^{133,134} Inflammatory response can also be activated in case of tissue injuries. Regardless of the nature of the evoking stimulus inflammation trends towards resolution and homeostasis.

In the context of obesity and metabolic syndrome, local and systemic inflammation is observed, but the process is quite different, as the resolution part is absent, and inflammation becomes chronic and progressively harmful. This process is known as chronic low-grade inflammation.^{133,134}

Evidence that obesity causes inflammation started emerging in the 1990s. Hotamisligil et al. showed that genetically obese rodents had increased expression of the TNF- α gene in WAT and that the neutralization of TNF- α protein by anti-TNF- α antibodies decreased the resistance of these animals to insulin action, hence, establishing the link between obesity, inflammation and insulin resistance.¹³⁵

During obesity, saturated fatty acids, particularly lauric acid and palmitic acid present in high concentration in AT stimulate inflammatory response through the TLR4 signaling pathway.¹³⁶ TLR4 is expressed in innate immune cells, including macrophages, but also in other cell types such as adipocytes. Once the FA is bound to TLR4, it activates the kinase proteins JNK-1 and IKK- β , which in turn activate the transcription factors nuclear factor kappa B (NF- κ B) and the activating protein (AP-1). Both proteins translocate to the nucleus and activate the transcription of many genes encoding pro-inflammatory cytokines including TNF- α , COX-2, and IL-6^{137,138} and chemokines such as MCP-1.¹³⁹ In adipocytes, JNK-1 and IKK- β are also capable of phosphorylating IRS-1 at the serine 307 residue, hence reducing IRS-1 interaction with the insulin receptor beta subunit, which results in decreased signal transduction and insulin resistance,^{140,141} (Figure 13).

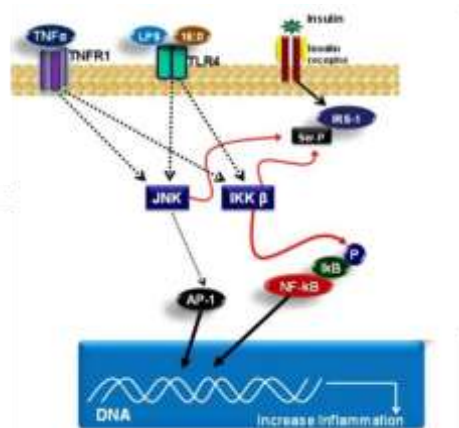


Figure 13: Molecular mechanism of the effects of saturated (16:0) fatty acids on the TLR4 and NF- κ B pathways. (Modified from Marcelo Macedo Rogero & al., *Nutrients* 2018)¹³⁴

Initial obesity-associated inflammation is generated as a stress response by the adipocytes themselves, and by the subsequent necroptotic cell death probably induced by adipocyte hypertrophy.¹⁰⁰ Then, progressively immune cells become more potent sources of inflammation inside AT.^{91,142}

Within the expanding AT, the recruitment of cells of the innate immune system such as macrophages, dendritic cells, neutrophils, and mast cells increases.^{91,143} These cells play in fact a key role in the initiation of inflammatory response and RBP4 was shown to have a crucial role in regulating and activating this process.¹⁴⁴ Recruited macrophages in turn activates adaptive immune cells and both B and T cells accumulate in the tissue (figure 14).

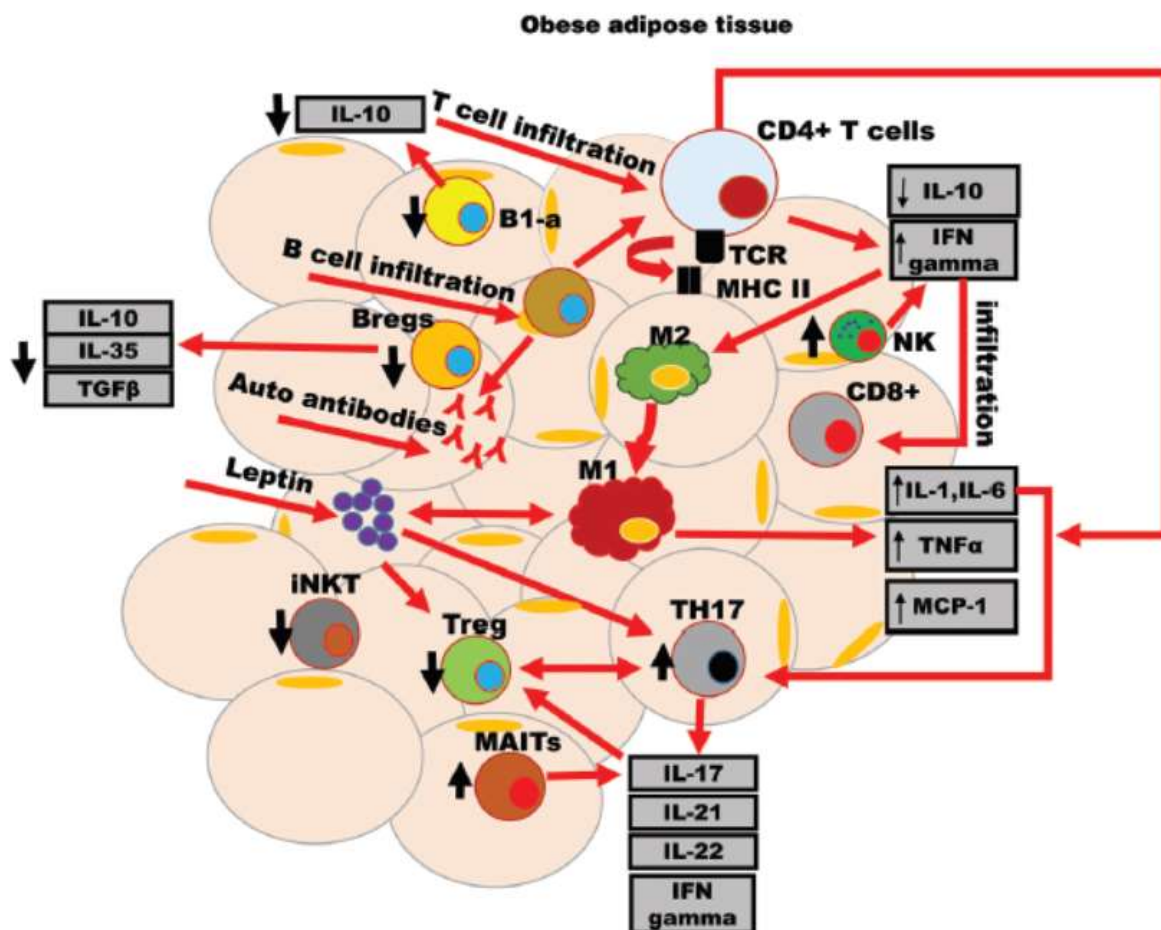


Figure 14: Immune cells infiltrates and inflammation in obese adipose tissue.
(From Bharath, L. P. & al., *Compr Physiol.* 2017)⁹¹

Macrophages correspond to about 40% of total WAT cells in obese human and mice as compared to only 18% in lean controls, and their accumulation was shown to be directly

proportional to adiposity in both models.^{145,146} The increase in ATM number is partly due to recruitment from monocyte trafficking and partly due to local proliferation of recruited macrophages.⁹² ATM cell populations are highly plastic during obesity and tend to switch toward pro-inflammatory phenotype (M1, MMe) with secretion of cytokines and chemokines such as IL-6, TNF- α , IL-12 and MCP-1, whereas lean AT is dominated by M2 macrophages and production of anti-inflammatory cytokines such as IL-10, IL-1Ra, IL-4 and IL-13.¹⁴⁷ A cross-talk between macrophages and adipocytes via cytokines and adipokines production and secretion contributes also significantly to the increasing inflammation and dysfunction,¹³⁴ (figure 15).

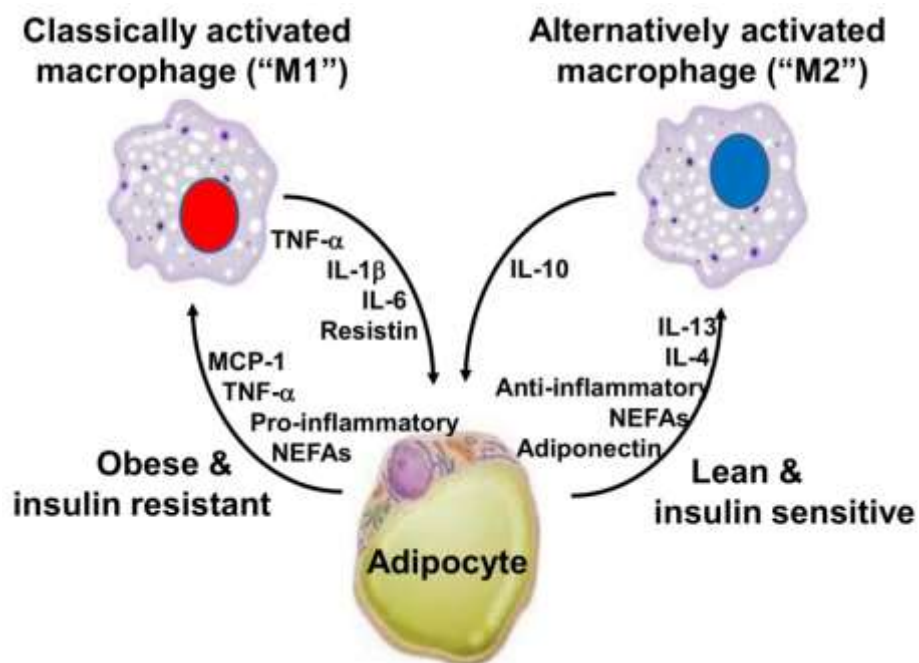


Figure 15: *Cross-talk between adipocytes and macrophages in lean or obese adipose tissue. (From Marcelo Macedo Rogero & al., Nutrients 2018)¹³⁴*

The role of AT macrophages in promoting inflammation, tissue dysfunction and insulin resistance was also demonstrated by Dalmas et al. Their work showed an increased production of AT macrophage-derived IL1- β , a proinflammatory cytokine, in obese patients compared to non-obese ones.¹⁴⁸ Furthermore, they managed to prevent obesity-induced metabolic dysfunction in mice by specifically inactivating these pro-inflammatory macrophages via specific deletion of *Irf5* transcription factor gene. Interestingly, these *Irf5*-myeloïd-deficient mice had smaller adipocytes due to increased AT remodeling.¹⁴⁹

Recruited ATMs are either found in adipogenic/angiogenic cell clusters, mostly observed in early stages of AT obesity (Figure 16b, e), or in crown-like structures (CLS) frequently seen in the late stages of obesity,¹⁵⁰ (figure 16c, f).

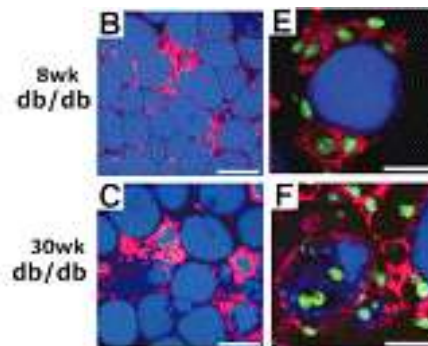


Figure 16: Pictures of immunofluorescent staining showing the morphological difference between adipogenic/angiogenic cell clusters (B, E : 8 weeks-old diabetic mouse) and crown-like structures (C, F : 30 weeks-old mouse). Blue color is BODIPY (lipids), red color is CD68 (macrophages), and green color is Hoechst (nuclei). (From Nishimura, S. & al., *Diabetes*. 2007)¹⁵⁰

Dendritic cells in obese AT are functioning to support proinflammatory Th17 T cell differentiation and their number is increasing with obesity in both humans and mice.¹⁵¹

Neutrophils are the most abundant, but have a short life and act rapidly, so they are increasing in the very initial phase of obesity and during a short term HFD (3 days).¹³¹ Evidence showed that neutrophils mediate insulin resistance through secreted elastase,¹⁵² so independently of inflammatory mechanisms mentioned earlier.

Mast cells play also an important role in the regulation of AT inflammation during the onset of obesity by releasing their granules that contain histamine, serotonin, heparin, and cytokines, inducing a rapid and strong immune response. Liu J et al. demonstrated that mice lacking mast cells are resistant to diet-induced obesity (DIO) and are protected from inflammation and insulin resistance.¹⁵³

Eosinophils are also implicated in pathogenesis of obesity and insulin resistance. They are the predominant source of IL-4 in AT inducing M2 polarization of macrophages. Their number is reduced in the AT of DIO and naturally leptin-null ob/ob mice,¹⁵⁴ and eosinophil-deficient mice show increased fat mass, increased inflammation and glucose intolerance underscoring the impact of their absence during the onset of obesity.¹⁵⁵

Obesity have been shown to affect also the distribution of lymphocytes in AT. B and T cells accumulate, except for Treg population which decreases.^{143,156} Treg cells have an anti-

inflammatory effect, directly, through their TCR receptor or indirectly, through cytokine production.^{157,158} B and T cells (CD4+ and CD8+) participate to sustain inflammation and promote insulin resistance, and their depletion in mice showed protection from metabolic disturbance in response to HFD feeding, despite important weight gain.^{159,160}

Chapter 3: Obesity and adipose tissue fibrosis

Fibrosis is defined as an excessive accumulation of extracellular matrix (ECM) components, which results from an imbalance between excess synthesis of fibrillar components such as collagens and fibronectin, and an impairment in degradation of these proteins. ECM production is part of a regenerative step occurring in response to tissue injury and inflammation, however, if the damage persists, like in the context of obesity and low-grade inflammation, central cellular actors remain activated, and continuously produce fibrillar molecules that accumulate in the tissue as fibrotic deposition.²⁰ Thus, while ECM synthesis and tissue remodeling are initially a physiological response with beneficial effect, excessive accumulation of fibrosis in the absence of resolution of inflammation have deleterious effect on tissue homeostasis and function.^{20,161}

Fibrosis has been extensively studied in the liver, as we will describe later, whereas adipose tissue fibrosis has been recently identified in obesity and associated with metabolic disorders. Now it is considered as a hallmark of metabolically dysfunctional AT (figure 17).

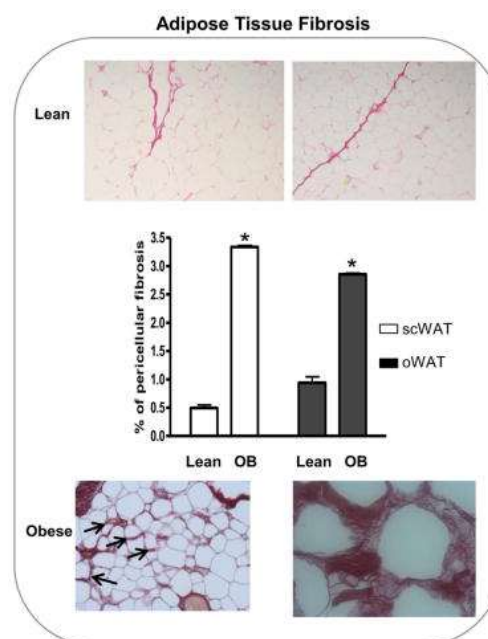


Figure 17: *Quantification of total fibrillar collagens by picrosirius red staining in subcutaneous and visceral AT in obese versus lean subjects. Data are represented as mean \pm SEM. (From Sun, K & al., Cell Metab 2013)²⁰*

The components involved in the formation of adipose ECM are mostly collagens and fibronectin with collagen type I being the major ECM framework, hence playing a key role in the structure and function of mesenchymal tissues.²⁰ Collagen type VI is another major ECM protein found in AT, which contribute to ECM stability. Mature collagen VI is composed of three subunits: $\alpha 1$, $\alpha 2$, and $\alpha 3$, which are required for stable formation of the protein and are regulated both at transcript and posttranslational levels.²⁰ Obese mice lacking collagen VI showed reduced AT fibrosis and improved metabolic parameters.¹⁶²

During the onset of obesity, adipose tissue expansion and adipocyte hypertrophy is faster than neovascularization and, rapidly, adipocytes reach the diffusional limit of oxygen. This hypoxic environment causes an increase in the level of hypoxia-inducible factor 1 α (HIF-1 α) and the activation of HIF target genes including collagen type I, alpha 1 (COL1A1), COL3A1, and lysyl oxidase, an enzyme that mediates cross-linking of collagens,¹⁶³⁻¹⁶⁵ (figure 18). Inhibition of HIF-1 α activity both pharmacologically and genetically resulted in significant metabolic improvements and reduction of adipose tissue fibrosis and immune cell infiltration.¹⁶⁶

Hypoxia also stimulates cytokine and chemokine release from AT macrophages and inhibits preadipocyte differentiation by down regulating PPAR γ in these cells.¹⁶⁷ In parallel, TGF- β , whose levels correlate with adiposity in humans and rodents, also inhibits adipogenesis by upregulating connective tissue growth factor (CTGF) in adipocytes.¹⁶⁸

In AT, ECM components are mostly produced by stromal vascular cells, among which preadipocytes and macrophages are central players. Both express and secrete collagens, but more importantly, they tightly regulate fibrogenesis process under both physiological and pathological conditions,^{169,170} (figure 18).

In vitro studies demonstrated that, when they are in contact with activated macrophages, preadipocytes display a fibroblastic-like phenotype and produce high level of ECM molecules such as collagen I, tenascin-C, fibronectin and its receptor $\alpha 5$ -integrin, and activin A.^{169,171}

Marcelin et al. identified a special subset of progenitor cells: the CD9^{high} PDGFR α ⁺ progenitors that become profibrotic in obese patients and mice and responsible for AT fibrosis with a loss of tissue expandability and increased insulin resistance.¹⁷²

Macrophages regulate fibrogenesis process also by releasing chemokines that attract fibroblasts and other inflammatory cells. On the other hand, macrophages produce soluble mediators including TGF- $\beta 1$ and platelet-derived growth factor (PDGF) which activate fibroblasts and control ECM dynamics by regulating the matrix metalloproteinases (MMPs, a

family of endopeptidases that cleave collagenous proteins) and their inhibitors (TIMPs).¹⁷³ Activated fibroblasts differentiate into α -smooth muscle actin (SMA) expressing myofibroblasts to produce collagens, elastins, and proteoglycans.^{174,175}

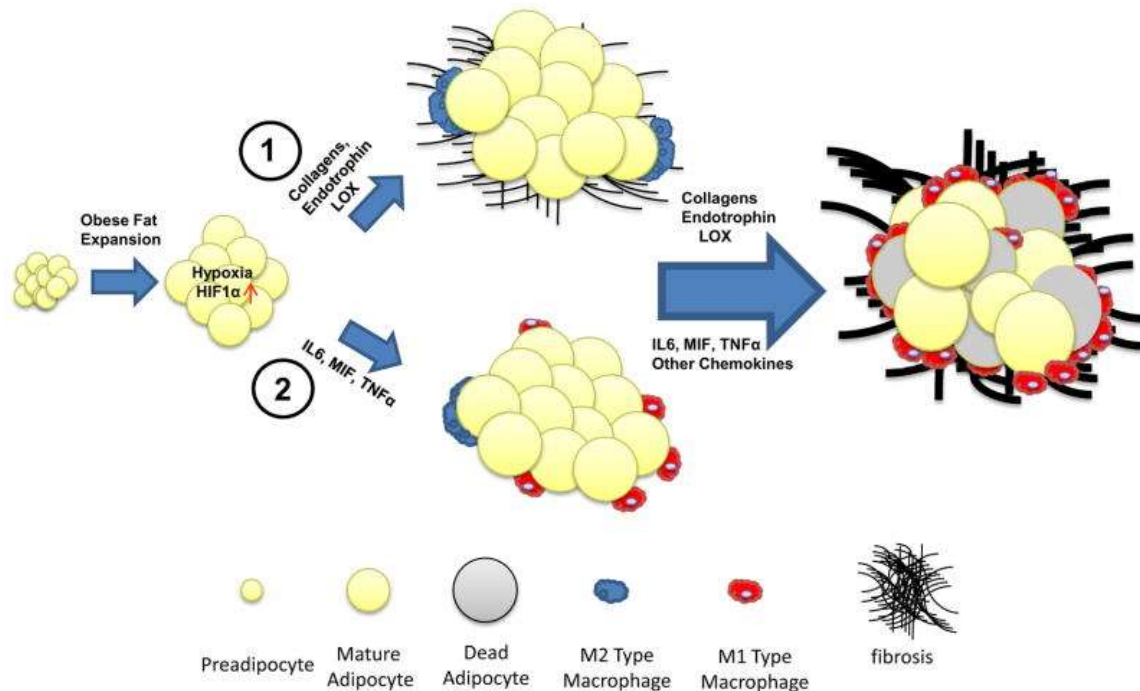


Figure 18: Proposed models for the sequential steps leading to adipose tissue fibrosis and metabolic dysfunction. (From Sun, K & al., *Cell Metab* 2013)²⁰

Obesity-induced AT fibrosis may induce rigid extracellular environment that restrains adipocyte expansion and then triggers adipocyte cell death and inflammation. In this context, AT growth is limited, and excess lipids are stored in ectopic tissues (figure 19). This was further confirmed by observations made in collagen VI knockout obese mice that showed increased flexibility of the ECM and bigger adipocytes compared to obese control mice, together with reduced cell death and inflammation and subsequently improved metabolic situation.¹⁶⁵

Giving the important role of AT fibrosis in obesity-associated metabolic dysfunction, targeting this parameter seems to be of interest in the context of clinical research. Indeed, studies have shown that collagen levels are reduced by adiponectin and by treatment with PPAR γ agonists in mouse AT.¹⁶² However, in patients, AT fibrosis is still persistent two years after surgical-induced body weight reduction.

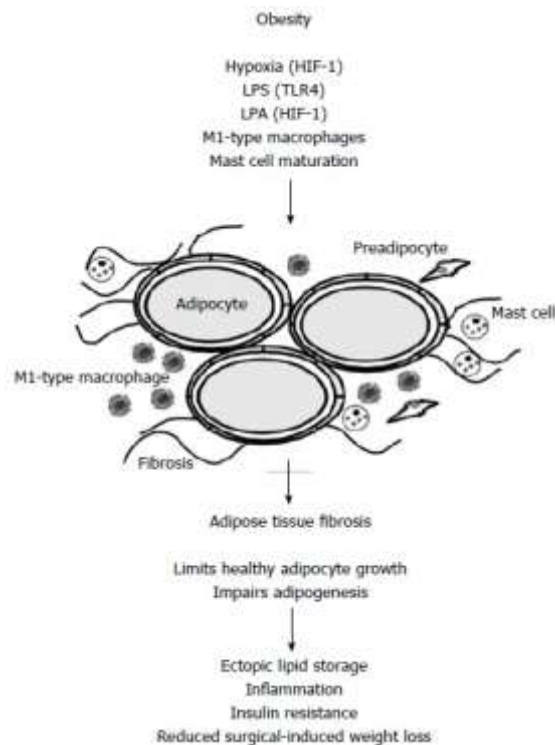


Figure 19: Obesity and adipose tissue dysfunction.
 (From Buechler, C. & al., *World J Diabetes* 2015)¹⁶⁵

Chapter 4: Obesity and adipose tissue senescence

Cellular senescence is considered as an important mechanism involved in the development and progression of several diseases including metabolic diseases such as obesity and type-2 diabetes.¹⁷⁶⁻¹⁷⁸

I) Definition of cellular senescence

Cellular senescence was originally identified by Hayflick and Moorhead, in 1965, as a state of “permanent” cell cycle arrest resulting from the limited proliferative capacity of human fibroblasts in culture condition (replicative cellular senescence).^{179,180} This process was later associated with telomere shortening or dysfunction which triggers DNA damage response (DDR) and subsequent cell cycle arrest.¹⁸¹⁻¹⁸⁴ However, senescence can also be induced in response to other stress conditions such as oncogene activation, oxidative stress, or metabolic stress before any telomere shortening. This is defined as premature cellular senescence.¹⁸⁵ Thus, senescence is rather defined as a state of stable cell cycle arrest in response to various stresses.^{182,184,186} Cells lose their ability to proliferate, ensuring they do not become

cancerous. Senescent cells are usually characterized by a flattened morphology, a higher activity of β -galactosidase, cell cycle arrest, they are metabolically active, and they produce a wide range of cytokines, chemokines, matrix-remodeling proteases and growth factors. Collectively, these secreted factors are known as senescent-associated secretory phenotype (SASP).¹⁸⁷ Recent data suggest that the SASP is not a unique entity, but functionally distinct senescent states depending on the stress-inducing condition, the cell type, and the time that the cells were maintained in senescence.¹⁸⁸ Important distinctions include senescence with or without persistent DNA damage that would lead to the activation of distinct signalling pathways.

II) Replicative cellular senescence

Replicative cellular senescence is induced by telomere shortening. Telomeres are regions of repetitive nucleotide sequences at each end of a chromosome (5'-TTAGGG-3' for vertebrates). Each round of DNA replication reduces the telomere length because the telomerase cannot continue their duplication all the way to the end of a chromosome, so after each duplication the end of the chromosome is shortened and once the critical length is reached, cell division is stopped,¹⁸⁹⁻¹⁹¹ (figure 20). Critically short, uncapped telomeres induce DDR which triggers senescence.¹⁹² *In vivo*, replicative senescence is a physiological process accumulating with age and measurement of telomere length in peripheral blood mononuclear cells (PBMC) is a commonly used technique and established marker of organismal aging in humans.¹⁹³

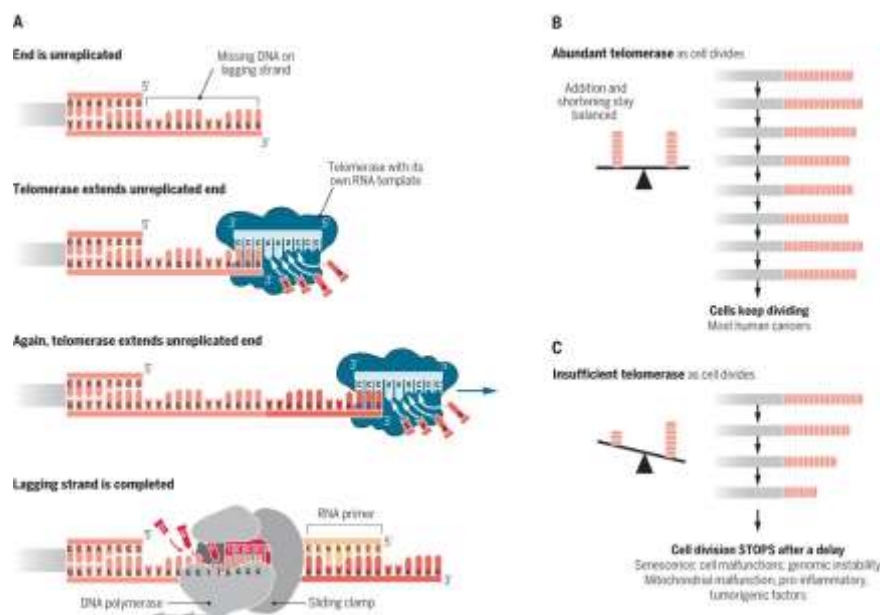


Figure 20: Schematic representation of replicative cellular senescence. (From Blackburn, E. & al., *Science* 2015)¹⁹⁴

III) Premature cellular senescence

As previously mentioned, senescence can be activated through telomere-independent mechanisms and independently of the age (figure 21). Oncogene-induced senescence (OIS) appears in response to the hyperactivation of oncogenes such as Ras or Raf, or the inactivation of tumor suppressors like PTEN.¹⁹⁵⁻¹⁹⁷ The oncogenic stress leads to hyperproliferation with increased DNA replication and accumulation of incomplete replication intermediates. This activates DDR which induces senescence.^{195,198-200} Oxidative stress, with the generation of reactive oxygen species (ROS), leads to the accumulation of DNA single-strand breaks, activation of DDR and finally emergence of premature senescence.^{185,201-203}

Metabolic stress is another factor inducing premature senescence. Excessive calorie intake was shown, for instance, to promote oxidative stress and senescence in the adipose tissue of mice.^{176,204} High glucose levels were also shown to be responsible for *in vitro* senescence induction in other cell types such as endothelial cells²⁰⁵ and proximal tubule cells²⁰⁶.

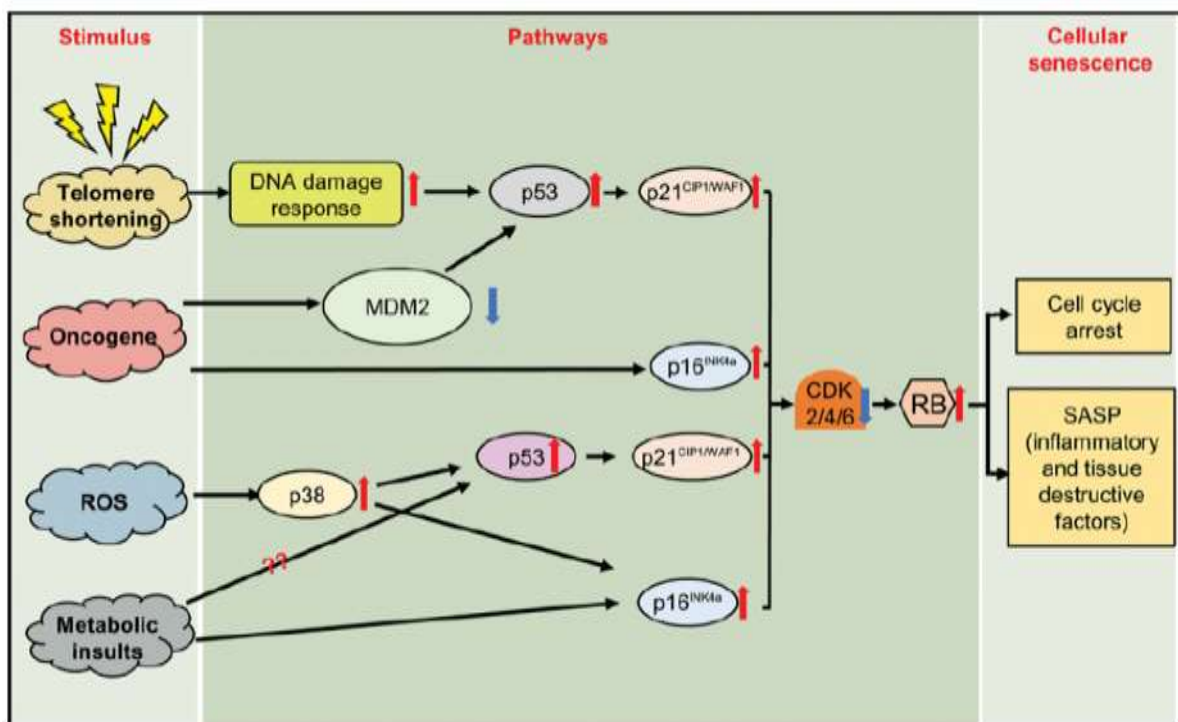


Figure 21: A general overview of premature cellular senescence. (From Liu, Z. & al., *Clin Sci* 2020)¹⁷⁷

IV) Biomarkers of senescence

1.1) Cell cycle arrest

As we previously indicated, stable cell cycle arrest is a feature of senescence, and occurs mainly in response to DNA damage following telomere attrition or other stresses. Cell cycle arrest is mediated by the activation of either the p53/p21^{CIP1} or p16^{INK4A}/phospho-Rb tumor suppressor pathways,^{176,204,207} and many cancer types are associated with mutations in those pathways.

Persistent DDR activates ATR and ATM kinases which in turn activates p53 through Chk1 and Chk2. Then p53 activates p21^{CIP1} to initiate cell cycle arrest by inhibiting cyclin dependent kinase 2 (CDK2), hence preventing the progression of cell cycle from G1 to S phase. CDK inhibition, which can also result directly from p16^{INK4A} activation (inhibits CDK4 or CDK6), blocks phosphorylation of Retinoblastoma tumor suppressor protein (Rb), and that prevents E2F-mediated transcription of genes that are required for DNA replication,¹⁹⁵ (figure 22).

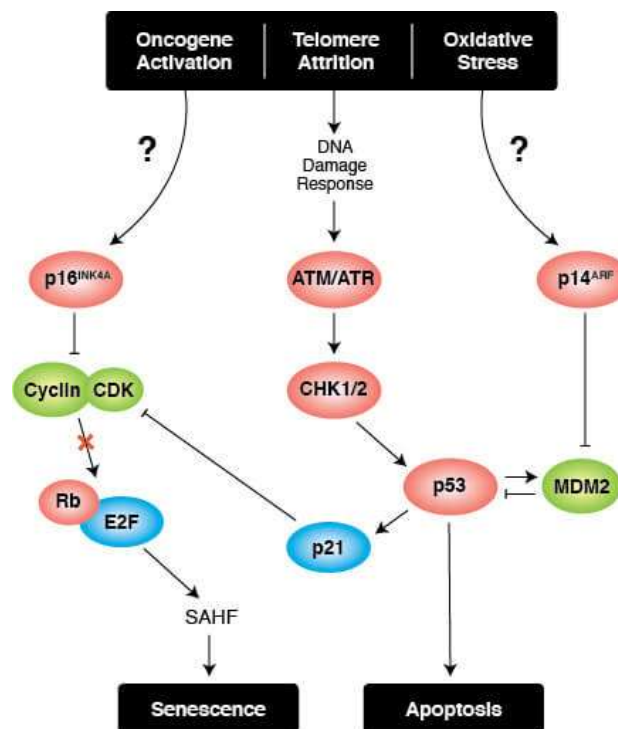


Figure 22: Mechanisms of cell cycle arrest (From <https://www.cellsignal.com>)

1.2) Morphological and metabolic changes

Senescent cells are characterized by a specific morphology, they are enlarged and flattened when compared to their dividing cell counterparts. They have several vacuoles and sometimes more than one nucleus. In addition, nuclear membrane integrity is disrupted due to a downregulation of Lamin B1 gene expression, a protein that plays an important role in nuclear structure.^{208,209} Furthermore, accumulation of dysfunctional mitochondria and increased levels of reactive oxygen species (ROS) are observed in senescent cells.²¹⁰ Lysosomal activity in those cells is also altered, resulting in increased levels of β -galactosidase activity at pH 6.0. Senescence-associated β -galactosidase (SA- β -gal) is now a common and widely adopted biomarker of cellular senescence.²¹¹

1.3) Chromatin reorganization and changes in gene expression

Chromatin is composed of DNA wrapped around nucleosomes that are formed from histones and associated proteins that bind DNA or the histones. The canonical histones are highly synthesized in S phase to package the newly replicated DNA. Non-canonical histone variants are endowed with specific functional properties determined by their non-canonical protein sequences and their constitutive expression in contrast with the replication-dependent expression of canonical histones.

Chromatin reorganization and formation of senescence-associated heterochromatin foci (SAHF) are another feature of senescent cells (figure 23). These modifications in chromatin likely contribute to differential genome expression and the maintenance of the senescent state.^{195,212} SAHFs were originally described in oncogene-induced senescence (OIS) and DNA damage-induced senescence.²¹³ Those structures are enriched for repressive epigenetic marks, including lysine 9 di-or-tri-methylated histone H3 (H3K9me2/3), heterochromatin protein 1 (HP1), and macroH2A, whereas euchromatic marks are absent.^{213,214} SAHFs structures were shown to play an important role in silencing genes that promote proliferation, like E2F-target genes.²¹³

Certain histone variants and modifications do not just coincide with senescence, but they seem to have a functional role in inducing senescence. Specifically, a recently discovered N-terminal proteolytic product of histone H3.3 represses the expression of proliferation

genes.²¹⁵ Moreover, macroH2A1 has been implicated in the feedback regulation of SASP gene expression during RASval12-induced senescence.²¹⁶ The epigenetic angle in regulating senescence is further underscored by observations suggesting that histone methyltransferase MLL1 is required for the expression of SASP components in oncogene-induced senescence.²¹⁷ Most recently, the Mann group identified H2A.J, a novel histone variant, differing from the canonical H2A by only five amino acids with an emerging functional role in senescence, aging and cancer.²¹⁸

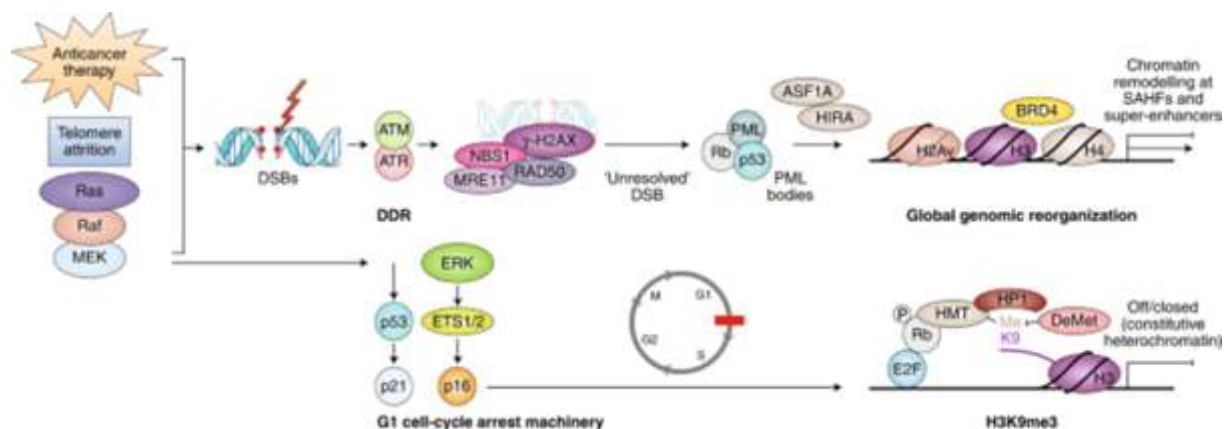


Figure 23: *Global and focal chromatin remodeling in senescence.*
(From Lee, S. & al., *Nat Cell Biol* 2019)²¹⁹

1.4) DNA damage response (DDR)

Activation of DDR pathways is involved in both the induction and maintenance of senescent state. DDR kinases including ATM, ATR, CHK1, and CHK2, and other proteins like p53 and CDC25 are the main effectors of this pathway,¹⁹⁸ (figure 22). Another indicator of DNA damage is the phosphorylated form of H2A.X, a variant of the H2A protein family, which is required for checkpoint-mediated cell cycle arrest and DNA repair following double-stranded DNA breaks.²²⁰

1.5) Senescent-associated secretory phenotype (SASP)

Senescent cells are characterized by pro-inflammatory SASP that mediates non-cell autonomous effects of senescence. This secretome is comprised of a complex mixture of cytokines, chemokines, growth factors, and proteases, among others.^{191,221} However, the precise composition of this secretome depends on many factors such as cell type, micro-

environment, or senescence-inducing stimulus, and its regulation is achieved at different levels, from transcriptional regulation to autocrine feedback loops.^{187,222} Interestingly, persistent DDR appears to be critical for the development of the SASP.¹⁸⁷ SASP has both beneficial and deleterious effects, for example, it mediates immune cell recruitment to senescent cells and/or cancer cells in order to facilitate their clearance, which prevents tumor development.^{223,224} Paradoxically, however, SASP have been shown to promote cancer cell progression via secretion of pro-angiogenic factors and other proteins involved in extracellular matrix remodeling.²²²

1.6) Concluding remarks

The numerous features that characterize senescent cells make them easy to identify using specific markers (figure 24).

However, the described mechanisms of senescence are not necessarily dependent on one another and hence a senescent cell might not display all the biomarkers that we mentioned. For instance, it has been shown that expression of CDK inhibitors p16^{INK4A} and p21^{CIP1} is not always associated with DNA damage, and in this case, this senescent phenotype lacks a pro-inflammatory SASP.^{182,187,225-227} Moreover, most of the cells expressing markers of DNA damage *in vivo*, especially in a non-pathological context, are not necessarily senescent and might just be responding to a transient repairable damage. Another example is the p53- and p16^{INK4A}-independent induction of senescence by chromatin-dependent alteration of S-phase progression that occurs without DNA damage and checkpoint activation, but leads to cell cycle arrest.²²⁸

Protein or Marker	Role in Senescence
Senescence-associated β -galactosidase	Increased activity at pH 6.0 in senescent cells
p53	Activation can trigger cell cycle arrest
Rb (Retinoblastoma tumor suppressor protein)	Inhibition triggers cell cycle arrest
p21 ^{CIP1}	Inhibits cyclin dependent kinases; downstream of p53
p16 ^{INK4A}	Inhibits phosphorylation and inactivation of pRb
Bcl-2	Increased expression in senescent cells, inhibits apoptosis
macroH2A1.1	macroH2A1 isoform; marker of SAHF
macroH2A1.2	macroH2A1 isoform; marker of SAHF
H3K9Me2/3 (lysine 9 di-or-tri-methylated histone H3)	Marker of SAHF
HP1 (heterochromatin protein 1)	Marker of SAHF
Phospho-Histone H2A.X (Ser139)	Marker of DNA damage
Lamin B1	Expression reduced in senescent cells leading to disruption of nuclear envelope
HMGB1 (High mobility group protein B1)	SASP component
IL-6 (Interleukin 6)	SASP component
TNF- α (Tumor necrosis factor α)	SASP component
MMP3 (Matrix metalloproteinase-3)	SASP component

Figure 24: Common biomarkers of senescence (From <https://www.cellsignal.com>)

V) Adipose tissue senescence in aging and obesity

Senescent cells accumulate in AT with aging¹⁷⁸ and obesity^{193,204} and studies showed that visceral AT is more prone to senescence compared to subcutaneous AT.²²⁹

Senescent cells have been shown to be involved in the development and progression of numerous diseases including obesity and type 2 diabetes.^{176,177} Senescent AT also interferes with normal physiological functions of remote tissues and organs via SASP, inducing pathologies such as cardiovascular disease (CVD) and kidney disease.^{177,230,231} In particular, our team has identified a profibrotic SASP that induces cardiac remodeling and dysfunction.²⁶ Hence, cell senescence is known to promote metabolic and other kinds of diseases, however, the potential role of these metabolic diseases as drivers of cell senescence and accelerators of biological aging was also proposed and extensively studied.²³²⁻²³⁶

Senescent AT is characterized by several types of dysfunction. Alteration of AT renewal and defective adipogenesis were for instance linked to accumulation of AT senescent cells in aging and obesity.²³⁷ Changes toward inflammatory status in senescent AT of both aged and obese

humans and mice,^{238,239} and aberrant adipocytokine production have been observed. Indeed, increased expression of plasminogen activator inhibitor-1 (PAI-1) and interleukin-6 (IL-6),²⁴⁰ elevated levels of IL-1 β ,^{241,242} TNF α ,²⁰⁴ and secretion of C-C motif chemokine ligand 2 (CCL2) and C-X-C motif chemokine ligand 1 (CXCL1) accompanied with activation and migration of macrophages and neutrophils,²⁴³ have been described.

Accumulation of senescent cells and chronic inflammation in AT in both obesity and aging give rise to insulin resistance,^{244,245} and activated p53 has been proposed to be a central player given that transgenic overexpression of activated p53 results in senescence and insulin resistance, whereas its inactivation results in opposite effects in diabetic animal models.^{178,204} Other senescent molecules such as p16^{INK4a} and p21^{CIP1} were associated with insulin resistance.^{246,247} However, it still remains unclear how activated p53, p16^{INK4a} and p21^{CIP1} lead to insulin resistance in AT and whether other parameters such as inflammation are required in this context.

Although senescent AT in obesity and aging show multiple similarities, several studies demonstrated that pathways leading to senescence in these two states are different.^{248,249} For instance, Zhuohao Liu et al. showed that during aging, unrestrained p53 activation in adipocytes elicits AT senescence through downregulation of murine double minute 2 (MDM2) expression, however, this protein was found to be upregulated, together with p53 protein in obese AT.²⁵⁰

VI) Adipose tissue cell-type specific senescence

AT is composed of various cell types including mature adipocytes, progenitor cells, endothelial cells and immune cells. The composition as well as senescent status of those different cell populations change with aging and obesity (figure 25).

Mature adipocytes develop senescence in response to various oxidative stresses that appears with aging and obesity. P53 levels were higher in adipocytes differentiated from aged animals when compared with those differentiated from younger animals.²⁵¹ P53 levels were also

found upregulated, together with p21 in adipocytes from diabetic subjects,²⁰⁴ and DNA damage in adipocytes was described as an early event during the onset of obesity.^{243,252}

Senescent progenitor cells including preadipocytes are highly increased in obese and aged AT,^{178,237} and this was shown to impair AT regeneration due to a decrease in adipogenic capacity of those cells on one hand,^{253,254} and inhibition of adipogenesis in nearby progenitor cells through SASP molecules on the other hand.^{237,255} Activin A, a member of the transforming growth factor superfamily which is regulated by p21^{CIP1} is one of those molecules.^{237,256} Adipogenesis was shown to be regulated by p16^{INK4a} as in the absence of this protein in progenitor cells, adipogenesis was enhanced.²⁵⁷

Endothelial cells play an important role in AT by participating to lipid handling function of AT and to the regulation of adipogenesis.²⁵⁸ An impairment in endothelial function was observed in both aging and obesity,^{258,259} and increased expression of the senescent marker γ -H2AX in AT endothelial cells of obese people was reported.²⁶⁰ Moreover, p16^{INK4a} expression has been found upregulated in AT endothelial cells with aging. This increase in p16^{INK4a} expression was associated with a decrease in the gene expression of CD36 and adipocyte-fatty acid binding protein (A-FABP), proteins involved in lipid handling.²⁶¹

Immune cells are also affected by senescence. For instance, two populations of senescent T cells were recently identified in adipose tissue from obese and diabetic animals and humans,^{262,263} and one of them was shown to increase inflammation and insulin resistance in visceral AT by producing osteopontin, a macrophage activating cytokine highly expressed in obese adipose tissue.²⁶⁴ Senescent macrophages were also identified in adipose tissue of aged mice by using a mouse model with luciferase expression under the control p16^{INK4a} promoter.²⁶⁵ Another study showed upregulation of senescence-related genes in resident AT macrophages in response to activation of inflammasome pathway in aged mice which was linked to alterations in lipolysis in adipocytes.²⁶⁶ Furthermore, Minamino et al. demonstrated that upregulation of p53 in adipocytes and macrophages induced senescence, insulin resistance and inflammatory cytokine production in mouse fat. Conversely, when they repressed p53 in adipocytes and macrophages under high-fat diet condition, using a dominant-negative approach, those effects were not observed anymore.²⁰⁴

These data suggest that AT immune cell senescence play an important role in tissue dysfunction and associated metabolic disorders both in aging and obesity, however very few things are known about this and the mechanisms involved. The chronological order of events leading to and initiating AT senescence and dysfunction are unclear as well and need to be defined.

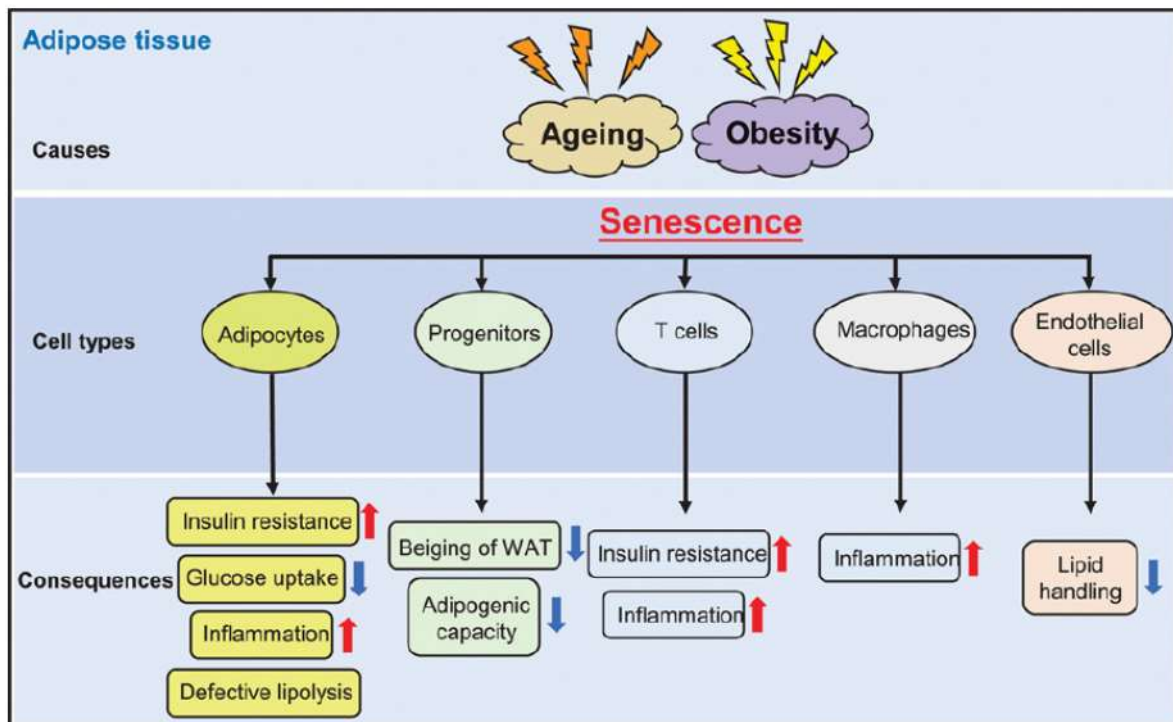


Figure 25: Causes and consequences of cellular senescence in different AT cell types. (From Liu, Z. & al., *Clin Sci* 2020)¹⁷⁷

VII) Adipose tissue senescence as a therapeutic target for the treatment of aging- and obesity-related metabolic disorders

AT senescent cells are important drivers of local and systemic dysfunction, yet targeting them to alleviate aging- and/or obesity-related metabolic disorders has been challenging. Preventing the emergence of senescent cells by interfering with pathways that lead to senescence-associated growth arrest, eliminating senescent cells (senolytic approach), or interfering with

the deleterious effects of senescent cells by targeting the SASP (senomorphic approach) are potential therapeutic options.

Several studies were conducted in this field and Deursen et al. (2011) were the first to show that removal of p16^{INK4a} positive senescent cells prevents age-associated metabolic dysfunction in mice. They generated a transgenic mouse model, the INK-ATTAC mice which display inducible caspase activation under the control of p16^{INK4a} promoter. Administration of the activating drug AP20187 to those mice exclusively induce apoptosis in p16^{INK4a} positive cells.^{240,267} Since then, this became a commonly used model for research in the senescence field to study the role and the impact of senescent cells in different contexts and various diseases.^{237,240,268,269}

Few years later, Kirkland et al. (2015) developed the first chemical mixture of compounds that specifically target and eliminate senescent cells.²⁷⁰ Dasatinib and Quercetin (D+Q) are used in combination to act as a senolytic drug which can kill cells by targeting the pro-survival pathways (as they are up-regulated in senescent cells) such as Bcl-2/ Bcl-Xl. This drug showed beneficial effects on aging- and obesity-induced metabolic disorders by improving insulin sensitivity, reducing inflammation and AT macrophage infiltration, and restoring AT integrity in mouse models.^{271,272} These drugs are now being tested in clinical trials and have proved beneficial effects in diabetic kidney disease and pulmonary fibrosis.^{273,274} Several other senolytics were later developed including fisetin, a quercetin analog targeting PI3K-Akt signaling pathway,^{275,276} Bcl-2 inhibitor or heat shock protein 90 (HSP90) inhibitor, etc, some of which proved their efficiency and showed beneficial effects whereas some others require more investigations.^{277,278}

Targeting the SASP components instead of senescent cells resulted in great improvements of metabolic function, as well. Indeed, Kirkland et al. managed to improve insulin sensitivity, promote adipogenesis and reduce AT inflammation in aged mice by treating them with a pharmacological compound that inhibit pro-inflammatory SASP production.^{237,279}

Preventing the emergence of senescent cells by interfering with pathways that can induce senescence-associated replicative arrest are an interesting option but it carries the risk of promoting cancer, as it occurs when p16^{INK4a}, the retinoblastoma (Rb) protein, or p53 are diminished or inactivated.^{280,281}

Lifestyle interventions are another kind of treatment that proved efficiency in reducing senescence and preventing aging- and obesity-associated metabolic abnormalities. Caloric restriction for instance delays cellular senescence and increase life span.²⁸² Exercise and physical activity, whose beneficial effects have been shown to be mainly mediated by AT,^{283,284} has both senolytic and senomorphic effects. Indeed, the number of p16^{INK4a} positive cells in AT of old women was shown to negatively correlate with physical activity,²⁸⁵ and some other studies indicated reductions in AT pro-inflammatory cytokine expression in obese subjects.^{286,287} These non-targeted approaches have the great advantage to physiologically improve metabolic parameters without any side-effects and with a more global action.

Chapter 5: Conclusion

As we explained and described in the previous sections, low grade inflammation, fibrosis and senescence are the main features characterizing the obese AT and those were extensively studied over the past few years. Obesity-induced AT inflammation was first described in 2003 by Stuart P. Weisberg et al.²⁸⁸ Then the first descriptions of fibrosis as a feature of obese AT started in 2009.¹⁶² At the same period, senescence, which up to then was only studied in the context of aging was, for the first time, associated with obesity, when Minamino et al. identified a crucial role for AT p53 in the regulation of insulin resistance.²⁰⁴

Since then, inflammation, fibrosis and senescence are extensively studied in obese individuals as well as in animal models of obesity. In particular, models of HFD-induced obesity are our main interest here, so we browsed the current state of knowledge in the literature and the models that were used i.e. durations of HFD (table 2). In exploring AT in C57BL6/Rj mice under HFD (60% of fat) little attention has been given to early events that may trigger deleterious secondary changes. More specifically these studies focused on the global changes in adipose tissue and description of senescence feature without detailing:

- the underlying mechanisms initiating the process of cellular senescence within adipose tissue
- the specific role of adipose tissue cell populations
- the time course of the occurrence of senescence after initiation of high fat diet
- the confounding effect of age
- the impact of a dysfunctional adipose tissue on remote organs such as the heart.

Our work aimed to contribute to these important unresolved questions.

Authors	Mouse model: Duration of HFD				
	< 5 weeks	< 10 weeks	12 to 15 weeks	20 weeks	30 weeks
Feng et al., <i>Diabetes</i> 2011	x				
Xu et al., <i>JCI</i> 2003	x				
Williams et al., <i>PLoS One</i> 2014	x		x		
Strissel et al., <i>Diabetes</i> 2007		x		x	
Wang et al., <i>Nat med</i> 2013					
Paglialunga et al., <i>Diabetologia</i> 2015	x				
Kumar et al., <i>International Journal of Obesity</i> 2018		x x	x x x	x x x	
Shirawaka et al., <i>Plos One</i> 2017					x x x
Bennett et al., <i>Obesity</i> 2014				x	
Observed parameters: Inflammation Fibrosis Senescence					

Table 2: Bibliography summarizing the current literature about inflammation, fibrosis, and senescence parameters in AT of HFD-induced obesity mouse models.

OBJECTIVES

Objectives of my thesis:

Obesity epidemic increases worldwide and is associated with major risk for chronic disease such as type 2 diabetes mellitus (T2DM), hypertension, and cardiovascular disease.^{1,2} Despite a better understanding of underlying mechanisms, many questions remain to be answered since the role of adipose tissue senescence has recently emerged as a potential key contributor to the noxious effects of adiposity and development of a myriad of co-morbidities representing the “obesity diseasome”.

Therefore, my thesis project aimed to study the senescence of visceral adipose tissue, as a key player in premature aging and more specifically in cardiac remodeling and dysfunction.^{25,26,178,204}

My work was organized around murine models of aging and high-fat diet-induced obesity in order to:

- 1) Compare the impact of high-fat diet-induced obesity on adipose tissue function and remodeling in young and aged mice:
 - a. To identify potential age-dependent response,
 - b. To establishing the chronological order of events leading to visceral adipose tissue alterations and senescence in high fat diet young mice,
 - c. To explore the role of senescent adipose tissue macrophages in metabolic and cardiac dysfunction,
 - d. To compare different strategies in order to mitigate visceral adipose tissue senescence.
- 2) Evaluate the role of osteopontin on visceral adipose tissue remodeling and dysfunction in the context of aging, and in the cross-talk between adipose tissue and heart.
- 3) Understand the mechanisms initiating adipose tissue senescence by focusing on the role of mitochondria in the context of high-fat diet induced-obesity.
- 4) Contributing to the analysis of the mechanisms associated with cardiac aging.

METHODS

Technical sheet n°1

Animal models

Objective & Rationale

In vivo models were used in order to assess physiological functions and systemic interactions between organs, that is not feasible via *in vitro* models because it requires a whole organism.

Ethics

All animal experiments were approved by the Institutional Animal Care and Use Committee of the French National Institute of Health and Medical Research (INSERM)-Unit 955, Créteil, France (ComEth 15-001).

Methods

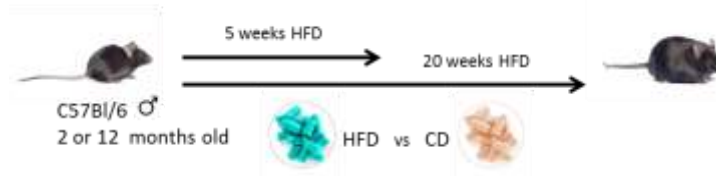
All mice were housed in a specific pathogen free platform at a constant temperature (22°C), kept in individually ventilated cages with a 12-hour light-dark cycle and unrestricted access to a chow diet (CD, A0310, Safe Diets, France) and water. Chow diet composition corresponded to 13.5% of fat, 61.3% of carbohydrate and 25.2% of protein

1st study: Adipose tissue senescence time course assessment

C57/BL6JRj male mice (referred as wild-type: WT) purchased from Janvier were kept in individually ventilated cages with 12-hour light-dark cycle, and controlled temperature (20-22°C) and humidity. All mice were randomly assigned to chow diet (CD, A0310, Safe Diets, France) or high-fat diet (HFD, D12492i, Research Diets, USA) regimen. HFD composition corresponded to 60% of fat, 20% of carbohydrate (including sucrose 7% of total composition) and 20% of protein. Water and food were provided ad libitum. Body weight, status of glucose homeostasis (metabolic tests: ITT, GTT) and heart function (echocardiography) were monitored at baseline and before sacrifice.

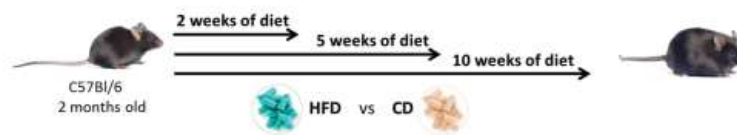
- **Comparison between young and aged mice:**

2- and 12- month-old WT male mice were used and were separated in 2 groups each. First group was put under CD or HFD for 5 weeks and second one was put under CD or HFD for 20 weeks. A total of 8 groups (4 young and 4 aged) composed of 4-5 mice each.



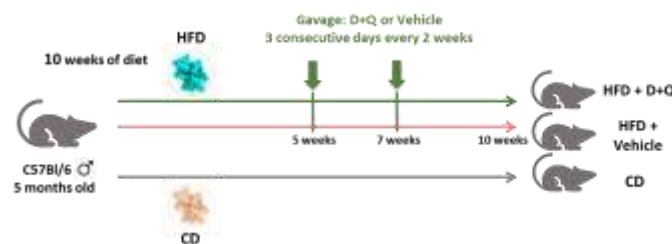
- **AT and heart time course assessment:**

2-month-old WT male mice were maintained on CD or HFD for 2, 5 or 10 weeks. A total of 6 groups composed of 5 to 7 animals each.



- **Senolytic treatment:**

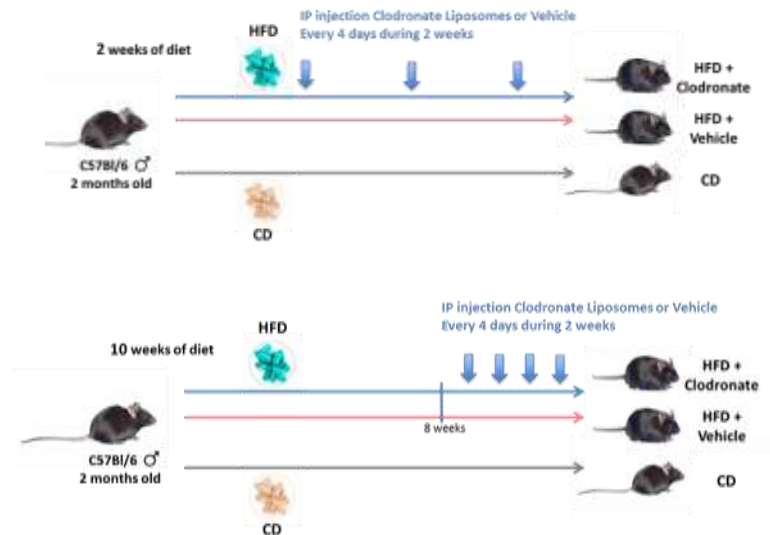
5-month-old WT male mice were used. They were separated in 3 groups composed of 5 to 9 mice each with similar bodyweights: CD, HFD, or HFD + senolytic and the duration of diet was 10 weeks. The treatment started 5 weeks after beginning of diet, (see details of the treatment in the technical sheet n°5).



- **Clodronate treatment:**

2-month-old WT male mice were used. They were separated in 2 groups. First group was put under CD or HFD for 2 weeks and second one was put under CD or HFD for 10 weeks. Each group was separated in 3 sub-groups (CD, HFD Vehicle, HFD Clodronate). A total of 6 groups composed of 7 to 13 mice each. The group of mice undergoing 2 weeks of diet started the

treatment together with the diet whereas the group of mice undergoing 10 weeks of diet started the treatment 8 weeks after the beginning of diet, (see details of the treatment in the technical sheet n°6).



2nd study: Adipose tissue osteopontin promotes macrophage senescence

C57/BL6Jrj mice (referred as wild-type: WT) were purchased from Janvier Labs, France. Osteopontin knockout mice (B6.129S6(Cg)-Spp1tm1Blh/J) were purchased from Jackson laboratory (ME, USA), which had been back-crossed with C57/BL6J mice more than 10 generations, and kept as homozygous (referred as OPN^{-/-}). p16-luciferase mice (Strain Code 01XBT--B6.Cg-Cdkn2a tm3.1Nesh Tyr c-2J/Nci) were obtained from the NCI mouse repository via Dr Norman Sharpless (University of North Carolina).²⁸⁹ During follow-up, animals underwent a monthly body-weight (BW) evaluations.

3rd study: Adipose tissue senescence is mediated by increased ATP content after a short-term high fat diet exposure

Five-month-old C57/BL6Jrj mice (WT, Janvier Labs, France) were subjected to chow diet (CD) and HFD (60% calories from fat, D12492, irradiated; Research Diets Inc., New Brunswick, NJ) for 1, 2 and 5 weeks to assess the kinetics of epididymal white adipose tissue (WAT)

senescence, and another group for 10 weeks which was in parallel submitted to exercise training (Derumeaux et al., 2008), starting 5 weeks after the initiation of HFD. Another group of HFD mice was treated with allopurinol (1mM in the drinking water) (Bravard et al., 2011), starting 5 weeks after the initiation of HFD, alone or in combination with exercise, up to 10 weeks of HFD. Body weight and status of glucose homeostasis (metabolic tests: ITT, GTT) were monitored at baseline before starting the exercise or the pharmacological intervention and at the end of the protocols, (see details of the treatment in the technical sheet n°8).

In a separate set of experiments, 3 months-old p16LUC heterozygote mice (obtained from N E Sharpless (Chapel Hill, NC, USA) and bred at CNRS-TAAM, France), harboring a knock-in of the luciferase gene into the Cdkn2a locus (Sorrentino et al., 2014), were exposed to CD and HFD for 10 weeks. Body weight gain and luminescence analysis were followed after 1, 2, 5 and 10 weeks of HFD, (see details of the treatment in the technical sheet n°9).

4th study: Impaired phenylalanine catabolism is a key determinant of cardiac aging

Global p21^{-/-} mice backcrossed to C57BL/6 background for at least 10 generations (Jackson Laboratory, USA) as well as wild-type (WT) littermates were used. For cardiac phenotyping, male WT and p21^{-/-} mice were followed from the age of 2 to 15 months and myocardial structure and function were sequentially evaluated. Animals were euthanized and tissues harvested for histology and molecular biology at ages 2, 6, 10 and 15 months. For the drug treatment (Phe and BH4), 11-month-old WT mice (Janvier Labs, France) were used, (see details of the treatment in the technical sheet n°7).

Z. Mezdari contributed to the follow-up and the treatment of the different animal cohorts involved in the four studies presented in this thesis document together with **M. Pini, D. Sawaki, G. Czibik and Y. Zhang.**

Technical sheet n°2

***In vivo* Energy Metabolism Assessment**

Definition

Glucose tolerance test (GTT) and Insulin tolerance test (ITT) are non-invasive techniques used in order to assess systemic glucose metabolism *in vivo* in physiological and pathological conditions.

Objective

GTT measures the capacity of the organism to use glucose as energy substrate and eventual defects in peripheral disposal. ITT measures the global insulin sensitivity and points out potential insulin signalling defects.

Methods

Metabolic tolerance tests were carried out in mice starved for 5-6 hours. GTT was performed after intraperitoneal injection of glucose (0.8-1.5 mg/g body weight in distilled water) and glucose concentration was measured in blood samples obtained from tail vein at baseline, 15, 30, 60, 90, 120 minutes after injection with an automatic glucometer (Accu-Chek Performa, Roche, Germany). For ITT, insulin solution was injected intraperitoneally (0.3- 0.5 mU/g body weight, Humulin, Lilly, France) with evaluation of blood glucose levels at baseline, 30, 60, 90, 120 minutes after injection (figure 26).

Data analysis

The values obtained were plotted using the software Prism-Graphpad to perform a graph showing blood glucose values over the time (figure 26). The areas under the curves were then measured and compared between groups.

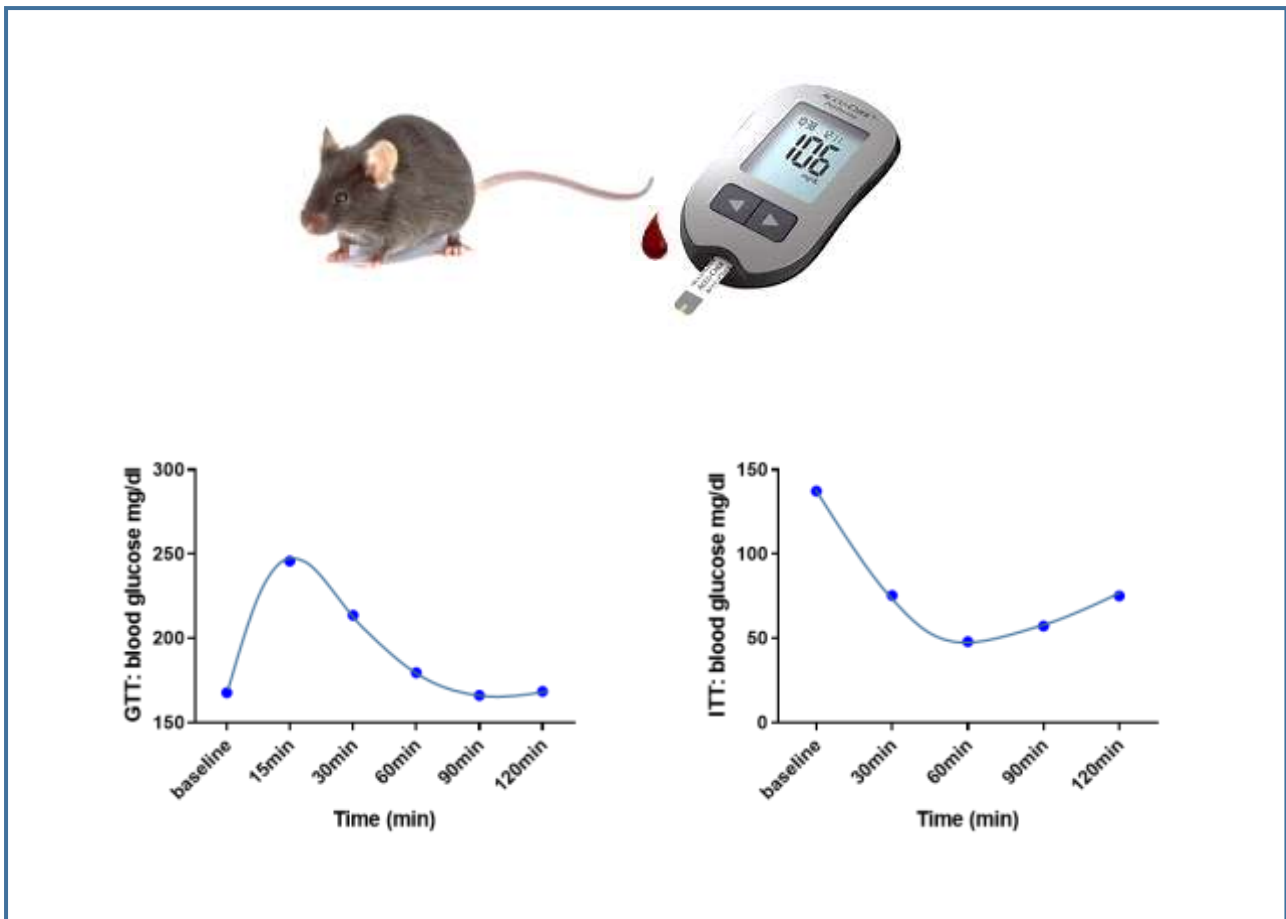


Figure 26: Representative curves of blood glucose concentrations obtained after Glucose tolerance test (GTT) and Insulin tolerance test (ITT)

GTT and ITT were performed by **Z. Mezdari, M. Pini, D. Sawaki, G. Czibik, Y. Zhang, S. Naushad, and M. Halfaoui.**

Technical sheet n°3

Echocardiographic Assessment

Definition/ Objective

In animal studies, echocardiography is a technique used to explore cardiac function of live animals in a non-invasive way. It gives the advantage to assess cardiac function during the course of the experimental protocol without interfering with it.

Principle

This procedure consists in analysing heart morphology and assessing wall motion and dimensions using a 2-dimensional transthoracic echocardiography in conscious mice. Echocardiography transducer (or probe) is placed on the thorax , and images are taken through the chest wall.

Methods

Anesthesia: Mice were accustomed to handling before being subjected to transthoracic echocardiography in conscious state to avoid cardiac depressor effect of anesthetic agents.

Acquisition: In such a state heart rates were typically above 600 beats per minute (bpm). Data acquisition was performed by a single person for each cohort of animals and images were acquired from a parasternal position at the level of the papillary muscles using a 13-MHz linear-array transducer with a digital ultrasound system (Vivid 7, GE Medical System, Horton, Norway). Left ventricular diameters and ejection fraction, and anterior and posterior wall thicknesses were serially obtained from gray-scale M-mode acquisition. Peak systolic values of radial strain rate of the anterior and posterior wall were obtained using Tissue Doppler Imaging.

Data analysis

Radial strain rate was analyzed offline with the EchoPac software (GE Medical Systems) by a single operator blinded to the identity of study groups.



Figure 27: *Pictures of the echocardiographic machine (left) and a conscious mouse undergoing echocardiography (right)*

Data acquisition was performed by **E. Riant** or **T. D’humière** and data analysis was done by **G. Derumeaux**.

Haemodynamic Cardiac Assessment

Definition/ Objective

This procedure aims to assess *in vivo* haemodynamic of cardiac left ventricular function by measuring systolic and diastolic arterial pressure as well as blood pressure in the left ventricle including isovolumetric pressure development (dP/dt_{max}) and pressure decay (dP/dt_{min}).

Methods

In vivo haemodynamic measurements were performed just before mice were sacrificed following protocol as indicated before.²⁹⁰ Briefly, haemodynamic evaluation was performed in mice placed on a homeothermic operating table in supine position under 1.5% isoflurane anesthesia with spontaneous breathing. A 1.4-Fr microcatheter (Millar Instruments, Houston, USA) was calibrated manually before each experiment, inserted via the right carotid artery into the aorta and subsequently advanced to the left ventricle. Data were collected after at least 10 min of baseline, using the lowest isoflurane concentration tolerated to ensure minimal cardiodepression during measurement of peak rates of isovolumetric pressure development (dP/dt_{max}) and pressure decay (dP/dt_{min}). The microcatheter was then withdrawn to the aorta for measurement of systolic and diastolic pressure. Data were analyzed using the IOX software (EMKA, France).

In vivo haemodynamic cardiac assesment was performed by **Dr C. Radu**

Senolytic Treatment

Definition

Senolytic drugs are chemical compounds that target and eliminate senescent cells by inducing apoptosis in those cells which are initially protected against cell death. Here we used Dasatinib and Quercetin (D+Q) drug which target the pro-survival pathways such as Bcl-2/ Bcl-XL to selectively kill senescent cells over non-senescent ones. This drug showed beneficial effects on aging- and obesity-induced metabolic disorders by improving metabolic parameters and restoring AT integrity in mice models.^{271,272}

Objective

Senolytic drugs are used in basic research for a better understanding of senescent cells by analysing the direct or indirect consequences of senescent cells elimination, and also in clinical trials to target the fundamental aging mechanisms that contributes to several disorders.

Methods

The drug was composed of a combination of two senolytic compounds: Dasatinib (SIGMA-CDS023389-25MG) and QUERCETIN(BIO-TECHNE 1125/100). The treatment was given to the mice through oral gavage at a concentration of 5 mg/kg for Dasatinib and 50 mg/kg for Quercetin per day (solution was prepared at 1 µg/µL for D and 10 µg/µL for Q in PEG 400 10%), for three consecutive days every 2 weeks as previously described.²⁷¹

Z. Mezdari participated to this experiment under the supervision of **M. Pini** and **D. Sawaki**

Technical sheet n°6

Clodronate Treatment

Definition

Clodronate-containing liposomes promote macrophage self-destruction. Macrophages phagocytose the liposomes, which are subsequently degraded by lysosomal phospholipases and clodronate is then released into the cell and induce apoptosis.²⁹¹

Objective

Clodronate-liposome treatment is used in basic research to deplete macrophages in a variety of tissues and also in clinic to treat some kinds of tumors.

Methods

HFD study (Study 1): Mice were injected intraperitoneally with 12,5 mg/kg (group 2 weeks of HFD) or 16,7 mg/kg (group 10w of HFD) clodronate in liposomes or PBS control liposomes (HFD Clo & HFD Veh respectively; Liposoma BV, Amsterdam, Netherlands) every 4 days during 2 weeks (protocol adapted from Westwell-Roper et al., 2013).²⁹²

Aging study (Study 2): The total of 17 male WT mice, 12-month old were used. Mice were injected intraperitoneally with 70 mg/kg clodronate in liposomes or PBS control liposomes (ClodLip BV, Amsterdam, Netherlands) every 4 days for 4 weeks (70% dose used in reference).²⁹²

Z. Mezdari performed this experiment under the supervision of **D. Sawaki** and **G. Czibik**.

Phenylalanine and BH4 Treatment

Definition

Phenylalanine (Phe) is an essential amino acid which is degraded into Tyrosine by the hepatic enzyme phenylalanine hydroxylase (Pah). BH4 is the essential cofactor for Pah.

Objective

These treatments were used to explore the role of Phe in driving cardiac aging and the impact of aging on liver Phe catabolism.

Methods

Phe was subcutaneously administered to the old mice in a dose of 200 mg/kg twice a day or vehicle (1x PBS) for one month. BH4 was intraperitoneally administered in a dose of 10 mg/kg/die 2x/die or vehicle (1x PBS with 10 mM sodium ascorbate and citric acid to pH4.5) over six weeks. General state of the mice (body weight & wellbeing) was closely monitored.

Z. Mezdari performed this experiment under the supervision of **G. Czibik**.

Technical sheet n°8

Exercise Training

Objective

This intervention is used to mimic physical exercise in humans and aims to explore and decipher the mechanisms associated with metabolic improvements in the context of HFD-induced obesity. Recent findings show that exercise initiated after long-term HFD reduces senescent phenotype markers in visceral adipose tissue.²⁸³ In our protocol of short-term HFD, exercise was used to evaluate through which mechanism the amelioration of HFD-induced adipose tissue senescence could happen.

Methods

Mice underwent 4 weeks of physical training together with CD or HFD that they started 5 weeks before. Exercise training consisted in 2 daily swimming sessions in a water tank maintained at 30°C to 32°C separated by a 6-hour break. Swimming sessions were supervised to avoid floating and/or clinging of individual animals and increased by 10 minutes each day until 90 minutes sessions were reached (Derumeaux et al., 2008).²⁹³

Z. Mezdari performed this experiment under the supervision of **M Pini**.

Technical sheet n°9

In vivo Luciferase Detection

Definition

Luciferase is an oxidative enzyme that produce bioluminescence by catalyzing the reaction between the luciferin substrates and other co-factors. The oxidized luciferin resulting from this reaction which is electronically excited releases photons when returning to the ground state. Luciferase bioluminescence, an established model in the field of cancer and aging^{294,295} was used in our study to detect p16^{INK4A} protein in P16-LUC mice: a transgenic mouse model where luciferase is expressed under the control of p16^{INK4A} promoter.

Objective

This technic was used to detect p16^{INK4A} protein and determine the precise location of senescence and its evolution over time under HFD-induced obesity.

Methods

Luciferase activity was detected and analyzed with the collaboration of Dr Seguin, Paris Descartes University as previously described.²⁸⁹ Mice were anesthetized with isoflurane, and then injected intraperitoneally with D-luciferin substrate (Caliper Life Sciences; 15 mg/ml in PBS), 10 ul/g body weight. Images were taken with the PhotonIMAGER system (BIOSPACE). After substrate administration, peak luminescence was measured at 6–8 minutes. For simultaneous image capture of more than 3 animals, a wide-angle lens was used. To compare multiple images taken at the same exposure point, PhotoAcquisition Software for PhotonIMAGER (BIOSPACE) was used following substrate administration, and acquisition lasted for 10 minutes (from t=10min to t=20min after luciferin injection). An additional ROI was employed to normalize for background luminescence on each image for all analyses.

This experiment was performed by **M. Pini** and **D. Sawaki**.

Dissection: Blood and Tissue Harvesting

Objective

Dissection step is particularly important and critical because the way of collecting blood and harvesting tissues impacts the experiments outcome. So, this procedure must be done as carefully as possible to keep the sample integrity and at the same time, as quick as possible to avoid any protein degradation in the samples.

Methods

At the end of the indicated period of diet or treatment, mice were weighed, then anesthetized and blood was collected directly from inferior vena cava (figure 28). After blood collection, they were euthanized by cervical dislocation, followed by excision of organs starting with the heart. Heart was cannulated and washed with PBS (figure 28). All samples were weighed before processing and then cut in two parts: one for histology and one molecular biology. Samples intended for histology were kept in formalin at 4°C for at least 48 hours before embedding. For molecular biology, tissues were snap-frozen and stored at -80 °C, until they were powdered and aliquoted using mortar, pestle and liquid nitrogen. Plasma was prepared from whole blood samples by centrifugation at 5000g for 10 minutes at 4°C and supernatant was stored at -80°C.



Figure 28: *Dissection pictures: Abdominal excision (left), blood collection (middle), and cannulation of heart (right)*

Dissection, blood and tissue harvesting were performed by **Z. Mezdari, Dr. M. Pini, Dr. D. Sawaki, Dr. G. Czibik, Dr. Y. Zhang, S. Naushad, M. Halfaoui, H. Liang and Dr. L. Lamendour.**

Technical sheet n°11

Plasma Assay

Objective

To assess metabolic parameters and also identify the factors implicated in the crosstalk between the organs, we measured protein concentrations in plasma using Enzyme Linked ImmunoSorbent Assay (ELISA) or Luminex bead-based multiplex assay.

Principle

ELISA assay is based on immuno-enzymatic detection of proteins in a liquid sample and their quantification by colorimetry. Luminex technology is also used to detect and quantify proteins in a liquid sample but it is a bead-based multiplex assay, so, as opposed to ELISA, it has the advantage to analyse several proteins at the same time using only a small amount of the sample.

Methods

For ELISA assay, we used the kit ELISA R&D Systems, (Minneapolis, MN, USA) (figure), and for Luminex assay, we used the kit Luminex R&D Systems, (Minneapolis, MN, USA) (figure). Plasma cytokines were measured following the manufacturer's instructions. Used specific kits are described in the supplemental table.

Data analysis

ELISA plates were analysed with an absorbance microplate reader TECAN infinite 200 and data obtained were processed with Magellan software. Luminex plates were processed and analysed with a Bio-Plex 200 device using xMAP technology of Luminex (Bio-Rad, USA).

Plasma assay was supervised and performed by **M. Pini** with the help of **S. Naushad** and **M. Halfaoui**.

Senescence-associated β -galactosidase staining

Definition

Senescent cells display an altered lysosomal activity resulting in increased levels of β -galactosidase activity at pH 6.0.

Objective

Senescence-associated β -galactosidase (SA- β -gal) is commonly used as a biomarker of cellular senescence,²¹¹ and it was used here to assess senescence in freshly dissected hearts and fat pads.

Methods

Sections of freshly harvested hearts were incubated for 1 hour at 37°C in β -galactosidase staining solution containing 1 mg/ml X-Gal (Sigma), 40 mM citric acid, 150 mM NaCl, 2 mM MgCl₂, 5 mM potassium ferrocyanide and 5 mM potassium ferricyanide with the pH adjusted to 6.0. Stained sections were then scanned. For AT, small pieces (5 mm-square pieces) of freshly dissected tissues were directly subjected to staining solution (1 mg/ml Xgal, Sigma-Aldrich), and kept at 37°C for 8 to 12 hours. The images were taken by GR digital camera (RICOH, Japan).

Z. Mezdari participated to this experiment under the supervision of **M. Pini** and **D. Sawaki**.

Technical sheet n°13

Flow Cytometry

Definition

Flow cytometry is a technology that rapidly analyzes single cells or particles as they flow past single or multiple lasers while suspended in a buffered salt-based solution. Each particle is analyzed for visible light scatter and one or multiple fluorescence parameters.

Methods

Dissected adipose tissues were kept on ice and minced to 1-3 mm pieces in heparinized cold PBS. After snap vortexing, PBS was removed and tissues were digested with collagenase II solution (2mg/mL, Sigma-Aldrich) at 37°C water bath with gently shaking for 20 min. Digested tissue was then passed through 70 µm mesh and centrifuged to spin down stromal vascular fraction (SVF). After RBC lysis (ACK Lysing Buffer, Gibco, A1049201), the SVF cells were suspended in PBS supplemented 2% fetal-calf serum (FCS), and stained with appropriate antibodies for surface marker and isotype controls for 30 min at 4°C in the dark chamber. Used antibodies and fluorophores are listed in the supplemental table. Living and dead cell discrimination was performed with 7-AAD staining (Molecular Probes). For intracellular p16 staining, SVF cells stained with surface markers were then fixed and permeabilized with Cytofix/Cytoperm solution (BD Bioscience). The cells were then stained with Alexa 488 conjugated p16 antibody (2D9A12, Abcam) and corresponding isotype controls. Flow cytometry was performed with LSRII (BD Bioscience). Data was evaluated and analyzed with FlowJo (TreeStar).

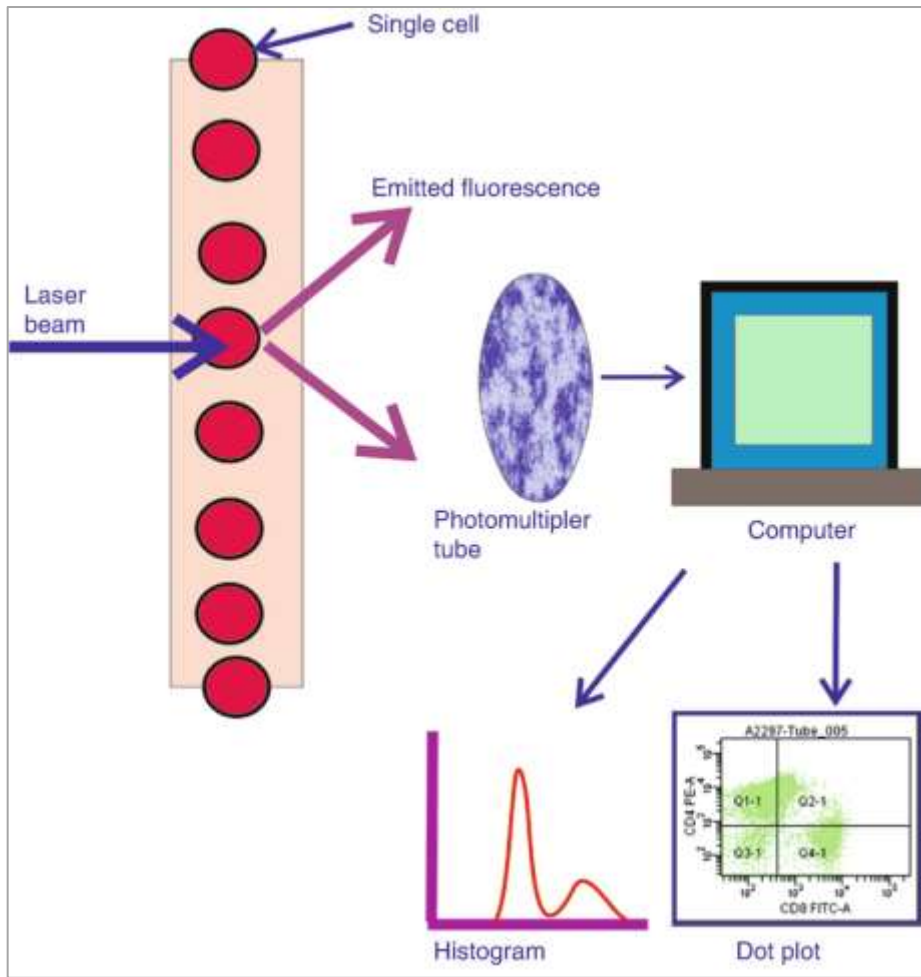


Figure 29: *Flow cytometry: Description and principles (from Pranab Day, 2018).*²⁹⁶

Preparation of samples for flow cytometry was performed by **Z. Mezdari** under the supervision of **D. Sawaki** and **Y. Zhang**. Analysis were performed by **Y. Zhang**.

Isolation and cell culture of Bone Marrow-Derived Macrophages

Objective

These cells are used as a model to study macrophage cells *in vitro* for a mecanistic approach that would be complementary of *in vivo* interventions and observations.

Methods

Mouse bone-marrow cells were isolated from femurs and tibias. After RBC lysis (LCK buffer, Sigma-Aldrich) and filtration through 70 µm mesh, bone-marrow cells were plated with macrophage culture media (MC media: RPMI 1640 medium (Gibco) supplemented with 5%FCS, penicillin/streptomycin (Gibco) and 30 ng/ml MCSF (R&D systems)). Five days after differentiation into macrophages, the cells were dissolved with Accutase (Sigma-Aldrich), counted and re-plated at 2×10^5 /well density in 12-well non-coated plate.

We confirmed that over 95% of cells were diferentiated into CD11b/F4/80 double positive macrophages by this method.

Z. Mezdari participated to isolation and cell culture of BMDM under the supervision of **D. Sawaki** with the support of **Y. Zhang** and **M. Pini**

Cell culture experiments on BMDM

BMDM stimulation by osteopontin

Modulation of BMDM by OPN protein was evaluated as previously described with minor modification.²⁹⁷ Briefly, 12-well plates were coated with 20 or 40 µg of mouse recombinant OPN (R&D systems) for 20 hours at 4°C and then stabilized with 0.5% polyvinylpyrrolidone (Sigma-Aldrich) for 1 hour at room temperature. BMDM (1.5×10^5 /well) were re-plated in RPMI 1640 medium supplemented with 5%FCS and 30 ng/ml MCSF. Twenty-four or 36 hours after passage, the cells were harvested for RNA extraction.

BMDM immunofluorescent staining

BMDM were passed onto an OPN-coated 8-well Lab-Tek II chambered cover glass (Nalge Nunc) at 1.5×10^4 /well density. After incubated as described above, the BMDM were washed with chilled PBS buffer and fixed with 2% paraformaldehyde solution for 10 min at room temperature and permeabilized with 0.05% Triton-X (Sigma-Aldrich). The cells were blocked with 2% BSA solution (Sigma-Aldrich) and subjected to p16 and F4/80 antibody treatment for overnight. Corresponding 2nd antibodies conjugated with fluorescent dyes were used to visualize with DAPI nucleus counter-staining. The images were taken using an Axioplan M2 Imaging microscope (Zeiss).

Phagocytosis assay

Isolated BMDM were used as effector cells and Human leukemia cell-line (HL60) was used as target cells. HL60 cells were labeled with pHrodo as previously described ²⁹⁸ with minor modification. In brief, the HL60 cells were washed twice with PBS buffer and incubated at room temperature for 30 min with 0.1 µg/ml pHrodo. The cells were washed with PBS buffer twice, and suspended in the RPMI medium containing 0.5% FCS, and used for engulfment. To 5.0×10^4 BMDM in 500 µl of RPMI medium containing 5% FCS in a 12-well plate, 2.0×10^5 pHrodo-labeled HL60 cells were added, and incubated at 37°C for 0, 30, 60, and 120 min. The cells were detached from the plate by incubating with 0.25% trypsin and 1mMEDTA, and

collected by centrifugation. After stained with appropriate antibodies for surface marker and isotype controls, cells were further suspended in 500 μ l of PBS buffer containing 2% FCS and analyzed by flow cytometry on the LSRII (BD Bioscience). Data was evaluated and analyzed with FlowJo (TreeStar). For time-lapse imaging, 1.5×10^4 /well BMDM were passed onto an 8-well Lab-Tek II chambered cover glass (Nalge Nunc), and incubated at 37°C for 0, 30, 60, and 120 min with 6×10^4 pHrodo-labeled HL60 cells in 250 μ l of RPMI medium containing 5% FCS and observed by fluorescence microscopy.

Z. Mezdari participated and was trained to phagocytosis assay under the supervision of **D. Sawaki** and **Y. Zhang**.

Isolation and cell culture of Preadipocytes

Methods

Preadipocytes were isolated from iWAT and eWAT stroma vascular fraction (SVF) and differentiated in an adipogenic culture media after two passages to eliminate non-preadipocyte cell contamination. In detail, WAT was aseptically minced and incubated with collagenase Type II (1 mg/mL, Sigma-Aldrich) at 37°C for 45 min. After digestion, serum-containing medium was added to the suspension and filtered through a 100 µm cell strainer. SVF cells were centrifuged for 10 min at 350 g and suspended in pre-warmed adipogenic culture media, consisting of DMEM high glucose with Glutamax (Gibco) supplemented with 10% new born calf serum (Thermofisher), 2.4 nM human insulin (Sigma) and 1% antibiotic solution (Pen-Strep solution, Sigma). To induce differentiation, SVF cells were seeded near confluence and medium was replenished every day to allow selection by adhesion during the first 3 days and then changed every 2 days. SVF cells were cultured in an atmosphere of 5% CO₂ and 20% O₂ at 37°C. Based on preliminary experiments, day 7 was the time of differentiation used for all experiments.

This experiment was performed by **M. Pini**

Cell culture experiments on preadipocytes

Primary cell metabolic rate measurements

For bioenergetics assessment, the Mitochondrial Stress Test was performed on iWAT- and eWAT-differentiated adipocytes (20,000 cells/well) using the XF24 Extracellular Flux Analyzer (Agilent Technologies, Santa Clara, CA, USA). Oxygen consumption rate (OCR), indicative of mitochondrial activity, and extracellular acidification rate (ECAR), an index of glycolysis, were determined as described ²⁹⁹.

ATP measurements

Differentiated primary preadipocytes and 3T3-L1 were lysed and intracellular ATP content measured by the ATP-lite assay kit (Perkin Elmer, Villebon-sur-Yvette, France) ³⁰⁰.

Cell culture treatments

Primary preadipocytes were isolated from WAT of 5-month-old CD male mice. At differentiation, cells were incubated at different time points (for the time course: 30 min-3h-6h-24h or as specified in the figure legend) with adenosine triphosphate (ATP)- and uric acid-loaded liposomes (200 μ M, Sigma-Aldrich, France) as compared to two control applications: liposome-free (lipo-free) and liposome alone (CTL).

In addition, to assess the role of ATP as a senescence trigger, we performed interference experiments by co-administration of the xanthine oxidase (XO) an allopurinol inhibitor. Preadipocytes were subjected for 6 hours to *in vitro* caloric overload in the form of either high glucose/palmitate (Metabolic media: MM) or ATP-loaded liposomes and co-administration of allopurinol (1mM).

Fully differentiated 3T3-L1 adipocytes, cultured in an atmosphere of 5% CO₂ and 20% O₂ at 37°C, were incubated for 24 hours with ATP or uric acid (200 μM, Sigma-Aldrich, France). ATP and the other molecules were encapsulated in liposomes (Sigma-Aldrich, France)

Superoxide level measurement

Cytosolic and mitochondrial ROS levels were measured in differentiated preadipocytes (7000/well) by quantification of CellROX (10 μM) and MitoSOX (5 μM) fluorescence intensity levels, respectively. Fluorescence readings were done by a microplate reader (Tecan, Männedorf, Switzerland).

This experiment was performed by **M. Pini**

Cell culture experiments on C2C12 and AML-12

C2C12 cell line

C2C12 (ATCC® CRL-1772™) myoblasts maintained in DMEM supplemented with L-glutamine (2 mM), penicillin/streptomycin (1%) and 5% fetal bovine serum (FBS) were seeded either at a density of 5×10^4 cells (<50%) per well in 24-well plates or 10^4 cells in 4-well chamber slides. At 80% confluence, cells were treated with L-phenylalanine (1-10 mM), BH4 (10 μ M), 4-CPA (1.5 mM) and/or N-acetylcysteine (500 μ M) vs. vehicle overnight as indicated. Cells were analyzed for oxidative stress with MitoSOX™ (mitochondrial superoxide; 5 μ M, ThermoFisher Scientific), CellROX™ (cytosolic superoxide; 5 μ M, ThermoFisher Scientific), gene or protein expression, or various metabolites (see below).

AML-12 cell line

AML-12 (ATCC® CRL-2254™) hepatocytes were maintained in DMEM/F-12 (1:1) culture media supplemented with 10% FBS, 10 μ g/ml insulin, 5.5 μ g/ml transferrin, 5 ng/ml selenium, 40 ng/ml dexamethasone and 1% penicillin/streptomycin. Cells were sub-cultivated from subconfluent flasks with a ratio from 1:4 to 1:8. For WB analysis, cells were plated on 6-well plates and harvested at 80-90% of confluence. AML-12 cells were treated with Nutlin3a (10 μ M) against vehicle (DMSO) and transfected with indicated siRNA (Supplementary Table 2) at 80% confluence using Lipofectamine RNAiMAX Transfection Reagent (ThermoFisher Scientific 13778030) following the manufacturer's instructions. Transfection efficiency was constantly checked using BLOCK-IT Alexa Fluor Red Fluorescent Control (ThermoFisher Scientific 14750100). In other experiments AML-12 cells were treated with Nutlin3a without or with BH4 (10 μ M). Cells were lysed for protein extraction, whilst conditioned media was used to determine tyrosine concentration.

This experiment was performed by **G.Czibik**

Histological Assessment

Objective

Histological assessment consists in analysing the structure and properties of biological tissues. It is also used in order to get information about spatial location and/or evaluate the density of molecules and proteins of interest by histochemistry or immunohistochemistry technics.

Principle

Histochemical staining is based on biochemical reactions that can detect specific tissue components such as lipids, carbohydrates, or proteins. Immunohistochemical staining is based on immunochemical reaction used to detect a specific antigen thanks to a specific antibody.

Methods

Histochemical staining: Formalin-fixed organs were paraffin-embedded and sectioned into 7 μm thickness using a rotary microtome (Leica). The sections were deparaffinized using xylene and a graded series of ethanol dilutions. For general overview, adipocyte size measurements and counting of CLS sections were stained with hematoxylin and eosin (Sigma-Aldrich, France). For determination of adipose tissue, liver and cardiac fibrosis, sections were stained with Picrosirius red using a commercial kit (Polysciences Europe GmbH, Germany) following the manufacturer's instructions.

Immunohistochemical staining: Immunofluorescence was used to detect proteins of interest within their native environment, including co-localization with cell-specific markers. Briefly, paraffin-embedded sections were rehydrated, followed by heat-mediated antigen retrieval with citrate buffer pH6.0 (Dako). Sections were blocked with 30% goat serum and incubated overnight at +4 °C with primary antibodies (described in the supplemental table). The following day sections were washed, incubated with corresponding Alexa Fluor 488, 555 or

647 conjugated secondary antibodies (Invitrogen), washed again and mounted with Fluoroshield Mounting Medium With DAPI (Dako).

BODIPY fluorescent staining: Dissected adipose tissues were washed in PBS and cut into 3-5 mm pieces. Tissues were then incubated for 1h with BODIPY dye (Invitrogen D3835), a lipid marker, at a concentration of 1/1000, Isolectin GS-IB4 (Invitrogen I21411), a capillary marker, at a concentration of 1/100, and TO-PRO™-3 Iodide (642/661; Invitrogen T3605), marker of nuclei, at 1/1000 concentration. After PBS wash, tissues were put on the ibidi culture slide with 10% glycerol solution and observed under confocal microscope.

Data analysis

The pictures with hematoxyline & eosin and Sirius Red staining were captured using an Axioplan 2 Imaging microscope (Zeiss). Immunohistochemical staining images were obtained with an Axioimager M2 fluorescent microscope (Zeiss). Confocal microscope (Zeiss LSM 510 Meta) was used for BODIPY fluorescent staining. All quantifications were done blindly, using the ImageJ software

Histological assesment was performed by **Z. Mezdari, Dr. M. Pini, Dr. D. Sawaki, Dr. G. Czibik, S. Naushad, M. Halfaoui, H. Liang, and Dr. D. Altintas.**

Evaluation of Gene Expression

Objective

Gene expression is a variable parameter depending on several factors including time (phase of development, age, circadian rhythm...), location (cells, tissues, organs...), or biological context (physiological state, pathological state, specific response to a stimulus...)

Evaluation of gene expression consists in measuring associated transcript levels (mRNA levels) in order to highlight potential relative changes that may give indications about pathways and mechanisms involved.

Methods

Total RNA extraction : Total RNA was isolated from powdered snap-frozen tissues using the RNeasy mini kit (Qiagen) for adipose tissue, after a chloroform-mediated lipid removal step, or RNeasy mini fibrous kit (Qiagen) for heart and liver, following the manufacturer's instructions. RNA concentration was then measured with NanoDrop ND-2000.

Reverse transcription: Because RNA is very unstable molecule, we use an enzyme called reverse transcriptase in order to convert the extracted RNA into complementary DNA (cDNA). This step was performed using the High Capacity cDNA kit as instructed by the manufacturer (Applied Biosystems).

Quantitative reverse transcriptase–polymerase chain reaction (qRT–PCR): This technique consists in amplifying a specific DNA fragment thanks to a DNA polymerase and a combination of two DNA primers that are complementary to the 3' ends of each of the sense and anti-sense strands of the DNA target (also known as “forward” and “reverse” PCR primers respectively) . A thermocycler machine (ref) was used for the amplification and amplicon products were detectable in real time by fluorescence.

For more precision and efficacy (as compared with Syber green method for example), we used Taqman probes (Applied Biosystems). This technology consists of a fluorophore covalently attached to the 5'-end of the oligonucleotide probe and a quencher at the 3'-end. The quencher inhibits any fluorescence signal as long as it stays close to the fluorophore. This probe anneals within the specific DNA region (single stranded DNA) and once the Taq polymerase extends the primer and synthesizes the nascent strand, its exonuclease activity degrades the probe and releases the fluorophore, which, relieved from the quenching effect, becomes fluorescent. Hence, the fluorescence detected in the thermocycler is directly proportional to the amount of DNA template present in the PCR. So, quantitative measurements of the accumulation of the product during the exponential stage provide an estimation of transcript levels.

Our qRT-PCR experiments were performed in fast multiplexed reactions using two different fluorophores: FAM for the gene of interest and VIC for the β -actin as endogenous control. We used TaqMan probes which were conjugated to a minor groove binder (MGB) moiety with increased binding affinity. All qRT-PCR reagents, including inventoried Taqman-MGB probes (described in the supplemental table) as well as qRT-PCR instrument were products of Applied Biosystems.

Data analysis

Relative quantification was based on the comparative Ct method (ref). The Ct value or threshold cycle value is the cycle number at which the fluorescent signal crosses the background fluorescence threshold. This corresponds to the point when a detectable amount of amplicon product has been generated. The higher transcript levels we have, the smaller Ct value we obtain. Ct values of target genes (tg) are then compared to Ct value of the endogenous control (ec) β -actin and initial transcript levels are determined using the following calculation:

$Ct(tg) - Ct(ec) = \text{coefficient} * \log(N(tg)/N(ec))$ with N=initial transcript levels.

The values obtained were plotted using the software Prism-Graphpad to perform a graph showing gene expression fold change relative to a control group.

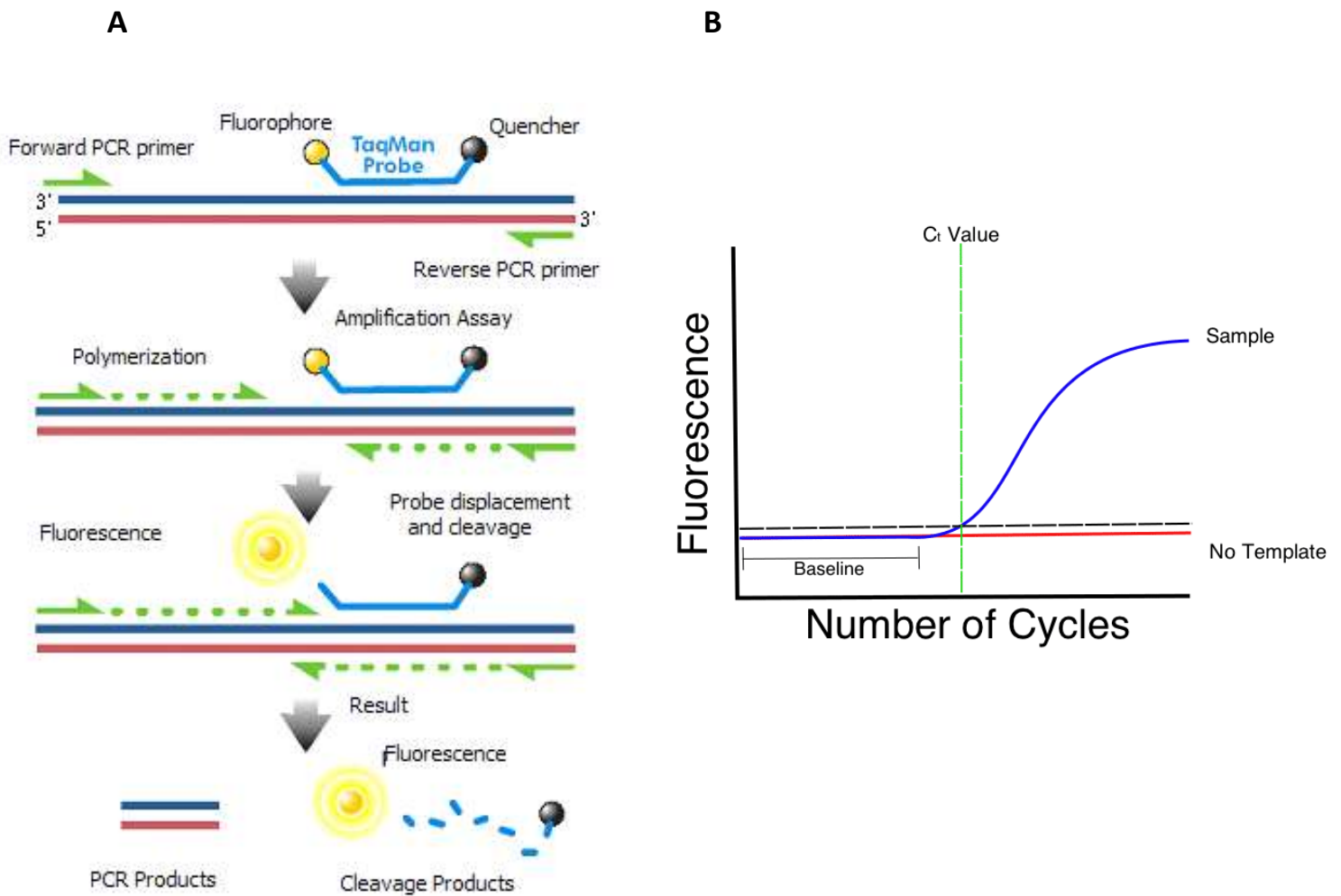


Figure 30: (A) Principle of the TaqMan technology (from <https://en.wikipedia.org/wiki/TaqMan>) ; (B) Representative qPCR amplification curve (from <https://bitesizebio.com/24581/what-is-a-ct-value/>)

Evaluation of gene expression was performed by **Z. Mezdari, Dr. M. Pini, Dr. D. Sawaki, Dr. G. Czibik, S. Naushad, M. Halfaoui, H. Liang, Dr. L. Lamendour and Dr. D. Altintas.**

Evaluation of Protein Expression

Objective

Protein synthesis results from mRNA translation by ribosomes. Thus, protein expression should be reflecting gene expression. However, this is not always the case, given that protein expression can be regulated at different levels. So, when deciphering the mechanisms underlying potential changes observed in physiological, pathological or experimental condition, both gene and protein expression should be evaluated.

Methods

Total protein extraction: Pulverised tissue samples (100-150 mg of eWAT) were lysed with T-PER lysis buffer (ThermoFisher) supplemented with 0.05 mM phenylmethylsulphonyl fluoride (PMSF), 0,05 mM proteasome inhibitor MG-132 (Sigma-Aldrich), and protease/phosphatase inhibitor cocktail tablet (ThermoFisher) complete with sonication and passing through a 21 G needle. To pellet any debris, lysates were centrifuged at 12,000 g for 15 minutes at 4°C, and the middle fraction (between pellet and lipid layer) was transferred to fresh tubes.

Protein assay: Bradford assay (BioRad) was used to determine protein concentrations, sample concentrations were then equalised with lysis buffer and boiled with Laemmli buffer.

Western blot: Equal amounts of protein lysates were loaded onto precast denaturing polyacrylamide gels (Nupage 12% Bis Tris gel, Novex, Invitrogen). Proteins were separated by electrophoresis, then transferred onto polyvinylidene difluoride (PVDF) membrane (Invitrogen) using a transfer cell (Bio-Rad) in ice-cold transfer buffer (48 mM Tris base, 390 mM glycine, 0.1% SDS, 20% methanol (v/v)) at 125V for 2 hours. Membranes were blocked in 1x skimmed milk for 1 hour at room temperature, followed by overnight incubation with primary antibody (described in the supplemental table) diluted in blocking buffer at 4°C. The following morning membranes were washed, incubated with the corresponding horseradish

peroxidase (HRP)-conjugated secondary antibody in blocking buffer for one hour. Blots were developed with the aid of enhanced chemiluminescence (ECL) reagents (normal, Prime & Select) and digital images were obtained with a dedicated imaging system (Azure Biosystems). Membranes were stripped of antibodies and reprobred with an antibody raised against β -actin conjugated to HRP as loading control. This procedure consisted in incubation for 15min in Guanidine-HCl-based stripping solution (6M Guanidine-HCl, 0.2% Nonidet P-40, 0.1M β -mercaptoethanol, 20mM Tris-HCl, pH7.5 and 100 mM 2-mercaptoethanol) and at room temperature with gentle agitation, followed by extensive washing and blocking.³⁰¹

Data analysis

The images obtained were analysed using imageJ software. Intensity of signals corresponding to the protein of interest were normalized on the intensity of signals corresponding to the β -actin and values were plotted using Prism-Graphpad software.

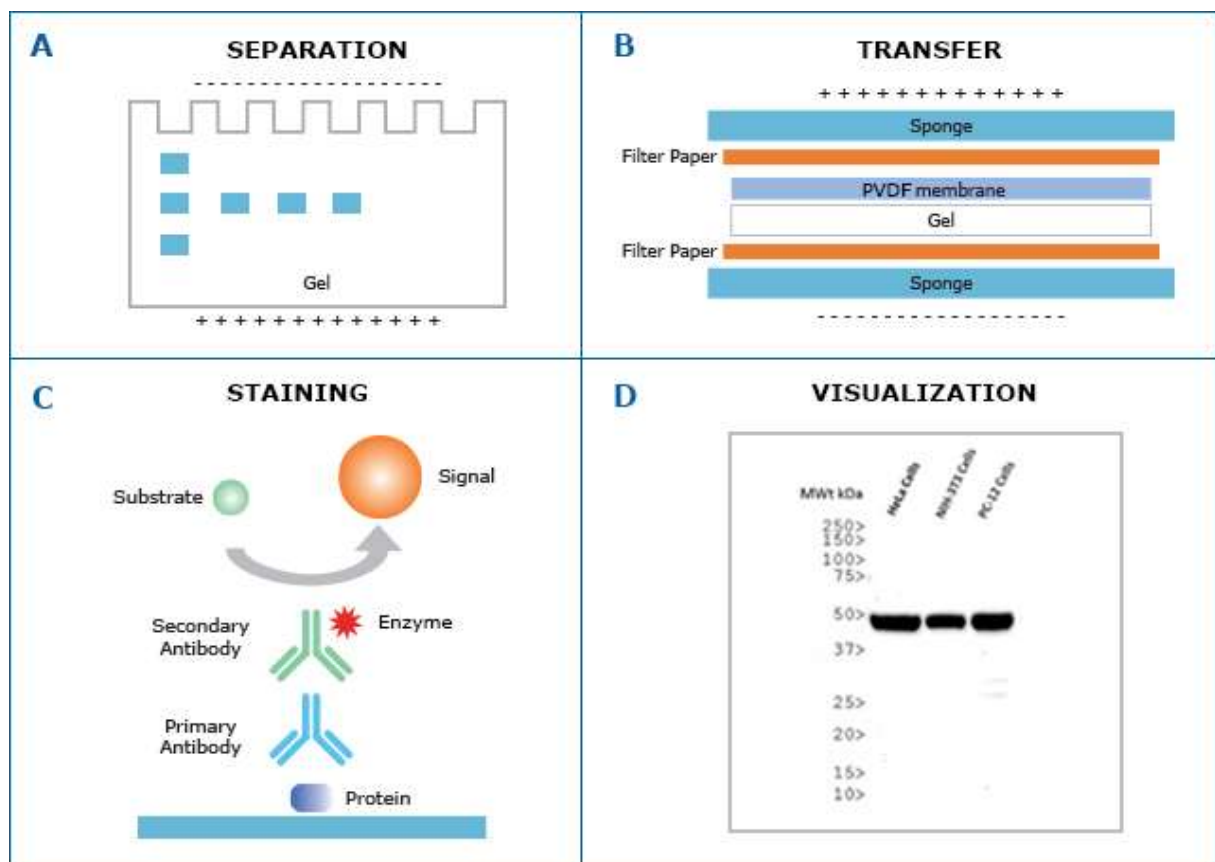


Figure 31: Representation of the different steps of Western blot (from <https://www.novusbio.com/application/western-blotting>)

Evaluation of protein expression was performed by **Z. Mezdari, Dr. D. Sawaki, Dr. G. Czibik, and Dr. D. Altintas.**

Statistical Analysis

Data were acquired and analysed blind to age or treatment. Unpaired, two-tailed t-test was used to compare two groups. More than two groups were compared with one-way analysis of variance (ANOVA), with Bonferroni or Tukey's correction for multiple comparisons. Two-way ANOVA was used to compare groups with time-dependent changes, with Bonferroni or Tukey's correction for more than two groups. Data are presented as original images or mean \pm SEM. Annotations: ns: non-significant, * $p < 0.05$, ** $p < 0.01$, *** $p < 0.001$, **** $p < 0.0001$ as indicated. A p value of < 0.05 was considered significant and p value > 0.05 was considered non-significant.

RESULTS

The result section is presented in two main sections:

➤ **Assessment of adipose tissue senescence in the context of high fat diet-induced obesity and in the context of aging:**

1) The first study is entitled “Visceral adipose tissue macrophage senescence promotes metabolic and cardiac disorders during the onset of HFD-induced obesity”. It is presented as commented figures and the article is being finalised and prepared for submission in Diabetes journal.

This study is the core of my thesis work. I conducted this project and performed most of the experiments, with the support and participation of my team.

2) The second study is entitled “Osteopontin promotes adipose tissue remodeling through macrophage senescence”. It is presented as an article submitted to JCI Insight and is associated to a published letter to Circulation in which I was co-author. This aims at evaluating the role of osteopontin on visceral adipose tissue remodeling and dysfunction in the context of aging, and in the cross-talk between adipose tissue and heart. My participation to this study consisted in helping with organ isolation, preparation for FACS analysis, quantitative PCR analysis, and imaging experiments.

3) The third study is entitled “Adipose tissue senescence is mediated by increased ATP content after a short-term high fat diet exposure” and is presented as original article under revision in Aging Cell. My contribution to this study consisted in participating to the bibliographic searches, helping with in vivo procedures (body weight measurements, metabolic tests, exercise training), organ isolation, imaging experiments and data analysis.

➤ **Analysis of the mechanisms associated with cardiac aging:**

The fourth study is entitled “Dysregulated phenylalanine catabolism is a defining characteristic of cardiac aging”. It is presented as original article under revision in Circulation. My contribution to this study consisted in participating to the in vivo procedures (animal handling, measurement of body weight, water and food intake, drug administration, metabolic tests), organ isolation and processing, preparation of sample aliquots for collaborators, quantitative PCR analysis, imaging experiments, data analysis and critically reading the manuscript with suggestions.

STUDY 1

ETUDE 1

Résumé

Le tissu adipeux viscéral est un facteur de risque majeur des comorbidités associées à l'obésité tel que le diabète de type 2 et les maladies cardiovasculaires. Cependant, malgré les études effectuées sur cet organe dans le contexte de l'obésité, très peu de choses sont connues sur les événements primaires qui sont à l'initiation des altérations du tissu adipeux observées chez les individus obèses.

Nous avons donc focalisé notre attention sur les mécanismes initiateurs du remodelage du tissu adipeux et de la sénescence du TA viscéral en établissant une cinétique des événements en analysant chaque type cellulaire et en particulier les macrophages de cet organe du fait de leur rôle reconnu dans les altérations métaboliques et cardiaques.

Nous avons utilisé un modèle murin pour comparer l'effet d'un régime riche en graisses chez des souris jeunes et des souris âgées puis dans un second temps observé chez les souris jeunes les modifications du tissu adipeux viscéral et du cœur à différentes durées de ce régime. Enfin, nous avons traité ces souris par sénolytiques (association Dasatinib/Quercétine) puis par clodronate afin d'éliminer spécifiquement les macrophages.

Les résultats obtenus ont montré que les souris jeunes répondent de manière plus rapide et plus intense au stress métabolique comparé aux souris âgées. Nous avons également pu observer que la sénescence du tissu adipeux était un élément précoce au cours du régime riche en graisses et qu'elle affectait en priorité les macrophages chez les souris jeunes, en apparaissant avant l'inflammation et la fibrose qui caractérisent habituellement le tissu adipeux dans le cadre de l'obésité. De plus, la survenue de sénescence coïncide avec l'apparition de troubles métaboliques et cardiaques. Enfin, le rôle crucial des macrophages a été confirmé par une complète restauration des paramètres métaboliques et cardiaques à la suite de leur élimination par clodronate alors que le traitement sénolytique ne normalisait pas ces paramètres.

Ces résultats montrent donc l'importance et le rôle clé que jouent les macrophages sénescents dans les complications métaboliques et cardiaques lors de l'obésité et apportent des arguments pour le développement de traitements ciblant spécifiquement les macrophages.

Ce travail a fait l'objet d'une communication au congrès «European Society of Cardiology (ESC)» en 2018

This work was exposed during an oral communication during European Society of Cardiology (ESC) congress in 2018

Role of adipose tissue macrophages in the cross-talk between visceral adipose tissue and heart during high fat diet

Authors:

Z. Mezdari¹, M. Pini¹, G. Czibik¹, J. Ternacle¹, C. Radu¹, Y. Zhang¹, S. Adnot¹, C. Henegar¹, G.A. Derumeaux², D. Sawaki¹, ¹University Hospital Henri Mondor, DHU ATVB, APHP, UPEC - Creteil - France, ²Inserm U886, University Claude Bernard Lyon 1 - Lyon - France,

Topic(s):

Obesity

Citation:

European Heart Journal (2018) 39 (Supplement), 496

Funding Acknowledgements:

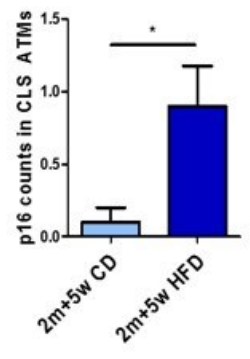
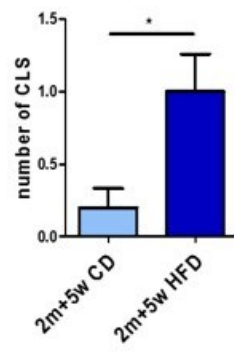
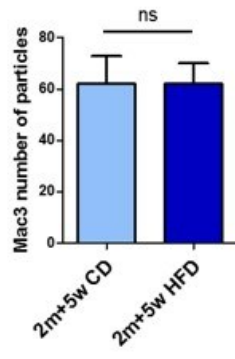
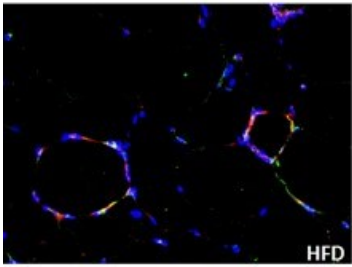
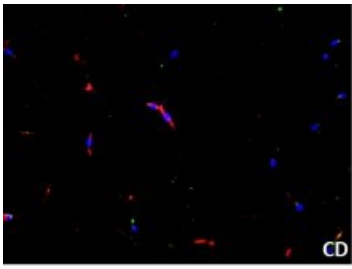
ANR

Background: Obesity is associated with remodeled and dysfunctional visceral white adipose tissue (vWAT). Recent studies suggest a cross-talk between vWAT and heart contributing to cardiac alteration. We hypothesize that adipose tissue macrophages (ATM) play a key role in the vWAT remodeling through a premature senescence mechanism in the context of high fat diet (HFD)-induced obesity.

Method: C57BL/6 male mice (2 months old, n=5/group) fed with HFD (60% fat, 7% sucrose) or chow diet (CD) for 5 weeks underwent an in vivo cardiac evaluation (echocardiography, strain rate) and metabolic tests (glucose (GTT) and insulin (ITT) tolerance tests) before sacrifice. After sacrifice, myocardial fibrosis (Sirius Red), vWAT remodeling and ATM infiltration (Mac 3) and senescence (p16) were assessed.

Results: After 5 weeks HFD induced a significant increase in body weight as compared with CD (30±0.9 vs 41.1±1.3, p<0.0005) and intolerance to glucose and insulin. Myocardial function in HFD as compared with CD as shown by strain rate (27±0.8 vs 21±0.8, p<0.05) together with a slight increase in myocardial fibrosis. These changes were parallel with vWAT remodeling, i.e. increase in adipocyte size and in crown-like structures (CLS), an inflammatory phenomenon consisting of macrophages surrounding dead adipocytes. We did not observe any increase in ATM number but a marked senescence phenotype as shown by the increase in p16 staining. These early changes in ATM phenotype might account for the senescence-associated secretory phenotype of vWAT which is profibrotic (increase in TGFβ plasma level).

Conclusion: Our data show 1) HFD-induced senescence of adipose tissue macrophage occurring as early as 5 weeks of HFD and preceding inflammation, 2) increase in profibrotic cytokines and 3) early myocardial dysfunction and fibrosis.



Visceral adipose tissue macrophage senescence promotes metabolic and cardiac disorders during the onset of HFD-induced obesity

Abstract

Visceral adipose tissue (VAT) plays an important role in the obesity “diseasome”, involving type 2 diabetes mellitus (T2DM) and cardiovascular diseases. Despite extensive literature on the characteristics of VAT in the context of obesity, little attention has been given to early events that may trigger deleterious subsequent changes.

In order to investigate specifically the time course of VAT changes after initiation of high fat diet (HFD), we analyzed wild-type (WT) male mice on high-fat diet (HFD, 60% fat +5% sucrose vs. control diet) during 10 weeks and sequentially evaluated VAT and cardiac changes. Although HFD did not increase body and fat pad weights until five weeks of HFD, glucose homeostasis was compromised as early as two weeks. Interestingly VAT senescence was mainly linked to the upregulation of P16 and P21 in CD68-positive macrophages at this stage, without any signs of inflammation or remodeling. Furthermore, two weeks of HFD compromised myocardial contractility as evaluated by strain rate, an index of cardiac fiber shortening. The crucial involvement of macrophages was confirmed through rescue of cardiometabolic function by their pharmacological clearance by clodronate, whilst senolytic treatment was less effective.

These results demonstrate the importance of early macrophage senescence in high fat diet-induced cardiometabolic dysfunction and may shed new light on the search for developing better therapeutic options in metabolic disorders et cardiac-associated impairment.

Introduction

The world faces an obesity epidemic afflicting the entire cross-section of society, with increased risk for type 2 diabetes mellitus (T2DM), dyslipidaemia and cardiovascular disease.³⁰² As an inseparable part of chronic positive imbalance, surplus energy accumulates in adipose tissue (AT) as fat. Contrary to early beliefs,³⁰³ AT is not an inert storage structure, but an organ with significant plasticity and secretory activity with potential impact on the function of remote organs.^{50,304} Moreover, not all adipose tissue pads are equal; accumulation of visceral adipose tissue (VAT) corrodes health more than subcutaneous fat does.³⁰⁵ This suggests the existence of VAT-specific pathological processes spreading injury to other organs, such as the heart, as we recently demonstrated in the context of aging.²⁶

Observations in obese individuals and in high-fat diet (HFD)-induced obesity murine models, led to the discovery of chronic low-grade inflammation³⁰⁶ and increased leptin secretion.^{48,288,307-309} Moreover, adipocyte hypertrophy, tissue remodeling,¹⁷² hypoxia,^{310,311} and accelerated senescence^{204,283,312} have been implicated in cardiometabolic dysregulation. These studies used long dietary regimens (typically >15 weeks) without focusing on the initiation of VAT abnormalities.

Therefore, our study aimed at studying the time-course of abnormalities occurring early in VAT after initiation of high fat diet. We also aimed to compare young (2 months old) and aged (12 months old) wild type C57BL6-J mice, in order to identify the potential confounding factor of aging which may *per se* affect VAT and heart.

Here we present the comparison of VAT changes in young and old mice undergoing HFD regimen and we focus on the presentation of the analysis of the time-course in young mice to characterize the changes in VAT during this short exposure to HFD.

Similar analysis are scheduled in the group of old mice and work is in progress.

Results

I) Metabolic parameters in young and aged mice undergoing HFD

To explore the response of differently aged mice to caloric overload, C57BL/6 (WT) male mice of 2 and 12 months of age were fed a high-fat diet (HFD; vs. chow as control diet) for the duration of 5 or 20 weeks (figure 1).

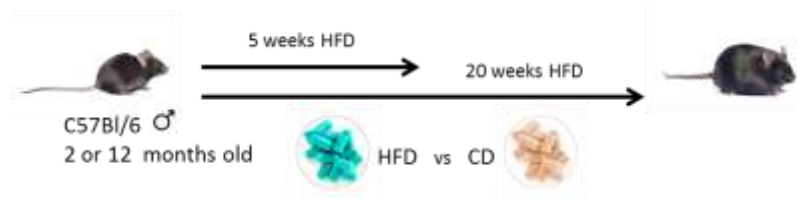


Figure 1: Schematic of treatment protocol. Young (2m) or aged (12m) mice fed CD or HFD either for 5 weeks or for 20 weeks, a total of 8 groups ($n=4-5$ /group).

Compared to control diet groups, HFD increased body weight in all groups, except in 12-month-old mice on HFD for 5 weeks (figure 2A). Adiposity index, i.e. the sum of major fat pads (EWAT, IWAT & PRWAT) normalised to body weight, increased in HFD-groups to a similar extent regardless of age or duration of HFD (figure 2B). Weight of the intraperitoneal visceral adipose tissue or epididymal adipose tissue (EWAT) greatly increased in all HFD groups as early as 5 weeks after initiation of HFD (figure 2C).

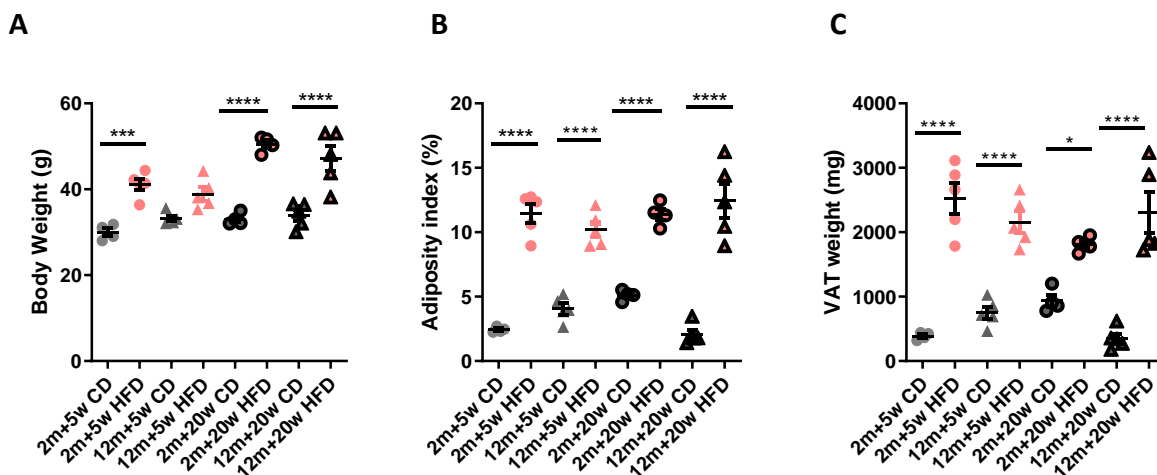


Figure 2: A, Body weight. B, Adiposity index. C, VAT weight; ($n=4-5$ /group). Data are presented as mean \pm SEM analysed with ANOVA with Tukey's post-hoc test; ns: non-significant, * $p < 0.05$, ** $p < 0.01$, *** $p < 0.001$, **** $p < 0.0001$ as indicated.

After initiation of HFD, cross-sectional area of adipocytes increased as early as 5 weeks as compared with CD groups in both young and aged mice (figure 3A, B).

However, the number of crown-like structures (CLS) significantly increased only in young mice at a later stage of 20 weeks as compared with CD mice, whilst a similar trend was observed in old mice (figure 3C).

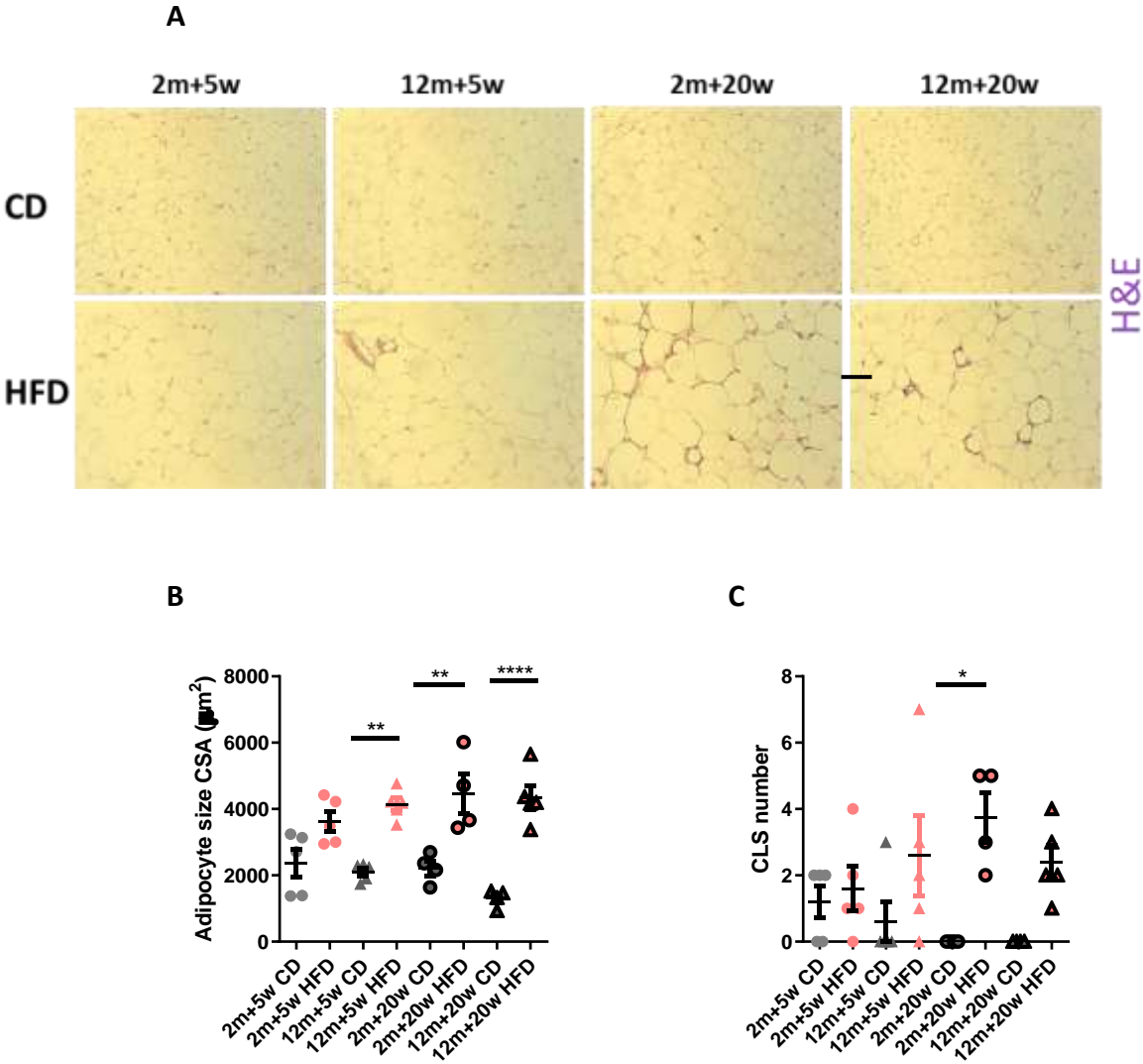
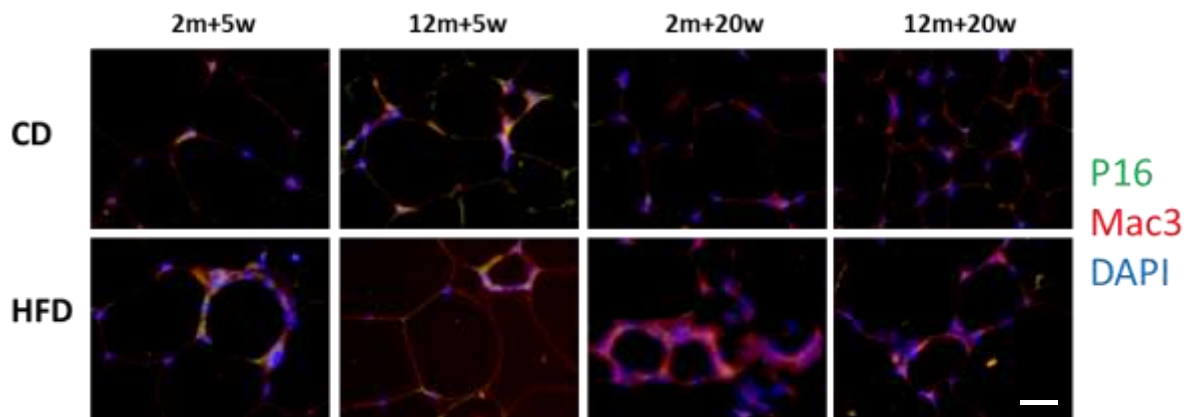


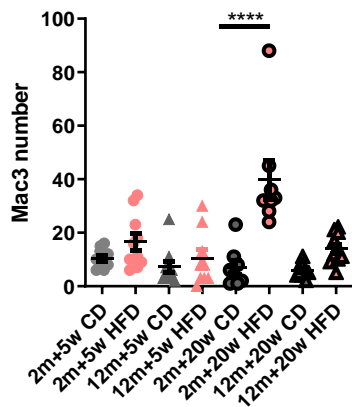
Figure 3: A, Representative images of VAT stained with Hematoxylin and Eosin (H&E), magnification: 100x, scale-bar: 100 µm. B, Quantification of adipocyte cross-sectional area (CSA). C, number of crown like structures (CLS); (n=4-5/group). Data are presented as mean ± SEM analysed with ANOVA with Tukey’s post-hoc test; ns: non-significant, *p < 0.05, **p < 0.01, ***p < 0.001, ****p < 0.0001 as indicated.

Adipose tissue macrophages (ATMs) are important cellular components of the adipose tissue and they are concentrated in CLS. Interestingly, HFD significantly increased the total number of ATM (Mac 3) in young mice after a 20-weeks duration of HFD but not in old mice. This increase in ATM was with a higher number of ATMs, which were positive for p16 (figure 4).

A



B



C

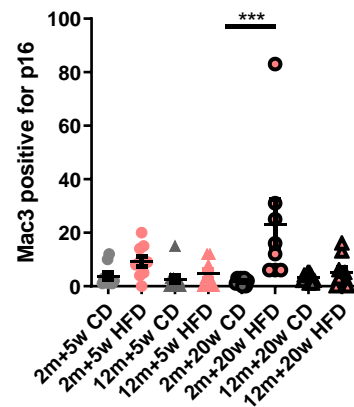
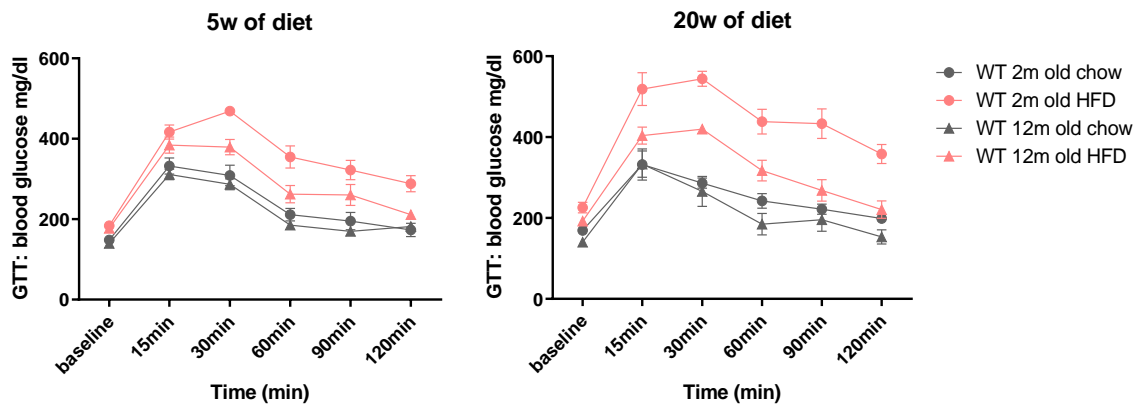
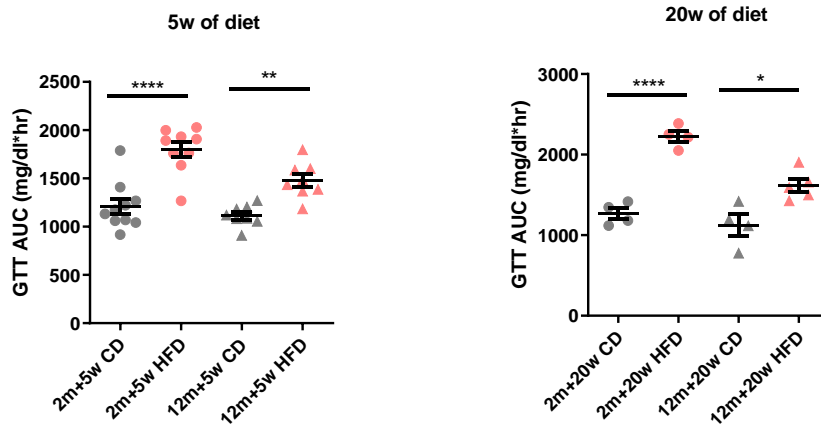
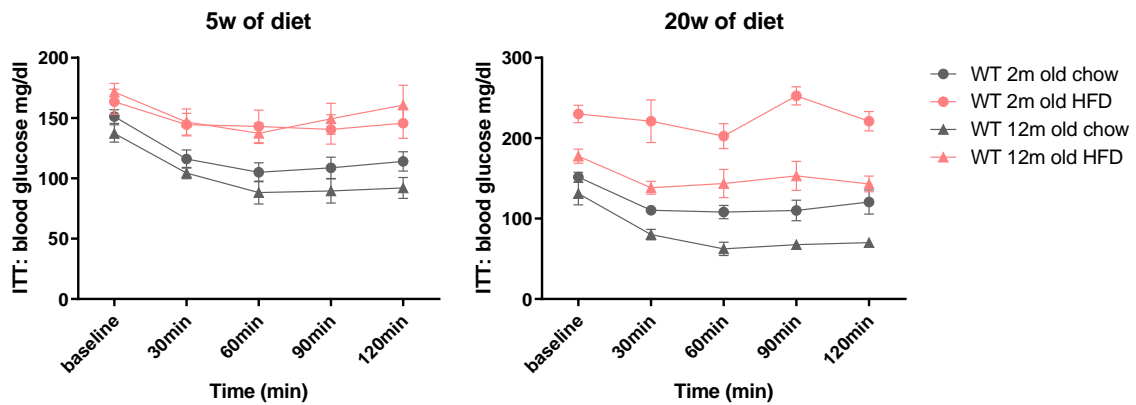


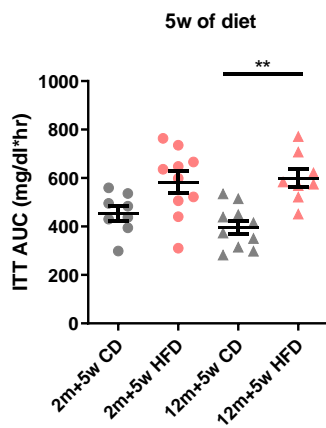
Figure 4: *A*, Representative images of VAT co-stained with p16 (senescence marker), Mac3 (macrophage marker), and DAPI (nuclei), magnification: 400x, scale-bar: 25 μ m. *B*, Quantification of Mac3 positive cells. *C*, Quantification of p16 and Mac3 double positive cells; ($n=4-5$ /group). Data are presented as mean \pm SEM analysed with ANOVA with Tukey's post-hoc test; ns: non-significant, * $p < 0.05$, ** $p < 0.01$, *** $p < 0.001$, **** $p < 0.0001$ as indicated.

Next, systemic glycaemia was evaluated. HFD worsened glucose tolerance as early as 5 weeks with further aggravation at 20 weeks in all groups, but at a lesser extent in 12-month-old than in 2-month-old mice.

After 20 weeks of HFD, a more severe pattern of insulin resistance was observed in young versus old mice on HFD as compared with control chow diet groups, whilst ITT curves between 2- and 12-month-old mice on HFD were comparable after 5 weeks of HFD and worse than those of CD group (figure 5).

A**B****C****D**

E



F

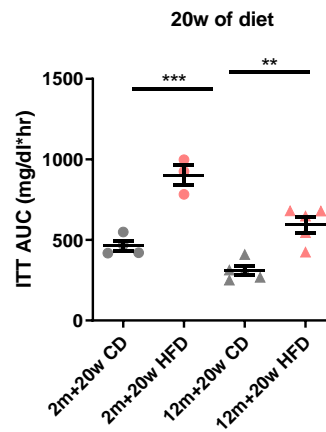


Figure 5: A-F, Temporal plot and area-under-curve (AUC) analysis of Glucose tolerance test (GTT; A-C) and insulin tolerance test (ITT; D-F); ($n=4-5/\text{group}$). Data are presented as mean \pm SEM analysed with ANOVA with Tukey's post-hoc test; ns: non-significant, * $p < 0.05$, ** $p < 0.01$, *** $p < 0.001$, **** $p < 0.0001$ as indicated.

II) Time course of metabolic alterations in young mice submitted to HFD

In order to explore early sequence of structural, functional and molecular alterations in high fat diet-induced obesity, 2-month-old C57BL/6 male mice were fed chow (CD) or high-fat diet (HFD) and euthanized at 2, 5 and 10 weeks after the initiation of the diet (figure 6).



Figure 6: Schematic of treatment protocol. 2-months-old mice fed CD or HFD either for 2 weeks or 5 weeks or 10 weeks, a total of 6 groups ($n=5-10/\text{group}$).

The alteration of ITT and GTT occurred as early as 2 weeks of HFD (figure 7A-D) without any significant change in body weight and adiposity index before 5 weeks of HFD (figure 7E-F).

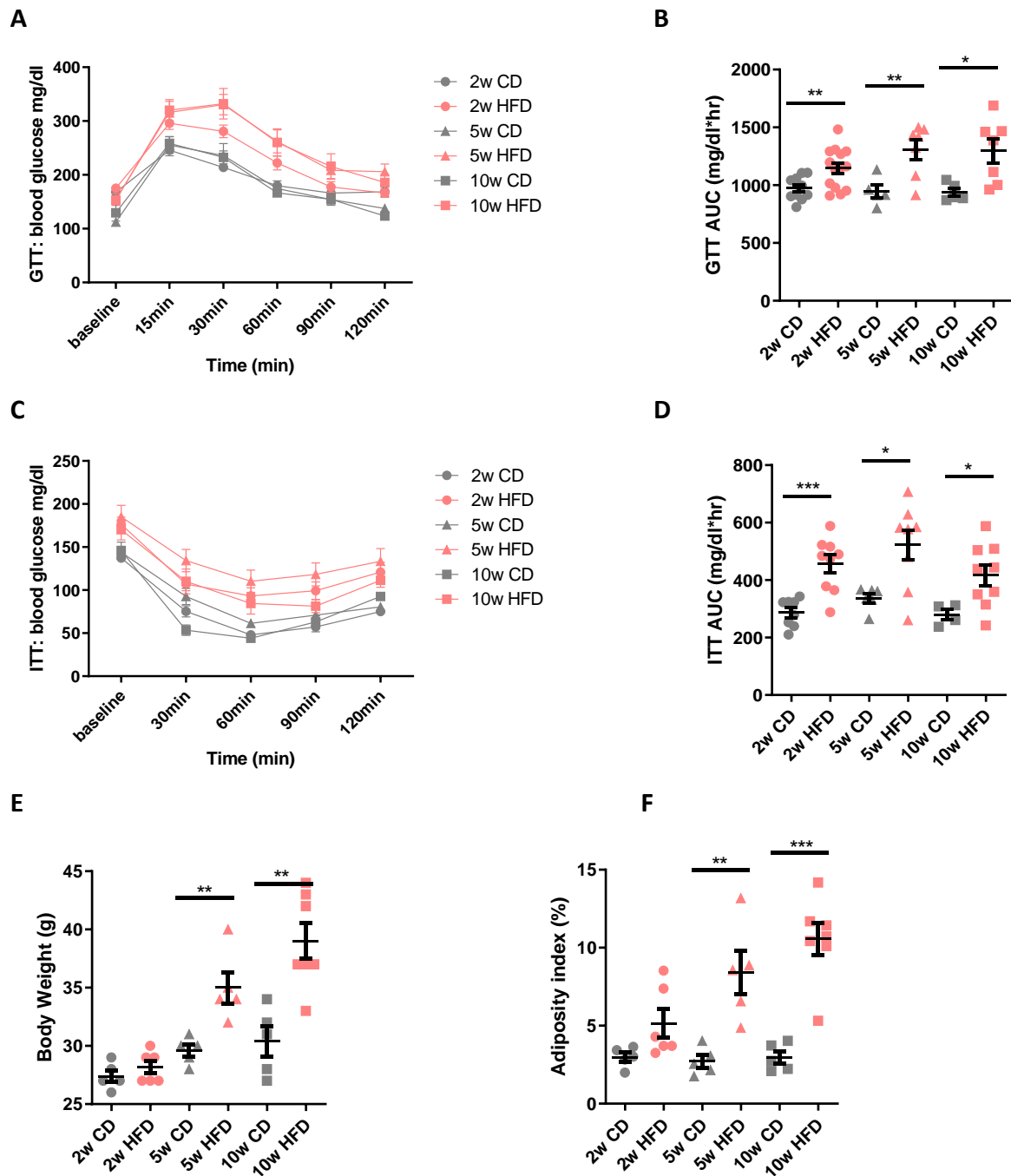


Figure 7: A-D, Temporal plot and area-under-curve (AUC) analysis of Glucose tolerance test (GTT; A, B) and insulin tolerance test (ITT; C, D). E, Body weight. F, Adiposity index; (n=5-9/group). Data are presented as mean \pm SEM analysed with ANOVA with Tukey's post-hoc test; ns: non-significant, * $p < 0.05$, ** $p < 0.01$, *** $p < 0.001$, **** $p < 0.0001$ as indicated.

Plasma levels of adipokines (leptin and adiponectin) and insulin showed a significant upregulation of leptin as early as 2 weeks of HFD, whilst no significant change was observed for adiponectin. Insulin levels significantly increased after 10 weeks of HFD (figure 8).

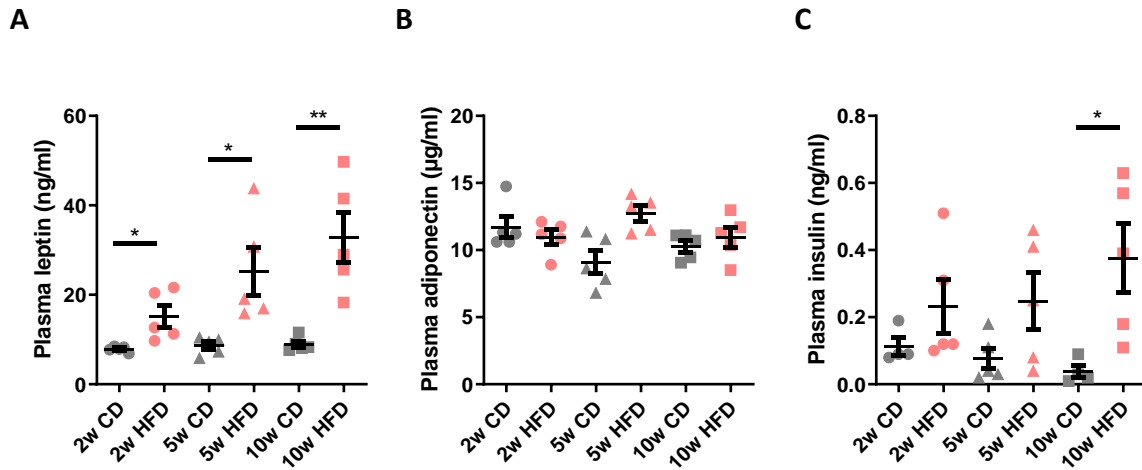


Figure 8: A-C, Plasma levels of Leptin (A), Adiponectin (B), and Insulin (C); ($n=5/\text{group}$). Data are presented as mean \pm SEM analysed with ANOVA with Tukey's post-hoc test; ns: non-significant, * $p < 0.05$, ** $p < 0.01$, *** $p < 0.001$, **** $p < 0.0001$ as indicated.

III) Time course of VAT alterations and remodeling during the onset of obesity

Since VAT is commonly regarded as a source of major cardiometabolic risk in both mice,³¹³⁻³¹⁵ and humans,³¹⁶⁻³¹⁸ we analysed VAT remodeling time course during a 10-week HFD duration. Adipocyte size progressively increased as early as 2 weeks after HFD initiation (figure 8A-B), followed by an increase of crown like structures at 5 weeks (figure 8C).

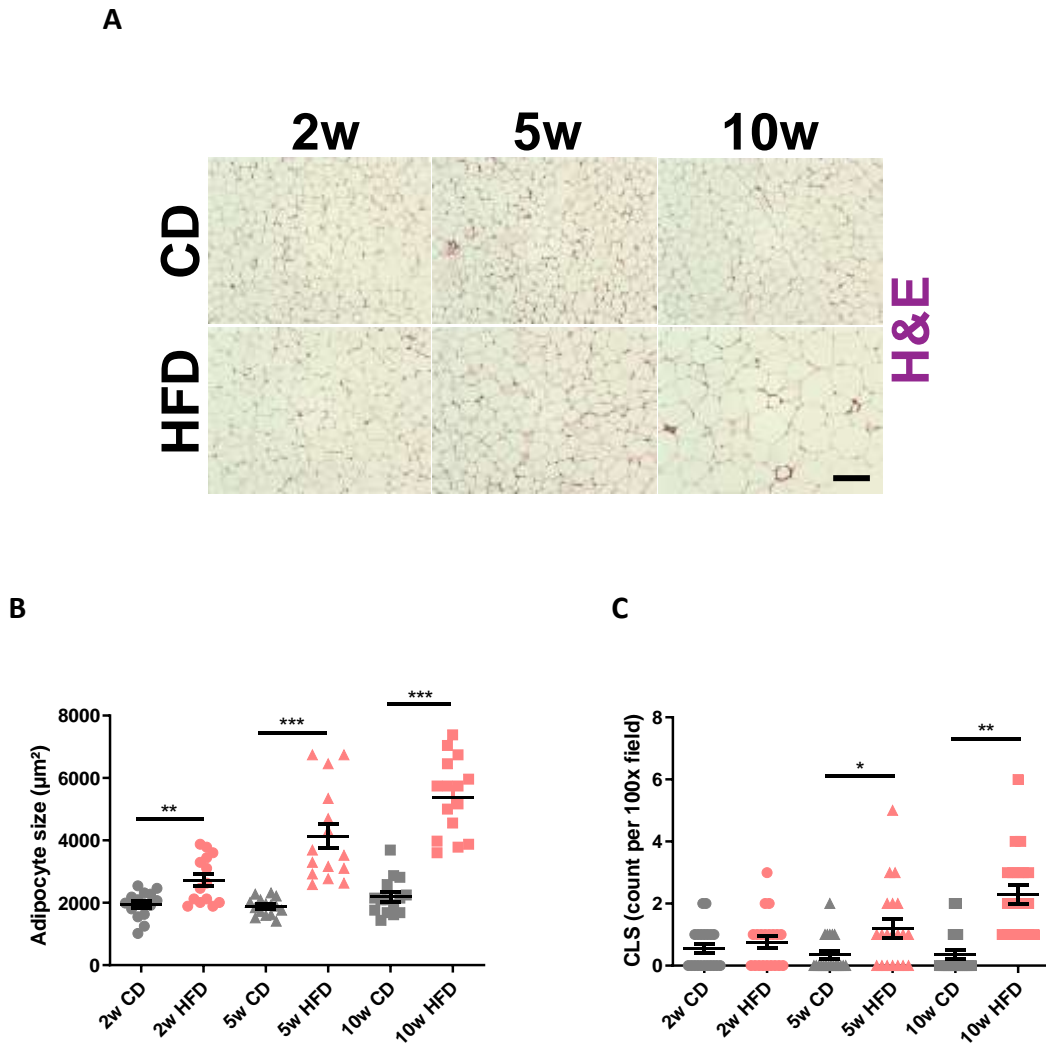


Figure 8: *A*, Representative images of VAT stained with Hematoxylin and Eosin (H&E), magnification: 100x, scale-bar: 100 μm . *B*, Quantification of adipocyte cross-sectional area (CSA). *C*, number of crown like structures (CLS) ; ($n=15-20$ images/group). Data are presented as mean \pm SEM analysed with ANOVA with Tukey's post-hoc test; ns: non-significant, * $p < 0.05$, ** $p < 0.01$, *** $p < 0.001$, **** $p < 0.0001$ as indicated.

The number of immune cells, such as macrophages and lymphocytes (CD3 and CD68 positive cells, respectively), increased at 10 weeks of HFD (figure 9A-D) indicative a recruitment from circulating immune cells and consistent with the increased expression of genes involved in immune cell recruitment (CCL2) at 5 of HFD (figure 9 E-H).

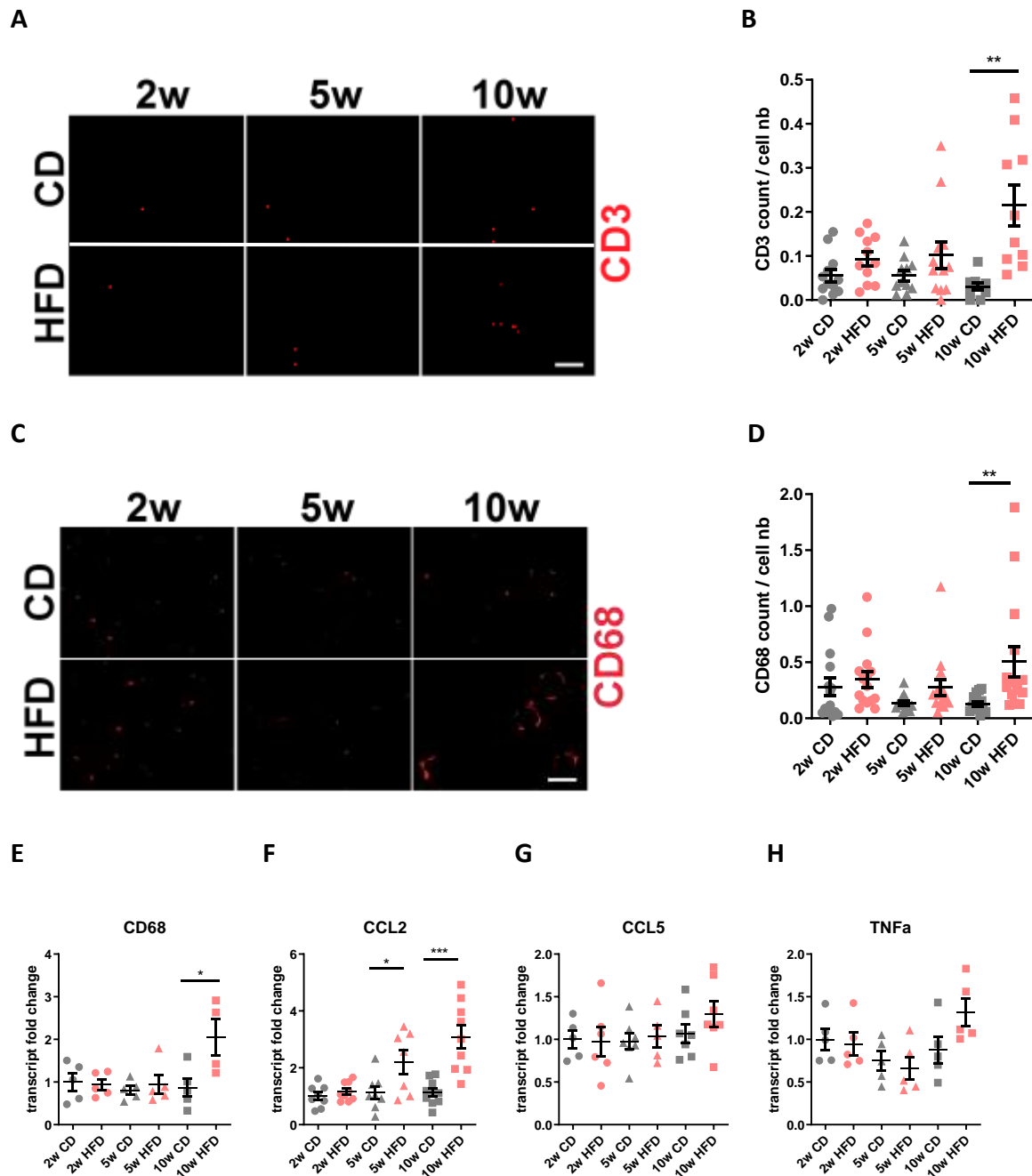


Figure 9: *A-B*, Representative images of CD3 (lymphocyte marker) immunostaining in VAT (*A*) and quantification of CD3 positive cells (*B*). Representative images of CD68 (macrophage marker) immunostaining in VAT (*C*) and quantification of CD68 positive cells (*D*). Magnification: 200x, scale-bar: 50 μ m; ($n=9-12$ images/group). *E-H*, Quantitative RT-PCR analysis of inflammation-related genes in VAT; ($n=5-10$ /group). Data are presented as mean \pm SEM analysed with ANOVA with Tukey's post-hoc test; ns: non-significant, * $p < 0.05$, ** $p < 0.01$, *** $p < 0.001$, **** $p < 0.0001$ as indicated.

As angiogenesis lagged behind the rate of adipocyte expansion, we also demonstrated a capillary rarefaction after 10 weeks of HFD (figure 10).

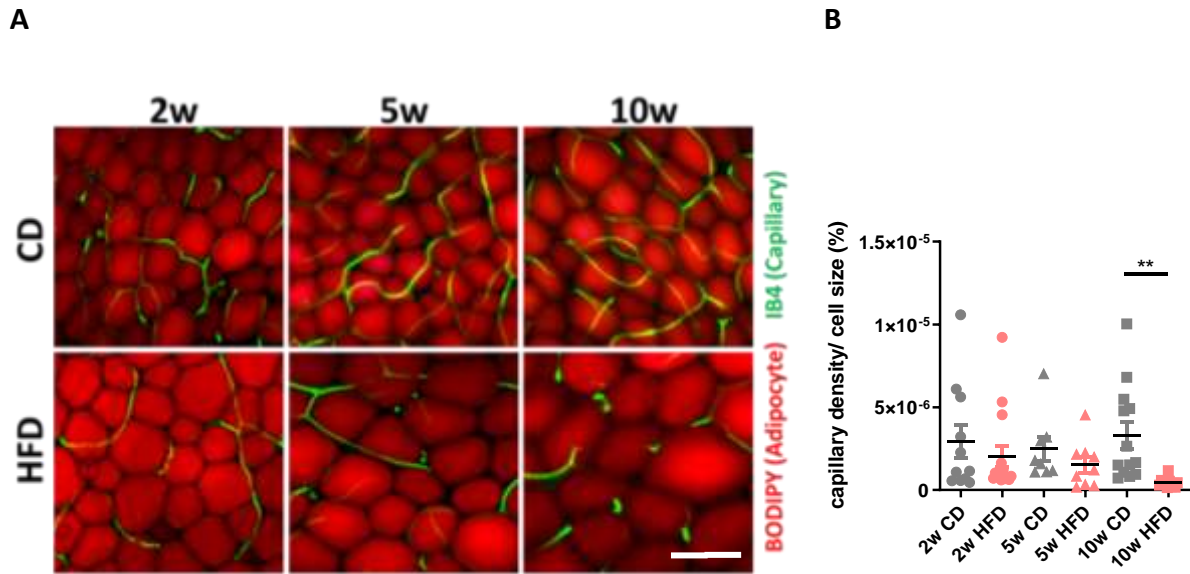


Figure 10: *A*, Representative images of VAT co-stained with BODIPY (lipid marker) and Isolectin B4 (IB4; capillary marker). Magnification: 400x, scale-bar: 50 μ m. *B*, Quantification of capillary density normalized to cell size; (n=8-15 images/group). Data are presented as mean \pm SEM analysed with ANOVA with Tukey's post-hoc test; ns: non-significant, * $p < 0.05$, ** $p < 0.01$, *** $p < 0.001$, **** $p < 0.0001$ as indicated.

Whilst interstitial adipose tissue fibrosis has been reported in long-lasting obesity, we analysed WAT by Picosirius red staining but did not observe any significant increase in WAT fibrosis after 10 weeks of HFD (figure 11).

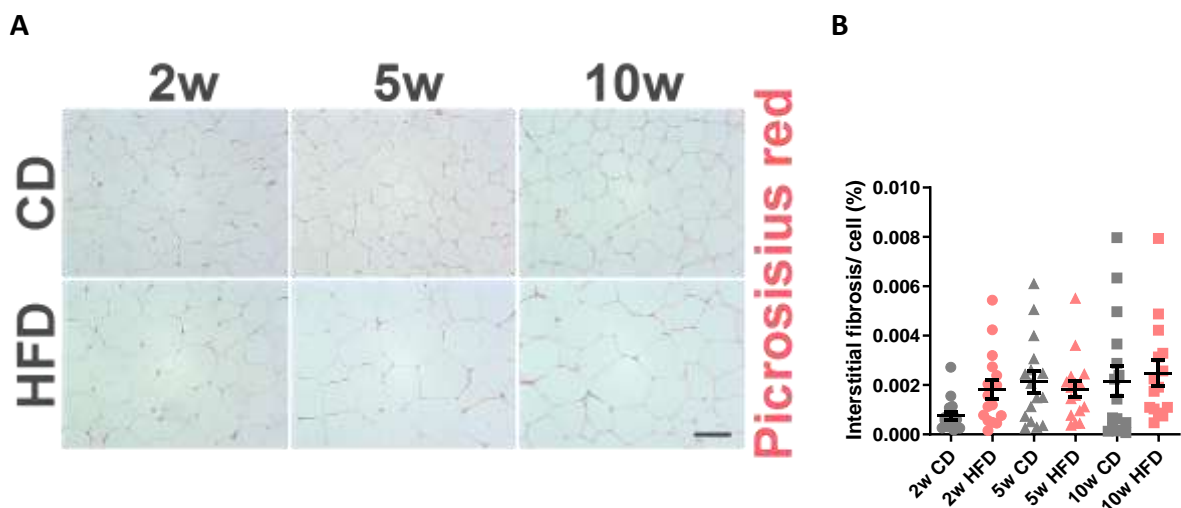


Figure 11: *A*, Representative images of VAT stained with Picosirius red (collagen marker), magnification: 200x, scale-bar: 50 μ m. *B*, Quantification of interstitial fibrosis normalized to cell number; (n=16 images/group). Data are presented as mean \pm SEM analysed with ANOVA with Tukey's post-hoc test; ns: non-significant, * $p < 0.05$, ** $p < 0.01$, *** $p < 0.001$, **** $p < 0.0001$ as indicated.

We then analysed the transcript levels of genes VAT involved in the regulation of energy metabolism: we observed an upregulation of leptin gene expression as early as 2 weeks of HFD but no variation for adiponectin (figure 12A-B) and a downregulation of the genes coding for Insulin-like growth factor-1 (Igf-1) and for Glucose transporter-4 or GLUT-4 protein (Slc2a4) at 10 weeks of HFD (figure 12C-D) which may result from insulin resistance.

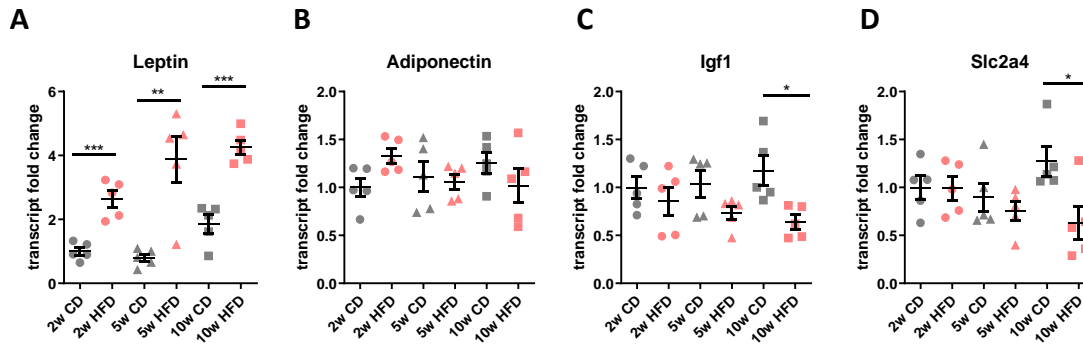


Figure 12: A-D, Quantitative RT-PCR analysis of metabolism-related genes in VAT; (n=5/group). Data are presented as mean \pm SEM analysed with ANOVA with Tukey's post-hoc test; ns: non-significant, * $p < 0.05$, ** $p < 0.01$, *** $p < 0.001$, **** $p < 0.0001$ as indicated.

Metabolic dysfunction detectable before systemic inflammation and major VAT remodeling prompted us to seek for other potential causes of impaired glucose homeostasis. Since adipose tissue senescence has been proposed to contribute to dysmetabolic state in obesity,^{204,252,283} we assessed senescence markers in VAT and identified an increase in VAT senescent cells as early as 2 weeks of HFD, as shown by the upregulation of transcript and protein levels of senescence markers Cdkn2a (p16) and Cdkn1a (p21) (figure 13).

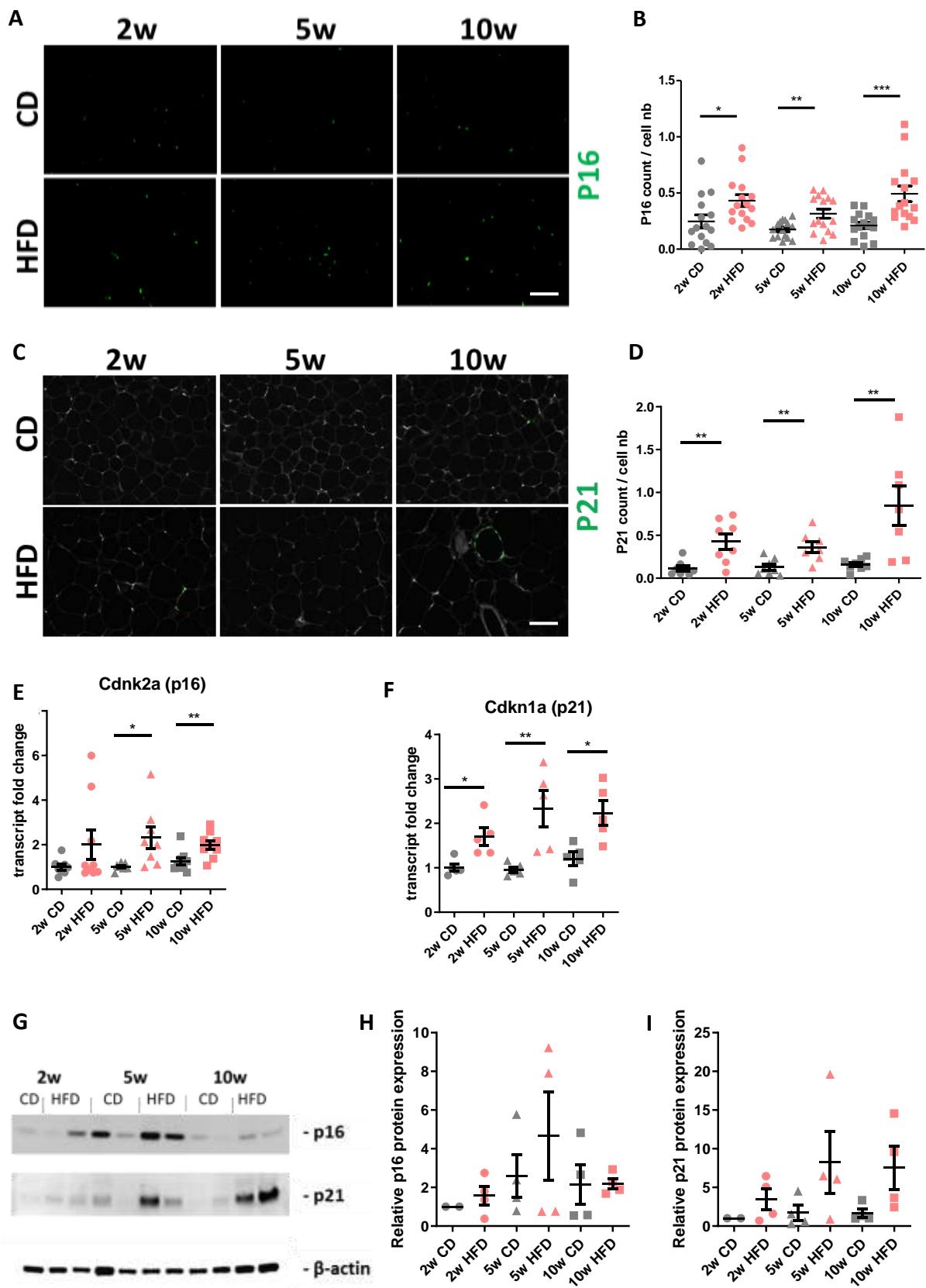


Figure 13: A-B, Representative images of P16 (senescent marker) immunostaining in VAT (A) and quantification of P16 positive cells (B); (n=15 images/group). C-D, Representative images of P21 (senescent marker) immunostaining in VAT (C) and quantification of P21 positive cells (D); (n=7-8 images/group). Magnification: 200x, scale-bar: 50 μ m. E-F, Quantitative RT-PCR analysis of p16 (E)

and p21 (F) genes in VAT; (n=5/group). **G-I**, Immunoblot of indicated markers of senescence in VAT (G) and quantification of p16 and p21 protein expression (H, I); (n=2-4/group). Data are presented as mean \pm SEM analysed with ANOVA with Tukey's post-hoc test; ns: non-significant, * $p < 0.05$, ** $p < 0.01$, *** $p < 0.001$, **** $p < 0.0001$ as indicated.

These data indicative of cellular senescence were not associated with significant increase in DNA damage as demonstrated by γ H2AX staining (figure 14).

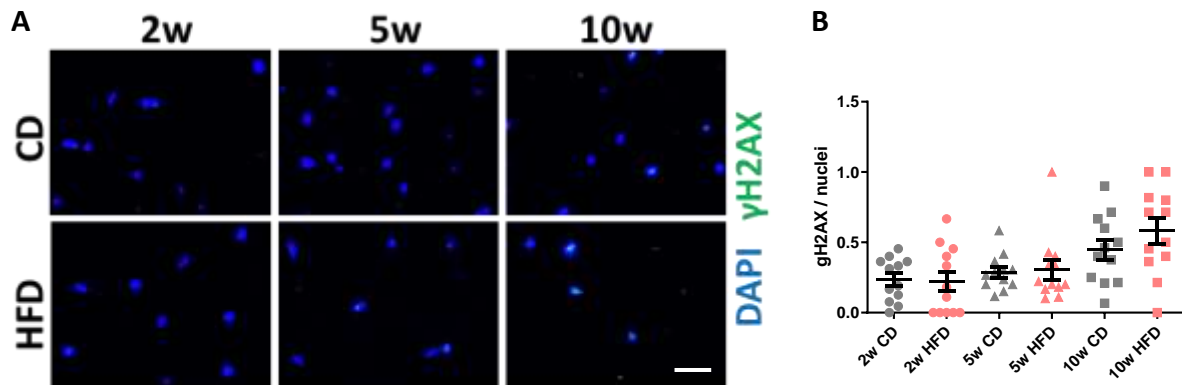


Figure 14: A-B, Representative images of γ H2AX (DNA damage marker) and DAPI (nuclei marker) co-immunostaining in VAT (A) and quantification of γ H2AX positive nuclei (B); (n=12 images/group). Magnification: 400x, scale-bar: 25 μ m. Data are presented as mean \pm SEM analysed with ANOVA with Tukey's post-hoc test; ns: non-significant, * $p < 0.05$, ** $p < 0.01$, *** $p < 0.001$, **** $p < 0.0001$ as indicated.

Taken together, our data show that VAT senescence is induced at a very early stage, through DNA damage-independent pathway, and precedes inflammation and fibrosis during VAT remodeling. This chronological order is also confirmed when we look at transcript levels of senescence-, inflammation-, and fibrosis-related genes (figure 15).

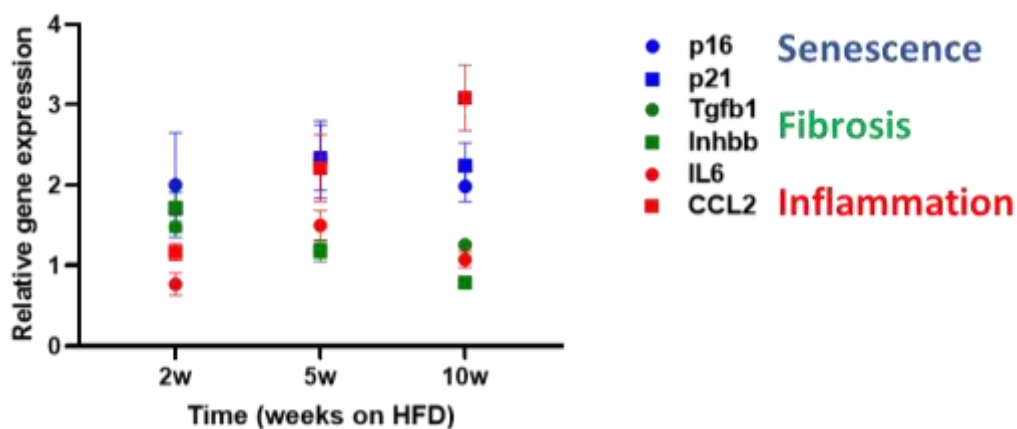


Figure 15: Summary of quantitative RT-PCR analysis of senescence-, fibrosis-, inflammation-related gene in VAT; Data are presented as mean \pm SEM (n=5/group).

IV) Time course of cardiac alterations during HFD-induced obesity

Obesity is known to alter the cardiac structure and function.²⁵ In order to analyse the time course of cardiac remodeling and dysfunction, echocardiography was sequentially performed in both CD and HFD mice and hearts were examined for structural changes after 2, 5 and 10 weeks of HFD vs CD. As opposed to long-term HFD feeding (20 weeks),²⁵ 10 weeks of HFD did not increase heart weight to tibia length, an index of cardiac hypertrophy (figure 16A). Left ventricular ejection fraction, an index of systolic function, remained unaltered (figure 16B). By contrast, systolic strain rate, a sensitive index of myocardial contractility obtained by deformation imaging identified a reduced contractility as early as 2 weeks of HFD, followed by progressive aggravation with duration of HFD (figure 16C). Interestingly, strain rate also declined in CD-fed mice with time, which is consistent with age-related decline (figure 16C).

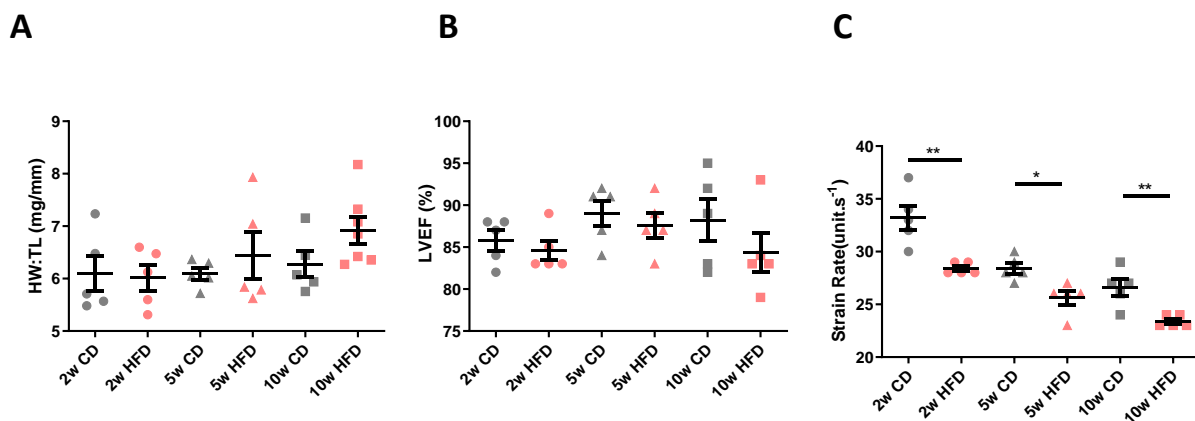


Figure 16: A-C, Evaluation of cardiac function; Heart weight to tibia length (HW/TL; **A**); Left ventricular ejection fraction (LVEF; **B**); Systolic strain rate (**C**); (n=5-7/group). Data are presented as mean \pm SEM analysed with ANOVA with Tukey's post-hoc test; ns: non-significant, * $p < 0.05$, ** $p < 0.01$, *** $p < 0.001$, **** $p < 0.0001$ as indicated.

Cross-sectional area (CSA) of transversely sectioned cardiomyocytes did not increase by HFD until 10 weeks of HFD (figure 17A-B). Myocardial interstitial fibrosis, another important component of cardiac remodeling, also remained unchanged in the duration of observation with a trend to a slight increase after 10 weeks of HFD (figure 17C-D).

Collectively, we did not find major changes in cardiac structure within 10 weeks of HFD, but 2 weeks of HFD sufficed to compromise cardiac contractility.

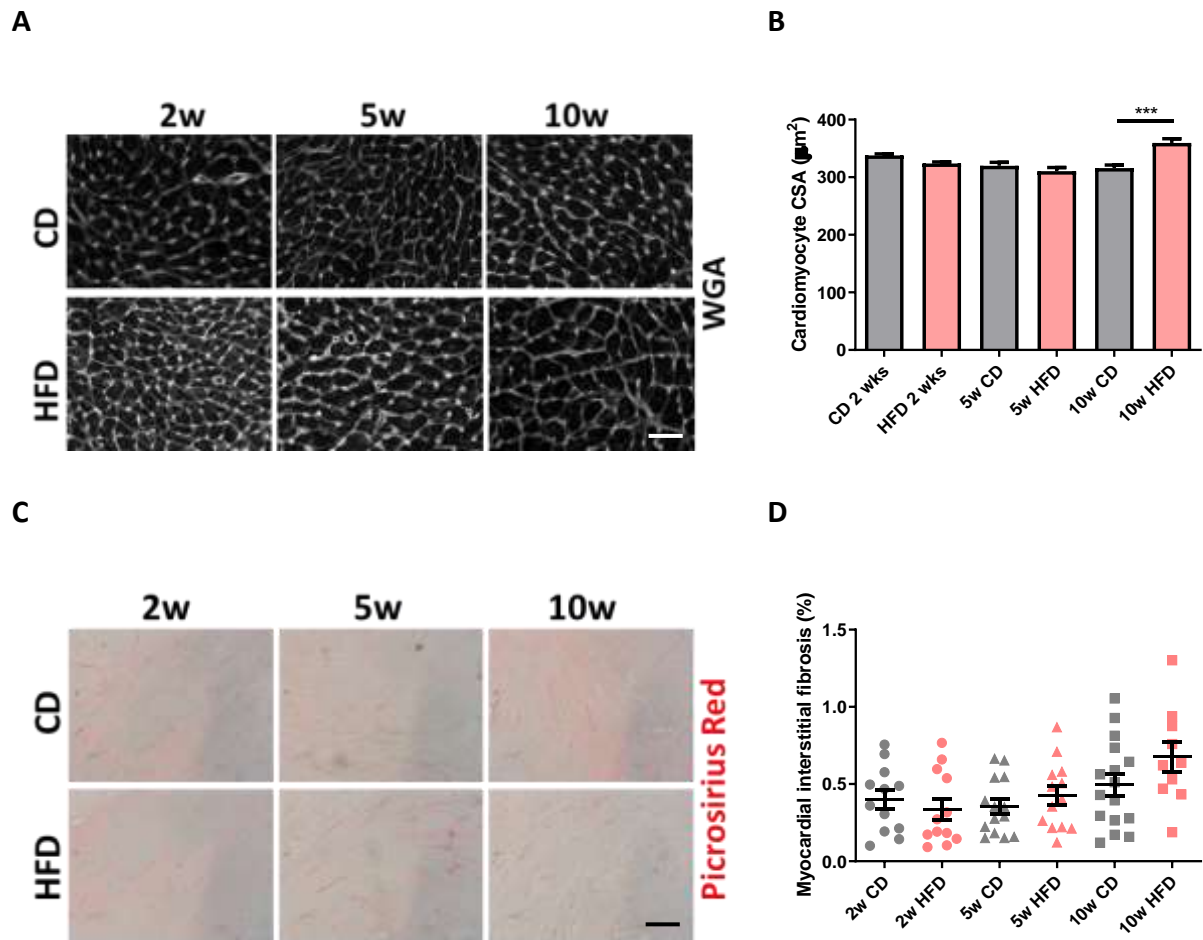


Figure 17: *A-B*, Representative images of hearts stained with wheat-germ agglutinin (WGA: plasma membrane marker; **A**), and quantification of cardiomyocyte cross-sectional area (CSA; **B**). Representative images of hearts stained with Picrosirius red (collagen marker; **C**) and quantification of interstitial fibrosis normalized to cell number (**D**); ($n=10-16$ images/group). magnification: 200x, scale-bar: 50 μm . Data are presented as mean \pm SEM analysed with ANOVA with Tukey's post-hoc test; ns: non-significant, $*p < 0.05$, $**p < 0.01$, $***p < 0.001$, $****p < 0.0001$ as indicated.

V) Senolytic treatment as a therapeutic option to rescue metabolic and cardiac function

Our previous data showed that VAT senescence as compared to inflammation and fibrosis is the only parameter which is concordant with cardiometabolic alterations observed at 2 weeks of HFD. Hence, we used a senolytic treatment to specifically eliminate senescent cells. We used 5-months old mice for a 10-week HFD regimen followed by a 4-week Dasatinib + Quercetin (D+Q vs. Vehicle) treatment and compared them to a CD group (figure 18).

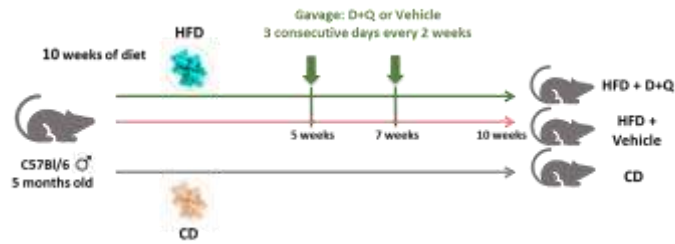


Figure 18: Schematic of treatment protocol. 5-months-old mice fed CD or HFD for 10 weeks and treated with or without senolytics (D+Q) for the HFD ones, a total of 3 groups ($n=5-11/\text{group}$).

While p16 senescent marker was increased by HFD, senolytic treatment decreased the number of p16 positive cells without any significant change in body weight or adiposity index between the two HFD groups (figure 19).

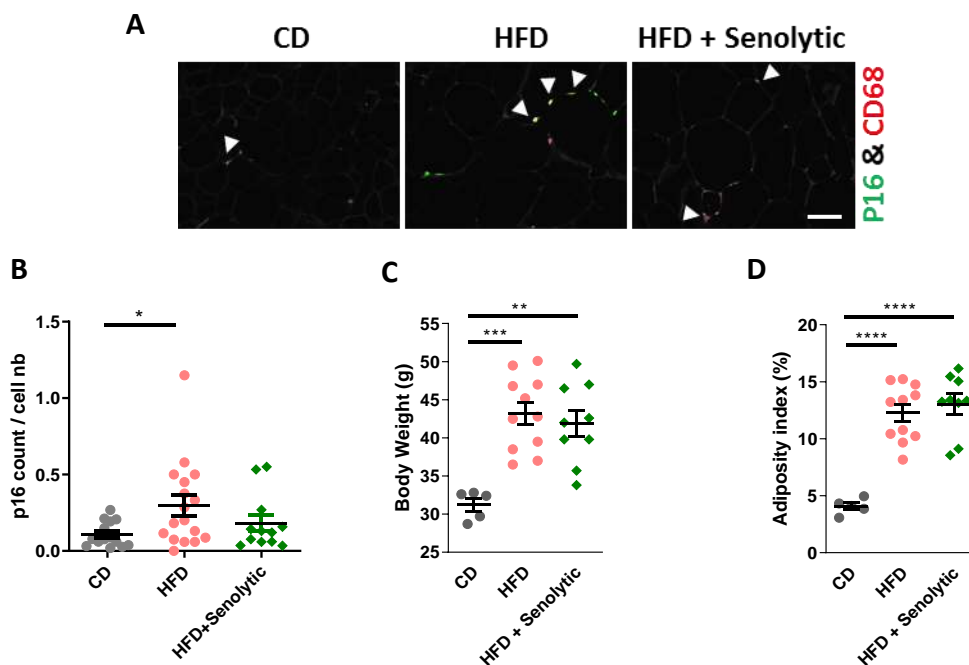


Figure 19: A-B, Representative images of P16 (senescence marker) and CD68 (macrophage marker) co-immunostaining in VAT, white arrows show colocalisation (A) and quantification of P16 and CD68 double positive cells (B); ($n=12-17$ images/group). Magnification: 200x, scale-bar: 50 μm . C, Body weight ($n=5-11/\text{group}$). D, Adiposity index ($n=5-11/\text{group}$). Data are presented as mean \pm SEM analysed with ANOVA with Tukey's post-hoc test; ns: non-significant, * $p < 0.05$, ** $p < 0.01$, *** $p < 0.001$, **** $p < 0.0001$ as indicated.

Senolytic treatment did not improve glucose tolerance (GTT, figure 20A-B) whereas it slightly improved HFD-induced insulin resistance (figure 20C-D). While alleviation of senescent cells decreased heart weight in HFD at a similar level as observed in CD mice, HFD-induced cardiac

dysfunction was not improved by D+Q (figure 20E-F). Therefore, senolytic treatment was not efficient to prevent the cardiac functional alteration induced by HFD.

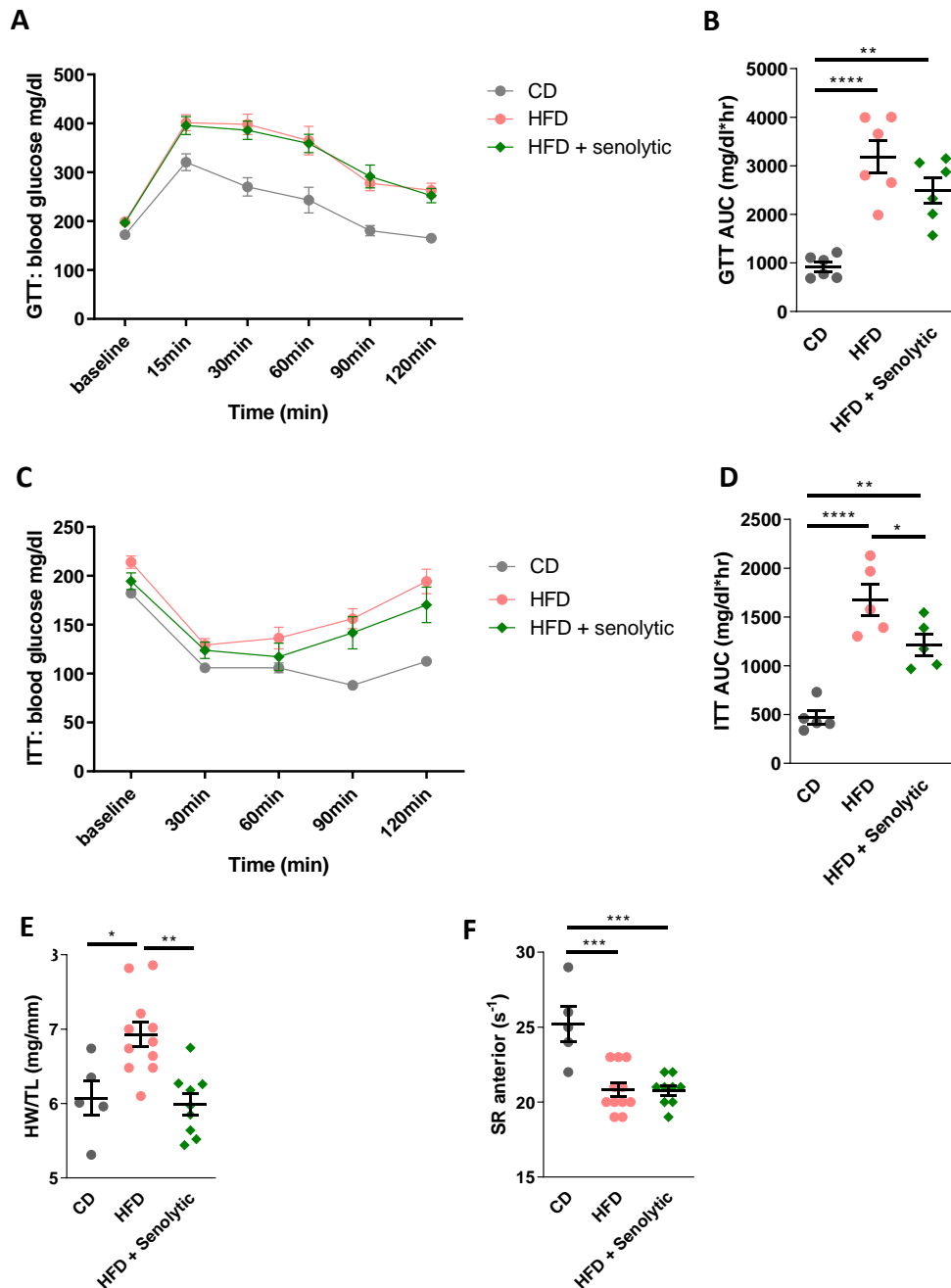


Figure 20: A-D, Temporal plot and area-under-curve (AUC) analysis of Glucose tolerance test (GTT; A, B) and insulin tolerance test (ITT; C, D). E, Heart weight to tibia length (HW/TL). F, Systolic strain rate; (n=5-11/group). Data are presented as mean \pm SEM analysed with ANOVA with Tukey's post-hoc test; ns: non-significant, * $p < 0.05$, ** $p < 0.01$, *** $p < 0.001$, **** $p < 0.0001$ as indicated.

VI) Time course of AT cell-specific senescence during HFD-induced obesity

As the efficiency of global elimination of senescent cells was not convincing, we shifted toward more specific and targeted options. So, we determined which cell-type(s) were affected by HFD-induced senescence in VAT of 2-month old mice using immunofluorescent co-labelling. We found an increased co-localization between p16 and macrophage marker CD68 in HFD at all time-points investigated (figure 21A). Similar observations were made with p21 marker (figure 21B). By contrast, senescence did not occur in CD3+ lymphocytes before 5-10 weeks of HFD (figure 21C,D) and in PDGFR α + preadipocytes before 10-week HFD (figure 21 E,F).

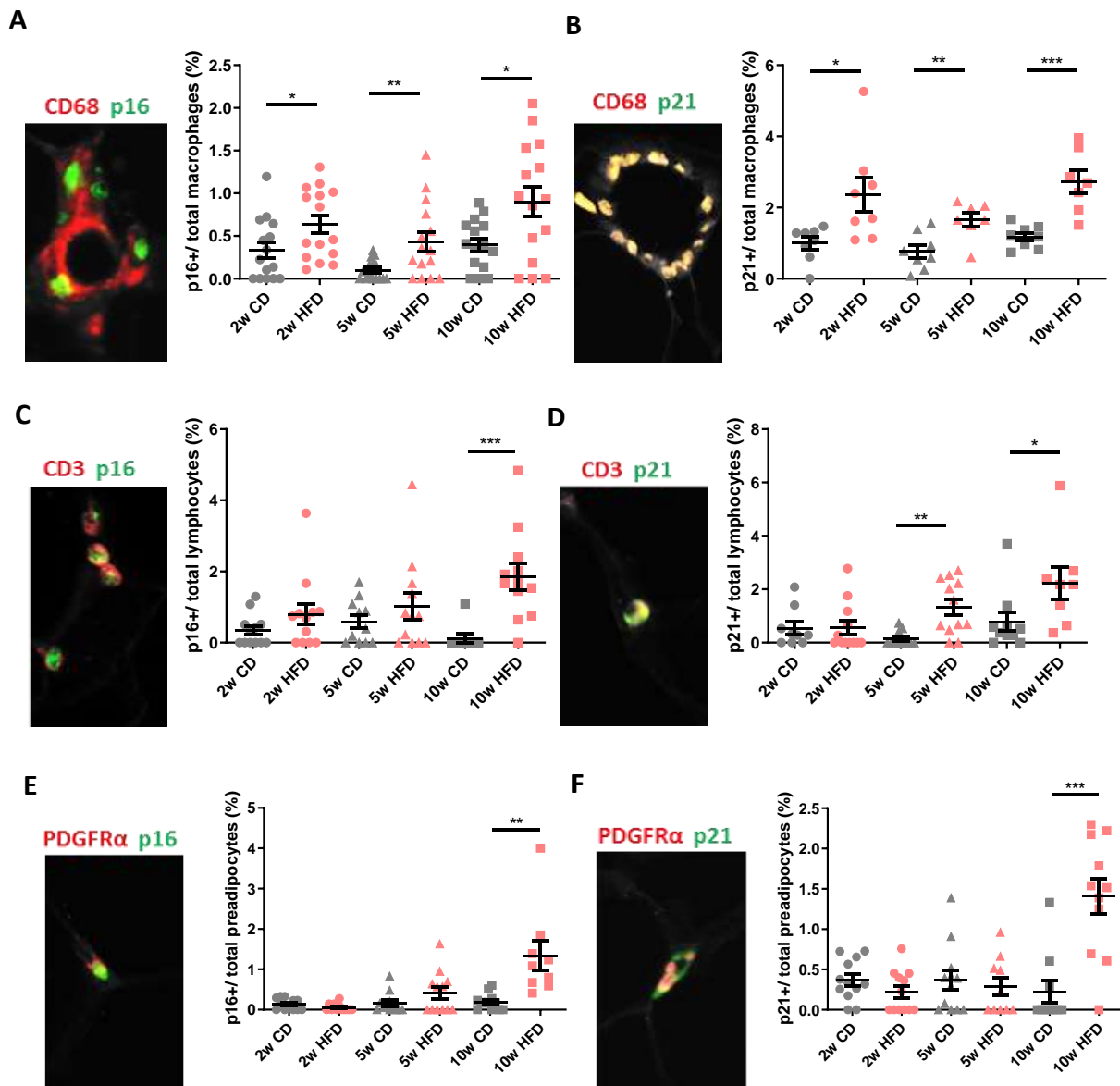


Figure 21: *A, Representative images of P16 (senescence marker) and CD68 (macrophage marker) co-immunostaining in VAT and quantification of P16 and CD68 double positive cells. B, Representative images of P21 (senescence marker) and CD68 (macrophage marker) co-immunostaining in VAT and quantification of P21 and CD68 double positive cells. C-D, Representative images of P16 or P21 (senescence marker) and CD3 (lymphocyte marker) co-immunostaining in VAT and quantification of P16 or P21 and CD3 double positive cells. E-F, Representative images of P16 or P21 (senescence marker) and PDGFR α (preadipocyte marker) co-immunostaining in VAT and quantification of P16 or P21 and PDGFR α double positive cells. (n=7-15 images/group). Magnification: 200x. Data are presented as mean \pm SEM analysed with ANOVA with Tukey's post-hoc test; ns: non-significant, * $p < 0.05$, ** $p < 0.01$, *** $p < 0.001$, **** $p < 0.0001$.*

Globally, in VAT, under HFD, p16 positive signal was not only found in macrophages while the majority of p21 positive signal was colocalised to CD68+ macrophages (figure 22).

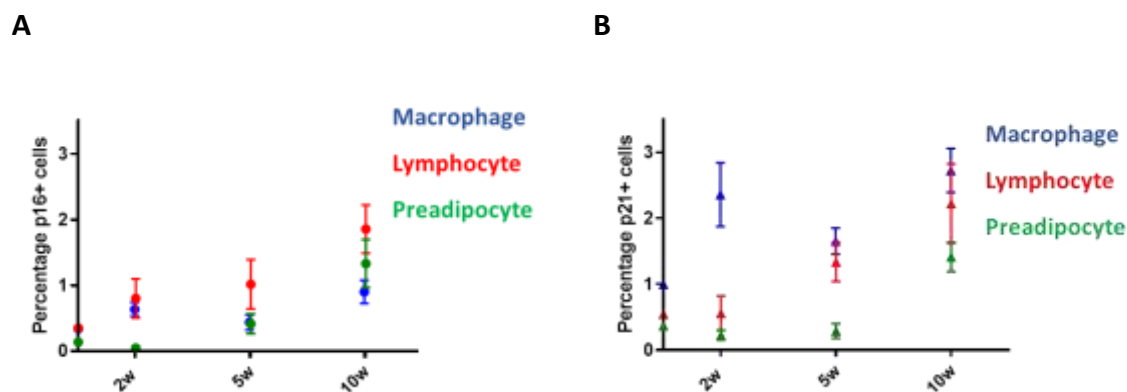


Figure 22: *A, Percentage of p16 positive cells per cell type. B, Percentage of p21 positive cells per cell type. Data are presented as mean \pm SEM (n=7-15/group).*

Taken together, these data showed that senescence induction in response to HFD was occurring in adipose tissue macrophages at an early stage preceding that of other cells.

To further confirm that induction of senescence in adipose tissue macrophages occurs in response to caloric overload, we subjected in vitro bone marrow-derived macrophages (BMDMs) from 2-month-old mice to metabolic stimulation with high glucose + palmitate (metabolic media: MM) and observed an increase in both p16 and p21 protein expression (figure 23). These findings confirm that macrophages undergo senescence in response to caloric overload.

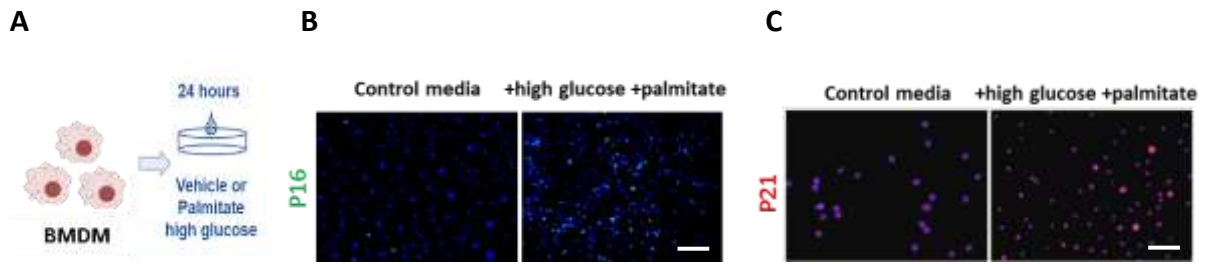


Figure 23: *A*, Schematic of treatment protocol: Bone Marrow-Derived macrophages (BMDM) cells treated with metabolic media. *B-C*, Representative images of P16 (*B*) and P21 (*C*) immunostaining in BMDM

VII) Macrophage elimination as a proof-of-concept for their role in early cardiometabolic dysfunction

Since our data identified macrophage senescence as an early HFD-related change in VAT, we hypothesized the role of senescent macrophages in the early pathogenesis of HFD-induced obesity. To confirm this hypothesis, we specifically targeted macrophages with liposome-packaged clodronate in 2-month-old mice fed with HFD (Clodronate vs. liposome-PBS: Vehicle; figure 24) for 2 weeks, a treatment known to deplete macrophages through induction of apoptosis.²⁹¹

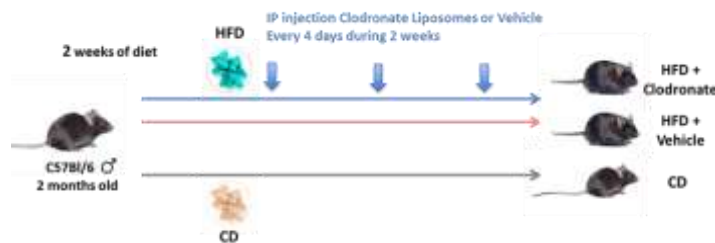


Figure 24: Schematic of treatment protocol. 2-months-old mice fed CD or HFD for 2 weeks and treated with or without clodronate for the HFD ones, a total of 3 groups ($n=5-11$ /group).

Clodronate-liposome treatment reduced the number of adipose tissue macrophage (ATM) (figure 25A-B). Interestingly, clodronate-liposome treatment was associated with a significant reduction in the number of p21+ cells (figure 25C), whilst the number of p16+ cells was not changed (figure 25D-E), consistent with the observation that the majority of p21 but not p16 colocalised to CD68+ macrophages (figure 22). However, a closer look at senescent macrophages, i.e. p16+ CD68+ and p21+ CD68+ clearly showed a reduction of both

populations by clodronate (figure 25F-G). Besides, clodronate treatment prevented adipocyte hypertrophy as shown by reduced adipocyte size (figure 25H).

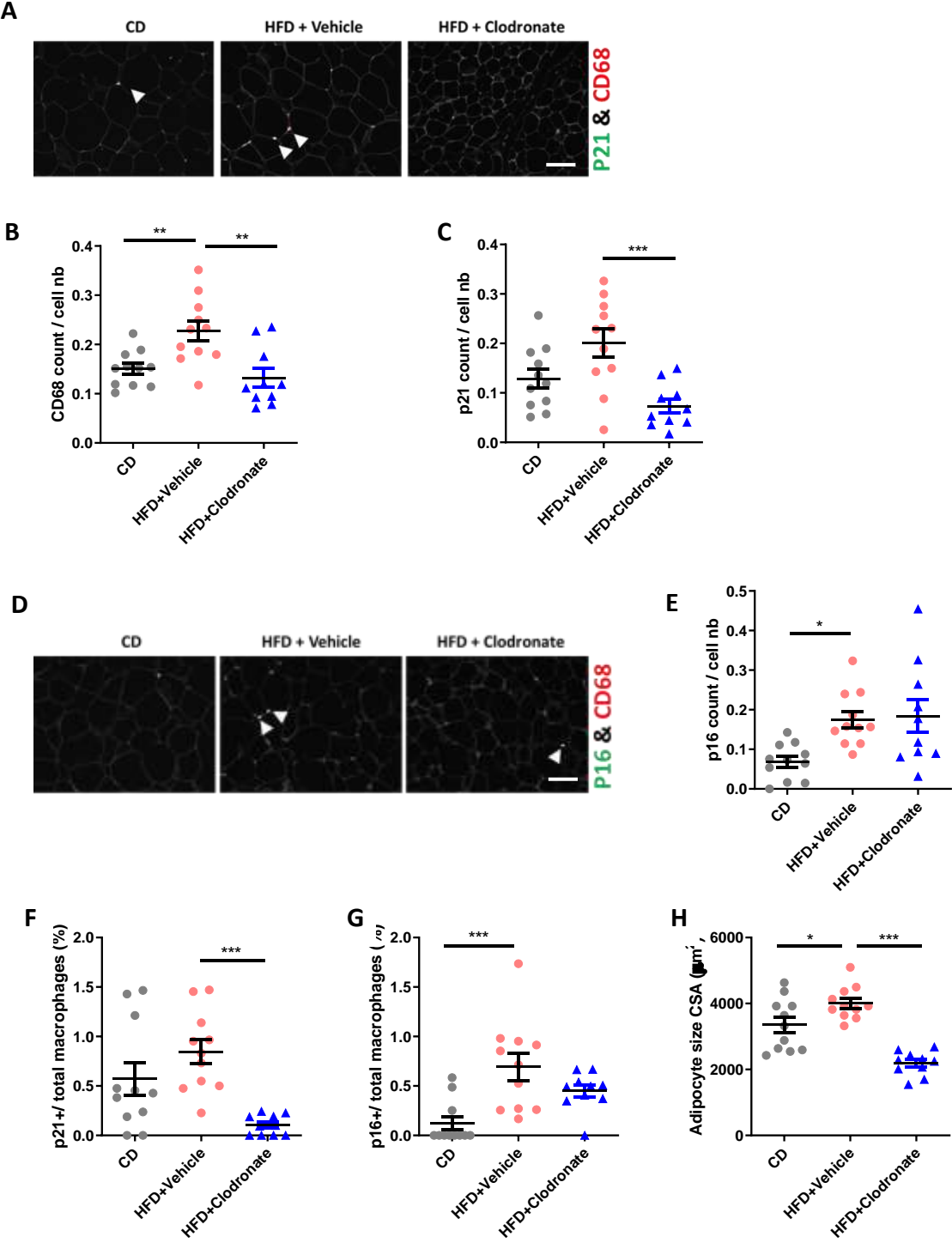


Figure 25: A-C, Representative images of P21 (senescence marker) and CD68 (macrophage marker) co-immunostaining in VAT, white arrows show colocalisation (A) and quantification of CD68 positive cells (B), and quantification of P21 positive cells (C); D-E, Representative images of P16 (senescence marker) and CD68 (macrophage marker) co-immunostaining in VAT, white arrows show colocalisation (D) and quantification of P16 positive cells (E). F, Quantification of P21 and CD68 double positive cells. G, Quantification of P16 and CD68 double positive cells. H, Quantification of adipocyte cross-sectional area (CSA). N=10-11 images/group. Magnification: 200x, scale-bar: 50 μm . Data are

presented as mean \pm SEM analysed with ANOVA with Tukey's post-hoc test; ns: non-significant, * $p < 0.05$, ** $p < 0.01$, *** $p < 0.001$, **** $p < 0.0001$ as indicated.

Interestingly, clearance of senescent macrophages was associated with a complete rescue of glucose metabolism as shown by glucose tolerance and insulin resistance tests (figure 26A-D) despite no significant change in body weight (figure 26E). Similarly, plasma adipokine levels were also normalized by clodronate treatment (figure 26F-G).

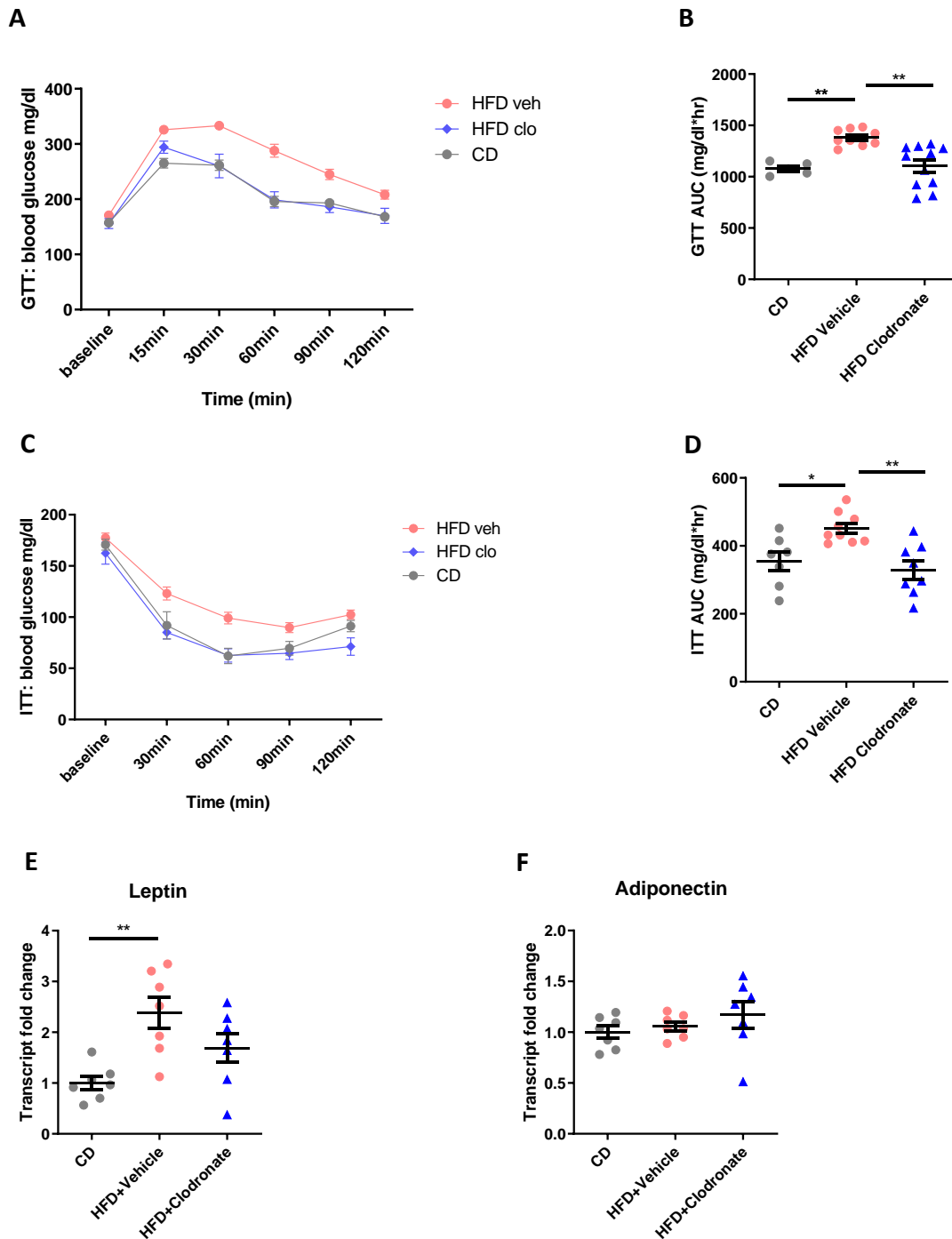


Figure 26: A-D, Temporal plot and area-under-curve (AUC) analysis of Glucose tolerance test (GTT; A, B) and insulin tolerance test (ITT; C, D); (n=5-10/group). E-F, Quantitative RT-PCR analysis of metabolism-related genes in VAT; (n=7/group). Data are presented as mean \pm SEM analysed with ANOVA with Tukey's post-hoc test; ns: non-significant, * $p < 0.05$, ** $p < 0.01$, *** $p < 0.001$, **** $p < 0.0001$ as indicated.

Furthermore, cardiac function was compromised with vehicle, as with HFD alone, but Clodronate-liposome treatment completely restored healthy cardiac function (figure 27).

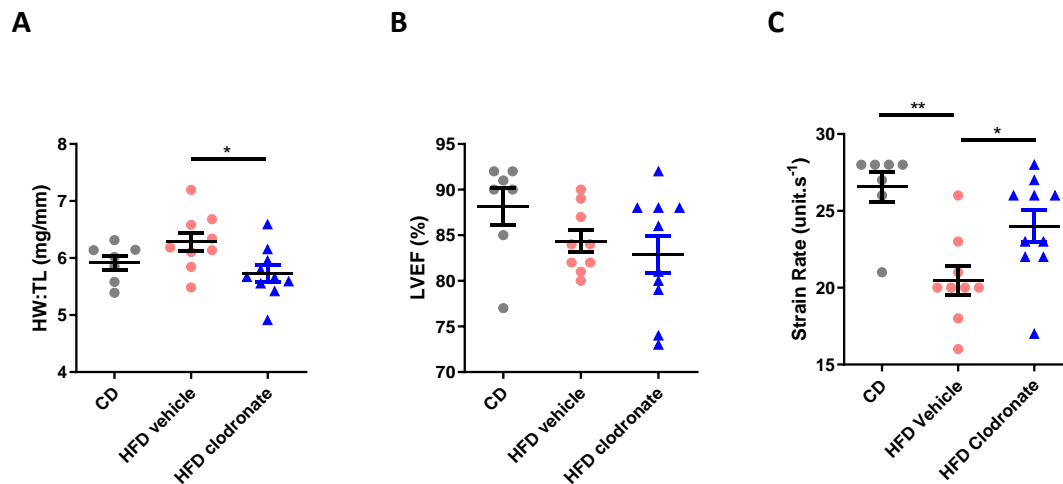


Figure 27: A-C, Evaluation of cardiac function; Heart weight to tibia length (HW/TL; A); Left ventricular ejection fraction (LVEF; B); Systolic strain rate (C); (n=7-9/group). Data are presented as mean \pm SEM analysed with ANOVA with Tukey's post-hoc test; ns: non-significant, * $p < 0.05$, ** $p < 0.01$, *** $p < 0.001$, **** $p < 0.0001$ as indicated.

To explore whether clearance of senescent macrophages could remedy adverse consequences of longer caloric overload, the above experiment was repeated with 10 weeks of HFD and clodronate/vehicle treatment 2 weeks prior to sacrifice (figure 28).

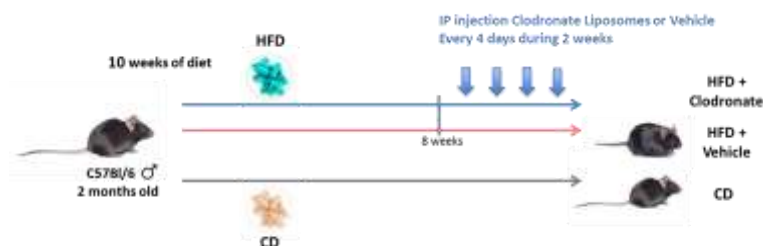


Figure 28: Schematic of treatment protocol. 2-months-old mice fed CD or HFD for 10 weeks and treated with or without clodronate for the HFD ones, a total of 3 groups (n=8-12/group).

In sharp contrast with observations made in 2-week HFD, these mice showed no improvement of metabolic function (figure 29A-D) with no change in body weight between the 2 HFD groups (figure 29E).

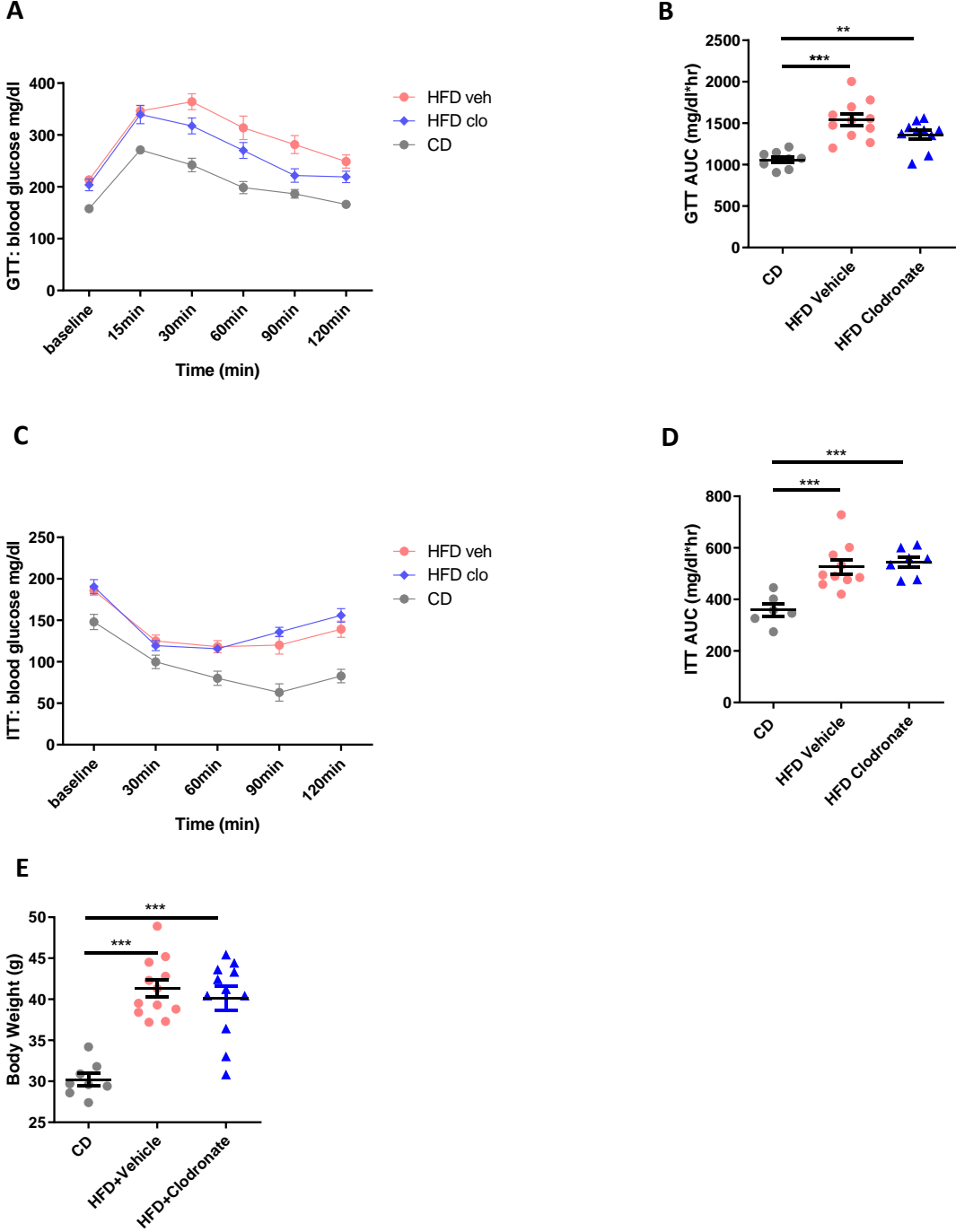


Figure 29: A-D, Temporal plot and area-under-curve (AUC) analysis of Glucose tolerance test (GTT; A, B) and insulin tolerance test (ITT; C, D). E, Body weight. N=8-12/group. Data are presented as mean \pm SEM analysed with ANOVA with Tukey's post-hoc test; ns: non-significant, * $p < 0.05$, ** $p < 0.01$, *** $p < 0.001$, **** $p < 0.0001$ as indicated.

Altogether, our findings clearly demonstrate an important pathogenic role of macrophage senescence to initiate the early cardiometabolic abnormalities observed in high fat diet-induced obesity.

STUDY 2

ETUDE 2

Résumé

Le tissu adipeux est un organe impliqué dans de nombreux processus pathologiques y compris ceux liés aux maladies métaboliques et à l'inflammation de bas grade. L'accumulation anormale de graisse ectopique ainsi que l'accumulation de cellules sénescentes dans le tissu adipeux sont des caractéristiques du vieillissement qui sont également retrouvées dans le contexte de l'obésité, considéré alors comme un état de sénescence accélérée ou prématurée. Des études récentes, effectuées dans des modèles murins, y compris celles menées par notre équipe, suggèrent que le vieillissement naturel induit des changements au niveau du tissu adipeux viscéral qui sont à l'origine de l'évolution du sécrétome vers un phénotype sénescent et pro-inflammatoire avec notamment une production de SASP (Senescence-Associated Secretory Phenotype). Parmi ces molécules sécrétées, on retrouve l'ostéopontine (OPN) dont la production augmente considérablement avec l'âge (Sawaki D, Circulation 2018). Notre groupe a ainsi démontré le rôle crucial de ce facteur pro-fibrotique circulant ainsi que d'autres tels que TGF β (transforming growth factor β), dans le développement du remodelage cardiaque (Sawaki D, Circulation 2018). Notre hypothèse était que, dans le contexte du vieillissement physiologique, l'OPN induirait la sénescence ainsi que le dysfonctionnement du tissu adipeux viscéral d'une part et participerait aux altérations cardiaques d'autre part. Le but de ce travail consistait donc à analyser et comprendre le rôle et les effets de la production d'OPN par le tissu adipeux viscéral sur le microenvironnement local mais également sur les organes distants et en particulier le cœur. Pour ce faire, des modèles murins (jeunes et âgés, sauvages et mutants : délétés pour le gène de l'OPN) et cellulaires (macrophages dérivés de la moelle osseuse) ont ainsi été utilisés et des traitements ont été administrés (traitement avec du clodronate (CLO), visant à éliminer les macrophages). Nos résultats ont démontré que l'OPN induit la sénescence des cellules immunitaires du TA et plus particulièrement des macrophages, conduisant ainsi à une diminution de leur capacité fonctionnelle à éliminer les débris apoptotiques et nécrotiques et permettant de maintenir l'intégrité du tissu et son homéostasie. L'OPN serait ainsi impliquée dans le remodelage du tissu adipeux, et par ce biais, dans le remodelage et la dysfonction cardiaque observée dans le contexte du vieillissement.

RESPONSE TO LETTER TO THE EDITOR

Response by Sawaki et al to Letter Regarding Article, “Visceral Adipose Tissue Drives Cardiac Aging Through Modulation of Fibroblast Senescence by Osteopontin Production”

In Response:

We appreciate the comments and further questions raised by Wang and his colleagues in relation to our recent work, stating the importance of the visceral adipose tissue (VAT) and its fibrotic secretome in the promotion of age-related cardiac remodeling and dysfunction.¹

As they suggested, the effect of aging on VAT and its secretome is still poorly understood. Fat tissue is a nexus of pathways involved in longevity, metabolic dysfunction, and low-grade inflammation. Abnormal ectopic fat accumulation (or visceral adiposity), a common hallmark of aging and obesity, represents per se a risk factor for accelerated aging with the accumulation of senescent cells within adipose tissue. Recent data, including ours, suggest that chronological aging induces cumulative alterations in the VAT leading to the modification of its secretome toward a senescent-associated secretory phenotype, including a major increase in osteopontin (OPN) production.^{1,2} We also recently demonstrated the predominant role of circulating profibrotic factors in comparison with the role of proinflammatory factors in triggering cardiac remodeling. Thus, an increased plasma level of fibrotic factor transforming growth factor β is released by VAT in a short-term high-fat diet model that induces cardiac alteration together with myocardial interstitial fibrosis as early as 5 weeks.³ Furthermore, we demonstrated that a high-fat diet promotes immune cell senescence before the actual development of obesity.⁴ Both aging and obesity induce immune cell senescence, which may result in a modification of their polarization and secretory profile. Our hypothesis is that adipose tissue macrophages (resident and recruited) undergo a senescent phenotype in the context of aging or a high-fat diet. These changes accelerate age-related tissue deterioration through paracrine mechanisms involving the secretion of senescent-associated secretory phenotype cytokines and initiate a vicious circle by promoting senescence in the local tissue microenvironment, eventually contributing to the deterioration of remote organs (heart).

Our observation that the OPN-knockout mouse or pharmacological inhibition of the OPN model ameliorated not only cardiac aging, but also age-related insulin resistance, indicates the crucial role of OPN in the induction of insulin resistance. It is of interest that OPN-knockout mice showed decreased insulin resistance despite their higher fat mass, suggesting that the senescence-associated remodeling of VAT, but not the VAT mass, is the culprit for insulin resistance progression. It is intriguing that remodeled myocardium (ventricle) itself shows a very low number of senescent cells despite an obvious age-related remodeling and dysfunction (D. Sawaki et al, unpublished data), which may indicate that influences from external organs such as VAT, and circulating factors, are more important.¹ Because heart failure with preserved ejection fraction is a multicomorbidity disease including aging and obesity as the biggest risk factors,⁵ we are currently investigating the role of OPN in heart failure conditions such as metabolic stress or pressure over-

Daigo Sawaki, MD, PhD
Gabor Czibik, MD, PhD
Maria Pini, PhD
Zaineb Mezdari, MSc
Yanyan Zhang, PhD
Corneliu Henegar, MD, PhD
Geneviève Derumeaux, MD, PhD

load with a focus on the mechanisms behind the VAT remodeling (senescence) and development of specific therapeutics against these conditions.

ARTICLE INFORMATION

Affiliation

INSERM U955, Université Paris-Est Creteil, France.

Disclosures

None.

REFERENCES

1. Sawaki D, Czibik G, Pini M, Ternacle J, Suffee N, Mercedes R, Marcelin G, Surenaud M, Marcos E, Gual P, Clément K, Hue S, Adnot S, Hatem SN, Tsuchimochi I, Yoshimitsu T, Hénégat C, Derumeaux G. Visceral adipose tissue drives cardiac aging through modulation of fibroblast senescence by osteopontin production. *Circulation*. 2018;138:809–822. doi: 10.1161/CIRCULATIONAHA.117.031358
2. Tchkonina T, Morbeck DE, Von Zglinicki T, Van Deursen J, Lustgarten J, Scoble H, Khosla S, Jensen MD, Kirkland JL. Fat tissue, aging, and cellular senescence. *Aging Cell*. 2010;9:667–684. doi: 10.1111/j.1474-9726.2010.00608.x
3. Ternacle J, Wan F, Sawaki D, Surenaud M, Pini M, Mercedes R, Ernande L, Audureau E, Dubois-Randé JL, Adnot S, Hue S, Czibik G, Derumeaux G. Short-term high-fat diet compromises myocardial function: a radial strain rate imaging study. *Eur Heart J Cardiovasc Imaging*. 2017;18:1283–1291. doi: 10.1093/ehjci/jew316
4. Mezdari Z, Pini M, Czibik G, Ternacle J, Radu C, Zhang Y, Adnot S, Henegar C, Derumeaux GA, Sawaki D. Role of adipose tissue macrophages in the cross-talk between visceral adipose tissue and heart during high fat diet. *Eur Heart J*. 2018;39(suppl 1):ehy565.P2536. doi.org/10.1093/eurheartj/ehy565.P2536
5. Dunlay SM, Roger VL, Redfield MM. Epidemiology of heart failure with preserved ejection fraction. *Nat Rev Cardiol*. 2017;14:591–602. doi: 10.1038/nrcardio.2017.65

1 **Title: Osteopontin promotes adipose tissue remodeling through macrophage senescence**

2
3 **Authors and affiliations**

4 Daigo SAWAKI¹, Maria PINI¹, Yanyan ZHANG¹, Zaineb MEZDARI¹, Suzain NAUSHAD¹,
5 Lucille LAMENDOUR¹, Dogus ALTINTAS¹, Marielle BREAU¹, Hao LIANG¹, Maissa
6 HALFAOUI¹, Mathieu SURENAUD^{1,2}, Déborah ROUSSEAU³, Takehiko YOSHIMITSU⁴,
7 Fawzia LOUACHE⁵, Serge ADNOT^{1,6}, Corneliu HENEGAR¹, Philippe GUAL³, Gabor CZIBIK¹,
8 Geneviève DERUMEAUX^{1,7}

9
10 ¹ INSERM U955, Université Paris-Est Créteil (UPEC), 51 Av de Lattre de Tassigny, 94100
11 Créteil, France.

12 ² AP-HP Vaccine Research Institute (VRI), F-94010 Créteil, France

13 ³ Université Côte d'Azur, INSERM, U1065, C3M, Nice, France

14 ⁴ Laboratory of Synthetic Organic and Medicinal Chemistry, Division of Pharmaceutical
15 Sciences, Graduate School of Medicine, Dentistry, and Pharmaceutical Sciences, Okayama
16 University, Okayama, Japan

17 ⁵ Institut National de la Santé et de la Recherche Médicale (INSERM) UMRS-1170,
18 Hématopoïèse normale et pathologique, CNRS GDR 3697 Micronit, Institut Gustave Roussy,
19 Univ. Paris-Sud, Université Paris-Saclay, 94805 Villejuif, France

20 ⁶ AP-HP, Department of Physiology, Henri Mondor Hospital, FHU SENECA, Créteil, France

21 ⁷ AP-HP, Department of Cardiology, Henri Mondor Hospital, FHU SENECA, Créteil, France.

22 These authors contributed equally: as 1st authors: Daigo SAWAKI, Maria PINI, Yanyan
23 ZHANG, and as supervising authors: Gabor CZIBIK, Geneviève DERUMEAUX.

24 Correspondence and requests for materials should be addressed to G.D. (email:
25 genevieve.derumeaux@inserm.fr)

26
27 **Conflict of interest statement**

28 The authors have declared that no conflict of interest exists.

30 **Abstract:**

31 Whilst the role of adipose tissue macrophage (ATM) senescence has been shown in obesity-
32 related adipose tissue remodeling, it is not yet fully understood in age-related adipose tissue
33 remodeling. Here we show that ATM undergo senescence during aging, and induce adipose
34 tissue remodeling and dysfunction. These senescent ATM show global decline of basic
35 macrophage functions such as efferocytosis, and are inefficient in clearing dysfunctional or
36 apoptotic cells. We also uncover a major role for age-associated accumulation of osteopontin, a
37 matricellular protein, which induces ATM senescence. Inversely, loss of osteopontin attenuates
38 ATM senescence, preserves efferocytosis, and finally rejuvenates adipose tissue in the context
39 of aging. Collectively these findings suggest that pharmacologic osteopontin inhibition could
40 be a viable therapeutic strategy to improve age-related adipose tissue dysfunction induced by
41 ATM senescence.

42

43 **Introduction**

44 In obesity, adipose tissue (AT) undergoes cellular senescence involving adipose tissue
45 macrophage (ATM) activation, which enhances AT remodeling through proinflammatory
46 signaling.(1-5)

47 During the aging process, AT remodeling has also been described,(6) but the underlying
48 mechanisms are not yet fully understood, and particularly the specific role of ATM in
49 aggravating such AT remodeling remains to be clarified. Aging increases ectopic AT
50 accumulation and more specifically, visceral AT (VAT) depots.(7) Age-associated VAT
51 remodeling includes adipocyte hypertrophy, deposition of extracellular matrix, and
52 accumulation of immune cells.(8) Furthermore, our group has identified a major role of VAT in
53 inducing remote tissue remodeling through the release of profibrotic factors, including
54 transforming growth factor (TGF β) and osteopontin (OPN), both components of the senescence-
55 associated secretory phenotype (SASP) amongst a variety of growth factors, proinflammatory
56 cytokines/chemokines as well as adipokines.(9) We recently established VAT as the major
57 source of OPN during aging, extending knowledge on the reported role of OPN to participate
58 in the AT pro-inflammatory status.(9-12) OPN is a matricellular protein involved in intra- and
59 extra-cellular signaling mediating cell-to-cell interaction, immune cell function, inflammation,
60 and tissue remodeling.(13) Notably, our group has demonstrated that OPN modulates the
61 function of fibroblasts and contributes to age-related cardiac disorders.(9) However, the link
62 between age-related OPN production, VAT senescence and impairment of macrophage function
63 is still elusive.

64 Here we show that during the aging process, ATM undergo a senescence phenotype, which
65 impairs ATM function and contributes to age-related VAT remodeling and dysfunction. These
66 senescent macrophages show global decline of cell motility, focal adhesion and endocytosis.
67 Thus senescent ATM are inefficient in clearing apoptotic VAT cells. Conversely, depleting
68 senescent ATM blunts VAT senescence and restores healthy VAT structure and function.
69 Importantly, we uncover a major role of OPN in inducing ATM senescence by demonstrating
70 that the loss of OPN attenuates ATM senescence, prevents age-related ATM dysfunction and
71 finally rejuvenates VAT. Reciprocally, extracellular OPN drives naïve macrophages toward a
72 senescent phenotype and impairs ATM phagocytic activity. Taken together, our data indicate
73 that age-related OPN accumulation in VAT governs ATM senescence, which is a major
74 contributor to VAT remodeling.

75

76

77 Results

78 Aging promotes accumulation of senescent cells in visceral adipose tissue

79 With aging, senescent cells accumulate in VAT as demonstrated by higher luciferase activity
80 in p16-luciferase mice (Fig.1a) and increased senescence-associated beta-galactosidase (SA-β-
81 Gal) activity within VAT (Fig.1b). This was in line with the age-related up-regulation of
82 transcript and protein levels of senescence markers (i.e. p16 and p21, Fig.1c) in the 12-month
83 VAT as compared with the 3-month VAT (Fig.1d, e).

84 VAT senescence was associated with an increase in gene expression of matricellular proteins
85 (Supplemental Fig.1a) and pro-inflammatory markers (Supplemental Fig.1b). This included
86 increased expression levels of Galectin3 (*Lgals3*) and osteopontin (OPN; *Spp1*), a key
87 component of SASP (14) that has been reported to induce a deleterious remodeling of the
88 heart.(9) Interestingly, upregulation of *Spp1* (OPN gene) was one of the strongest
89 discriminative genes associated with VAT aging, together with senescence (*Cdkna1* and
90 *Cdkna2*) and phagocytosis-related genes (Fig.1f, g). Based on this finding, first we established
91 senescent cells (p16-positive) mainly localizing in OPN-rich VAT areas (Fig.1h) OPN also co-
92 localized within macrophages (F4/80) and T-lymphocytes (CD3) (Fig.1i, Supplemental Fig.1c).
93 Of note, age-related VAT changes included an increase in body-weight, adipose tissue depot
94 weight, adipocyte size, and interstitial fibrosis together with an impaired glucose
95 tolerance/insulin resistance, higher adipokine levels and an alteration of glucose and fatty acid
96 metabolism-related gene expression (Supplemental Fig.1d-k).

97 Taken together, our data suggest that VAT senescence may be governed by tissue/local OPN
98 accumulation.

99

100 Osteopontin is a critical regulator of adipose tissue and macrophage senescence

101 Since OPN was highly expressed in aged VAT aging, we first aimed to dissect the role of OPN
102 in inducing VAT cellular senescence by genetic deletion and pharmacological inhibition.

103 We found a decreased VAT senescence in 12-month OPN-knockout (OPN^{-/-}) mice as compared
104 with wild-type littermates (WT) as evidenced by lower SA-β-Gal activity (Fig.2a) and p16
105 protein levels (but not p21 and p53, Fig.2b, c). Interestingly, this reduced VAT senescence in
106 OPN^{-/-} mice was associated with lower VAT fibrosis (Supplemental Fig.2a) and improved
107 glucose tolerance and insulin sensitivity (Supplemental Fig.2b, c) despite higher body weight,
108 larger adipose tissue mass and adipocyte size (Supplemental Fig.2d-f).

109 Similarly, pharmacological OPN inhibition by Agelastatin A (AA)(9) induced a dramatic
110 decrease of p16 expression in VAT (Fig.2d) and in CD68⁺ ATM (Fig.2e) in 12-month WT mice.
111 AA treatment also improved VAT structure (i.e. reduced adipocyte size), adipokine secretion
112 profile and glucose homeostasis (Supplemental Fig.2g-j). Taken together, these results show
113 that OPN deficiency or inhibition improves VAT structure, metabolic function and reduces the
114 percentage of senescent ATM.

115 To firmly establish the role of OPN in inducing senescence in macrophages, we next subjected
116 bone marrow-derived macrophages (BMDM) from 3-month WT mice to *in vitro* OPN-matrix
117 treatment (by dish coating, Fig.2f). In naïve BMDM, OPN induced p16 transcript and protein
118 expression in a dose- and time-dependent manner (Fig.2g & Supplemental Fig.2k).
119 Interestingly, this p16 induction was coupled with similarly increased *Ccl2* expression but with
120 decreased *Illb* expression (Supplemental Fig.2l). Exogenous OPN also promoted p16
121 expression levels in OPN^{-/-} macrophages (Supplemental Fig.2m). We then confirmed the role
122 of OPN *in vivo* with OPN-enriched Matrigel implantation (compared with vehicle), which
123 increased infiltration of macrophages and up-regulated p16 expression in recruited
124 macrophages in young WT mice (Fig.2h, i).

125 Collectively, our results indicate that OPN is an important extracellular matrix protein that
126 potentiates VAT senescence and metabolic dysfunction during aging through VAT immune cell
127 senescence.

128

129 **Role of adipose tissue macrophages to drive visceral adipose tissue senescence during aging**

130 To further establish the role of OPN in inducing ATM senescence and thus driving VAT
131 remodeling and dysfunction, we focused on ATM phenotype in 3- and 12-month WT and OPN-
132 ^{-/-} mice. First, we found that p16 was highly expressed in ATM (CD68⁺) in 12-month WT as
133 compared with 12-month OPN^{-/-} mice whilst it was not expressed in young mice (Fig.3a). FACS
134 phenotyping with conventional surface markers (Supplemental Fig.3a, b)(15, 16) confirmed
135 that aging increased the percentage of Ly6c-CD206⁺ cells within the CD11b⁺F4/80⁺ cells in
136 WT mice (Fig.3b) but did not show any significant difference in VAT immune cell
137 subpopulations between 12-month WT and OPN^{-/-} mice (Fig.3c). Interestingly, FACS analysis
138 targeting p16 showed higher p16 protein levels in F4/80⁺ ATM in 12-month vs 3-month WT
139 mice, and remarkably reduced p16 expression in ATM-derived 12-month OPN^{-/-} mice (Fig. 3d),
140 which was in line with our observation of lessened VAT senescence in 12-month OPN^{-/-} mice
141 (Fig. 2a-c). In parallel, T lymphocytes (CD3⁺) were expressing p16 with aging whilst OPN
142 deficiency reduced it (Supplemental Fig.3c).

143 As a proof of concept for a key role of ATM senescence to induce VAT senescence, we eliminated
144 ATM with liposome-packaged clodronate in 12-month WT mice (Fig.3e). We first observed
145 depletion of ATM by clodronate (Fig.3f and Supplemental Fig.3d) together with reduced OPN
146 (Fig. 3g) and p16 levels in VAT (Fig. 3h). This was associated with a dramatic improvement in
147 VAT remodeling (decreased adipocyte size), adipokine secretion profile and glucose
148 tolerance/insulin resistance (Fig.3i-l).

149 Collectively our data reinforce the hypothesis of a key role of OPN-related ATM senescence to
150 drive age-dependent VAT alterations. This led us to further characterize the link between OPN
151 and the occurrence of senescence in ATM.

152

153 **Impact of aging on adipose tissue macrophage function**

154 Hence, we evaluated the effects of ATM senescence and the role of OPN on efferocytosis, an
155 important macrophage function to eliminate cell debris and apoptotic cells and to maintain
156 tissue integrity.(17) First, staining of VAT showed an increased co-localization between
157 TUNEL and CD45+ cells together with a shorter distance between TUNEL+/CD45+ cells in
158 12-month OPN^{-/-} as compared to WT animals (Fig.4a-c). However, there was a similar age-
159 dependent increase in TUNEL+ cells in WT and OPN^{-/-} (Supplemental Fig.4a), whilst the
160 CD45+ cell percentage was higher in the aged OPN^{-/-} as compared with aged WT mice
161 (Supplemental Fig.4b).

162 Since TUNEL positivity may not represent only apoptotic chromatin change but also DNA
163 strand break and DNA repair process,(18, 19) we stained VAT for phosphorylated H2AX
164 (γ H2AX) in both 3- and 12-month WT and OPN^{-/-} mice and found a comparable age-dependent
165 increase in γ H2AX+ cells between genotypes (Fig.4d, e). In sharp contrast, however, γ H2AX+
166 cells mainly co-localized with CD45+ cells in OPN^{-/-} VAT but not in WT, as observed with
167 TUNEL+ cells (Fig.4f). We then performed staining for cleaved-caspase 3, a central executioner
168 of apoptosis, to evaluate the final step of apoptosis in the VAT (Fig.4g).(20) Cleaved-caspase 3
169 mostly co-localized with CD45+ cells in 12-month OPN^{-/-}, but not in WT (Fig. 4h). The
170 genotype-related difference in TUNEL, γ H2AX and cleaved-caspase 3 demonstrates an
171 impairment in ATM phagocytic function to clear the age-related cellular damage accumulation
172 in aged WT as opposed to OPN^{-/-} mice. To confirm this *in vivo* observation, we performed an
173 *in vitro* phagocytosis assay (Supplemental Fig.4c-e), which displayed impaired phagocytic
174 activity in BMDM derived from 12-month WT mice, which was prevented in BMDM derived
175 from age-matched OPN^{-/-} mice (Fig.4i and Supplemental Fig.4d, e). In line with these results,
176 phagocytosis-related gene expression levels were higher in OPN^{-/-} VAT (Fig. 4j) and in OPN^{-/-}
177 BMDM (Supplemental Fig.4f) compared to WT. Conversely, OPN decreased BMDM phagocytic
178 activity and related-gene expression levels compared to vehicle treatment (Supplemental
179 Fig.4g, h).

180 These results highlight that, coincident with the induction of senescence, OPN impairs a major
181 ATM function, i.e. efferocytosis. By contrast, genetic OPN deletion restores ATM functionality
182 whilst preventing ATM senescence.

183

184 **OPN^{-/-} BMDM transplantation rejuvenates visceral adipose tissue and restores metabolic
185 function during aging**

186 To further establish the role of OPN in VAT aging, we conducted bone marrow transplantation
187 (BMT) from 4-month WT and OPN^{-/-} donors to WT recipients after total body irradiation, and
188 kept them until the age of 16-month (Fig.5a). Blood leukocytes were reconstituted with donor-
189 derived cells (CD45.2+) over 95%, without affecting their number (Supplemental Fig.5a-c).
190 After OPN^{-/-} BMT, VAT SA- β -Gal staining slightly decreased as compared with WT BMT

191 (Fig.5b), together with decreased total p16-positive cells and p16-positive ATM (Fig.5c,d), but
192 without any change in p16+CD3+ cells (Supplemental Fig.5d). OPN positive cells markedly
193 decreased in OPN^{-/-} BMT VAT (Fig.5e), along with OPN gene expression (Fig.5f). Blunted
194 senescence and OPN expression in OPN^{-/-} BMT VAT associated with normalized adipokine
195 gene expression pattern, smaller adipocyte size, and improved glucose tolerance/insulin
196 sensitivity (Fig.5g-j). Finally, OPN^{-/-} BMT reduced TUNEL+ cells (Fig.5k) and increased co-
197 localization of cleaved caspase-3+CD45+ cells in VAT (Fig.5l), along with higher efferocytosis-
198 related gene expression (Fig.5m).

199 Collectively, our results indicate that ATM-derived OPN exerts an important role in promoting
200 ATM/VAT senescence and dysfunction.

201

202

203 **Discussion**

204 In this study, we showed that age-related VAT remodeling and senescence are strongly related
205 to ATM senescence with impairment of major macrophage functions, such as efferocytosis.
206 Importantly, we uncovered a key role for the matricellular protein OPN to drive these processes.

207

208 **VAT senescence during aging**

209 Our data pointed out that VAT remodeling occurs during the aging process together with
210 cellular senescence. Indeed, comparison of 3-month and 12-month mice highlighted that VAT
211 aging begins in middle-aged mice, earlier than previously reported in the literature.(21) VAT
212 aging is associated with structural remodeling (i.e. enlargement of adipocytes, fibrotic
213 deposition), metabolic dysfunction (i.e. impaired glucose tolerance, insulin sensitivity, and
214 adipokine secretion) and senescence (SA- β -Gal activity and p16/p21/p53).

215 Interestingly, we demonstrated that matricellular protein and senescence marker genes were
216 the more discriminative than proinflammatory genes to drive VAT aging, whilst efferocytosis-
217 related genes were strongly down-regulated. This observation focused our attention on how
218 OPN and ATM govern VAT senescence.

219 First, our results highlighted the important role of OPN, a member of the matricellular protein
220 family, during VAT aging.(13) Whilst the role of many matricellular proteins including OPN
221 has been shown in VAT remodeling in obesity,(10, 22-24) we previously reported that VAT was
222 the major source of OPN during aging.(9) Our current data reinforce this age-related
223 upregulation of OPN (*Spp1*) and galactin3 (*Lgals3*), both involved in the regulation of
224 macrophage function.(25) Genetic deletion and pharmacological inhibition of OPN reduced
225 VAT and ATM senescence, whilst restoring efferocytosis, as shown by *in vitro* and *in vivo*
226 assays. By contrast, OPN induced a senescent-like phenotype in naïve macrophages with
227 reduced phagocytic activity, indicating that OPN has a key role in modulating ATM senescence
228 and function. Interestingly, ATM's endocytotic dysfunction might be considered as one of the
229 primary events to mediate VAT dysfunction in both aging and obesity as recently reported.(15,
230 26)

231 Another interesting finding is that genetic OPN deletion resulted in significantly larger
232 adipocyte-size and VAT mass in spite of their better metabolic function. This indicates that the
233 OPN/senescence-free developmental aspects are more important to the adipocyte function than
234 the demerit of cell-size enlargement.

235 **Importance of macrophage senescence in VAT aging**

236 Thus, to dissect the interplay between OPN and ATM senescence, we explored how OPN-
237 inducible ATM senescence may spread senescence to the adjacent tissue ultimately leading to
238 VAT remodeling and dysfunction during the aging process. Indeed, the specific consequences
239 of ATM senescence have not yet been fully addressed whilst other adipose tissue cell
240 components have been reported to undergo senescence during aging.(1-3, 6) Better

241 understanding of pathological processes affecting ATM, the most abundant AT immune cell-
242 type in natural aging,(27) is particularly important given their key role in AT homeostasis and
243 functional maintenance.(28) By contrast, ATM have been referred to as a source of harmful
244 effects under stress-conditions such as over-nutrition responsible for a chronic, low-grade
245 proinflammatory state.(29) First, we established that aging induced p16 up-regulation in ATM
246 of WT mice, which was blunted by OPN deficiency. The impact of ATM senescence was further
247 demonstrated by deletion of ATM by clodronate-liposome treatment that ameliorated VAT
248 structural remodeling (i.e. adipocyte hypertrophy), and more broadly, metabolic function (i.e.
249 glucose tolerance and adipokine secretion profile). This clodronate-mediated improvement
250 paralleled with reduced ATM senescence (lessened p16+CD68+ cells), indicating that ATM is
251 a major contributor to age-related VAT and systemic metabolic dysfunction.

252 Next we demonstrated a senescence-associated impairment of ATM function regulated by
253 OPN both *in vivo* and *in vitro*. In particular, we studied efferocytosis, which is crucial in
254 maintaining AT homeostasis by removing apoptotic cells and cell debris. Whilst aging was
255 associated with an increase in TUNEL+ cells in both WT and OPN^{-/-} VAT, only aged OPN^{-/-}
256 mice but not WT manifested efficient efferocytosis as observed by higher engulfment of
257 TUNEL+ or cleaved-caspase 3+ cells. *In vitro* functional assay further indicated that aged
258 OPN^{-/-} BMDM exerted preserved phagocytic activity with higher expression levels of key
259 efferocytosis-related genes such as *Mertk*.(30, 31) The importance of our findings is
260 underscored by recent studies pointing out that tissue microenvironment is the most important
261 determinant for macrophage phenotype and functionality.(32) For instance, tissue
262 macrophages are differently programmed for efferocytosis, depending on apoptotic signals.(33,
263 34) In this regard, during the aging process, adipose tissue extracellular OPN would be crucial
264 to direct recruited or naïve tissue macrophages to senescent reprogramming at the cost of
265 phagocytic function.

266 Most of the recent publications mentioned favorable effects by systemic elimination of
267 senescent cells with senolytic drugs.(5, 35-37) On the other hand, induction of senescence in
268 some cell types is beneficial during aging and repair processes.(9, 38-40) Beside senolytic drugs,
269 we have identified OPN as a novel target for ameliorating cellular senescence in specific cell
270 types such as adipose tissue macrophages, complementing our previous observations in cardiac
271 fibroblasts.(9) Collectively, our results showed that elimination of senescent ATM ameliorated
272 AT remodeling and dysfunction, suggesting that macrophage-specific and senescence-targeted
273 therapeutics (such as macrophage-directed pharmacological OPN inhibition) could be a viable
274 strategy to control AT senescence and subsequent systemic metabolic alterations resulting
275 from aging.

276

277 **Methods**

278 **Mice:** C57/BL6JRj mice (referred as wild-type: WT) were purchased from Janvier Labs, France.
279 Osteopontine knockout mice (B6.129S6(Cg)-Spp1^{tm1Blh/J}) were purchased from Jackson
280 laboratory (ME, USA), which had been back-crossed with C57/BL6J mice more than 10
281 generations, and kept as homozygous (referred as OPN^{-/-}). p16-luciferase mice (Strain Code
282 01XBT⁻-B6.Cg-Cdkn2a^{tm3.1Nesh Tyr c-2J/Nci}) were obtained from the NCI mouse repository
283 via Dr Norman Sharpless (University of North Carolina).(21) All mice were housed in a specific
284 pathogen free platform at a constant temperature (22°C), with a 12-hour light-dark cycle and
285 unrestricted access to a chow diet (CD, A0310, Safe Diets, France) and water. Chow diet
286 composition corresponded to 13.5% of fat, 61.3% of carbohydrate and 25.2% of protein. During
287 follow-up, animals underwent a monthly body-weight (BW) evaluations.

288

289 ***In Vivo* luciferase Detection**

290 Exited luciferase activity was detected and analyzed under collaboration with Dr Seguin, Paris
291 Descartes University as previously described.(21) Briefly, mice were anesthetized with
292 isoflurane, and then injected intraperitoneally with D-luciferin substrate (Caliper Life
293 Sciences; 15 mg/ml in PBS). Images were taken with the PhotonIMAGER system (BIOSPACE).
294 After substrate administration, peak luminescence was measured at 6–8 minutes. For
295 simultaneous image capture of more than 3 animals, a wide-angle lens was used. In our aging
296 studies, in which animal size varied, mice were injected with 10 µl/g body weight of substrate.
297 To compare multiple images taken at the same exposure point, PhotoAcquisition Software for
298 PhotonIMAGER (BIOSPACE) was used following substrate administration, and acquisition
299 lasted for 10 minutes (from t=10min to t=20min after luciferin injection). An additional ROI
300 was employed to normalize for background luminescence on each image for all analyses.

301

302 **Metabolic tolerance tests:**

303 Glucose Tolerance Test (GTT): Mice were fasted for 6-7 hours before the study, and then given
304 glucose solution intraperitoneally (1.5 mg/g body weight). Blood samples were collected from
305 tail vein at baseline, 15, 30, 60, 90, 120 minutes after injection, and glucose concentration was
306 measured with an automatic glucometer (Accu-Chek Performa, Roche, Germany).

307 Insulin Tolerance Test (ITT): Mice were fasted for 6-7 hours before study, and then given
308 insulin solution intraperitoneally (0.5 mU/g of body weight, Umelin, Lilly, France). Blood
309 samples were collected from tail vein at baseline, 30, 60, 90, 120 minutes after injection, and
310 glucose concentration was measured as above.

311

312 ***In vivo* Matrigel plug assay.**

313 OPN-enriched *in vivo* matrigel plug assay was performed according to the manufacture's
314 instruction and previous report.(41) The total of 6 male, 5-month old WT mice were used. In

315 brief, total 500 μ l of Matrigel,(cat#. 354234, Corning) was mixed with 100 μ l of mouse
316 recombinant OPN (R&D) 50 μ g or PBS (as vehicle). Mixed solution was subcutaneously
317 injected to groin sites of anesthetized mice. After 14 days, the Matrigel plug was removed,
318 fixed in 4% formaldehyde with mesh-cassettes (Trajan), and further processed for
319 immunohistochemistry.

320

321 ***In vivo* macrophage depletion**

322 The total of 17 male WT mice, 12-month old and weighed 30~36 g were used. Before *in vivo*
323 macrophage depletion, mice were undergone baseline assessment of metabolic functions (GTT
324 and ITT). The mice were then injected intraperitoneally with 70 mg/kg clodronate in liposomes
325 or PBS control liposomes (ClodLip BV, Amsterdam, Netherlands) every 4 days for 4 weeks
326 (70% dose used in reference).(42) Their body weights were recorded at the same time. After
327 final metabolic assessments, the mice were euthanized by neck-dislodgement. The organs and
328 bloods were harvested and processed for further evaluations.

329

330 **Osteopontin inhibition by small molecule**

331 The total of 20 male WT mice, approximately 11-month old and weighed 28~35 g were used.
332 Agelastatin A (AA), small organic molecule known to inhibit OPN production *in vivo*, was
333 synthesized and kindly provided by Professor Takehiko Yoshimitsu at Graduate School of
334 Pharmaceutical Sciences, Okayama University, Okayama, Japan. After baseline assessment
335 of metabolic functions (GTT and ITT), the mice were given 1.5 mg/kg of AA or vehicle only (2-
336 Hydroxypropyl- β -cyclodextrinonly, Sigma-Aldrich) intraperitoneally every 4 days for 4
337 weeks.(9)Their body weights were recorded at the same time. This protocol was developed with
338 informative advices from Pro.Yoshimitsu. After final metabolic assessments, the mice were
339 euthanized by neck-dislodgement. The organs and bloods were harvested and processed for
340 further evaluations.

341

342 **Mouse bone-marrow transplantation (BMT)**

343 Irradiated (9.5 Gy, whole-body), 8-week old male wild-type mice (CD45.1: B6.SJL-Ptprca
344 Pepcb/BoyCrl, congenic strains, C57BL/6 background) were purchased from Charles-River
345 Laboratory (France) as recipient. Bone-marrow cells were taken from femurs of donor mice (4-
346 month old male WT and OPN^{-/-} mice as described above; CD45.2) and 1-day after irradiation,
347 the 3-month old recipient mice received 2 millions of donor bone-marrow cells by intravenous
348 tail injection. Mice were kept and aged in house until 16-month old. Body weight was recorded
349 monthly, and peripheral blood reconstitution was analyzed by FACS at 2, 4, 5, 9 and 12-month
350 after BMT. Used antibodies and fluorophores are listed in the supplemental table.

351

352 **Plasma adipokine measurement**

353 Collected whole blood samples were centrifuged and plasma fraction was separated, stored at
354 -80 °C. Plasma levels of adipokines were assessed with a Magnetic Luminex screening assay
355 kit (Adiponectin: LXSAMSM-1, Leptin: LXSAMSM-19, Bio-Techne, Abington, UK) following
356 the manufacturer's instructions.

357

358 **Tissue processing and Histology**

359 Dissected organs were fixed with 4% formaldehyde solution (Sigma-Aldrich) immediately and
360 subjected to paraffin-embedding after at least 1 week fixation. The sections were
361 deparaffinized using xylene and a graded series of ethanol dilutions. Adipose tissue sections (5
362 μm thickness) were stained with hematoxyline & eosin (Sigma-Aldrich, France) for general
363 appearance observation and adipocyte size measurement, and Sirius Red for tissue fibrosis
364 measurement, respectively.

365 For immunofluorescent staining, deparaffinized and hydrated sections were subjected to heat-
366 mediated antigen retrieval (Citrate buffer pH6.0, Dako) and blocking with 30% goat serum.
367 Primary antibodies were applied with antibody diluent (Dako) over-night at 4°C in humidified
368 chamber. Corresponding 2nd antibodies conjugated with fluorescent dyes were used followed
369 with DAPI nucleus counter-staining.

370 The pictures with hematoxyline & eosin and Sirius Red staining were captured using an
371 Axioplan 2 Imaging microscope (Zeiss). Fluorescent images were taken using an Axioplan M2
372 Imaging microscope (Zeiss). For adipocyte size, at least 200–300 cells per sample were traced
373 and quantified surface area. For interstitial fibrosis, 3-5 images per sample were measured.
374 Red area normalized by total surface area. All data were measured with the ImageJ software
375 (NIH).

376

377 **SA- β -Gal staining**

378 Dissected VATs in 5 mm-square pieces were directly subjected to staining solution (1 mg/ml X-
379 gal, Sigma-Aldrich), and kept at 37°C for 12 hours. The images were taken by GR digital
380 camera (RICOH, Japan).

381

382 **TUNEL staining**

383 TUNEL (terminal deoxynucleotidyl transferase-dUTP nick end labeling) staining was
384 performed according to the manufacture's instruction (ApopTag® Plus In Situ Apoptosis
385 Fluorescein Detection Kit, Millipore) with minor modifications. Briefly, deparaffinized and
386 hydrated sections were subjected proteinase K treatment (20 mg/mL, Qiagen), and incubated
387 with TdT enzyme for 1 hour. After stopping the reaction, digoxigenin-conjugated fluorescein
388 was applied to visualize the signals. CD45 immunohistochemistry and DAPI counter-staining
389 was performed to show the TUNEL positive cell localization.

390

391 **Quantitative PCR**

392 Total RNA was extracted from 80mg powdered adipose tissue samples with RNA easy fibrous
393 kit (Qiagen). RNA from cultured macrophages was extracted with RNA easy mini kit (Qiagen)
394 as manufacturer's instruction. First strand DNA synthesis was synthesized from 0.5-1.0 µg
395 total RNA with High-Capacity cDNA Reverse Transcription Kit (Applied Biosystems) and a
396 thermal cycler SimpliAmp (Applied Biosystems) according to manufacturer's instruction.
397 Quantitative PCR was performed and analyzed with TaqMan® Universal PCR Master Mix
398 and StepOne™ Real-Time PCR System (Applied Biosystems). Beta-actin was used as internal
399 control. Used Taqman primers are described in the supplemental table.

400

401 **Western Blot Analysis**

402 Eighty-90 mg of adipose tissues was homogenized in "Platonic" urea lysis buffer containing 7
403 M urea, 10% glycerol (v/v), 10 mM Tris-HCl (pH6.8), 1% SDS, 1 mM dithiothreitol,
404 supplemented with protease and phosphatase inhibitor cocktail tablets (Pierce/ThermoFisher,
405 88265, France). After vortexing, lysates were sonicated, passed through a 21G needle at least
406 6 times, rotated for 30 minutes at 4°C and spun to obtain supernatant. Protein concentration
407 was adjusted according to Bradford method (Bio-rad). Denatured total protein (20µg) was
408 loaded to 10% SDS-PAGE. Separated proteins were transferred to PVDF membranes
409 (Invitrogen), blocked in Pierce™ Clear Milk Blocking Buffer (ThermoFisher, 37587, France)
410 and probed for selected proteins with a specific primary antibody at 4°C overnight, followed by
411 incubation with the corresponding HRP-conjugated secondary antibodies (Abcam).
412 Densitometric quantification was performed with ImageJ software, and normalized to β-actin
413 levels in each sample. Primary antibodies are described in the supplemental table.

414

415 **Adipose tissue immune cell and macrophage flow cytometric analysis (FACS).**

416 Dissected adipose tissues were kept on ice and minced to 1-3 mm pieces in heparinized cold
417 PBS. After snap vortexing, PBS was removed and tissues were digested with collagenase II
418 solution (Sigma-Aldrich) at 37°C water bath with gently shaking for 20 min. Digested tissue
419 was then passed through 70 µm mesh and centrifuged to spin down stromal vascular fraction
420 (SVF). After RBC lysis (ACK Lysing Buffer, Gibco, A1049201), the SVF cells were suspended
421 in PBS supplemented 2% fetal-calf serum (FCS), and stained with appropriate antibodies for
422 surface marker and isotype controls for 30 min at 4°C in the dark chamber. Used antibodies
423 and fluorophores are listed in the supplemental table. Living and dead cell discrimination was
424 performed with 7-AAD staining (Molecular Probes). For intracellular p16 staining, SVF cells
425 stained with surface markers were then fixed and permeabilized with Cytofix/Cytoperm
426 solution (BD Bioscience). The cells were then stained with Alexa 488 conjugated p16 antibody
427 (2D9A12, Abcam) and corresponding isotype controls. Flow cytometry was performed with
428 LSRII (BD Bioscience). Data was evaluated and analyzed with FlowJo (TreeStar).

429

430 **Generation of bone-marrow derived macrophages (BMDM)**

431 Mice bone-marrow cell was isolated from femurs and tibias from 3- or 12-month old WT and
432 OPN^{-/-} mice. After RBC lysis (LCK buffer, Sigma-Aldrich) and passed through 70 µm mesh,
433 bone-marrow cells were plated with RPMI 1640 medium (Gibco) supplemented with 5%FCS,
434 penicillin/streptomycin (Gibco) and 30 ng/ml MCSF (R&D systems). Five days after
435 differentiation into macrophages, the cells were treated with Accutase (Sigma-Aldrich),
436 counted and re-plated at 1.5×10^5 /well in 12-well non-coated plate. The BMDMs were further
437 subjected to OPN stimulation experiment or phagocytosis assay.

438

439 **BMDM stimulation by osteopontin**

440 Modulation of BMDM by OPN protein was evaluated as previously described with minor
441 modification.(43) Briefly, 12-well plates were coated with 20 or 40 µg of mouse recombinant
442 OPN (R&D systems) for 20 hours at 4°C and then stabilized with 0.5% polyvinylpyrrolidone
443 (Sigma-Aldrich) for 1 hour at room temperature. BMDM (1.5×10^5 /well) were re-plated in
444 RPMI 1640 medium supplemented with 5%FCS and 30 ng/ml MCSF. Twenty-four or 36 hours
445 after passage, the cells were harvested for RNA extraction.

446

447 **BMDM immunofluorescent staining**

448 BMDM were passed onto an OPN-coated 8-well Lab-Tek II chambered cover glass (Nalge
449 Nunc) at 1.5×10^4 /well density. After incubated as described above, the BMDM were washed
450 with chilled PBS buffer and fixed with 2% paraformaldehyde solution for 10 min at room
451 temperature and permeabilized with 0.05% Triton-X (Sigma-Aldrich). The cells were blocked
452 with 2% BSA solution (Sigma-Aldrich) and subjected to p16 and F4/80 antibody treatment for
453 overnight. Corresponding 2nd antibodies conjugated with fluorescent dyes were used to
454 visualize with DAPI nucleus counter-staining. The images were taken using an Axioplan M2
455 Imaging microscope (Zeiss).

456

457 **Phagocytosis assay**

458 Human leukemia cell-line, HL60 cells were labeled with pHrodo; iFL Green STP Ester (amine
459 reactive) (Thermofisher) as previously described (44) with minor modification. In brief, the
460 HL60 cells were washed twice with PBS buffer and incubated at room temperature for 30 min
461 with 0.1 µg/ml pHrodo. The cells were washed with PBS buffer twice, and suspended in the
462 RPMI medium containing 0.5% FCS, and used for engulfment. To 5.0×10^4 BMDM in 500 µl of
463 RPMI medium containing 5% FCS in a 12-well plate, 2.0×10^5 pHrodo-labeled HL60 cells were
464 added, and incubated at 37°C for 0, 30, 60, and 120 min. The cells were detached from the
465 plate by incubating with 0.25% trypsin and 1mM EDTA, and collected by centrifugation. The
466 cells were labelled with surface marker of CD11b and F4/80, further suspended in 500 µl of

467 PBS buffer containing 2% FCS and analyzed by flow cytometry on the LSRII (BD Bioscience).
468 Data was evaluated and analyzed with FlowJo (TreeStar). For time-lapse imaging, 1.5×10^4
469 /well BMDM were passed onto an 8-well Lab-Tek II chambered cover glass (Nalge Nunc), and
470 incubated at 37°C for 0, 30, 60, and 120 min with 6×10^4 pHrodo-labeled HL60 cells in 250 μ l
471 of RPMI medium containing 5% FCS and observed by fluorescence microscopy.

472

473 **Discriminative gene analysis**

474 In addition to exploring individual changes involving various molecular targets, we aimed to
475 evaluate also the contextual importance of the changes affecting major themes that
476 characterize the adipose tissue functional signature under the effect of aging. To this purpose
477 we measured the VAT expression profile of a panel of 43 genes selected to illustrate 5 major
478 themes characterizing the functional signature of the adipose tissue: efferocytosis,
479 matricellular proteins, senescence, inflammation, adipose tissue functions and secretome. A
480 random-forest supervised learning algorithm was applied iteratively to evaluate and rank the
481 relative discriminative value (i.e. feature importance) associated with changes in these gene
482 expression profiles induced by aging. These computations were performed using the R
483 environment for statistical computing and the algorithmic implementation available in the
484 “randomForest” R package (version 4.6-12). To assess the relative discriminative value
485 associated with each measured expression profile we averaged the feature importance
486 provided by the random forest algorithm over 10,000 successive iterations performed for each
487 of the analyzed situations. The individual discriminative value of each transcriptional profile
488 was expressed as percentages of the total discriminative power of the panel of selected
489 transcriptional descriptors. The resulting values were plotted after grouping them by
490 functional category and ranking the available categories in the decreasing order of their
491 strongest transcriptional descriptor, to illustrate the contextual importance of the functional
492 changes induced by VAT aging

493

494 **Statistics**

495 All data are presented as mean+SEM. Difference between two groups was analyzed by
496 unpaired t-test. Comparisons between multiple groups were done using one- or two-way
497 ANOVA followed by Tukey or Bonferroni test. These analysis were performed in GraphPad
498 Prism 5.0. for Win (GraphPad Software, La Jolla, California, USA). All t-tests were two-tailed.
499 P-value <0.05 was considered significant (*P \leq 0.05; **P \leq 0.01; ***P \leq 0.001).

500

501 **Study approval**

502 All animal experiments were approved by the Institutional Animal Care and Use Committee
503 of the French National Institute of Health and Medical Research (INSERM)-Unit 955, Créteil,
504 France (ComEth 15-001) and Institut Gustave Roussy’s Institutional Animal Care and Use

505 Committee (Villejuif, France).

506

507 **Author contributions**

508 D.S., M.P. and Y.Z. designed, conducted most of the experiments and data analysis, and
509 prepared the manuscript; Z.M., S.N., H.L. and M.H. helped with organ isolation and imaging
510 experiments; L.L. and D.A. performed gene and protein expression analysis; M.B. assisted
511 with mouse work and live imaging experiments; M.S. performed plasma analysis; D.R., P.G.
512 and T.Y. donated materials and provided helpful suggestions; F.L. and S.A. provided helpful
513 suggestions and contributed to the manuscript; C.H. performed gene discriminative analysis;
514 and G.C. and G.D. supervised this work and helped to write the manuscript.

515

516 **Acknowledgements**

517 We thank for technical assistance Xavier Decrouy, Christelle Gandolphe, Wilfried Verbecq-
518 Morlot (imaging), Florian Beghi (animal experiments), Adeline Henry and Aurelie Guguin
519 (Flow cytometry). We also thank Pr. Norman Sharpless, University of North Carolina for the
520 donation of mice; Dr. Johanne Seguin, Paris Descarte University for help with *in vivo* luciferase
521 imaging; Pr. Elizabeth Blackburn, University of California, San Francisco for helpful
522 discussions and suggestions. This work was supported by RHU CARMMA grant (ANR-15-
523 RHUS-0003)

524

525 **Reference**

- 526 1. Minamino T, Orimo M, Shimizu I, Kunieda T, Yokoyama M, Ito T, Nojima A, Nabetani A,
527 Oike Y, Matsubara H, et al. A crucial role for adipose tissue p53 in the regulation of insulin
528 resistance. *Nat Med.* 2009;15(9):1082-7.
- 529 2. Briot A, Decaunes P, Volat F, Belles C, Coupaye M, Ledoux S, and Bouloumie A. Senescence
530 Alters PPARgamma (Peroxisome Proliferator-Activated Receptor Gamma)-Dependent
531 Fatty Acid Handling in Human Adipose Tissue Microvascular Endothelial Cells and Favors
532 Inflammation. *Arterioscler Thromb Vasc Biol.* 2018;38(5):1134-46.
- 533 3. Hall BM, Balan V, Gleiberman AS, Strom E, Krasnov P, Virtuoso LP, Rydkina E, Vujcic S,
534 Balan K, Gitlin I, et al. Aging of mice is associated with p16(Ink4a)- and beta-galactosidase-
535 positive macrophage accumulation that can be induced in young mice by senescent cells.
536 *Aging (Albany NY).* 2016;8(7):1294-315.
- 537 4. Trim W, Turner JE, and Thompson D. Parallels in Immunometabolic Adipose Tissue
538 Dysfunction with Aging and Obesity. *Front Immunol.* 2018;9(169).
- 539 5. Palmer AK, Xu M, Zhu Y, Pirtskhalava T, Weivoda MM, Hachfeld CM, Prata LG, van Dijk
540 TH, Verkade E, Casaclang-Verzosa G, et al. Targeting senescent cells alleviates obesity-
541 induced metabolic dysfunction. *Aging Cell.* 2019;18(3):e12950.
- 542 6. Tchkonja T, Morbeck DE, Von Zglinicki T, Van Deursen J, Lustgarten J, Scrbble H, Khosla
543 S, Jensen MD, and Kirkland JL. Fat tissue, aging, and cellular senescence. *Aging Cell.*
544 2010;9(5):667-84.
- 545 7. Kuk JL, Saunders TJ, Davidson LE, and Ross R. Age-related changes in total and regional
546 fat distribution. *Ageing Res Rev.* 2009;8(4):339-48.
- 547 8. Sun K, Kusminski CM, and Scherer PE. Adipose tissue remodeling and obesity. *J Clin*
548 *Invest.* 2011;121(6):2094-101.
- 549 9. Sawaki D, Czibik G, Pini M, Ternacle J, Suffee N, Mercedes R, Marcelin G, Surenaud M,
550 Marcos E, Gual P, et al. Visceral Adipose Tissue Drives Cardiac Aging Through Modulation
551 of Fibroblast Senescence by Osteopontin Production. *Circulation.* 2018;138(8):809-22.
- 552 10. Nomiya T, Perez-Tilve D, Ogawa D, Gizard F, Zhao Y, Heywood EB, Jones KL, Kawamori
553 R, Cassis LA, Tschop MH, et al. Osteopontin mediates obesity-induced adipose tissue
554 macrophage infiltration and insulin resistance in mice. *J Clin Invest.* 2007;117(10):2877-88.
- 555 11. Shimatani K, Nakashima Y, Hattori M, Hamazaki Y, and Minato N. PD-1+ memory
556 phenotype CD4+ T cells expressing C/EBPalpha underlie T cell immunodepression in
557 senescence and leukemia. *Proc Natl Acad Sci U S A.* 2009;106(37):15807-12.
- 558 12. Shirakawa K, Yan X, Shinmura K, Endo J, Kataoka M, Katsumata Y, Yamamoto T, Anzai
559 A, Isobe S, Yoshida N, et al. Obesity accelerates T cell senescence in murine visceral adipose
560 tissue. *J Clin Invest.* 2016;126(12):4626-39.
- 561 13. Frangogiannis NG. Matricellular proteins in cardiac adaptation and disease. *Physiol Rev.*
562 2012;92(2):635-88.

- 563 14. Saker M, Lipskaia L, Marcos E, Abid S, Parpaleix A, Houssaini A, Validire P, Girard P,
564 Nouredine H, Boyer L, et al. Osteopontin, a Key Mediator Expressed by Senescent
565 Pulmonary Vascular Cells in Pulmonary Hypertension. *Arterioscler Thromb Vasc Biol.*
566 2016;36(9):1879-90.
- 567 15. Silva HM, Bafica A, Rodrigues-Luiz GF, Chi J, Santos PDA, Reis BS, Hoytema van
568 Konijnenburg DP, Crane A, Arifa RDN, Martin P, et al. Vasculature-associated fat
569 macrophages readily adapt to inflammatory and metabolic challenges. *J Exp Med.*
570 2019;216(4):786-806.
- 571 16. Daemen S, and Schilling JD. The Interplay Between Tissue Niche and Macrophage Cellular
572 Metabolism in Obesity. *Front Immunol.* 2019;10(3133).
- 573 17. Henson PM. Cell Removal: Efferocytosis. *Annu Rev Cell Dev Biol.* 2017;33(127-44).
- 574 18. Kanoh M, Takemura G, Misao J, Hayakawa Y, Aoyama T, Nishigaki K, Noda T, Fujiwara T,
575 Fukuda K, Minatoguchi S, et al. Significance of myocytes with positive DNA in situ nick
576 end-labeling (TUNEL) in hearts with dilated cardiomyopathy: not apoptosis but DNA repair.
577 *Circulation.* 1999;99(21):2757-64.
- 578 19. Natale F, Rapp A, Yu W, Maiser A, Harz H, Scholl A, Grulich S, Anton T, Horl D, Chen W,
579 et al. Identification of the elementary structural units of the DNA damage response. *Nat*
580 *Commun.* 2017;8(15760).
- 581 20. Dull AB, Wilsker D, Hollingshead M, Mazcko C, Annunziata CM, LeBlanc AK, Doroshow
582 JH, Kinders RJ, and Parchment RE. Development of a quantitative pharmacodynamic
583 assay for apoptosis in fixed tumor tissue and its application in distinguishing cytotoxic
584 drug-induced DNA double strand breaks from DNA double strand breaks associated with
585 apoptosis. *Oncotarget.* 2018;9(24):17104-16.
- 586 21. Burd CE, Sorrentino JA, Clark KS, Darr DB, Krishnamurthy J, Deal AM, Bardeesy N,
587 Castrillon DH, Beach DH, and Sharpless NE. Monitoring tumorigenesis and senescence in
588 vivo with a p16(INK4a)-luciferase model. *Cell.* 2013;152(1-2):340-51.
- 589 22. Kos K, and Wilding JP. SPARC: a key player in the pathologies associated with obesity and
590 diabetes. *Nat Rev Endocrinol.* 2010;6(4):225-35.
- 591 23. Kong P, Gonzalez-Quesada C, Li N, Cavalera M, Lee DW, and Frangogiannis NG.
592 Thrombospondin-1 regulates adiposity and metabolic dysfunction in diet-induced obesity
593 enhancing adipose inflammation and stimulating adipocyte proliferation. *Am J Physiol*
594 *Endocrinol Metab.* 2013;305(3):E439-50.
- 595 24. Pejnovic NN, Pantic JM, Jovanovic IP, Radosavljevic GD, Milovanovic MZ, Nikolic IG,
596 Zdravkovic NS, Djukic AL, Arsenijevic NN, and Lukic ML. Galectin-3 deficiency accelerates
597 high-fat diet-induced obesity and amplifies inflammation in adipose tissue and pancreatic
598 islets. *Diabetes.* 2013;62(6):1932-44.
- 599 25. Shirakawa K, Endo J, Kataoka M, Katsumata Y, Yoshida N, Yamamoto T, Isobe S,
600 Moriyama H, Goto S, Kitakata H, et al. IL (Interleukin)-10-STAT3-Galectin-3 Axis Is

- 601 Essential for Osteopontin-Producing Reparative Macrophage Polarization After Myocardial
602 Infarction. *Circulation*. 2018;138(18):2021-35.
- 603 26. Jaitin DA, Adlung L, Thaïss CA, Weiner A, Li B, Descamps H, Lundgren P, Bleriot C, Liu
604 Z, Deczkowska A, et al. Lipid-Associated Macrophages Control Metabolic Homeostasis in a
605 Trem2-Dependent Manner. *Cell*. 2019;178(3):686-98 e14.
- 606 27. Bapat SP, Myoung Suh J, Fang S, Liu S, Zhang Y, Cheng A, Zhou C, Liang Y, LeBlanc M,
607 Liddle C, et al. Depletion of fat-resident Treg cells prevents age-associated insulin
608 resistance. *Nature*. 2015;528(7580):137-41.
- 609 28. Boutens L, and Stienstra R. Adipose tissue macrophages: going off track during obesity.
610 *Diabetologia*. 2016;59(5):879-94.
- 611 29. McNelis JC, and Olefsky JM. Macrophages, immunity, and metabolic disease. *Immunity*.
612 2014;41(1):36-48.
- 613 30. Zagorska A, Traves PG, Lew ED, Dransfield I, and Lemke G. Diversification of TAM
614 receptor tyrosine kinase function. *Nat Immunol*. 2014;15(10):920-8.
- 615 31. Watanabe S, Alexander M, Misharin AV, and Budinger GRS. The role of macrophages in
616 the resolution of inflammation. *J Clin Invest*. 2019;129(7):2619-28.
- 617 32. Lavin Y, Winter D, Blecher-Gonen R, David E, Keren-Shaul H, Merad M, Jung S, and Amit
618 I. Tissue-resident macrophage enhancer landscapes are shaped by the local
619 microenvironment. *Cell*. 2014;159(6):1312-26.
- 620 33. Cummings RJ, Barbet G, Bongers G, Hartmann BM, Gettler K, Muniz L, Furtado GC, Cho
621 J, Lira SA, and Blander JM. Different tissue phagocytes sample apoptotic cells to direct
622 distinct homeostasis programs. *Nature*. 2016;539(7630):565-9.
- 623 34. Roberts AW, Lee BL, Deguine J, John S, Shlomchik MJ, and Barton GM. Tissue-Resident
624 Macrophages Are Locally Programmed for Silent Clearance of Apoptotic Cells. *Immunity*.
625 2017;47(5):913-27 e6.
- 626 35. Baker DJ, Wijshake T, Tchkonïa T, LeBrasseur NK, Childs BG, van de Sluis B, Kirkland
627 JL, and van Deursen JM. Clearance of p16Ink4a-positive senescent cells delays ageing-
628 associated disorders. *Nature*. 2011;479(7372):232-6.
- 629 36. Baker DJ, Childs BG, Durik M, Wijers ME, Sieben CJ, Zhong J, Saltness RA, Jeganathan
630 KB, Verzosa GC, Pezeshki A, et al. Naturally occurring p16(Ink4a)-positive cells shorten
631 healthy lifespan. *Nature*. 2016;530(7589):184-9.
- 632 37. Xu M, Pirtskhalava T, Farr JN, Weigand BM, Palmer AK, Weivoda MM, Inman CL,
633 Ogrodnik MB, Hachfeld CM, Fraser DG, et al. Senolytics improve physical function and
634 increase lifespan in old age. *Nat Med*. 2018;24(8):1246-56.
- 635 38. Xue W, Zender L, Miething C, Dickins RA, Hernando E, Krizhanovsky V, Cordon-Cardo C,
636 and Lowe SW. Senescence and tumour clearance is triggered by p53 restoration in murine
637 liver carcinomas. *Nature*. 2007;445(7128):656-60.
- 638 39. Krizhanovsky V, Yon M, Dickins RA, Hearn S, Simon J, Miething C, Yee H, Zender L, and

639 Lowe SW. Senescence of activated stellate cells limits liver fibrosis. *Cell*. 2008;134(4):657-
640 67.

641 40. He S, and Sharpless NE. Senescence in Health and Disease. *Cell*. 2017;169(6):1000-11.

642 41. Perino A, Pols TW, Nomura M, Stein S, Pellicciari R, and Schoonjans K. TGR5 reduces
643 macrophage migration through mTOR-induced C/EBPbeta differential translation. *J Clin*
644 *Invest*. 2014;124(12):5424-36.

645 42. Westwell-Roper CY, Ehses JA, and Verchere CB. Resident macrophages mediate islet
646 amyloid polypeptide-induced islet IL-1beta production and beta-cell dysfunction. *Diabetes*.
647 2014;63(5):1698-711.

648 43. Frolova EG, Pluskota E, Krukovets I, Burke T, Drumm C, Smith JD, Blech L, Febbraio M,
649 Bornstein P, Plow EF, et al. Thrombospondin-4 regulates vascular inflammation and
650 atherogenesis. *Circ Res*. 2010;107(11):1313-25.

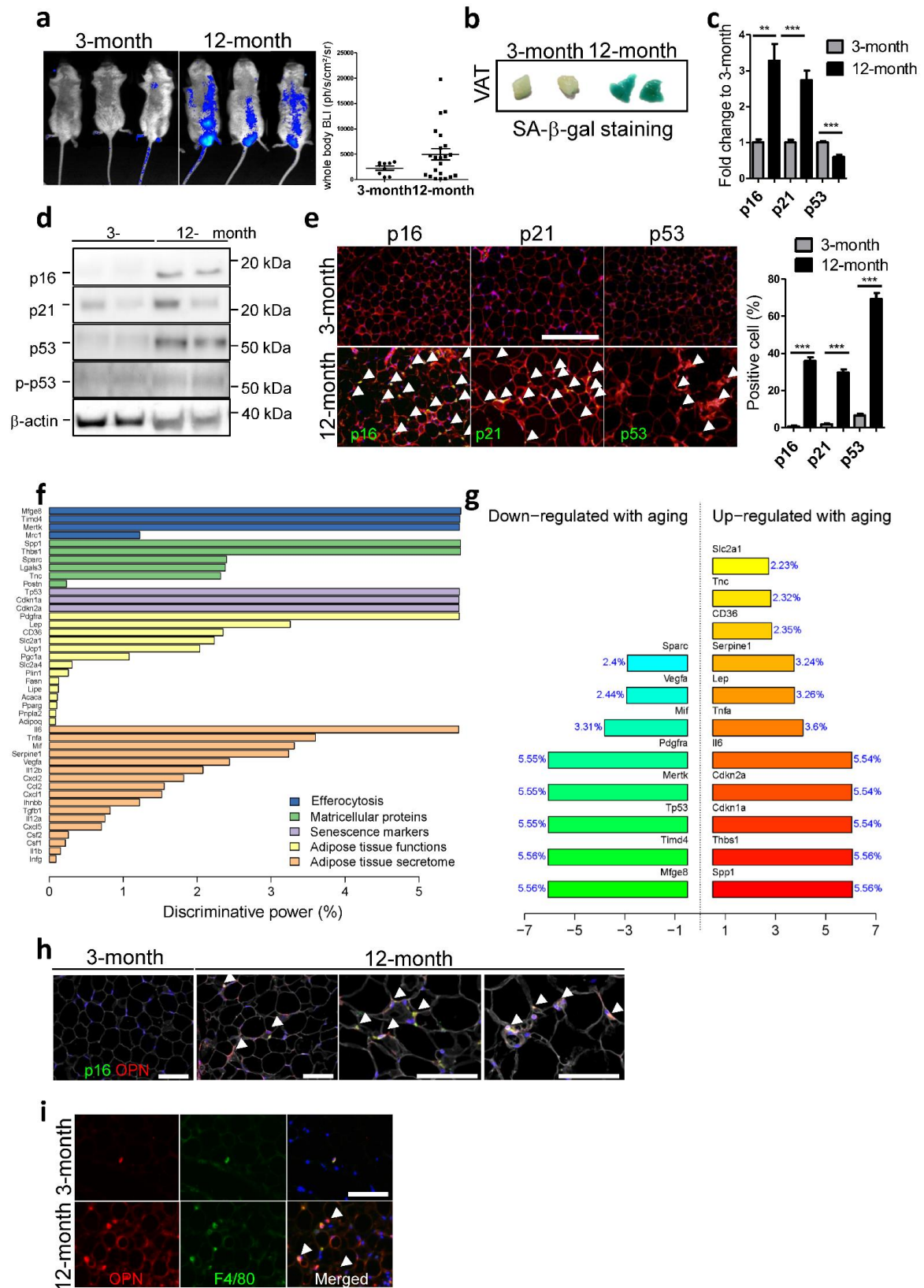
651 44. Nishi C, Toda S, Segawa K, and Nagata S. Tim4- and MerTK-mediated engulfment of
652 apoptotic cells by mouse resident peritoneal macrophages. *Mol Cell Biol*. 2014;34(8):1512-
653 20.

654

655

656

Figure 1. Aging promotes cellular senescence in white adipose tissue



658

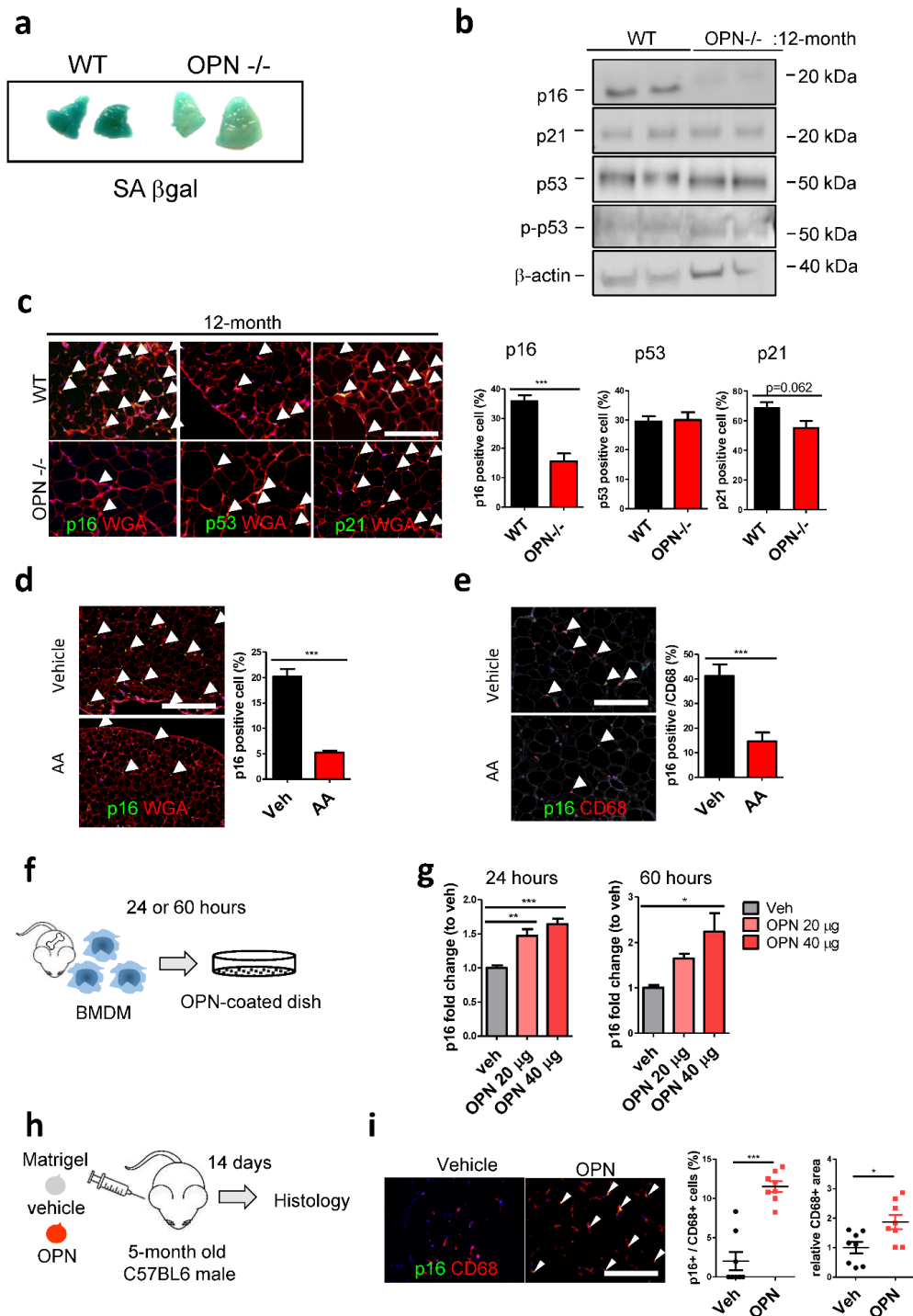
659 **Fig. 1** Aging promotes cellular senescence in white adipose tissue. **a** Representative

660 luminescent images (blue) from 3-month and 12-month old p16-luciferase mice, and dot plots
661 of quantification of whole-body luciferase activity. n=8/21 mice/group. **b** Representative SA- β -
662 Gal staining (blue-green) of epididymal visceral adipose tissue (VAT) from 3-month and 12-
663 month old mice. **c** Quantitative RT-PCR analysis on senescence marker genes expression
664 (whole VAT) normalized to expression levels of 3-month old mice. n=6 mice/group. **d**
665 Representative Western-blot analysis using lysates from 3-month and 12-month VAT. β -actin
666 was used as loading control. **e** Representative immunostaining of VAT (p16/p21/p53: green,
667 wheat germ agglutinin; WGA: red, DAPI: blue), arrow-heads indicate green-positive cells. Bar
668 graphs indicate quantification of positive cell (green) % to total cell number (DAPI). n=5 (p16),
669 4 (p21), 3 (p53) mice/group, scale bar=50 μ m. **f** Barplot presentation illustrating the
670 discriminative power of RT-PCR results for gene expressions of interest. Grouped in 5 ad-hoc
671 categories in relation to the aging, which are represented in the decreasing order of the most
672 discriminant parameter in each of them. **g** Barplot presentation illustrating the most
673 informative gene expression parameters in relation to the aging, and the sense (i.e. positive or
674 negative) of their association with aging. **h** Representative immunostaining of VAT from 3-
675 month and 12-month old WT mice (p16: green, OPN: red, WGA: white, DAPI: blue), arrow-
676 heads indicate green-positive cells. Scale bar=50 μ m. **i** Representative immunostaining of VAT
677 from 3-month and 12-month old WT mice (OPN: red, F4/80: green, DAPI: blue), arrow-heads
678 indicate green and red double-positive cells. Scale bar=50 μ m. **a, c, e** Data show mean \pm s.e.m.
679 **p<0.01, ***p<0.001 by two-tailed unpaired Student's t-test.

680

681

Figure 2. OPN is a critical regulator for VAT senescence

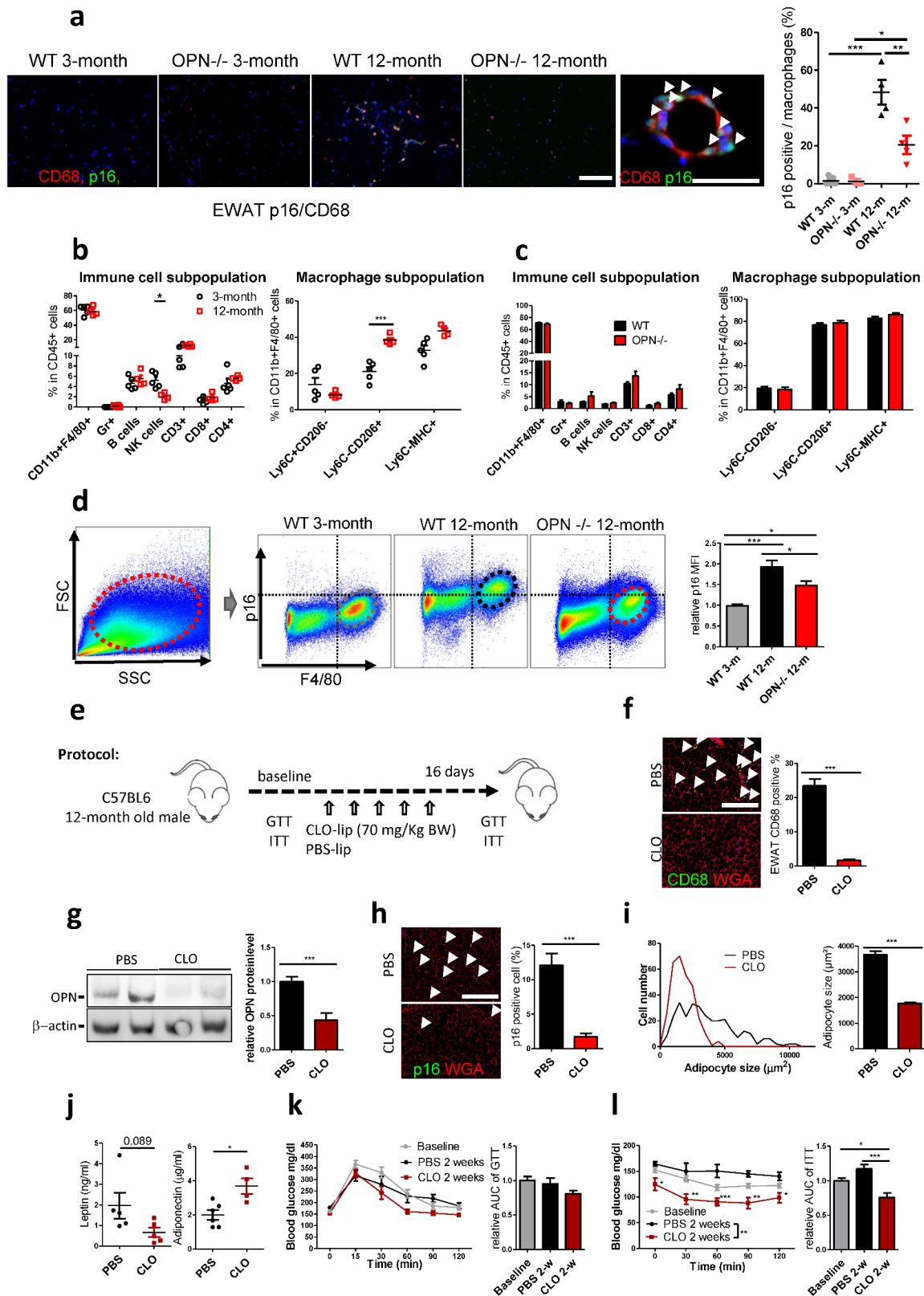


682

683 **Fig. 2** OPN is a critical regulator for VAT senescence. **a** Representative SA-β-Gal staining (blue-
 684 green) of epididymal VAT from 12-month old WT and OPN^{-/-} mice. **b** Representative Western-
 685 blot analysis using lysates from 12-month old WT and OPN^{-/-} mice VAT. β-actin was used as
 686 loading control. **c** Representative immunostaining of VAT (p16: /p21/p53: green, wheat germ
 687 agglutinin; WGA: red, DAPI: blue), arrow-heads indicate green-positive cells. Bar graphs

688 indicate quantification of positive cell (green) % to total cell number (DAPI). n=5 (p16)/3 (p21)/5
689 (p53) mice/group, scale bar=50 μ m. **d** Representative immunostaining of VAT from vehicle or
690 AA treated 12-month old WT mice (p16: green, WGA: red, DAPI: blue), arrow-heads indicate
691 green-positive cells. Bar graphs indicate quantification of positive cell (green) % to total cell
692 number (DAPI). n=5 mice/group, scale bar=50 μ m. **e** Representative immunostaining of VAT
693 from vehicle or AA treated 12-month old WT mice (p16: green, CD68: red, DAPI: blue), arrow-
694 heads indicate green and red double-positive cells. Bar graphs indicate quantification of
695 double-positive cell % to total CD68 positive cell number. n=5 mice/group, scale bar=50 μ m. **f**
696 Schematic protocol of *in vitro* bone marrow-derived macrophage (BMDM) stimulation by OPN.
697 **g** Quantitative RT-PCR analysis on *Cdkn2a* gene expression levels with OPN treatment
698 normalized by the expression levels of vehicle-treated BMDM (veh). BMDM were cultured on
699 vehicle or OPN-coated dish at indicated OPN amount for 24 hours (left-panel) and 60 hours
700 (right-panel). **h** Schematic protocol of *in vivo* Matrigel macrophage recruitment assay. **i**
701 Representative immunostaining of excised Matrigel after 14 days implantation (p16: green,
702 CD68: red, DAPI: blue), scale bar=50 μ m. Quantification of p16 positive cell % to total CD68
703 positive cells (left dot plots), and relative CD68 positive area (right dot plots). n=3 mice/group.
704 **c-e, g, i**, Data show mean \pm s.e.m. *p<0.05, **p<0.01, ***p<0.001 by two-tailed unpaired
705 Student's t-test (**c-e, i**) or one-way ANOVA with Tukey post-test (**g**).
706
707

Figure 3. ATM is a major contributor for AT senescence



708

709

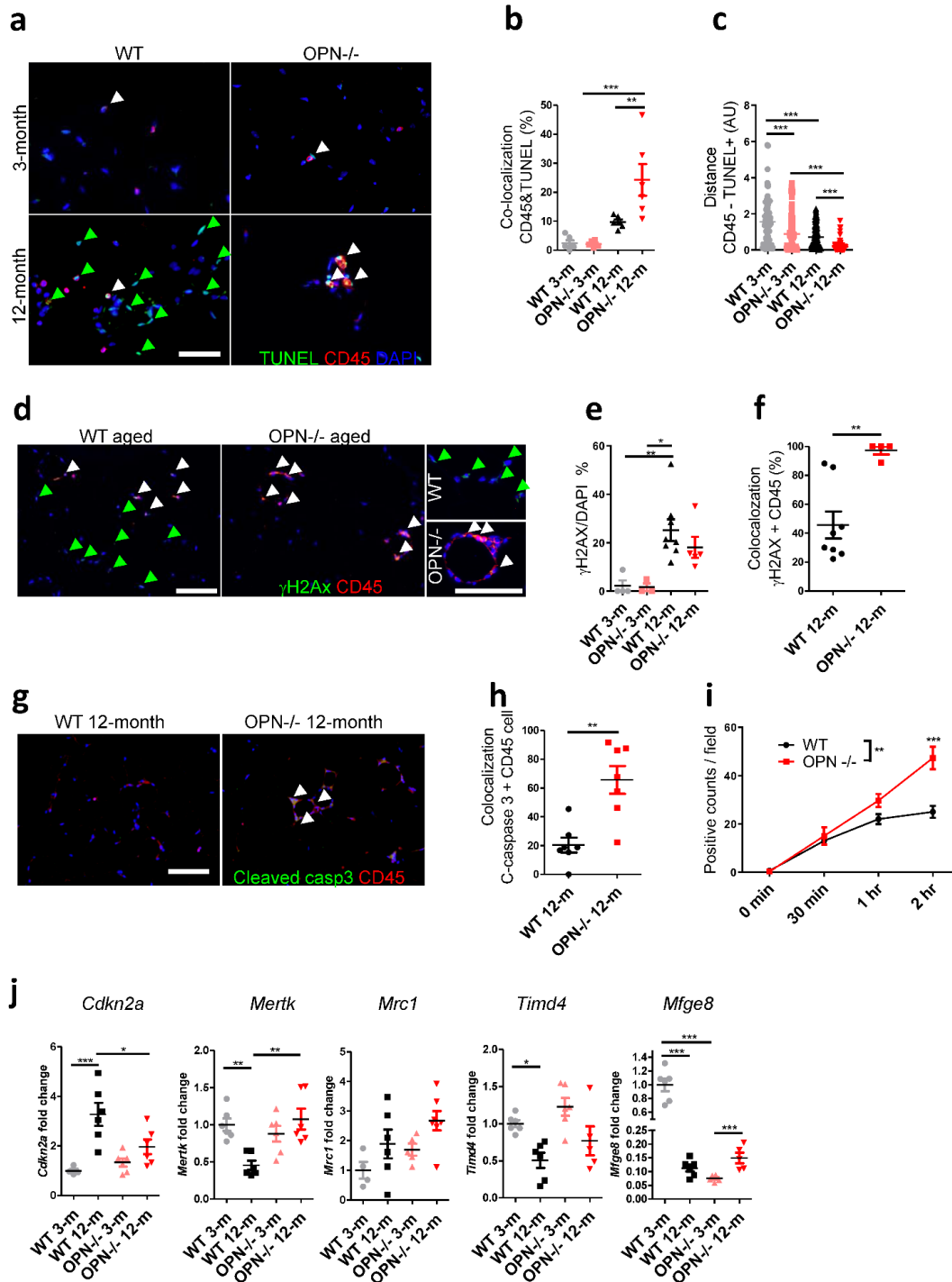
Fig. 3 ATM is a major contributor for AT senescence. **a** Representative immunostaining of VAT

710 from 3-month and 12 months WT and OPN^{-/-} mice (p16: green, CD68: red, DAPI: blue), and
711 quantification of p16 positive cell (green) % in CD68 positive cells (red), arrow-heads indicate
712 green and red double-positive cells. n=4 mice/group, scale bar=50 μ m. **b** Immune cell
713 population and macrophage/monocyte subpopulation in VAT from 3-month (black) and 12-
714 month (red dots) old WT mice. n=5/4 mice/group. **c** Immune cell population and
715 macrophage/monocyte subpopulation in VAT from 8-month old WT and OPN^{-/-} mice. n=5
716 mice/group. **d** Flow cytometry gating strategy to evaluate intracellular p16 protein levels in
717 F4/80+ ATM. Middle panels are representative p16 fluorescent intensity (in dotted circles) in
718 VAT-ATM from 3-month WT and 12-month WT and OPN^{-/-} mice. Right bar graphs denote
719 relative mean fluorescent intensity (MFI) to 3-month WT from 3 independent experiments. **e**
720 Schematic protocol of liposome-clodronate (CLO) treatment. **f** Representative immunostaining
721 of VAT from PBS or clodronate treated 12-month old WT mice (CD68: green, WGA: red, DAPI:
722 blue), and quantification of positive cell (green) % to total cell number (DAPI), arrow-heads
723 indicate green and red double-positive cells. n=4 mice/group, scale bar=50 μ m. **g**
724 Representative Western-blot analysis and densitometric quantification using lysates from VAT
725 subjected to PBS or CLO treatment. β -actin was used as loading control. n=4 mice/group. **h**
726 Representative immunostaining of VAT from PBS or CLO treated 12-month old WT mice (p16:
727 green, WGA: red, DAPI: blue), and quantification of positive cell (green) % to total cell number
728 (DAPI), arrow-heads indicate p16 positive cells. n=4 mice/group, scale bar=50 μ m. **i**
729 Distribution and difference of adipocyte size in VAT from PBS or CLO treated 12-month old
730 WT mice. n=5 mice/group. **j** Plasma adipokine levels by ELISA. n=5 mice/group. **k** Glucose
731 tolerance test and **(l)** insulin tolerance test, temporal plot and area-under-curve (AUC) analysis.
732 n=5 mice/group. **a-d, f-l** Data show mean \pm s.e.m. *p<0.05, **p<0.01, ***p<0.001 by two-tailed
733 unpaired Student's t-test (**b, c, f-j**), one-way ANOVA with Tukey post-test (**a, d, k, l**) or two-way
734 ANOVA with Bonferroni post-test (**k, l**).

735

736

Figure 4. Role of OPN in age-related ATM dysfunction

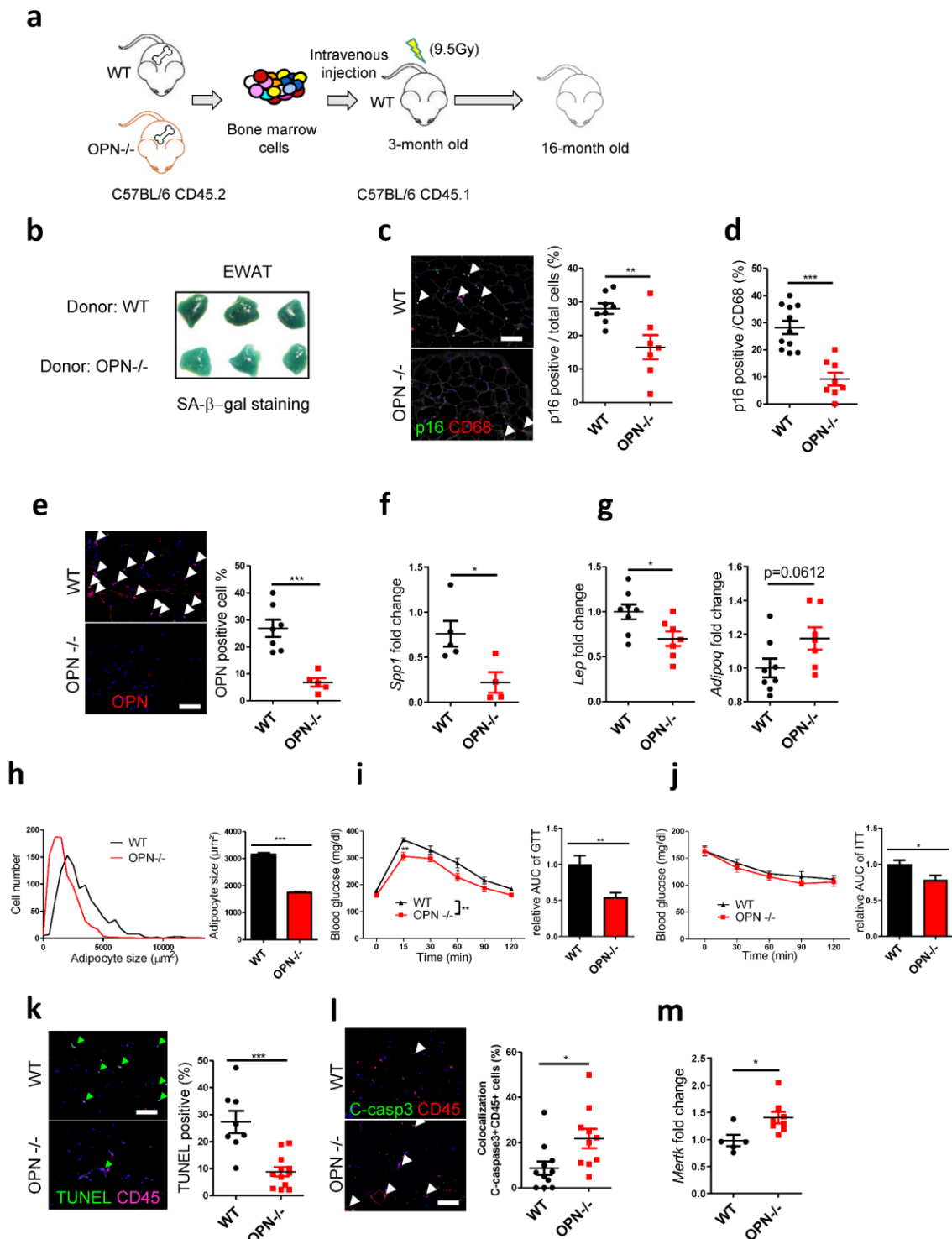


737

738 **Fig. 4** Role of OPN in age-related ATM dysfunction. **a** Representative immunostaining of VAT
 739 from 3- and 12-month WT and OPN^{-/-} mice (TUNEL: green, CD45: red, DAPI: blue). Green
 740 arrow-heads indicate TUNEL single-positive cells, and white arrow-heads indicate TUNEL
 741 and CD45 double-positive cells. Scale bar=50 μm. **b** Quantification of co-localization of TUNEL
 742 and CD45 positive cell % to total cell number. n=3 mice/group. **c** Quantification of distance

743 between TUNEL positive and CD45 positive cells (arbitrary unit). **d** Representative
744 immunostaining of VAT from 12-month WT and OPN^{-/-} mice (γ H2AX: green, CD45: red, DAPI:
745 blue). Green arrow-heads indicate γ H2AX single-positive cells, and white arrow-heads indicate
746 γ H2AX and CD45 double-positive cells. Scale bar=50 μ m. **e** Quantification of γ H2AX positive
747 cell % to total cell number (DAPI). **f** Quantification of co-localized γ H2AX positive and CD45
748 positive cell % to total CD45 positive cell number. n=3 mice/group. **g** Representative
749 immunostaining of VAT from 12-month WT and OPN^{-/-} mice (cleaved caspase-3: green, CD45:
750 red, DAPI: blue), arrow-heads indicate cleaved caspase-3 and CD45 double-positive cells. Scale
751 bar=50 μ m. **h** Quantification of co-localized cleaved caspase-3 positive and CD45 positive cell %
752 to total CD45 positive cell number. n=3 mice/group. **i** Microscopic quantification of fluorescent-
753 positive BMDM incubated with pHrodo-labeled human leukemia cells at indicated time lines
754 from 3 independent experiments. **j** Quantitative RT-PCR analysis (whole VAT) on senescent
755 and efferocytosis-related gene expressions normalized to expression levels of 3-month WT old
756 mice. n=6 mice/group. **b, c, e, f, h-j** Data show mean \pm s.e.m. *p<0.05, **p<0.01, ***p<0.001 by
757 one-way ANOVA with Tukey post-test (**b, c, e, j**), two-tailed unpaired Student's t-test (**f, h**) and
758 two-way ANOVA with Bonferroni post-test (**i**) .
759
760

Figure 5. OPN-deficient bone marrow-derived macrophage attenuates age-related AT senescence, remodeling and dysfunction

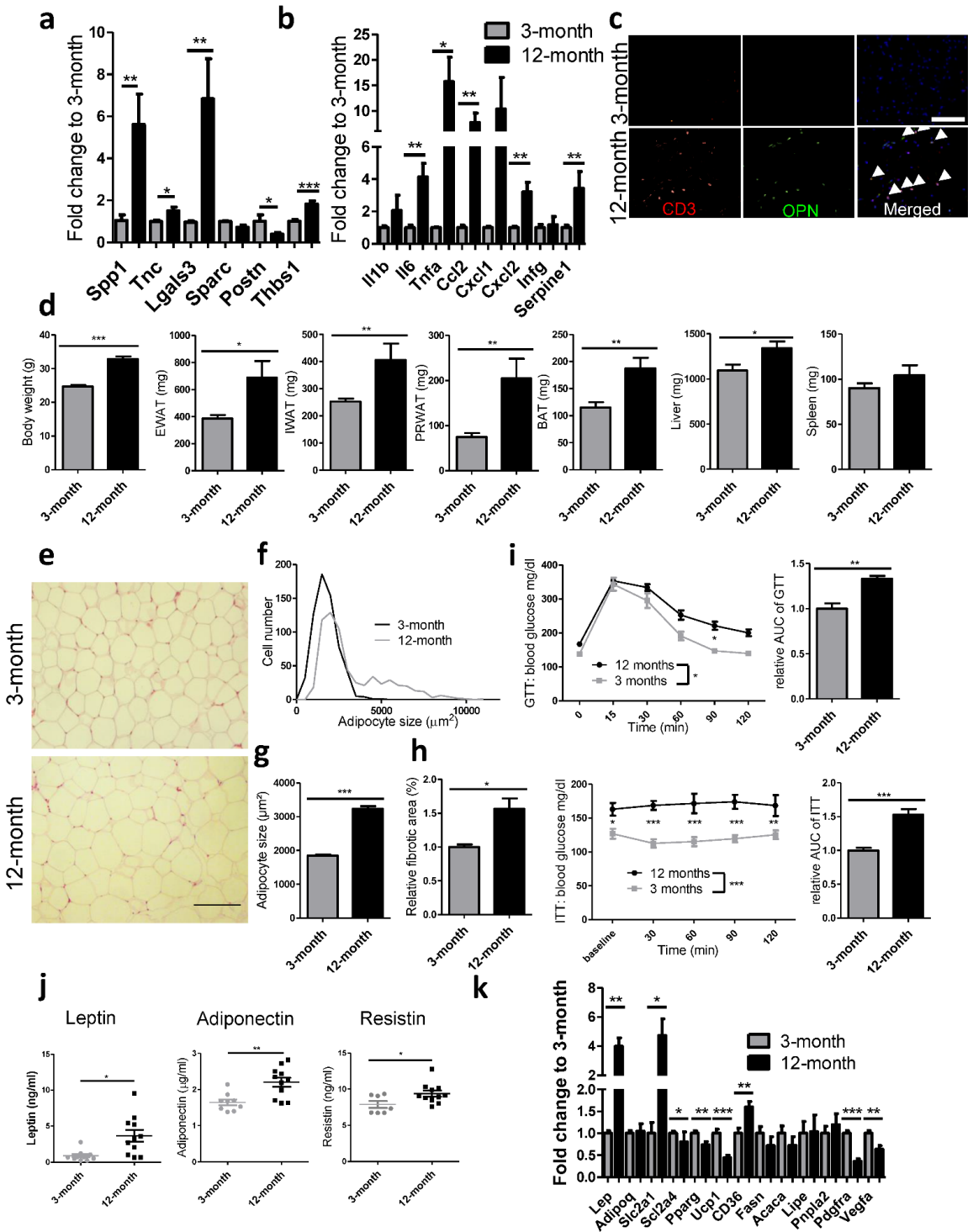


761

762 **Fig. 5** OPN-deficient bone marrow-derived macrophage attenuates age-related AT senescence,
 763 remodeling and dysfunction. **a** Schematic protocol of bone-marrow transplantation (BMT) from
 764 WT or OPN^{-/-} donor to WT recipient to evaluate the effect of OPN-deficient BMDM. **b**

765 Representative SA- β -Gal staining (blue-green) of epididymal VAT. **c** Representative
766 immunostaining of VAT (p16: green, CD68: red, DAPI: blue), arrow-heads indicate p16 and
767 CD68 double-positive cells, and quantification of p16 positive cell (green) % to total cell number
768 (DAPI), n=3 mice/group. Scale bar=50 μ m. **d** Quantification of p16 positive macrophage % to
769 total CD68 positive cell number. n=3 mice/group. Scale bar=50 μ m. **e** Representative
770 immunostaining of VAT (OPN: red, DAPI: blue), arrow-heads indicate OPN positive cells, and
771 quantification of OPN positive cell (red) % to total cell number (DAPI), n=4 mice/group. Scale
772 bar=50 μ m. **f, g** Quantitative RT-PCR analysis (whole VAT) on **(f)** OPN (*Spp1*) and **(g)** adipokine
773 (Leptin: *Lep*, and Adiponectin: *Adipoq*) gene expressions normalized to expression levels of
774 WT-BMT mice. n=8/7 mice/group. **h** Distribution and difference of adipocyte size in VAT from
775 WT or OPN^{-/-} BMT mice. n=5 mice/group. **i** Glucose tolerance test and **(j)** insulin tolerance test,
776 temporal plot and area-under-curve (AUC) analysis. n=9/7 mice/group. **k** Representative
777 immunostaining of VAT from WT or OPN^{-/-} BMT mice with TUNEL staining (TUNEL: green,
778 CD45: red, DAPI: blue), and quantification of TUNEL positive cell % to total cell number.
779 Green arrow-heads indicate TUNEL positive cells. n=4 mice/group. Scale bar=50 μ m. **l**
780 Representative immunostaining of VAT (cleaved caspase-3: green, CD45: red, DAPI: blue),
781 arrow-heads indicate cleaved caspase-3 and CD45 double-positive cells. n=4 mice/group. Scale
782 bar=50 μ m. **m** Quantitative RT-PCR analysis (whole VAT) on *Mertk* gene expressions
783 normalized to expression levels of WT-BMT mice. n=8/7 mice/group. **c-m** Data show mean \pm
784 s.e.m. *p<0.05, **p<0.01, ***p<0.001 by two-tailed unpaired Student's t-test (**b-m**) and two-
785 way ANOVA with Bonferroni post-test (**i, j**).
786

Supplemental Figure 1. Age-related adipose tissue remodeling and dysfunction



788

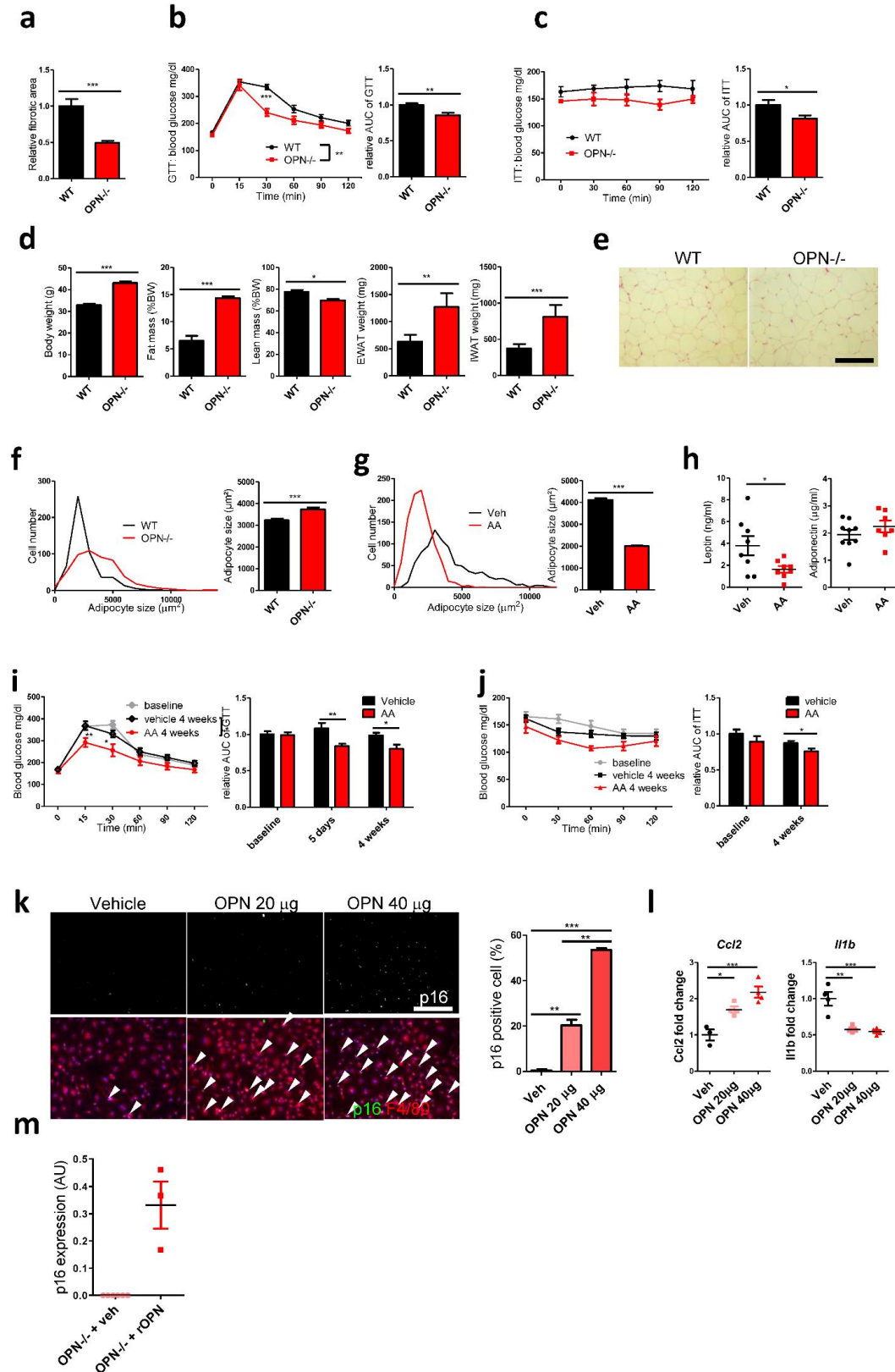
789 **Supplemental Fig. 1** Age-related adipose tissue remodeling and dysfunction. Quantitative RT-
 790 PCR analysis (whole VAT) on (a) matricellular protein and (b) proinflammatory gene
 791 expressions normalized to expression levels of 3-month old mice. n=6 mice/group. c

792 Representative immunostaining of VAT from 3-month and 12-month old WT mice (CD3: red,
793 OPN: green, DAPI: blue), arrow-heads indicate green and red double-positive cells. Scale
794 bar=50 μ m. **d** Body-weight and organ weight from 3-month and 12-month old mice. n=10
795 mice/group. **e** Representative Hematoxylin-Eosin staining of VAT from 3-month and 12-month
796 old mice, scale bar=25 μ m. **f, g** Distribution and difference of adipocyte size in VAT. n=5
797 mice/group. **h** Relative fibrotic area by Sirius-red staining. n=3 mice/group. **i** Glucose tolerance
798 test (GTT) and insulin tolerance test (ITT), temporal plot and area-under-curve (AUC) analysis.
799 n=10/6 mice/group. **j** Plasma adipokine levels by ELISA. n=10/11 mice/group. **k** Quantitative
800 RT-PCR analysis (whole VAT) on metabolism-related or other gene expression levels
801 normalized to expression levels of 3-month old mice. n=6 mice/group. **a, b, d, g-k** Data show
802 mean \pm s.e.m. *p<0.05, **p<0.01, ***p<0.001 by two-tailed unpaired Student's t-test or two-
803 way ANOVA with Bonferroni post-test (**i**).

804

805

Supplemental Figure 2. OPN deficiency attenuates AT remodeling and dysfunction



806

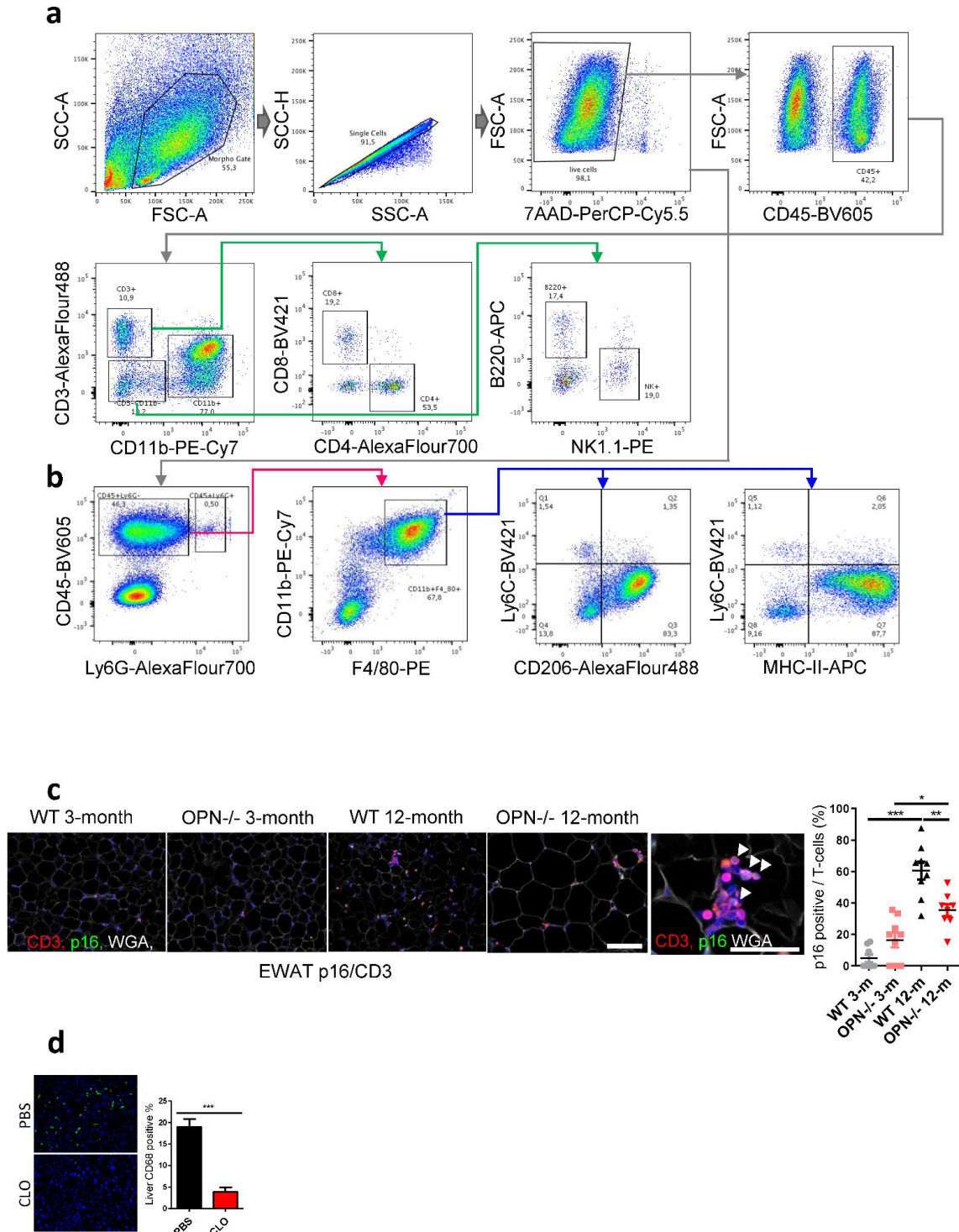
807 Supplemental Fig. 2 OPN deficiency attenuates AT remodeling and dysfunction. **a** Relative

808 fibrotic area by Sirius-red staining. n=7 mice/group. **b** Glucose tolerance test (GTT) and **(c)**
809 insulin tolerance test (ITT) with 12-month old WT and OPN^{-/-} mice, temporal plot and area-
810 under-curve (AUC) analysis. n=6 mice/group. **d** Body-weight and organ weight from 12-month
811 old WT and OPN^{-/-} mice. n=10 mice/group. **e** Representative Hematoxylin-Eosin staining of
812 VAT from 12-months old WT and OPN^{-/-} mice, Scale bar=50 μm. **f** Distribution and difference
813 of adipocyte size in VAT from 12-month old WT and OPN^{-/-} mice. n=5 mice/group. **g**
814 Distribution and difference of adipocyte size in VAT from vehicle- or AA-treated 12-month old
815 WT mice. n=8 mice/group. **h** Plasma adipokine levels by ELISA. n=8 mice/group. **i** GTT and **(j)**
816 ITT, temporal plot and area-under-curve (AUC) analysis from vehicle- or AA-treated 12-month
817 old WT mice. n=8 mice/group. **k** Representative immunostaining of p16 (white spots) of BMDM
818 treated with vehicle or OPN-coated dish at indicated amount (upper panels), and
819 representative merged images of immunostaining (lower panels, p16: green, F4/80: red, DAPI:
820 blue), arrow-heads indicate green and red double-positive cells. Scale bar=50 μm. Bar graphs
821 denote p16 positive cell % to total cell number from 3 independent experiments. **l** Quantitative
822 RT-PCR analysis on *Ccl2* and *Ill1b* gene expression levels with OPN treatment (20 or 40 μg for
823 60 hours) normalized by the expression levels of vehicle-treated BMDM (Veh). **m** Quantitative
824 RT-PCR analysis on *Cdkn2a* gene expression levels with OPN treatment. Dot plots indicate
825 relative expression levels of vehicle- or OPN-treated OPN^{-/-} BMDM. **a-d, f-m** Data show mean
826 ± s.e.m. *p<0.05, **p<0.01, ***p<0.001 by two-tailed unpaired Student's t-test (**a-d, f-j, m**), two-
827 way ANOVA with Bonferroni post-test (**b, c, i, j**), or one-way ANOVA with Tukey post-test (**k,**
828 **l**).

829

830

Supplemental Figure 3. Immune cells are major contributor for AT senescence



831

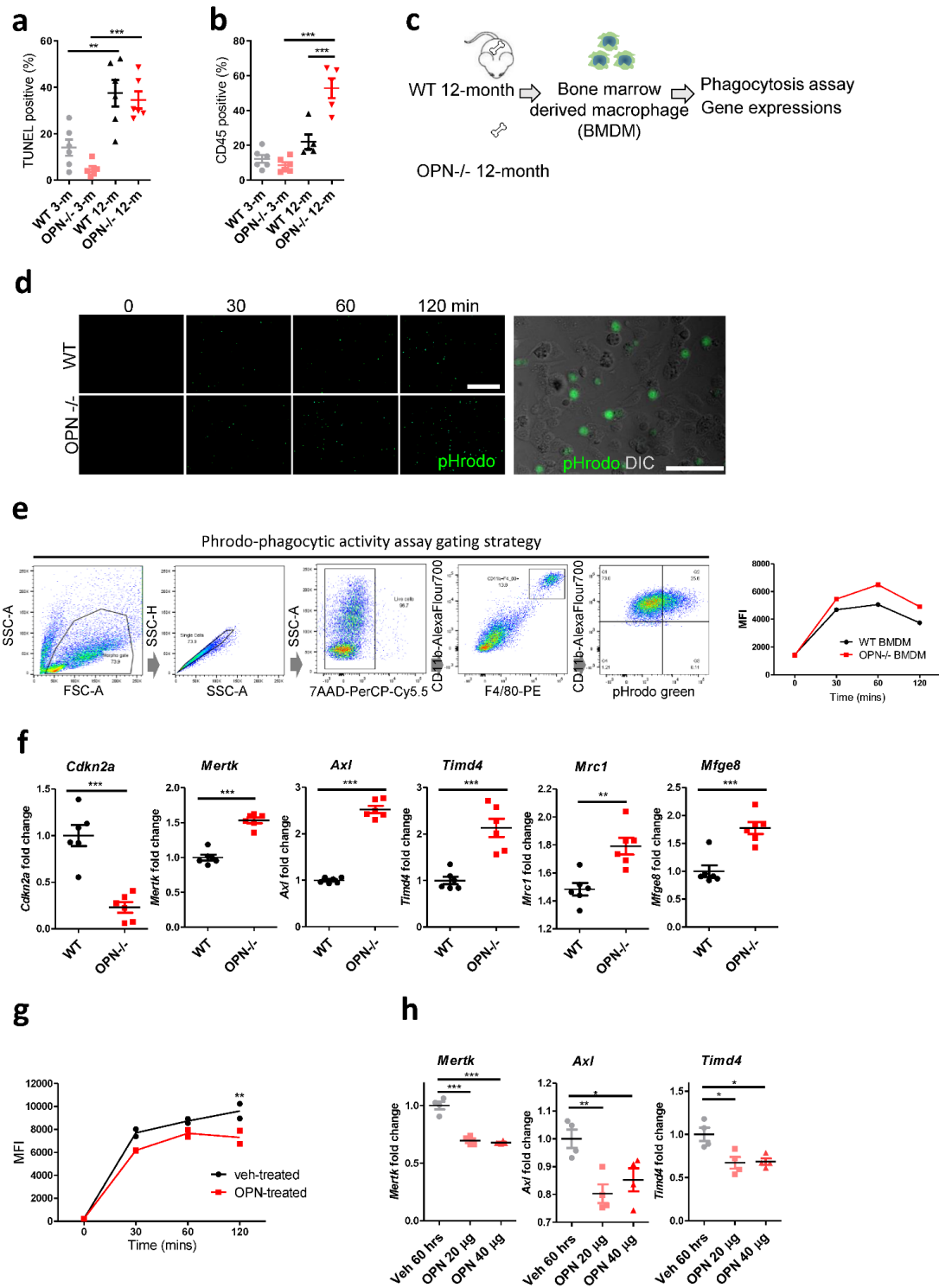
832 **Supplemental Fig. 3** ATM is a major contributor for AT senescence. **a** Flow cytometry gating
 833 strategy for separating immune cell population: CD11b+F4/80+; macrophage, Ly6G+;
 834 neutrophil, B220+; B-cell, NK1.1+; NK cell, CD3+CD4+ or CD8+; T-cell. **b** Flow cytometry
 835 gating strategy for separating macrophage/monocyte subpopulation: CD45+Ly6G-

836 CD11b+F4/80+; macrophage, further separated Ly6C/CD206 and Ly6C/MHC-II. **c**
837 Representative immunostaining of VAT from 3-month and 12-month WT and OPN^{-/-} mice (p16:
838 green, CD3: red, WGA: white, DAPI: blue), and quantification of p16 positive cell (green) % in
839 CD3 positive cells (red), arrow-heads indicate p16 positive cells. n=4 mice/group, scale bar=50
840 μm . **d** Representative immunostaining of liver from PBS or CLO treated 12 months old WT
841 mice (CD68: green, DAPI: blue), and quantification of positive cell (green) % to total cell
842 number (DAPI). n=4 mice/group, scale bar=50 μm . **c, d** Data show mean \pm s.e.m. * $p < 0.05$,
843 ** $p < 0.01$, *** $p < 0.001$ by one-way ANOVA with Tukey post-test (**c**) and two-tailed unpaired
844 Student's t-test (**d**).

845

846

Supplemental Figure 4. Role of OPN in age-related ATM dysfunction



847

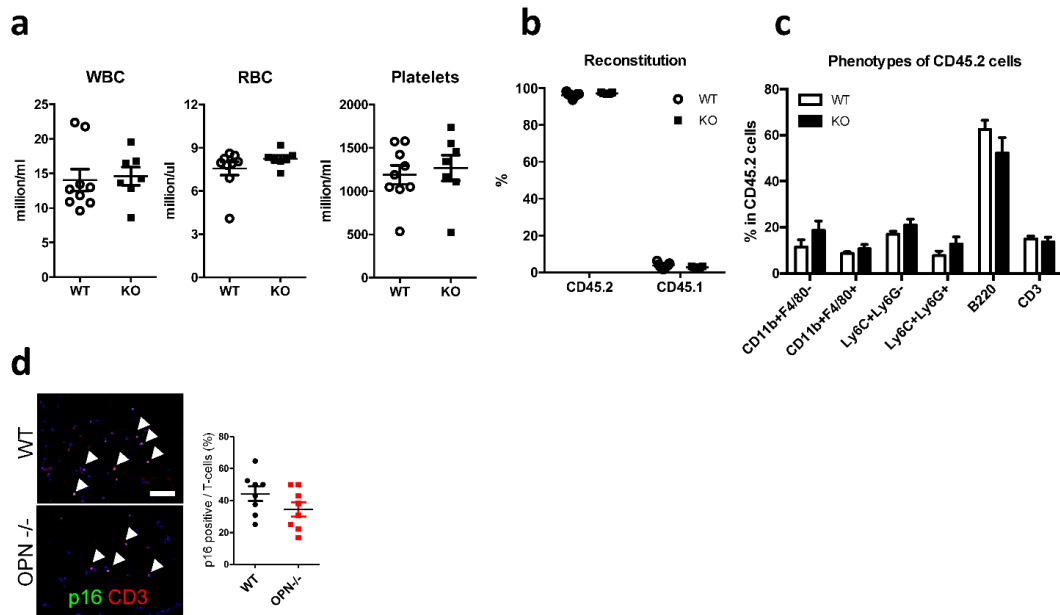
848 **Supplemental Fig. 4** Role of OPN in age-related ATM dysfunction. **a** Quantification of
 849 TUNEL positive cell % to total cell number. **b** CD45 positive cell % to total cell number. **c**
 850 Schematic protocol of in vitro BMDM assays. **d** Representative chronological fluorescent
 851 microscopy images using BMDM and pHrodo-labeled human leukemia cells (Green) and a

852 magnified picture with differential interference contrast image (DIC). Scale bar=50 μ m. **e**
853 Flow cytometry gating strategy of phagocytosis analysis using BMDM and pHrodo-labeled
854 human leukemia cells. Line plots denote chronological quantification of MFI of pHrodo green.
855 **f** Quantitative RT-PCR analysis (BMDM from 12-month WT and OPN^{-/-} mice) on senescence
856 and efferocytosis-related gene expressions normalized to expression levels of WT. n=6
857 mice/group. **g** Flow cytometry analysis of phagocytosis using vehicle- or OPN-treated BMDM
858 and pHrodo-labeled human leukemia cells. Line plots denote chronological quantification of
859 MFI of pHrodo green. **h** Quantitative RT-PCR analysis (vehicle- or OPN-treated BMDM for
860 60 hours) on efferocytosis-related gene expressions normalized to expression levels of vehicle-
861 treated. n=4/group. **a, b, e, f-h** Data show mean \pm s.e.m. **p<0.01, ***p<0.001 by one-way
862 ANOVA with Tukey post-test (**a, b, h**), two-way ANOVA with Bonferroni post-test (**e, g**), and
863 two-tailed unpaired Student's t-test (**f**).

864

865

Supplemental Figure 5. Extracellular OPN induces macrophage senescence



866

867 **Supplemental Fig. 5** OPN-deficient bone marrow-derived macrophage attenuates age-related
 868 AT senescence, remodeling and dysfunction. **a** Peripheral blood count for red blood cells (RBC),
 869 leukocytes (WBC), and platelets at the moment of sacrifice (12 months after reconstitution). **b**
 870 Quantification of CD45.1 or CD45.2 (chimerism) percentage in blood leukocyte population by
 871 flow-cytometry. n=9/7 mice/group. **c** Quantification of blood leukocyte subpopulation defined
 872 by indicated surface markers. n=6 mice/group. **d** Representative immunostaining of VAT from
 873 WT or OPN^{-/-} BMT mice (p16: green, CD3: red, DAPI: blue), and quantification of p16 positive
 874 cell (green) % in CD3 positive cells (red), arrow-heads indicate p16 and CD3 double-positive
 875 cells. n=4 mice/group, scale bar=50 μ m. **a-d** Data show mean \pm s.e.m. Statistical difference was
 876 evaluated by two-tailed unpaired Student's t-test.

877

878 Supplemental table: Used Taqman assays and antibodies

879 Taqman assays

Target gene	Taqman assay ID	Target gene	Taqman assay ID
<i>Cdkn2a</i>	Mm00494449_m1	<i>Acaca</i>	Mm01304257_m1
<i>Cdkn1a</i>	Mm04205640_g1	<i>Pparg</i>	Mm00440940_m1
<i>Tp53</i>	Mm01731290_g1	<i>Pnpla2</i>	Mm00503040_m1
<i>Mfge8</i>	Mm00500549_m1	<i>Adipoq</i>	Mm00456425_m1
<i>Timd4</i>	Mm00724709_m1	<i>Il6</i>	Mm00446190_m1
<i>Mertk</i>	Mm00434920_m1	<i>Tnf</i>	Mm00443258_m1
<i>Mrc1</i>	Mm01329362_m1	<i>Mif</i>	Mm01611157-g1
<i>Spp1</i>	Mm00436767_m1	<i>Serpine1</i>	Mm00435858_m1
<i>Thbs1</i>	Mm01335418_m1	<i>Vegfa</i>	Mm01283063_m1
<i>Sparc</i>	Mm00486332_m1	<i>Il12b</i>	Mm01288989
<i>Lgals3</i>	Mm00802901_m1	<i>Cxcl2</i>	Mm00436450_m1
<i>Tnc</i>	Mm00495662_m1	<i>Ccl2</i>	Mm00441242_m1
<i>Postn</i>	Mm00450111_m1	<i>Cxcl1</i>	Mm04207460_m1
<i>Pdgfra</i>	Mm01205760_m1	<i>Ihnb</i>	Mm03023992_m1
<i>Lep</i>	Mm00434759_m1	<i>Tgfb1</i>	Mm01178820_m1
<i>Cd36</i>	Mm00432403_m1	<i>Il12a</i>	Mm00434169_m1
<i>Slc2a1</i>	Mm00441480	<i>Cxcl5</i>	Mm00436451_g1
<i>Ucp1</i>	Mm01244861_m1	<i>Csf2</i>	Mm01290062
<i>Pgc1a</i>	Mm01208835_m1	<i>Csf1</i>	Mm00432686
<i>Slc2a4</i>	Mm00436615_m1	<i>Il1b</i>	Mm00434228_m1
<i>Plin1</i>	Mm00558672_m1	<i>Infg</i>	Mm01168134_m1
<i>Fasn</i>	Mm00662319_m1	<i>Actb</i>	Mm02619580_g1
<i>Lipe</i>	Mm00495359_m1	<i>Axl</i>	Mm00437221_m1

880 Antibodies used for immunohistochemistry and western-blot analysis

Target protein	Clone/product number	Company	Application/concentration
p16	2D9A12/ab54120	abcam	IF: 200 ⁻¹
p16	polyclonal/250804	Abbiotec	IF: 200 ⁻¹ , WB: 200 ⁻¹
p21	HUGO291	EuroMabNet	IF: 200 ⁻¹ , WB: 500 ⁻¹
p53	polyclonal/ab31333	abcam	IF: 200 ⁻¹ , WB: 500 ⁻¹
phospho-p53 (Ser15)	polyclonal/9284	Cell Signaling	WB: 1000 ⁻¹
Osteopontin	polyclonal/ab8448	abcam	IF: 200 ⁻¹ , WB: 500 ⁻¹
F4/80	A3-1/MCA497GA	Serotec	IF: 200 ⁻¹
β-actin	AC-15/ab49900	abcam	WB: 5000 ⁻¹
Wheat germ agglutinin	W11261	Invitrogen	IF: 200 ⁻¹

CD68	polyclonal/ab125212	abcam	IF: 200 ⁻¹
CD3	polyclonal/ab5690	abcam	IF: 200 ⁻¹
CD45	30-F11/550539	BD Pharmingen	IF: 200 ⁻¹
GammaH2A.X(phosphoS140)	3F2/ab22551	abcam	IF: 200 ⁻¹
Cleaved caspase3	5A1E/9664	Cell Signaling	IF: 200 ⁻¹

881

882 **Antibodies and reagents used for flow-cytometry and cell-sorting**

883

Antibodies or Reagents	Clone	Isotype	Source	Identifier
Brilliant Violet 605™ anti-mouse CD45	30-F11	Rat IgG2b, k	Biologend	103155
APC/Cyanine7 anti-mouse CD45.2	104	Mouse IgG2a, κ	Biologend	109823
Brilliant Violet 605™ anti-mouse CD45.1	A20	Mouse IgG2a, κ	Biologend	110737
PE/Cy7 anti-mouse/human CD11b	M1/70	Rat IgG2b, k	Biologend	101216
PE anti-mouse F4/80	BM8	Rat IgG2a, k	Biologend	123110
Alexa Fluor® 700 anti-mouse Ly-6G	1A8	Rat IgG2a, k	Biologend	127622
APC anti-mouse I-Ab	AF6-120.1	Rat IgG2a, k	Biologend	116418
Brilliant Violet 421™ anti-mouse Ly-6C	HK1.4	Rat IgG2c, k	Biologend	128031
<u>Brilliant Violet 785™ anti-mouse CD11c</u>	<u>N418</u>	<u>A. Hamster IgG</u>	<u>Biologend</u>	<u>117335</u>
FITC anti-mouse CD206	MR5D3	Rat IgG2a, k	Thermofisher Scientific	MA5-16870
Brilliant Violet 650™ anti-mouse CD206 (MMR)	C068C2	Rat IgG2a, k	Biologend	141723
APC/Cyanine7 anti-mouse CD3	17A2	Rat IgG2b, k	Biologend	100222
FITC anti-mouse CD3 ε	145-2C11	A. Hamster IgG	Biologend	100305
Alexa Fluor® 700 anti-mouse CD4	RM4-4	Rat IgG2b, k	Biologend	116021
Brilliant Violet 421™ anti-mouse CD8a	53-6.7	Rat IgG2a, k	Biologend	100737
APC anti-mouse/human CD45R/B220	RA3-6B2	Rat IgG2a, k	Biologend	103212
PE anti-mouse NK-1.1	PK136	Rat IgG2a, k	Biologend	108707
PE Rat IgG1, κ Isotype Ctrl	RTK2071		Biologend	400408
PE/Cy7 Rat IgG2b, κ Isotype Ctrl	RTK4530		Biologend	400617
FITC Rat IgG2a, κ Isotype Ctrl	RTK2758		Biologend	400505
APC Rat IgG2b, κ Isotype Ctrl	RTK4530		Biologend	400611
APC/Cy7 Rat IgG2a, κ Isotype Ctrl	RTK2758		Biologend	400523
Brilliant Violet 421™ Isotype Ctrl	TRK2758	Rat IgG2a, κ	Biologend	400535
Brilliant Violet 605™ Isotype Ctrl	RTK4530	Rat IgG2b, κ	Biologend	400649
Brilliant violet 650 isotype control	RTK2758	Rat IgG2a, k	Biologend	400541

Brilliant Violet 785™ Isotype Ctrl	HTK888	A. Hamster IgG	Biolegend	400947
Rat IgG2B Alexa Fluor® 700-conjugated	141945		R&D	IC013N
TruStain FcX™ (anti-mouse CD16/32)	93		Biolegend	101320
7-aminoactinomycin D (7-AAD)			In vitrogen	A1310
OneComp eBeads			In vitrogen	01-1111-42

884

885

886

887

STUDY 3

ETUDE 3

Résumé

Dans le contexte de l'obésité, une accumulation de cellules sénescentes est observée au niveau du tissu adipeux et présente un lien avec l'insulino-résistance caractérisant le tissu adipeux dans le contexte de l'obésité mais les mécanismes sous-jacents sont encore mal connus. L'objectif de cette étude est d'évaluer et de caractériser la sénescence du TA durant la phase d'initiation de l'obésité ainsi que d'étudier et de comprendre le rôle des mitochondries dans ce processus.

Pour ce faire, des modèles murins (sauvages et mutants : souris transgénique P16-luciférase) et cellulaires (préadipocytes primaires) ont ainsi été utilisés et différents traitements ont été effectués (traitement des souris avec un régime riche en graisse et/ou exercice physique, traitement des cellules avec de l'ATP, traitement des souris et des cellules avec de l'allopurinol qui bloque la dégradation de l'ATP).

Les résultats obtenus ont démontré que la sénescence du tissu adipeux est un évènement précoce au cours de l'obésité induite par un régime riche en graisse et que cette sénescence était concomitante avec une augmentation de l'activité glycolytique et mitochondriale, et donc une augmentation de la production d'ATP au sein du tissu adipeux viscéral. De plus, l'ATP a été identifié comme facteur induisant la sénescence du TA étant donné que les traitements avec l'ATP et l'allopurinol induisent la sénescence du tissu adipeux et des préadipocytes. Enfin, l'exercice physique a permis de réduire les concentrations d'ATP, tout comme la sénescence dans le tissu adipeux et d'améliorer ainsi les paramètres métaboliques initialement perturbés au cours de l'obésité.

Adipose tissue senescence is mediated by increased ATP content after a short-term high fat diet exposure

Maria Pini PhD^{1,*}, Gabor Czibik MD, PhD^{1,*}, Daigo Sawaki MD, PhD^{1,*}, Zaineb Mezdari MS¹, Laura Braud PhD², Julien Ternacle MD, PhD^{1,3}, Raquel Mercedes MD¹, Cécile Martel PhD⁴, Nelly Buron PhD⁴, Geneviève Marcelin PhD⁵, Annie Borgne-Sanchez PhD⁴, Roberta Foresti PhD², Roberto Motterlini PhD², Corneliu Henegar MD, PhD¹, Geneviève Derumeaux MD, PhD¹

¹ INSERM U955, Université Paris-Est Créteil (UPEC), AP-HP, Department of Physiology, Henri Mondor Hospital, FHU SENE C 94100 Créteil, France

² INSERM U955, Université Paris-Est Créteil, Faculty of Medicine, IMRB, F-94010 Créteil, France

³ AP-HP, Department of Cardiology, Henri Mondor Hospital, FHU SENE C, Créteil, France

⁴ Mitologics S.A.S., Université Paris-Est Créteil (UPEC), Créteil, France

⁵ Sorbonne Universities, INSERM UMR_S 1269, Nutriomics, F-75013, Paris, France

*Authors equally contributed to the work

Address for correspondence:

Maria Pini, INSERM U955 Université Paris-Est Créteil (UPEC), 51 Av de Lattre de Tassigny 94100 Créteil, France, Tel : +33 7 60 63 80 30 E-mail: maria.pini@inserm.fr

Geneviève Derumeaux, INSERM U955 Université Paris-Est Créteil (UPEC), 51 Av de Lattre de Tassigny 94100 Créteil, France, Tel: +33 1 49 81 Fax: +33 1 49 81 26 67 Email: genevieve.derumeaux@inserm.fr

Suggested running title:

Adipose tissue senescence and high fat diet

Keywords: obesity, exercise, adipose tissue senescence, preadipocytes, bioenergetics, ATP, xanthine oxidase

ABSTRACT

In the context of obesity, senescent cells accumulate in white adipose tissue (WAT). The cellular underpinnings of WAT senescence leading to insulin-resistance are not fully elucidated. The objective of the current study was to evaluate the presence of WAT senescence early after initiation of high fat diet (HFD, 1 to 10 weeks) in 5-months-old male C57BL/6J mice and the potential role of mitochondria.

We first showed that WAT senescence occurred 2 weeks after HFD as evidenced in whole WAT by increased senescence-associated β -galactosidase activity and cyclin-dependent kinase inhibitor 2A expression. WAT senescence affected various WAT cell populations, including preadipocytes, adipose tissue progenitors and immune cells, together with adipocytes. WAT senescence was associated with a higher glycolysis and mitochondrial activity leading to enhanced ATP content in HFD-derived preadipocytes, as compared with chow diet-derived preadipocytes. One-month daily exercise, introduced 5 weeks after HFD, was an effective senostatic strategy, since it reversed WAT cellular senescence, while decreasing glycolysis and production of ATP. Interestingly, the beneficial effect of exercise was independent of body weight and fat mass loss.

We demonstrated that WAT cellular senescence is one of the earliest events occurring after HFD initiation and is intimately linked to the metabolic state of the cells. Our data uncover the critical role of HFD-induced elevated ATP as a local danger signal initiating WAT senescence. Exercise exerts beneficial effects on adipose tissue bioenergetics in obesity, reversing cellular senescence and metabolic abnormalities.

INTRODUCTION

White adipose tissue (WAT) senescence has emerged as an important contributor to the development of comorbidities associated with obesity (Ahima, 2009; Tchkonina et al., 2010) and aging (Xu et al., 2018). Our group has recently highlighted the impact of WAT senescence on cardiac disorders in the context of aging (Sawaki et al., 2018) and obesity (Ternacle et al., 2017), strengthening evidence that WAT can develop a senescence-associated secretory phenotype (SASP) that entails the release of various profibrotic and pro-inflammatory proteins (Campisi, 2005; Coppe et al., 2008; Munoz-Espin and Serrano, 2014) and contribute to spreading the senescence to remote organs (Tchkonina et al., 2010). Release of bioactive lipids by WAT may additionally affect the senescence phenotype (Das, 2019). Cellular senescence is a fundamental process that drives aging and its consequences, such as frailty and the development of chronic diseases, leading to multi-morbidity and increasing mortality worldwide (McHugh and Gil, 2018). Senescence involves an irreversible arrest of the cell cycle, followed by increased expression of SASP and altered metabolic activity. The accumulation of senescent cells in multiple tissues is central to the pathogenesis of age-related diseases. Therefore, senolytic strategies targeting fundamental aging processes (Baker et al., 2016; Baker et al., 2011; Xu et al., 2018) and metabolic dysfunction (Palmer et al., 2019) are now extensively investigated. Importantly, exercise and physical activity were shown to attenuate progression of age-related disorders (Derumeaux et al., 2008), and also obesity and HFD-induced cardiometabolic disorders (Schafer et al., 2016).

Despite intensive investigation on the role of WAT in metabolic diseases, the timeline and the underlying mechanisms of WAT senescence have not been fully explored in the context of obesity. A better understanding of these processes could help developing effective strategies targeting senescent cells and preventing obesity-related tissue deterioration. Mitochondrial dysfunction and impairment of adenosine triphosphate (ATP) production are critical in the

pathogenesis of obesity-associated diseases and mitochondria are also fundamental in the regulation of fatty acid metabolism, energy expenditure and disposal of reactive oxygen species (ROS) (Lefranc et al., 2019; Lowell and Shulman, 2005). Notably, ATP released by malfunctioning mitochondria to extracellular space during cell death or from senescent cells is recognized as part of damage-associated molecular patterns (DAMP), molecules that induce inflammatory response and are critically involved in the pathogenesis of several diseases (Basisty et al., 2020; Nakahira et al., 2015). Therefore, the potential role of mitochondrial alterations in obesity-induced WAT senescence and their modulation by physical exercise remains to be elucidated. Here we hypothesized that energetic abundance in caloric overload leads to overproduction of ATP, contributing to the induction of senescence.

We used a short-term high fat diet (HFD, 1 to 10 weeks) versus a chow diet (CD) exposure in adult mice (5 months old) to follow the time-course of senescence induction in WAT and the impact on glucose homeostasis. We then used physical exercise as a senostatic strategy to investigate whether metabolic alterations were reversed together with WAT senescence in the context of ongoing HFD. Since mitochondria are at the nexus of both metabolic and aging associated disorders (Correia-Melo et al., 2016; Tavallaie et al., 2020), we investigated mitochondrial function in WAT and primary adipocytes.

We demonstrate here that WAT senescence: 1) occurred as early as 2 weeks of HFD in both subcutaneous (inguinal, iWAT) and visceral (epididymal, eWAT) WAT preceding the development of chronic systemic inflammation and WAT fibrosis; 2) was associated with increased WAT glycolytic and mitochondrial activity leading to increased local ATP.

We identified the role of ATP as a causal mechanism of WAT senescence by demonstrating that liposome-delivered ATP induced preadipocyte senescence *in vitro*, whilst inhibition of ATP degradation by allopurinol amplified WAT senescence in both *in vitro* and

in vivo experiments. Furthermore, short-term exercise decreased preadipocyte ATP content in iWAT but not in eWAT and, concomitantly prevented HFD-induced WAT senescence.

RESULTS

WAT cellular senescence occurs shortly after initiation of HFD

In order to assess the kinetic of WAT senescence after the initiation of HFD, we followed the animals during a 10-week time course and focused the analysis on eWAT. In parallel with an increase of body weight, fat mass and leptin expression (Fig. S1A), WAT senescence occurred as early as 2 weeks after the initiation of HFD, as demonstrated by a gradual increase in SA- β -galactosidase (SA- β -Gal) activity (Fig. 1A), progressive upregulation of p16 (cyclin dependent inhibitor 2A, Cdkn2a) and p21 (cyclin dependent inhibitor 1A, Cdkn1a) (Fig. 1B) and higher proportion of p16- and p21-positive cells in the adipocyte precursor pool (PDGFR α ⁺ cells) (Fig. 1C). This resulted in increased WAT senescence as assessed *in vivo* by a 10-week HFD intervention in p16^{LUC}/⁺ mice, demonstrating increased bioluminescence in the abdominal cavity area, in relation to the activation of p16INK4a (Fig. 1D).

Since obesity may compromise mitochondrial homeostasis (Lefranc et al., 2019), we next investigated mitochondrial function to assess its contribution to cellular senescence. During the first five weeks following HFD initiation, we found no evidence of mitochondrial dysfunction based on the assessment of mitochondrial genes (cytochrome C and Tfam), citrate synthase activity and activity of respiratory complexes, such as complex IV (cytochrome C oxidase) and complex V (ATP synthase) (Fig. S1B-C). In addition, we found no evidence for oxidative DNA damage (anti-8-oxoguanine staining), despite a modest increase in

mitochondrial ROS (MitoSOX), but not cytosolic ROS (CellROX), in both iWAT and eWAT HFD-derived preadipocytes compared with CD preadipocytes (Fig. S1D).

We then assessed the beneficial effect on WAT remodeling of an exercise intervention (daily swimming) initiated after 5 weeks of HFD in comparison with sedentary HFD and CD animals (Fig. S1E). To avoid the confounding effect of body weight loss with exercise, we selected mice with similar body weight (Fig. S1F) and fat mass (Fig. 1E) in each regimen group. As expected, HFD progressively increased body weight (Fig. S1F), adiposity (Fig. 1E) and adipocyte size in both iWAT and eWAT (Fig. S1G-H). Exercise reduced adipocyte size in both WAT depots and iWAT weight (Fig. S1G-H and Table S1), without altering the food intake (CD-SED 2.8 ± 1 g/day vs. CD-EX 3.4 ± 0.6 g/day, $p = \text{NS}$ and HFD-SED 3.7 ± 1.0 g/day vs. HFD-EX 3.7 ± 1.2 g/day, $p = \text{NS}$). Although 10-weeks HFD did not induce WAT fibrosis compared to CD (Fig. S1I-K), it increased the expression of key profibrotic factors such as transforming growth factor $\beta 1$ (Tgfb1), fibronectin (Fn1) and tissue inhibitor of metalloproteinase 1 (Timp1) in eWAT but not in iWAT (Fig. S1L). Exercise significantly reduced the expression of these profibrotic factors in eWAT of HFD animals.

Also, HFD increased leptin and decreased adiponectin levels in both plasma and tissue (Fig. S1M-N). Despite similar body weight, exercise decreased plasma leptin levels in HFD mice and increased plasma adiponectin levels in CD but not in HFD mice. Additionally, HFD impaired glucose tolerance (GTT) and insulin sensitivity (ITT) (Fig. S1O-P) whilst exercise improved them in HFD mice.

In parallel, the adipogenic function declined early in HFD mice as demonstrated by the downregulation of markers of lipogenesis (fatty acid synthase, Fasn) and lipolysis (perilipin 1, Plin1) in both iWAT and eWAT (Fig. S1Q). HFD also impaired glucose metabolism as shown by a decreased expression of insulin-sensitive glucose transporter (solute carrier family 2

member 4, *Slc2a4*) and hormone insulin-like growth factor 1 (*Igf1*) mRNA in both WAT depots (Fig. S1R).

We next focused on the impact of exercise on WAT senescence. Whilst SA- β -Gal activity was increased after 10 weeks of HFD in both WAT and preadipocytes, it was fully normalized by exercise (Fig. 1F-I).

HFD induces cellular senescence in various types of WAT cells, out of systemic inflammation.

Having demonstrated a HFD-induced SA- β -Gal activity in WAT, we then explored additional markers of cellular senescence. First, HFD increased p21 expression in both iWAT and eWAT when p16 was upregulated only in eWAT (Fig. 2A). Exercise decreased only p21 in the iWAT depot (Fig. 2A). Then we assessed p16 and p21 expression in preadipocytes after verifying that senescence was not influenced by culture conditions prior to differentiation (Fig. S2A). HFD upregulated p16 and p21 expression in eWAT- but not in iWAT-derived preadipocytes, whilst exercise normalized it (Fig. 2B). Furthermore, a 10-week HFD increased p16⁺/PDGFR α ⁺ by 6-fold in iWAT and 9-fold in eWAT (Fig. 2C). Similarly p21⁺/PDGFR α ⁺ increased by 4-fold in iWAT and 5.5-fold in eWAT (Fig. 2D). Interestingly, exercise blunted senescence in both WAT depots (Fig. 2C-D). In addition, WAT senescence was associated with adipocyte hypertrophy (Fig. S2B). HFD also increased the number of crown-like structures (CLS, 15-fold in eWAT vs. 3-fold in iWAT) - immune cells surrounding dying adipocytes (Fig. S2C). Both CD45⁺ and CD45⁻ cells exhibited a senescent phenotype, as demonstrated by an increase in the S139 phosphorylated form of γ H2A.X expression - a marker of double-stranded DNA break and senescence (Vergoni et al., 2016) - in HFD, but was ameliorated by exercise (Fig. S2C-D). Furthermore, HFD increased p16⁺ co-localization with both iWAT and eWAT Mac3⁺ macrophages whilst exercise normalized it (Fig. S2E). By contrast, p21⁺ co-localization with

macrophages increased only in eWAT and was not normalized with exercise (Fig. S2F). A similar pattern was observed with p16 staining in eWAT lymphocytes (Fig. S2G).

Remarkably, WAT senescence occurred without systemic inflammation as plasmatic levels of proinflammatory factors [C-C-Chemokine-Ligand (CCL2), tumor necrosis factor α (TNF α), interleukin 6 (IL6), interleukin 10 (IL10)] were undetectable. Despite upregulation of *Mcp1/Ccl2* in eWAT but not iWAT (Fig. S2H), HFD did not significantly increase proinflammatory factors in eWAT secretome (Fig. S2I).

To better discriminate the individual importance of the factors involved in the HFD-driven alteration of WAT, we applied a supervised predictive model to a panel of transcriptional descriptors selected to illustrate adipocyte function, senescence, inflammation and tissue remodeling in iWAT (Fig. 2E) and eWAT (Fig. 2F). Interestingly, the best predictors of HFD-induced changes in eWAT were leptin and the chemotaxis marker *Ccl2*, followed closely by the senescence marker *p21*, while leptin increase was the main change occurring in iWAT.

Altogether, these data reveal that, WAT cellular senescence induced by HFD affects multiple cell populations of adipogenic and immune origins in both depots, is rescuable by exercise and precedes systemic inflammation.

HFD-induced WAT senescence is associated with increased adipocyte bioenergetics.

We next assessed whether a 10-week HFD intervention compromised mitochondrial homeostasis and whether exercise exerted beneficial effects on WAT bioenergetics (Stanford et al., 2015). Mitochondrial biogenesis and oxidative metabolism in WAT were impaired by HFD (Fig. S3A-B). The expression of the master regulators of mitochondrial biogenesis, peroxisome proliferator-activated receptor gamma coactivator 1-alpha (*Pgc1 α*) and its downstream genes, were downregulated by HFD in both WAT depots and preadipocytes (Fig. S3A). HFD also downregulated genes related to fatty acid oxidation, such as peroxisome

proliferator-activated receptor alpha (Ppar α) and related genes in both WAT and preadipocytes (Fig. S3B). HFD increased iWAT and eWAT mitochondrial content as assessed by immunofluorescence staining of a mitochondria-specific marker, Tom20 (Fig. 3A) with unaltered citrate synthase activity in whole WAT (not shown) and in mature adipocytes (Fig. 3B). Exercise normalized mitochondrial content, blunted HFD-induced mitochondrial biogenesis alterations and upregulated genes related to WAT browning (Pgc1 α , Prdm16, and Ucp1) in iWAT (Fig. 3A-B; Fig. S3A-B). We further assessed mitochondrial expression profile in eWAT and found the HFD-induced downregulation of several genes related to mitochondrial homeostasis, beta-oxidation, morphogenesis (fission/fusion, autophagy and apoptosis), as illustrated by a heatmap representation of their expression profiles (Fig. S3C). These changes were associated with the downregulation of mitofusin2 (Mfn2) in both WAT (Fig. S3D).

Next, we analyzed mitochondrial oxygen consumption (OCR) and glycolytic activity (extracellular acidification rate, ECAR) in real time by the Seahorse technology in preadipocytes (Fig. S3E-F). HFD increased mitochondrial and non-mitochondrial OCR in preadipocytes derived from both WAT depots (Fig. 3C). In addition, HFD enhanced glycolysis (ECAR) in both WAT depots, while exercise restored it only in iWAT (Fig. 3D).

Interestingly, ATP-linked oxygen consumption was increased by HFD in preadipocytes from both iWAT and eWAT, suggesting a higher respiratory chain and ATP synthase activity (Fig. 3E). Accordingly we found a higher ATP content in preadipocytes derived from both WAT depots in HFD sedentary mice, whilst exercise reduced ATP content in iWAT but not eWAT, drawing our attention to potential differences in the purine catabolism pathway between the two fat depots (Fig. 3 F, G). Thus, we explored the first and only unidirectional purine catabolic enzyme, xanthine oxidase (XO), which catalyzes the oxidation of hypoxanthine to xanthine, and of xanthine to uric acid. Interestingly, XO protein level was considerably higher in iWAT than in eWAT, without any impact of diet- or exercise-intervention (Fig. 3H). This finding was

further confirmed by the increased XO staining of primary iWAT- versus eWAT-derived preadipocytes (Fig. 3I). As a consequence, plasmatic uric acid, the end-degradation product of ATP, slightly increased with HFD, but was normalized by exercise (Fig. S3G). Interestingly HFD did not increase uric acid content in both WAT depots (Fig. 3J). HFD also increased the expression of the purinergic receptor P2X, ligand-gated ion channel, 7 (P2rx7), a modulator of cell damage and ATP release, in eWAT but not in iWAT (Fig. 3K).

These results, highlighting the increase in HFD-related ATP content in both WAT depots and the normalization by exercise only in iWAT, are summarized in Figure 4 together with the impact on senescence.

Role of ATP in WAT senescence.

To evaluate the specific role of intracellular ATP in WAT senescence, we assessed SA- β -gal activity, p16 and p21 expression in iWAT- and eWAT-derived primary adipocytes treated with ATP-loaded liposomes. First, we demonstrated the difference between iWAT and eWAT after ATP-loaded liposome delivery and showed that ATP peaked at 30 minutes after treatment in iWAT-derived preadipocytes (Fig. S5A), followed at 6 hours by a decline in ATP content concomitant with an increase in uric acid. In contrast, in eWAT-derived preadipocytes, ATP levels remained elevated over 24 hours. This is consistent with the difference in XO protein expression in the respective WAT depots (Fig. 3H-I), whilst purinergic receptor expression increased in both iWAT- and eWAT-derived preadipocytes in a similar manner at 6 hours of ATP stimulation (Fig. S5C). Interestingly, ATP-loaded liposomes induced p21 expression at 6 hours after treatment in both iWAT and eWAT, and p16 expression at 6 hours in eWAT and delayed at 24 hours in iWAT (Fig. 5A-B). Thus, we evaluated ATP-inducible senescence compared to either liposome free, liposome control or uric acid-loaded liposome after 6-hour treatment (Fig. 5C-F). Senescence occurred only after delivery of ATP, but not uric acid, in

comparison with liposome-free and control conditions (Fig. 5C-F). Of note, ATP-induced senescence was higher in eWAT than in iWAT (1.5 fold vs 1.2 fold, $p=0.0011$).

Furthermore, to prove the role of ATP accumulation in initiating WAT senescence in the context of HFD, we inhibited ATP catabolism by allopurinol, a XO inhibitor, in both ATP- and in high glucose/palmitate- (metabolic media: MM, to mimic *in vitro* caloric overload) treated preadipocytes (Fig. 5C-D). Notably, MM increased SA- β -gal positivity only in eWAT, but not in iWAT, aligned with the differences in XO levels between the two fat depots (Fig. 5C-D). Preventing the degradation of ATP with allopurinol aggravated senescence in ATP- and MM-treated iWAT preadipocytes. In eWAT allopurinol increased SA- β -gal positivity only in ATP- but not MM-treated preadipocytes (Fig. 5C-D). Furthermore, allopurinol increased p21 expression in both iWAT and eWAT ATP-treated preadipocytes, and p16 only in eWAT (Fig. 5E-F). Similar results were obtained in treating 3T3-L1 adipocytes with ATP- and uric acid-loaded liposomes, lending support to the critical role of ATP, but not uric acid, in inducing WAT senescence (Fig. S5D-E).

To further establish ATP as a trigger of WAT senescence, we inhibited the degradation of ATP by allopurinol administration after 5-week HFD *in vivo*, alone or in combination with exercise (Fig. S5F). The effectiveness of allopurinol treatment was assessed by a 15% decrease in uric acid plasma levels together with a similar trend in eWAT lysates (Fig. S5G). Furthermore, allopurinol increased p21⁺ adipocyte precursors in iWAT, but not eWAT, of HFD-SED mice and reduced the beneficial effect of exercise mainly in iWAT (Fig. 5G). Allopurinol similarly increased p16⁺ adipocyte precursors and reduced exercise rescue in both HFD iWAT and eWAT. Allopurinol, as opposed to exercise, did not affect body weight, adiposity, SA- β -gal activity, insulin sensitivity (ITT) and glucose tolerance (GTT) (Fig. S5H-K).

Altogether these results indicate a key role of ATP, but not uric acid, in the induction of WAT senescence in a 10-week HFD intervention. Remarkably, addition of allopurinol reduced ATP degradation and amplified the pro-senescent effect of ATP in caloric overload *in vitro* and *in vivo*.

DISCUSSION

Our data highlight the accumulation of senescent cells within both visceral and subcutaneous WAT as a very early event occurring two weeks after HFD initiation in parallel with metabolic alterations but independent of systemic inflammation or WAT fibrosis. Furthermore, we identify HFD-induced ATP overproduction by increased glycolysis and oxidative phosphorylation, as a putative mechanism underlying WAT senescence. Exercise prevents metabolic alterations independently of major body weight and adiposity reduction and ameliorates senescence mainly in iWAT. This finding is consistent with the high expression of xanthine oxydase in iWAT, which allows ATP degradation and explains the full rescue of senescence during exercise in this fat depot.

WAT senescence occurs early after HFD initiation

In the context of caloric overload, the energy storage in WAT reaches a threshold that initiates a cascade of events leading ultimately to systemic inflammation and pathological consequences, including increased insulin resistance and remote organ damage (Minamino et al., 2009; Palmer et al., 2019; Ternacle et al., 2017). Whilst most of the literature evaluates long-term HFD, we focused our investigation on 10-week HFD in adult mice. Although we did not observe WAT fibrosis, nor local or systemic inflammation, HFD induced glucose intolerance, insulin resistance and leptin production consistent with increased fat mass and adipocyte hypertrophy together with organization of immune cells in crown-like structures (Murano et al., 2008).

From a detailed kinetic during the 10-week HFD exposure, our main observation is that cellular senescence represents one of the earliest events occurring in WAT, two weeks after the initiation of HFD as demonstrated by increase in SA- β -gal activity, senescence markers (Cdkn1a and Cdkn2a) and p16 and p21 positive staining. The increased positive staining was associated with adipocyte hypertrophy, as recently reported in other cell types (Anderson et al., 2019; Biran et al., 2017; Neurohr et al., 2019). Furthermore, we observed an increase in *in vivo* p16INK4a expression at 10-week HFD.

Senescence occurred in the different WAT cell populations, including mature adipocytes, preadipocytes, adipocyte progenitors and immune cells. Interestingly, the senescence phenotype was maintained in differentiated HFD-derived preadipocytes, reflecting the *in vivo* characteristics of parental tissue (Hausman et al., 2008). This finding is important considering the impact of WAT senescence on systemic disorders and lifespan (Baker et al., 2016).

Of note, we did not observe any tissue induction of classical pro-inflammatory SASP factors (CCL2, TNF α , IL6, IL10, PAI1) (Coppe et al., 2008; Munoz-Espin and Serrano, 2014; Saker et al., 2016) as opposed to longer (i.e. 30 vs 10 weeks in our model) HFD exposure in older (12-13 vs 7 months) animals (Schafer et al., 2016). Instead, we observed an upregulation of several SASP-associated chemokines (Mcp1) and profibrotic cytokines (Tgfb1, Fn1, Timp1) in eWAT but not iWAT. Indeed, MCP-1 is secreted by senescent cells and has recently been correlated with biological age in mammals (Yousefzadeh et al., 2018), whilst TGF β promotes matrix remodeling in remote organs (Sawaki et al., 2018). Our current data and recent observations (Sawaki et al., 2018; Ternacle et al., 2017) support the premise that senescent WAT is an important source of profibrotic cytokines, known to alter tissue homeostasis prior to the induction of a pro-inflammatory secretome. This profibrotic secretome contributes to organ remodeling, physical dysfunction and premature aging (Munoz-Espin and Serrano, 2014; Sawaki et al., 2018; van Deursen, 2014).

Increased ATP content initiates WAT senescence without mitochondria dysfunction

Mitochondria are important for senescence and the SASP production (Correia-Melo et al., 2016; Passos et al., 2010). In the context of high calorie intake mitochondria increase ROS generation as a toxic by-product of oxidative phosphorylation. Our data are consistent with this observation since the 10-week HFD regimen resulted in marginally increased mitochondrial ROS production in WAT exerting a potential trophic effect (Lee et al., 2009). Importantly, ROS mildly increased after WAT senescence occurred in the HFD kinetic. Additionally, mitochondria play a critical role in maintaining cellular activities by generating energy in the form of ATP. In HFD sedentary mice, our data show an elevated ATP content in both iWAT and eWAT preadipocytes, but exercise normalized it only in iWAT. Thus, we explored the possibility of increased purine catabolism in iWAT. First, we observed substantially higher expression of xanthine oxidase, the enzyme controlling purine degradation, in iWAT than in eWAT. Moreover, XO uses molecular O₂ as an essential cofactor, which is provided by exercise hyperemia that improves blood flow in the neighboring iWAT. The combination of high XO expression, HFD-increased levels of substrate for purine degradation and O₂ cofactor is consistent with the difference between iWAT and eWAT senescence prevention by exercise. We also show a HFD-induced expression of P2rx7, a modulator of cell senescence (Cho et al., 2014) increased in obesity, only in eWAT.

Since high concentrations of ATP and its end-degradation products have been shown to be endogenous “danger-associated molecular patterns”, DAMPs (Basisty et al., 2020; Nakahira et al., 2015), we further demonstrated that ATP treatment induced senescence in both primary preadipocyte and 3T3-L1 adipocyte culture, whilst uric acid did not. Indeed ATP, but not uric acid-loaded liposomes rapidly induced an increase in SA-β-gal activity and an upregulation of p16 and p21.

Exercise exerts a “senostatic” action preventing WAT senescence during HFD

Our study extends an important observation showing that exercise prevents adipose tissue senescence in HFD (Schafer et al., 2016) and adds mechanistic clues to a triggering role for ATP. The significance of our present findings is further highlighted by the lack of confounding factors known to interfere with senescence, such as physiological age (Sawaki et al., 2018) and weight loss (Ma et al., 2020), in our study design.

Exercise promotes mitochondrial biogenesis and improves function in multiple organs including the heart (Judge and Leeuwenburgh, 2007). In the current experimental stage of HFD, we show that exercise reduced global WAT respiration, mitochondrial ATP-linked oxygen consumption and glycolysis, ultimately resulting in reduced ATP accumulation in iWAT but not in eWAT. Moreover, exercise improved insulin sensitivity in obesity by modulating the excessive energy generation. These findings are in line with the normalization of HFD-induced increase in mitochondrial mass, a pattern closely reflecting that observed in other models of senescence (Korolchuk et al., 2017; Stab et al., 2016). As ATP acts as a danger signal on immune cells (Faas et al., 2017), our data show that exercise-related ATP decrease reduced p16 and p21 expression in WAT macrophages, which may improve the clearance of senescent cells. Our data are in line with a recent observation showing that restraining mitochondrial ATP synthesis by a respiratory chain complex IV moderate inhibitor might alleviate age-associated disorders (Tavallaie et al., 2020).

Clinical impact

Given the worldwide obesity epidemics, there is an increasing interest in public health programs encouraging healthy eating behavior and physical activity. Aerobic training is known to have a beneficial impact at different life stages on several aspects of human health, such as cognitive

function, cardiovascular, endocrine and immune responses. Importantly, the benefit of exercise has been demonstrated in pathological conditions, including diabetes, cancer, and cardiovascular disorders (Myers, 2003). Here we add mechanistic insights to the role of exercise in preventing both cellular senescence and metabolic alteration in the context of obesity, reinforcing the concept that adipose tissue dysfunction affects glucose homeostasis (Pini et al., 2016). Indeed, we demonstrate that exercise improves WAT cellular senescence, adipokine dysregulation and adipocyte bioenergetics independent of weight loss, favoring the recovery of glucose homeostasis in obesity. Therefore, exercise through the control of local ATP seems an interesting approach to prevent the induction of cellular senescence and its potential deleterious consequences.

In summary exercise is an excellent senostatic strategy without any side effect, for preventing obesity-associated senescence in WAT.

EXPERIMENTAL PROCEDURES

Animals

Five months old C57/BL6JRj mice (WT, Janvier Labs, France) were subjected to chow diet (CD) and HFD (60% calories from fat, D12492, irradiated; Research Diets Inc., New Brunswick, NJ) for 1, 2 and 5 weeks to assess the kinetics of epididymal white adipose tissue (WAT) senescence.

In a separate set of experiments, CD and HFD mice were followed up to 10 weeks. After 5 weeks on the respective diets, mice were randomly assigned to: CD-sedentary (CD-SED), CD-exercise (CD-EX), or HFD-sedentary (HFD-SED), HFD-exercise (HFD-EX); $n = 15/\text{group}$ (Fig. S1E). The exercise consisted of two swimming sessions/day for 5 days/week during 4 weeks (Derumeaux et al., 2008). Mice were 7 months old at necropsy. To avoid any bias related

to differences in body weight, the whole investigation was conducted in mice with matched body weights and adiposity levels, as measured at the end of the protocol (n=8/group).

In a separate set of experiments, 3 months-old p16^{LUC} heterozygote mice (obtained from N E Sharpless (Chapel Hill, NC, USA) and bred at CNRS-TAAM, France), harboring a knock-in of the luciferase gene into the Cdkn2a locus (Sorrentino et al., 2014), were exposed to CD and HFD for 10 weeks. This model aimed to explore *in vivo* the HFD-induced transcription of p16INK4a, a marker of senescence.

In a separate set of experiments, one group of HFD mice was treated with allopurinol (1mM in the drinking water) (Bravard et al., 2011), starting 5 weeks after the initiation of HFD, alone or in combination with exercise, up to 10 weeks of HFD (Fig. S5F).

All experiments were performed in accordance with the guidelines of our Institutional Animal Care and Use Committee (IACUC). The protocol was approved by the IACUC of the French National Institute of Health and Medical Research, U955, Creteil, France (ComEth 15-001).

In vivo procedures

During follow-up animals underwent weekly body weight (BW) measurements. Daily food consumption was monitored over one week in all groups. Insulin (ITT) and glucose (GTT) tolerance tests were performed at baseline, before exercise and at the end of exercise intervention (Sawaki et al. 2018).

Plasma and tissue collection and measurements

On the day of the sacrifice, mice were not fasted and CD and HFD exercise groups had the last swimming session 24 hours before. Blood was collected and processed as described (Sawaki et al. 2018). Subcutaneous (inguinal, iWAT), visceral (epididymal, eWAT) and perirenal (pWAT) WAT samples were collected, weighed and immediately processed for further analysis. Plasma

leptin and adiponectin were quantified by ELISA (R&D Systems, Minneapolis, MN, USA). Conditioned media (eWAT secretome) and plasma were analyzed for a selected panel of proinflammatory mediators (Campisi, 2005; Coppe et al., 2008; Munoz-Espin and Serrano, 2014; Saker et al., 2016), using a Luminex Bio-Plex cytokine assay kit (Bio-Rad, USA). Plasma and WAT uric acid was quantified by a colorimetric assay kit (BioVision, Milpitas, CA, USA). For WAT measurements, we used the sample deproteinization preparation kit (BioVision, Milpitas, CA, USA).

Histological assessment

Sections of iWAT and eWAT were stained with hematoxylin & eosin for adipocyte size measurements. Sirius Red and immunofluorescent staining procedures were performed as described (Sawaki et al., 2018). Antibodies are reported in the Table S2.

Primary cell culture

Preadipocytes were isolated from iWAT and eWAT stroma vascular fraction (SVF) and differentiated in an adipogenic culture media after two passages to eliminate non-preadipocyte cell contamination. In detail, WAT was aseptically minced and incubated with collagenase Type II (1 mg/mL, Sigma) at 37°C for 45 min. After digestion, serum-containing medium was added to the suspension and filtered through a 100 µm cell strainer. SVF cells were centrifuged for 10 min at 350 g and suspended in pre-warmed adipogenic culture media, consisting of DMEM high glucose with Glutamax (Gibco) supplemented with 10% new born calf serum (Thermofisher), 2.4 nM human insulin (Sigma) and 1% antibiotic solution (Pen-Strep solution, Sigma). To induce differentiation, SVF cells were seeded near confluence and medium was replenished every day to allow selection by adhesion during the first 3 days and then changed every 2 days. SVF cells were cultured in an atmosphere of 5% CO₂ and 20% O₂ at 37°C. Based on preliminary experiments, day 7 was the time of differentiation used for all experiments.

SA- β -galactosidase activity

For senescence assays, portions of iWAT and eWAT depots freshly dissected and respectively differentiated preadipocytes were incubated with staining solution (1 mg/ml Ultrapure X-gal, Sigma-Aldrich, France) (Itahana et al., 2007; Sawaki et al., 2018). For β -galactosidase activity in tissue, a score of relative intensity of the signal (0=absent, 1=low, 2=medium, 3=high, 4=very high) was used.

Primary cell metabolic rate measurements

For bioenergetics assessment, the Mitochondrial Stress Test was performed on iWAT- and eWAT-differentiated adipocytes (20,000 cells/well) using the XF24 Extracellular Flux Analyzer (Agilent Technologies, Santa Clara, CA, USA). Oxygen consumption rate (OCR), indicative of mitochondrial activity, and extracellular acidification rate (ECAR), an index of glycolysis, were determined as described (Foresti et al., 2015).

ATP measurements

Differentiated primary preadipocytes and 3T3-L1 were lysed and intracellular ATP content measured by the ATP-lite assay kit (Perkin Elmer, Villebon-sur-Yvette, France) (Braud et al., 2018).

Cell culture treatments

Primary preadipocytes were isolated from WAT of 5-month-old CD male mice. At differentiation, cells were incubated at different time points (for the time course: 30 min-3h-6h-24h or as specified in the figure legend) with adenosine triphosphate (ATP)- and uric acid-loaded liposomes (200 μ M, Sigma-Aldrich, France) as compared to two control applications: liposome-free (lipo-free) and liposome alone (CTL).

In addition, to assess the role of ATP as a senescence trigger, we performed interference experiments by co-administration of the xanthine oxidase (XO) an allopurinol inhibitor. Preadipocytes were subjected for 6 hours to *in vitro* caloric overload in the form of either high glucose/palmitate (Metabolic media: MM) or ATP-loaded liposomes and co-administration of allopurinol (1mM).

Fully differentiated 3T3-L1 adipocytes, cultured in an atmosphere of 5% CO₂ and 20% O₂ at 37°C, were incubated for 24 hours with ATP or uric acid (200 µM, Sigma-Aldrich, France). ATP and the other molecules were encapsulated in liposomes (Sigma-Aldrich, France) (Braud et al. 2018).

Superoxide level measurement

Cytosolic and mitochondrial ROS levels were measured in differentiated preadipocytes (7000/well) by quantification of CellROX (10 µM) and MitoSOX (5 µM) fluorescence intensity levels, respectively. Fluorescence readings were done by a microplate reader (Tecan, Männedorf, Switzerland).

Quantitative Real-Time PCR

Total RNA was isolated from total iWAT and eWAT, the differentiated preadipocytes and 3T3-L1 adipocytes using RNeasy Lipid Tissue Mini Kit (Qiagen, Valencia, CA, USA). Quantification was performed with Qubit RNA HS Assay Kit (Life Technologies, Thermo Fisher Scientific, MA, USA). First strand DNA synthesis was realized using 0.25-0.5 ng total RNA and qPCR was performed and analyzed as described (Sawaki et al. 2018). Taqman assays are reported in the Table S2.

RNA profiling

PAMM-087ZA RT² ProfilerTM PCR Array (Qiagen, Valencia, CA, USA) was performed on 600 ng of total RNA from eWAT. Real-time PCR was then performed using Brilliant II SYBR Green QPCR Master Mix (Agilent) and Mx3005 Pro thermocycler (Agilent).

Statistical analyses

All statistical analyses were carried out using GraphPad Prism 5 (La Jolla, CA) and the R environment for statistical computing. All data are reported as mean±SEM. Comparisons between multiple groups were done using one- or two-way ANOVA followed by Bonferroni correction. P-values <0.05 were considered as significant. All images were processed with the ImageJ (NIH, <https://imagej.nih.gov/ij/>). To evaluate the importance of the changes affecting major biological annotations that characterize the WAT functional signature under the effect of HFD, we measured the iWAT and eWAT expression profile of a panel of 22 genes illustrating adipocyte function, inflammation, tissue remodeling and senescence. A random-forest supervised learning algorithm (“randomForest” R package, version 4.6-12) was applied iteratively to evaluate and rank the relative discriminative power associated with changes in these gene expression profiles induced by HFD in iWAT and eWAT. To assess the relative discriminative power associated with each measured expression profile we averaged the feature importance provided by the random forest algorithm over 10,000 successive iterations performed for each of the analyzed situations. The individual discriminative power of each transcriptional profile was expressed as percentages of the total discriminative power of the panel of selected transcriptional descriptors. The resulting values were plotted after grouping them by functional category and ranking the available categories in the decreasing order of their strongest transcriptional descriptor, to illustrate the contextual importance of the functional changes induced by diet in the two WAT depots. Separately, the expression of a panel of several mitochondria genes was quantified by using RT² ProfilerTM PCR Array. A linear regression model was used to test for differential expression in relation to diet. Significant transcriptional

changes were then annotated in relation to three main themes characterizing mitochondrial function (i.e. morphogenesis, homeostasis and beta-oxidation) and illustrated graphically using a heat-map representation.

Acknowledgments.

This work was supported by ANR Grant RHU CARMMA (ANR-15-RHUS-0003). No conflict of interest relevant to this article were reported.

We are grateful to Prof. E. Blackburn (UCSF, San Francisco, USA) for inspiring discussion and wise comments, to Prof N. E. Sharpless (Chapel Hill, NC, USA) for providing the p16^{LUC} mice and to Dr J. Rieusset (INSERM U870, Lyon, France) and Dr A; Pizard for precious support in revision.

We thank C. Gandolphe and X. Decrouy (IMRB Imagery platform), M. Surenaud (IMRB Luminex platform) and the NGS platform of IMRB. We thank M. Breau, Y. Zhang, D. Altintas, M. Halfaoui, H. Liang (U955, Créteil), C. Pertuiset and M. Porceddu (Mitologics SAS, Créteil) and J. Seguin (Optical imaging platform LIOPA, Paris Descartes University) for technical contribution.

Author contributions. M.P., G.C. and D.S. helped designing the study, performed experiments, collected and analyzed the data, implemented follow-up experiments, and wrote the manuscript; Z.M., L.B., J.T., R.M. performed specific experiments and collected data; G.M. provided expertise in relation to adipose tissue fibrosis; C.M., N.B. and A.B.S. provided expertise for Seahorse data interpretation and specific experiments on mitochondrial function, and revised the manuscript; R.M. and R.F. helped for Seahorse experiment design and analysis, and revised the manuscript; C.H. helped analyzing and interpreting data, performed specific statistical tests and revised the manuscript; G.D. designed the study, interpreted data, wrote and reviewed the manuscript and provided study resources. All authors approved the final version of manuscript.

Data availability. All data are stored in a centralized and secured Clinical and Translational Research data Repository (CARMMA CTRDR) available at IMRB. Data and resource sharing are available upon request and presentation of a protocol to RHU CARMMA consortium.

References

- Ahima, R.S. (2009). Connecting obesity, aging and diabetes. *Nature medicine* *15*, 996-997.
- Anderson, R., Lagnado, A., Maggiorani, D., Walaszczyk, A., Dookun, E., Chapman, J., Birch, J., Salmonowicz, H., Ogrodnik, M., Jurk, D., *et al.* (2019). Length-independent telomere damage drives post-mitotic cardiomyocyte senescence. *Embo j* *38*.
- Baker, D.J., Childs, B.G., Durik, M., Wijers, M.E., Sieben, C.J., Zhong, J., Saltness, R.A., Jeganathan, K.B., Verzosa, G.C., Pezeshki, A., *et al.* (2016). Naturally occurring p16(Ink4a)-positive cells shorten healthy lifespan. *Nature* *530*, 184-189.
- Baker, D.J., Wijshake, T., Tchkonja, T., LeBrasseur, N.K., Childs, B.G., van de Sluis, B., Kirkland, J.L., and van Deursen, J.M. (2011). Clearance of p16Ink4a-positive senescent cells delays ageing-associated disorders. *Nature* *479*, 232-236.
- Basisty, N., Kale, A., Jeon, O.H., Kuehnemann, C., Payne, T., Rao, C., Holtz, A., Shah, S., Sharma, V., Ferrucci, L., *et al.* (2020). A proteomic atlas of senescence-associated secretomes for aging biomarker development. *PLoS Biol* *18*, e3000599.
- Biran, A., Zada, L., Abou Karam, P., Vadai, E., Roitman, L., Ovadya, Y., Porat, Z., and Krizhanovsky, V. (2017). Quantitative identification of senescent cells in aging and disease. *Aging Cell* *16*, 661-671.
- Braud, L., Pini, M., Muchova, L., Manin, S., Kitagishi, H., Sawaki, D., Czibik, G., Ternacle, J., Derumeaux, G., Foresti, R., *et al.* (2018). Carbon monoxide-induced metabolic switch in adipocytes improves insulin resistance in obese mice. *JCI Insight* *3*.
- Bravard, A., Bonnard, C., Durand, A., Chauvin, M.A., Favier, R., Vidal, H., and Rieusset, J. (2011). Inhibition of xanthine oxidase reduces hyperglycemia-induced oxidative stress and improves mitochondrial alterations in skeletal muscle of diabetic mice. *Am J Physiol Endocrinol Metab* *300*, E581-591.
- Campisi, J. (2005). Senescent cells, tumor suppression, and organismal aging: good citizens, bad neighbors. *Cell* *120*, 513-522.
- Cho, J., Yusuf, R., Kook, S., Attar, E., Lee, D., Park, B., Cheng, T., Scadden, D.T., and Lee, B.C. (2014). Purinergic P2Y₁(4) receptor modulates stress-induced hematopoietic stem/progenitor cell senescence. *J Clin Invest* *124*, 3159-3171.
- Coppe, J.P., Patil, C.K., Rodier, F., Sun, Y., Munoz, D.P., Goldstein, J., Nelson, P.S., Desprez, P.Y., and Campisi, J. (2008). Senescence-associated secretory phenotypes reveal cell-nonautonomous functions of oncogenic RAS and the p53 tumor suppressor. *PLoS Biol* *6*, 2853-2868.
- Correia-Melo, C., Marques, F.D., Anderson, R., Hewitt, G., Hewitt, R., Cole, J., Carroll, B.M., Miwa, S., Birch, J., Merz, A., *et al.* (2016). Mitochondria are required for pro-ageing features of the senescent phenotype. *EMBO J* *35*, 724-742.
- Das, U.N. (2019). Beneficial role of bioactive lipids in the pathobiology, prevention, and management of HBV, HCV and alcoholic hepatitis, NAFLD, and liver cirrhosis: A review. *Journal of advanced research* *17*, 17-29.
- Derumeaux, G., Ichinose, F., Raher, M.J., Morgan, J.G., Coman, T., Lee, C., Cuesta, J.M., Thibault, H., Bloch, K.D., Picard, M.H., *et al.* (2008). Myocardial alterations in senescent mice and effect of exercise training: a strain rate imaging study. *Circ Cardiovasc Imaging* *1*, 227-234.
- Foresti, R., Bucolo, C., Platania, C.M., Drago, F., Dubois-Rande, J.L., and Motterlini, R. (2015). Nrf2 activators modulate oxidative stress responses and bioenergetic profiles of human retinal epithelial cells cultured in normal or high glucose conditions. *Pharmacol Res* *99*, 296-307.
- Hausman, D.B., Park, H.J., and Hausman, G.J. (2008). Isolation and culture of preadipocytes from rodent white adipose tissue. *Methods Mol Biol* *456*, 201-219.
- Itahana, K., Campisi, J., and Dimri, G.P. (2007). Methods to detect biomarkers of cellular senescence: the senescence-associated beta-galactosidase assay. *Methods Mol Biol* *371*, 21-31.
- Judge, S., and Leeuwenburgh, C. (2007). Cardiac mitochondrial bioenergetics, oxidative stress, and aging. *Am J Physiol Cell Physiol* *292*, C1983-1992.
- Korolchuk, V.I., Miwa, S., Carroll, B., and von Zglinicki, T. (2017). Mitochondria in Cell Senescence: Is Mitophagy the Weakest Link? *EBioMedicine* *21*, 7-13.

Lee, H., Lee, Y.J., Choi, H., Ko, E.H., and Kim, J.W. (2009). Reactive oxygen species facilitate adipocyte differentiation by accelerating mitotic clonal expansion. *The Journal of biological chemistry* *284*, 10601-10609.

Lefranc, C., Friederich-Persson, M., Braud, L., Palacios-Ramirez, R., Karlsson, S., Boujardine, N., Motterlini, R., Jaisser, F., and Nguyen Dinh Cat, A. (2019). MR (Mineralocorticoid Receptor) Induces Adipose Tissue Senescence and Mitochondrial Dysfunction Leading to Vascular Dysfunction in Obesity. *Hypertension* *73*, 458-468.

Lowell, B.B., and Shulman, G.I. (2005). Mitochondrial dysfunction and type 2 diabetes. *Science* *307*, 384-387.

Ma, S., Sun, S., Geng, L., Song, M., Wang, W., Ye, Y., Ji, Q., Zou, Z., Wang, S., He, X., *et al.* (2020). Caloric Restriction Reprograms the Single-Cell Transcriptional Landscape of *Rattus Norvegicus* Aging. *Cell* *180*, 984-1001.e1022.

McHugh, D., and Gil, J. (2018). Senescence and aging: Causes, consequences, and therapeutic avenues. *J Cell Biol* *217*, 65-77.

Minamino, T., Orimo, M., Shimizu, I., Kunieda, T., Yokoyama, M., Ito, T., Nojima, A., Nabetani, A., Oike, Y., Matsubara, H., *et al.* (2009). A crucial role for adipose tissue p53 in the regulation of insulin resistance. *Nature medicine* *15*, 1082-1087.

Munoz-Espin, D., and Serrano, M. (2014). Cellular senescence: from physiology to pathology. *Nat Rev Mol Cell Biol* *15*, 482-496.

Murano, I., Barbatelli, G., Parisani, V., Latini, C., Muzzonigro, G., Castellucci, M., and Cinti, S. (2008). Dead adipocytes, detected as crown-like structures, are prevalent in visceral fat depots of genetically obese mice. *Journal of lipid research* *49*, 1562-1568.

Myers, J. (2003). Cardiology patient pages. Exercise and cardiovascular health. *Circulation* *107*, e2-5.

Nakahira, K., Hisata, S., and Choi, A.M. (2015). The Roles of Mitochondrial Damage-Associated Molecular Patterns in Diseases. *Antioxid Redox Signal* *23*, 1329-1350.

Neurohr, G.E., Terry, R.L., Lengefeld, J., Bonney, M., Brittingham, G.P., Moretto, F., Miettinen, T.P., Vaites, L.P., Soares, L.M., Paulo, J.A., *et al.* (2019). Excessive Cell Growth Causes Cytoplasm Dilution And Contributes to Senescence. *Cell* *176*, 1083-1097.e1018.

Palmer, A.K., Xu, M., Zhu, Y., Pirtskhalava, T., Weivoda, M.M., Hachfeld, C.M., Prata, L.G., van Dijk, T.H., Verkade, E., Casacang-Verzosa, G., *et al.* (2019). Targeting senescent cells alleviates obesity-induced metabolic dysfunction. *Aging Cell* *18*, e12950.

Passos, J.F., Nelson, G., Wang, C., Richter, T., Simillion, C., Proctor, C.J., Miwa, S., Olijslagers, S., Hallinan, J., Wipat, A., *et al.* (2010). Feedback between p21 and reactive oxygen production is necessary for cell senescence. *Mol Syst Biol* *6*, 347.

Pini, M., Touch, S., Poirier, H., Dalmas, E., Niot, I., Rouault, C., Druart, C., Delzenne, N., Clement, K., Andre, S., *et al.* (2016). Adipose tissue adaptive response to trans-10,cis-12-conjugated linoleic acid engages alternatively activated M2 macrophages. *FASEB J* *30*, 241-251.

Saker, M., Lipskaia, L., Marcos, E., Abid, S., Parpaleix, A., Houssaini, A., Validire, P., Girard, P., Noureddine, H., Boyer, L., *et al.* (2016). Osteopontin, a Key Mediator Expressed by Senescent Pulmonary Vascular Cells in Pulmonary Hypertension. *Arteriosclerosis, thrombosis, and vascular biology* *36*, 1879-1890.

Sawaki, D., Czibik, G., Pini, M., Ternacle, J., Suffee, N., Mercedes, R., Marcelin, G., Surenaud, M., Marcos, E., Gual, P., *et al.* (2018). Visceral Adipose Tissue Drives Cardiac Aging Through Modulation of Fibroblast Senescence by Osteopontin Production. *Circulation* *138*, 809-822.

Schafer, M.J., White, T.A., Evans, G., Tonne, J.M., Verzosa, G.C., Stout, M.B., Mazula, D.L., Palmer, A.K., Baker, D.J., Jensen, M.D., *et al.* (2016). Exercise Prevents Diet-Induced Cellular Senescence in Adipose Tissue. *Diabetes* *65*, 1606-1615.

Sorrentino, J.A., Krishnamurthy, J., Tilley, S., Alb, J.G., Jr., Burd, C.E., and Sharpless, N.E. (2014). p16INK4a reporter mice reveal age-promoting effects of environmental toxicants. *J Clin Invest* *124*, 169-173.

Stanford, K.I., Middelbeek, R.J., and Goodyear, L.J. (2015). Exercise Effects on White Adipose Tissue: Being and Metabolic Adaptations. *Diabetes* *64*, 2361-2368.

Tavallaie, M., Voshtani, R., Deng, X., Qiao, Y., Jiang, F., Collman, J.P., and Fu, L. (2020). Moderation of mitochondrial respiration mitigates metabolic syndrome of aging. *Proc Natl Acad Sci U S A*.

Tchkonia, T., Morbeck, D.E., Von Zglinicki, T., Van Deursen, J., Lustgarten, J., Scrable, H., Khosla, S., Jensen, M.D., and Kirkland, J.L. (2010). Fat tissue, aging, and cellular senescence. *Aging Cell* 9, 667-684.

Ternacle, J., Wan, F., Sawaki, D., Surenaud, M., Pini, M., Mercedes, R., Ernande, L., Audureau, E., Dubois-Rande, J.L., Adnot, S., *et al.* (2017). Short-term high-fat diet compromises myocardial function: a radial strain rate imaging study. *Eur Heart J Cardiovasc Imaging* 18, 1283-1291.

van Deursen, J.M. (2014). The role of senescent cells in ageing. *Nature* 509, 439-446.

Vergoni, B., Cornejo, P.J., Gilleron, J., Djedaini, M., Ceppo, F., Jacquet, A., Bouget, G., Ginet, C., Gonzalez, T., Maillet, J., *et al.* (2016). DNA Damage and the Activation of the p53 Pathway Mediate Alterations in Metabolic and Secretory Functions of Adipocytes. *Diabetes* 65, 3062-3074.

Xu, M., Pirtskhalava, T., Farr, J.N., Weigand, B.M., Palmer, A.K., Weivoda, M.M., Inman, C.L., Ogrodnik, M.B., Hachfeld, C.M., Fraser, D.G., *et al.* (2018). Senolytics improve physical function and increase lifespan in old age. *Nature medicine* 24, 1246-1256.

Yousefzadeh, M.J., Schafer, M.J., Noren Hooten, N., Atkinson, E.J., Evans, M.K., Baker, D.J., Quarles, E.K., Robbins, P.D., Ladiges, W.C., LeBrasseur, N.K., *et al.* (2018). Circulating levels of monocyte chemoattractant protein-1 as a potential measure of biological age in mice and frailty in humans. *Aging Cell* 17.

Supportive information

- **Supplementary methods**
- **Supplementary tables: 1, 2**
- **Supplementary figure legends**

FIGURE LEGENDS

Figure 1. Short-term high fat diet regimen induces adipose tissue senescence. Detailed kinetics of epididymal adipose tissue (eWAT) senescence after initiation of HFD at 1, 2, 5 and 10 weeks compared with chow diet (CD) group (n=5/group). **A:** β -galactosidase (SA- β -gal) activity in eWAT. **B:** Gene expression for senescence markers, p16 (Cdkn2a) and p21 (Cdkn1a), in eWAT. **C:** Representative images of 5-week HFD and quantification by immunofluorescence staining in eWAT of co-localization with p16 (green) or p21 (green) and marker of adipocyte precursor platelet-derived growth factor receptor alpha, PDGFR α (red). Sections were counterstained with DAPI (blue). Double positive cells are expressed as the mean number positive cells over adipocytes (n=3-4/group, 5 pictures per mouse; magnification x200, scale bar = 50 μ m). **D:** Whole-body luminescence for individual p16^{LUC} transgenic male mice are depicted at 10-week HFD. Bioluminescence (BLI) is expressed in arbitrary unit (AU) and calculated as BLI = BLI ROI area of interest (in Ph/s/sr) / BLI ROI LED (internal control – LED- in ph/s/sr), where Ph/s/sr is photon per second per steradian (CD n = 2, HFD n = 3). **E:** Fat mass (adiposity index) of four groups of mice: CD-sedentary (CD-SED), CD-exercise (CD-EX), HFD-sedentary (HFD-SED), HFD-exercise (HFD-EX); n=8/group. Adiposity index calculated by the ratio between the sum of three WAT weights and body weight per mouse. **F-G:** Representative images of SA- β -gal in iWAT and eWAT and quantification of relative intensity of signal (0=absent, 1=low, 2=medium, 3=high, 4=very high). **H-I:** Representative images and quantification of SA- β -gal in preadipocytes derived from iWAT and eWAT (n=4 mice/group, 8 pictures/mouse; magnification x200, scale bar = 50 μ m). For gene expression, results are expressed as fold mRNA change relative to CD-SED values set to 1; n = 5/group. All data are presented as mean \pm SEM. For the kinetics after HFD initiation (panels A-B-C), statistical significance was evaluated by one- or two-way ANOVA followed by Bonferroni correction. *P < 0.05 vs. CD; π < 0.05 vs. 1-week HFD. For all other experiments, statistical significance was evaluated by a one- or two-way ANOVA followed by Bonferroni correction. *P < 0.05; **P < 0.01; ***P < 0.001 for differences due to diet regimen within sedentary and exercise groups (* = diet effect) and ^eP < 0.05; ^{ee}P < 0.01; ^{eee}P < 0.001 for differences between sedentary and exercise groups fed the same diet (^e = exercise effect).

Figure 2. HFD induces cellular senescence in various types of WAT cells, independent of systemic inflammation. **A-B:** Gene expression for p16 and p21 in iWAT and eWAT (A) and in iWAT- and eWAT-derived preadipocytes (B); n=3-6/group. **C:** Representative images and quantification by immunofluorescence staining in iWAT and eWAT of co-localization with p16 (green) and PDGFR α (red). Sections were counterstained with DAPI (blue). Double positive cells are expressed as the mean number of positive cells over adipocytes (n=4 mice/group, 5 pictures per mouse; arrow, original magnification x200, scale bar = 50 μ m). **D:** Representative images and quantification by immunofluorescence staining in iWAT and eWAT of co-localization with p21 (green) and PDGFR α (red). Sections were counterstained with DAPI (blue). Double positive cells are expressed as the mean number of positive cells over adipocytes (n=4 mice/group, 5 pictures per mouse; arrow, original magnification x200, scale bar = 50 μ m). **E-F:** The discriminative power of four major functional themes illustrating the HFD impact on WAT transcriptional profile. Transcriptional changes of a panel of selected genes were

evaluated separately in iWAT and eWAT. Their discriminative power was estimated by iterative testing in a supervised predictive model and is expressed as percentage of their total discriminative power. All data are presented as mean \pm SEM. *P < 0.05; **P < 0.01; ***P < 0.001 for differences due to diet regimen within sedentary and exercise groups (* = diet effect) and ^eP < 0.05; ^{ee}P < 0.01; ^{eee}P < 0.001 for differences between sedentary and exercise groups fed the same diet (^e = exercise effect).

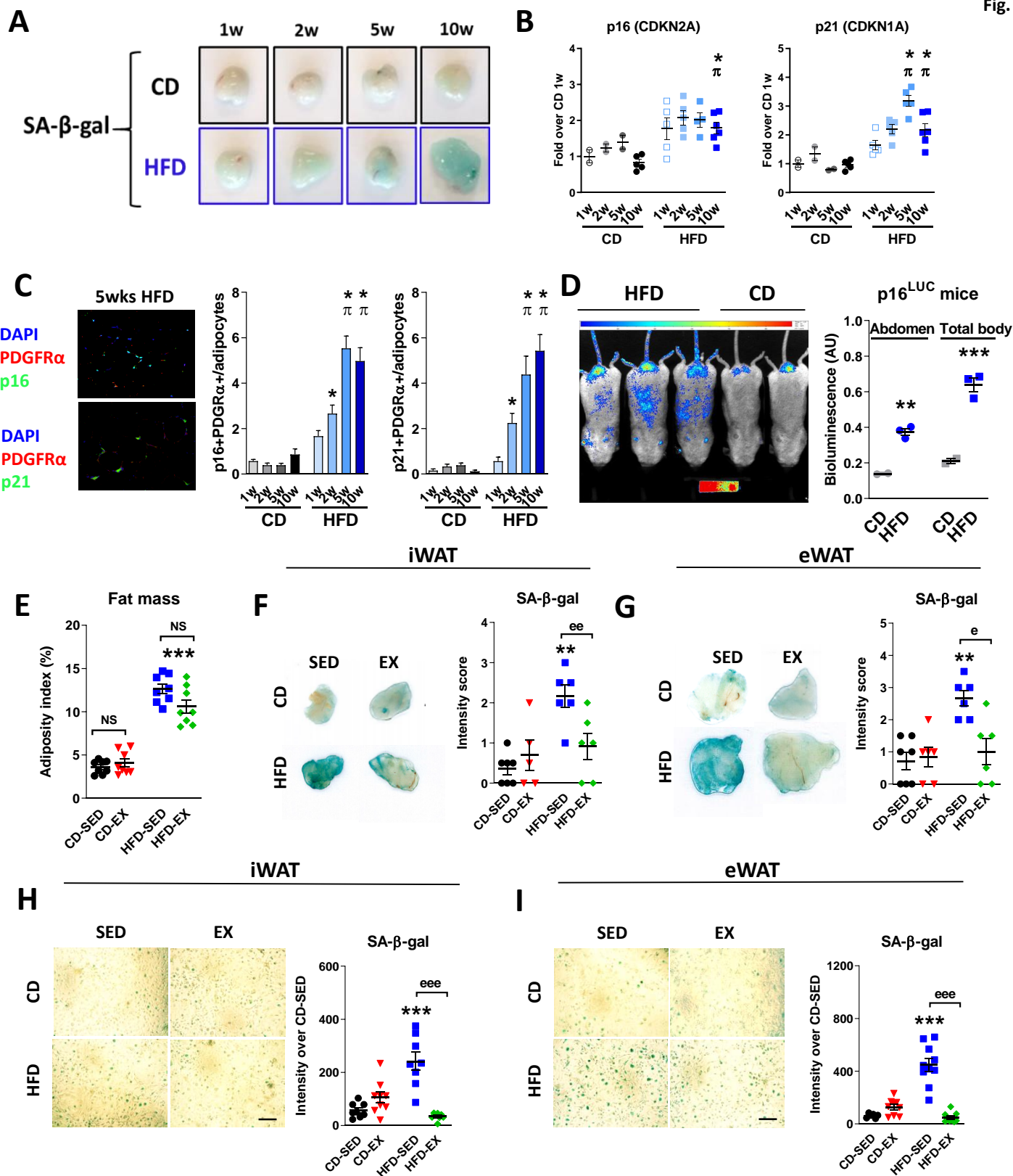
Figure 3. Adipose tissue senescence is associated with increased adipocyte bioenergetics.

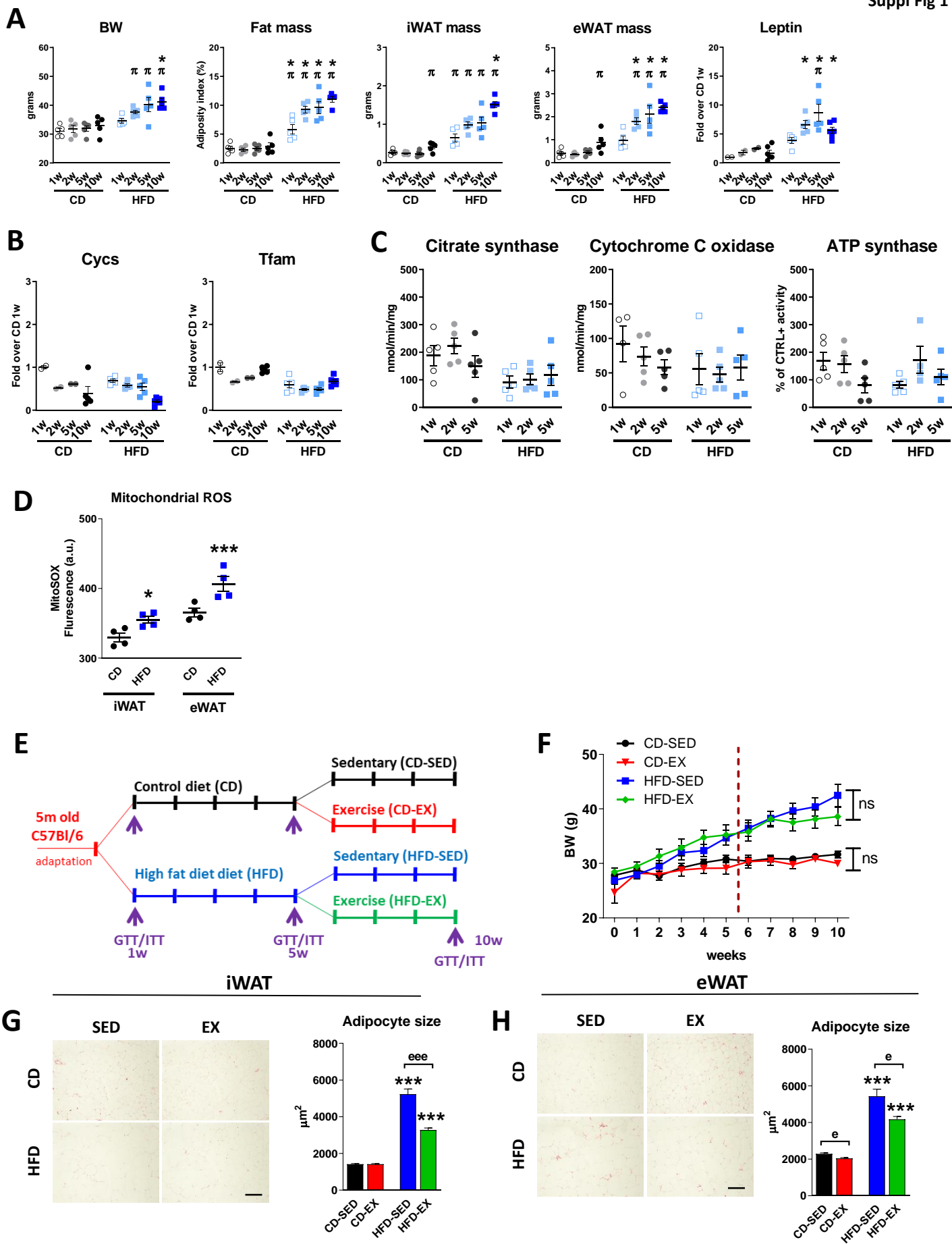
A: Representative images of CD-SED and HFD-SED mice and quantification by immunofluorescence staining in iWAT and eWAT of translocase of outer mitochondrial membrane 20 (Tom20) over adipocytes (n=5 mice/group, 4 pictures per mouse; arrow, original magnification x200, scale bar = 50 μ m). **B:** Citrate synthase activity in iWAT and eWAT; n = 5/group. **C:** Changes in mitochondrial and non-mitochondrial oxygen consumption (OCR) after bioenergetic analysis of iWAT- and eWAT-derived preadipocytes isolated from CD and HFD mice, sedentary (SED) or exercise (EX) groups. Data are mean \pm SEM of four independent experiments with five technical repeats. **D:** Changes in extracellular acidification rate (ECAR), an index of glycolysis. Glycolysis is determined through measurements of the surrounding media before injection of compounds. Data are mean \pm SEM of four independent experiments with five technical repeats. **E:** Changes in ATP-linked oxygen consumption. Data are mean \pm SEM of four independent experiments with five technical repeats. **F:** Purine degradation scheme. **G:** Intracellular ATP content in iWAT- and eWAT-derived preadipocytes; n = 6-8 wells/group. **H:** Representative images and quantification by immunofluorescence staining in iWAT and eWAT of xanthine oxidase (XO, green). Positive cell expressed as the mean number of positive cells over adipocytes (n=3 mice/group, 3 pictures per mouse; magnification x200, scale bar = 50 μ m). **I:** Representative images of immunofluorescence XO staining in iWAT- and eWAT-derived preadipocytes (magnification x400, scale bar = 25 μ m). **J:** Uric acid concentration in iWAT and eWAT tissue lysates, n = 6-12/group). **K:** Gene expression analysis in iWAT and eWAT for purinergic receptor P2X, ligand-gated ion channel, 7 (P2rx7). For gene expression, results are expressed as fold mRNA change relative to CD-SED values set to 1; n = 6/group. All data are presented as mean \pm SEM. *P < 0.05; **P < 0.01; ***P < 0.001 for differences due to diet regimen within sedentary and exercise groups (* = diet effect) and ^eP < 0.05; ^{ee}P < 0.01; ^{eee}P < 0.001 for differences between sedentary and exercise groups fed the same diet (^e = exercise effect).

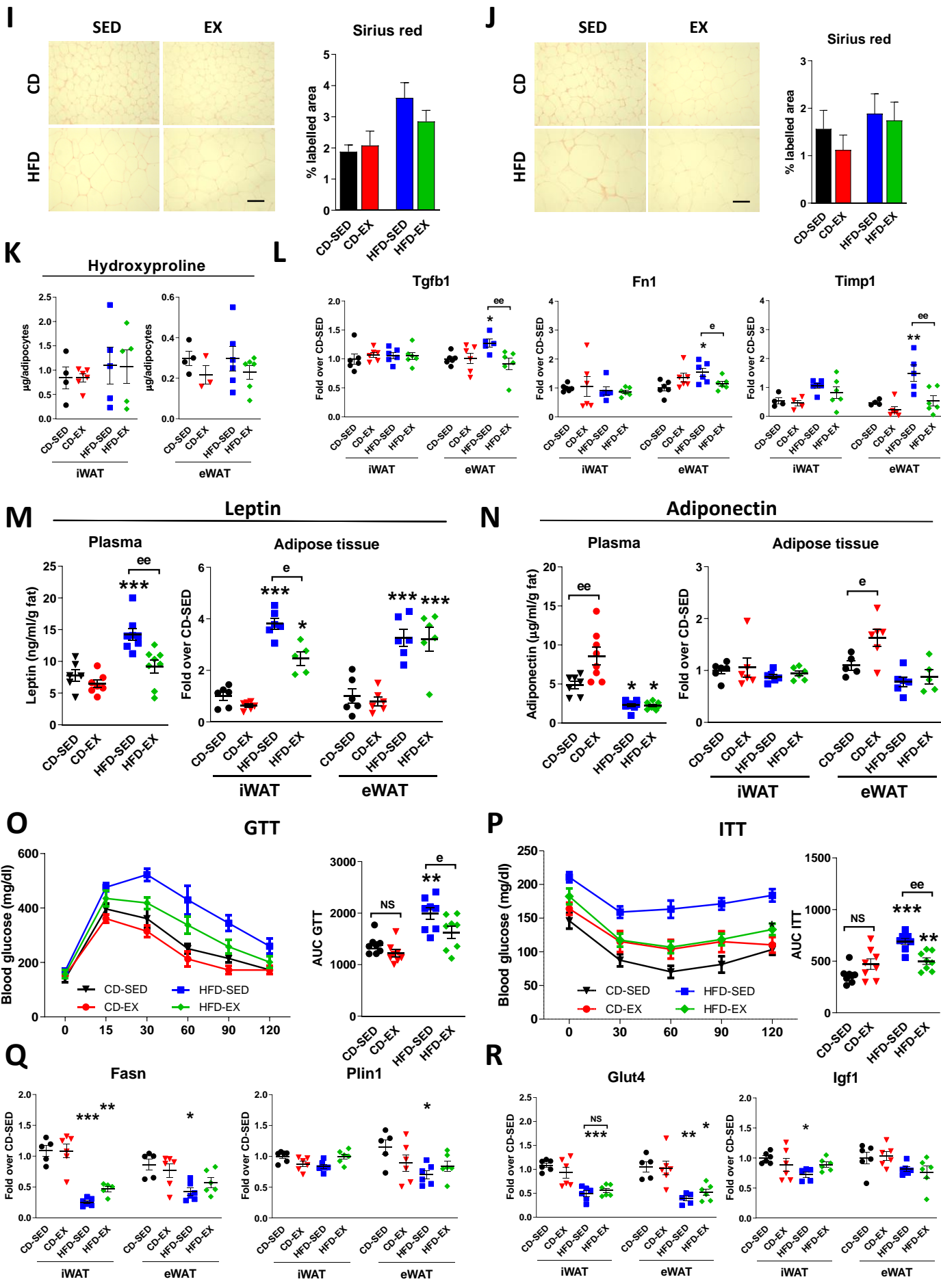
Figure 4. A “heat map-like” table. The table displays the differences between iWAT and eWAT together with the effect of regimen and exercise in terms of adipose tissue function, senescence markers and ATP and uric acid contents.

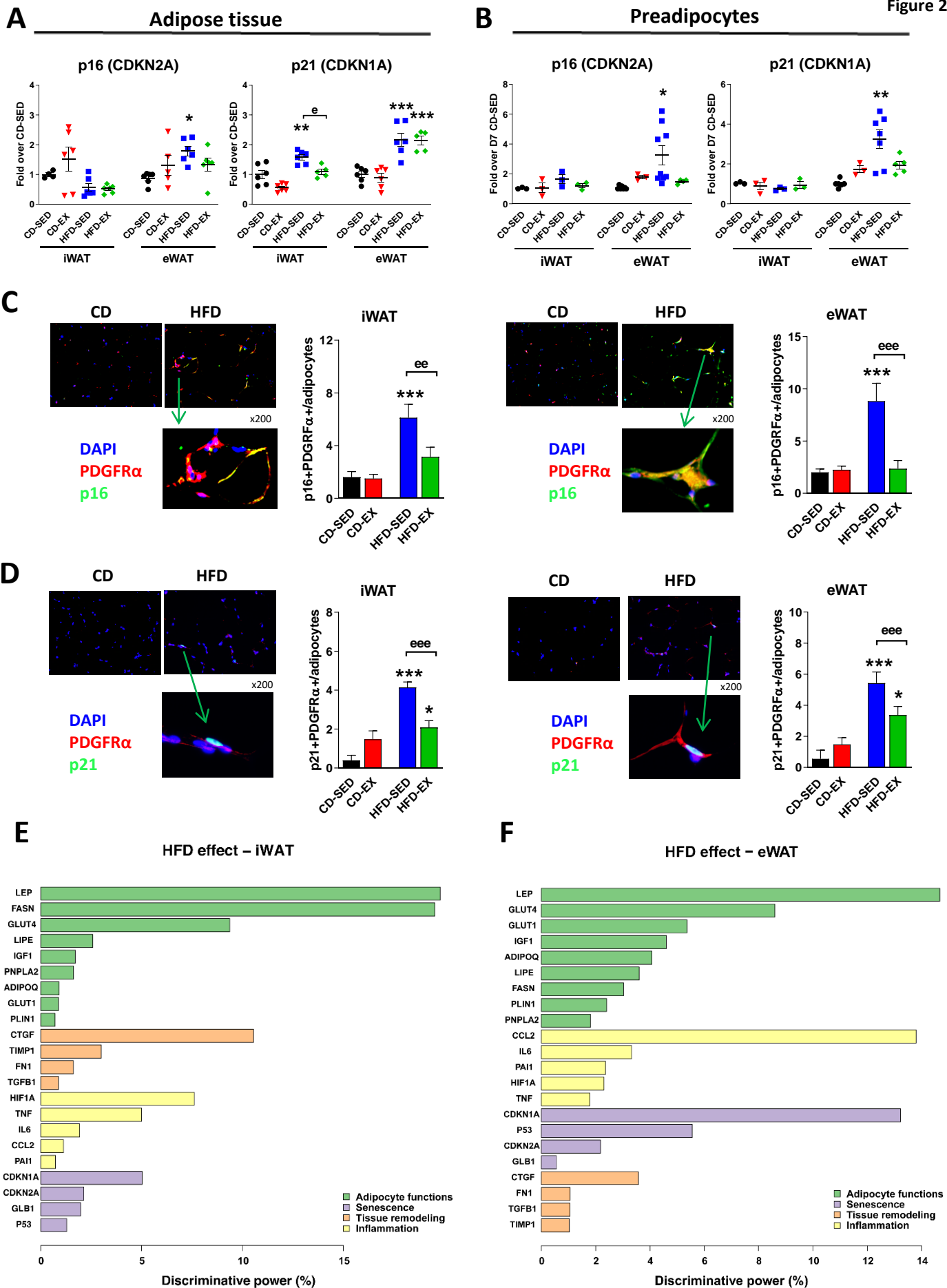
Figure 5. Role of ATP in adipose tissue senescence. A-B: Gene expression analysis for senescence (Cdkn1a, Cdkn2a) in chow diet (CD) iWAT- and eWAT-derived preadipocytes after 7 days of differentiation and treatment with ATP-loaded liposomes compared with two control applications: liposome-free (lipo-free, red line) and liposome alone (CTL); n = 4-6/group. **C-D:** Representative images of SA- β -gal in chow diet (CD) iWAT- and eWAT-derived

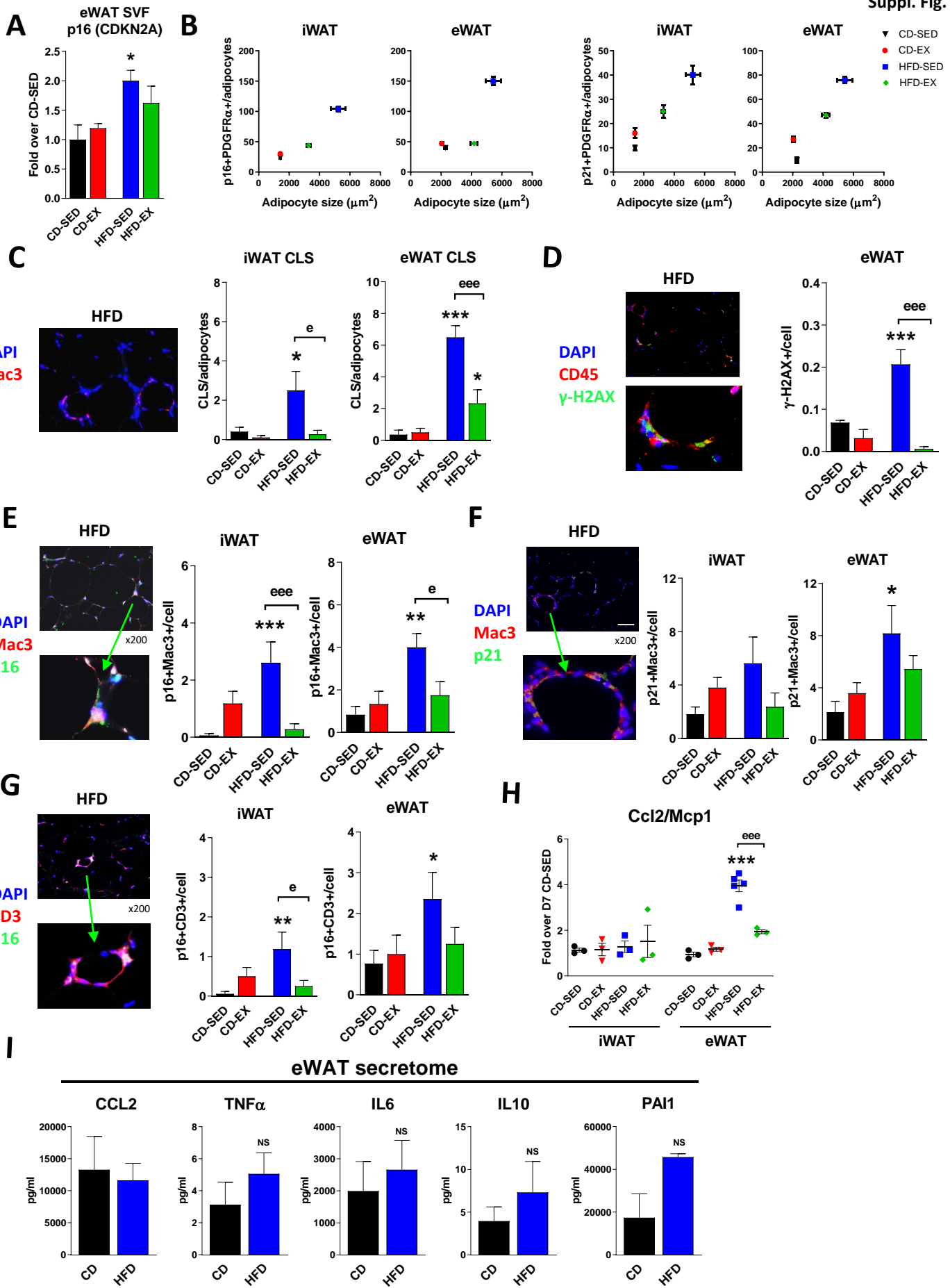
preadipocytes stimulated for 6h with uric acid, high glucose/palmitate (metabolic media: MM) or ATP-loaded liposomes alone or in combination with allopurinol (5 pictures per condition; magnification x400, scale bar = 25 μ m). **E-F:** Gene expression analysis for senescence (Cdkn1a, Cdkn2a) in chow diet (CD) iWAT- and eWAT-derived preadipocytes stimulated for 6h with uric acid- or ATP-loaded liposomes alone or in combination with allopurinol. For gene expression, results are expressed as fold mRNA change relative to Lipo-free values set to 1; n = 3/group. **G:** Representative images and quantification by immunofluorescence staining in iWAT and eWAT of co-localization with p21/CDKN1A (green) and PDGFR α (red). Sections were counterstained with DAPI (blue). Double positive cells are expressed as the mean number of positive cells over adipocytes (n=3-4/group, 5 pictures per mouse; magnification x200, scale bar = 50 μ m). All data are presented as mean \pm SEM. *P < 0.05; **P < 0.01; ***P < 0.001 for differences with reference control (liposome alone *in vitro* and control diet *in vivo*), ^eP < 0.05 for differences between sedentary and exercise groups fed the same diet (^e = exercise effect) and [#]P < 0.05; ^{##}P < 0.01 for the effect of allopurinol treatment between groups.

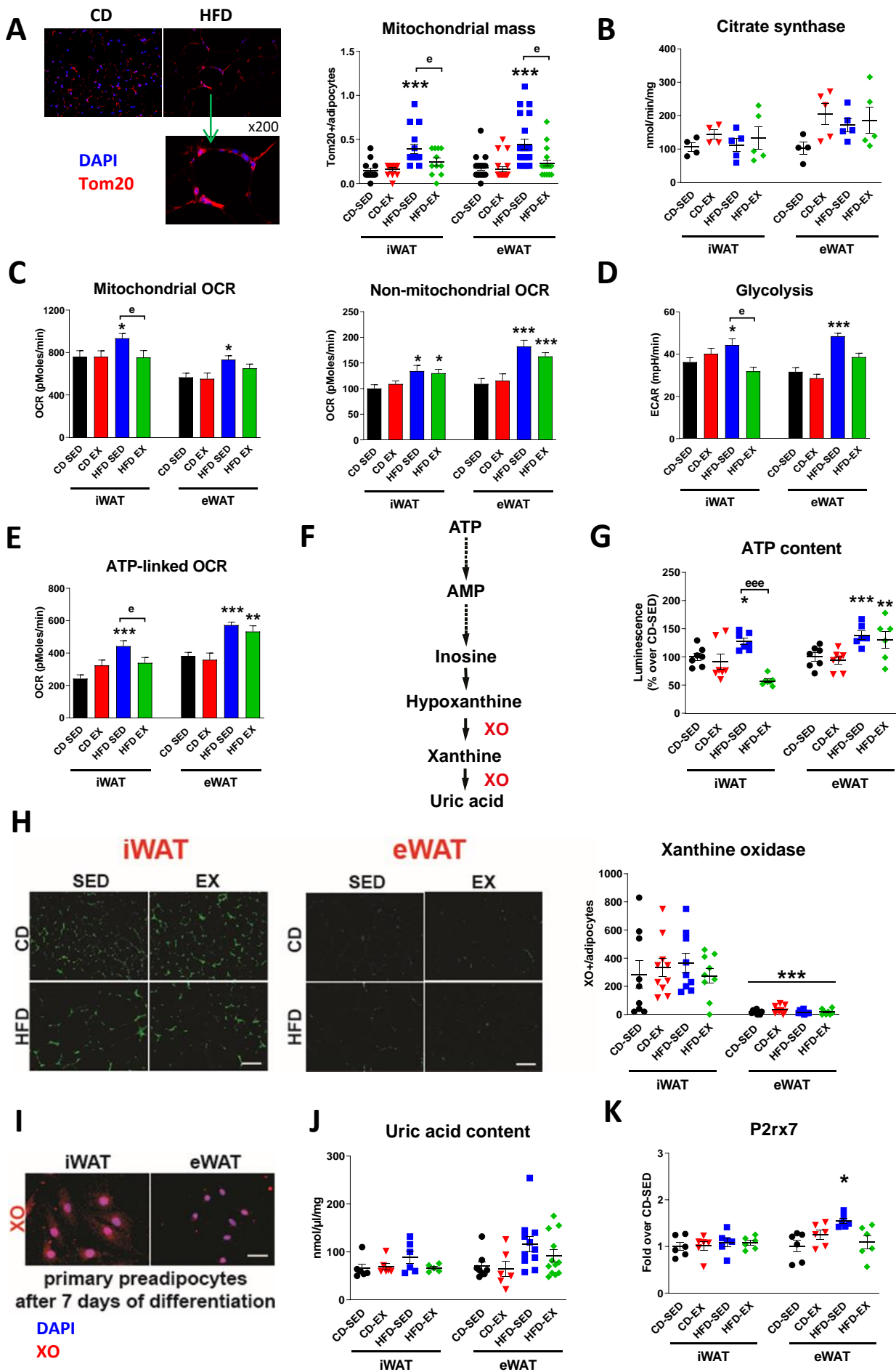


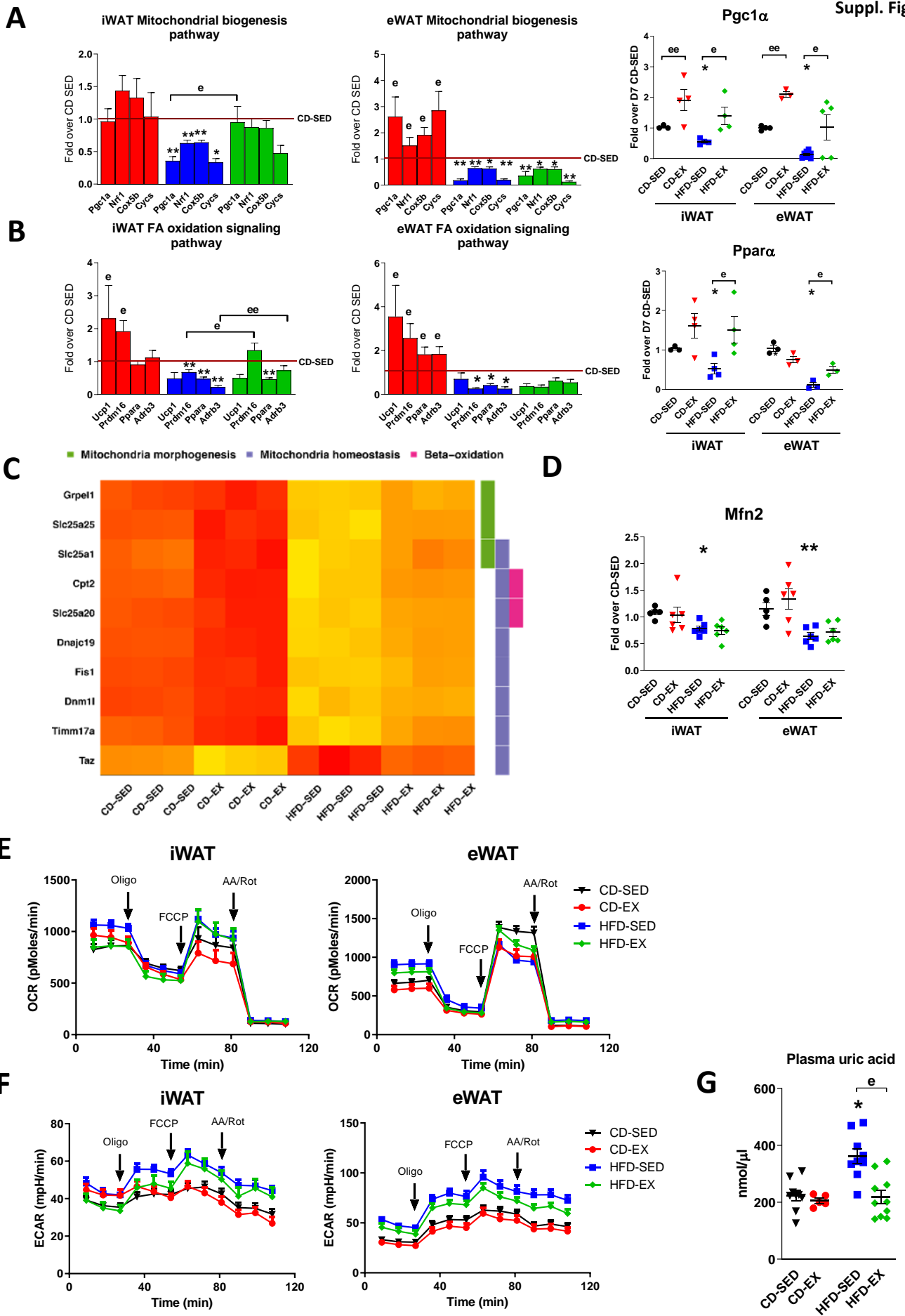


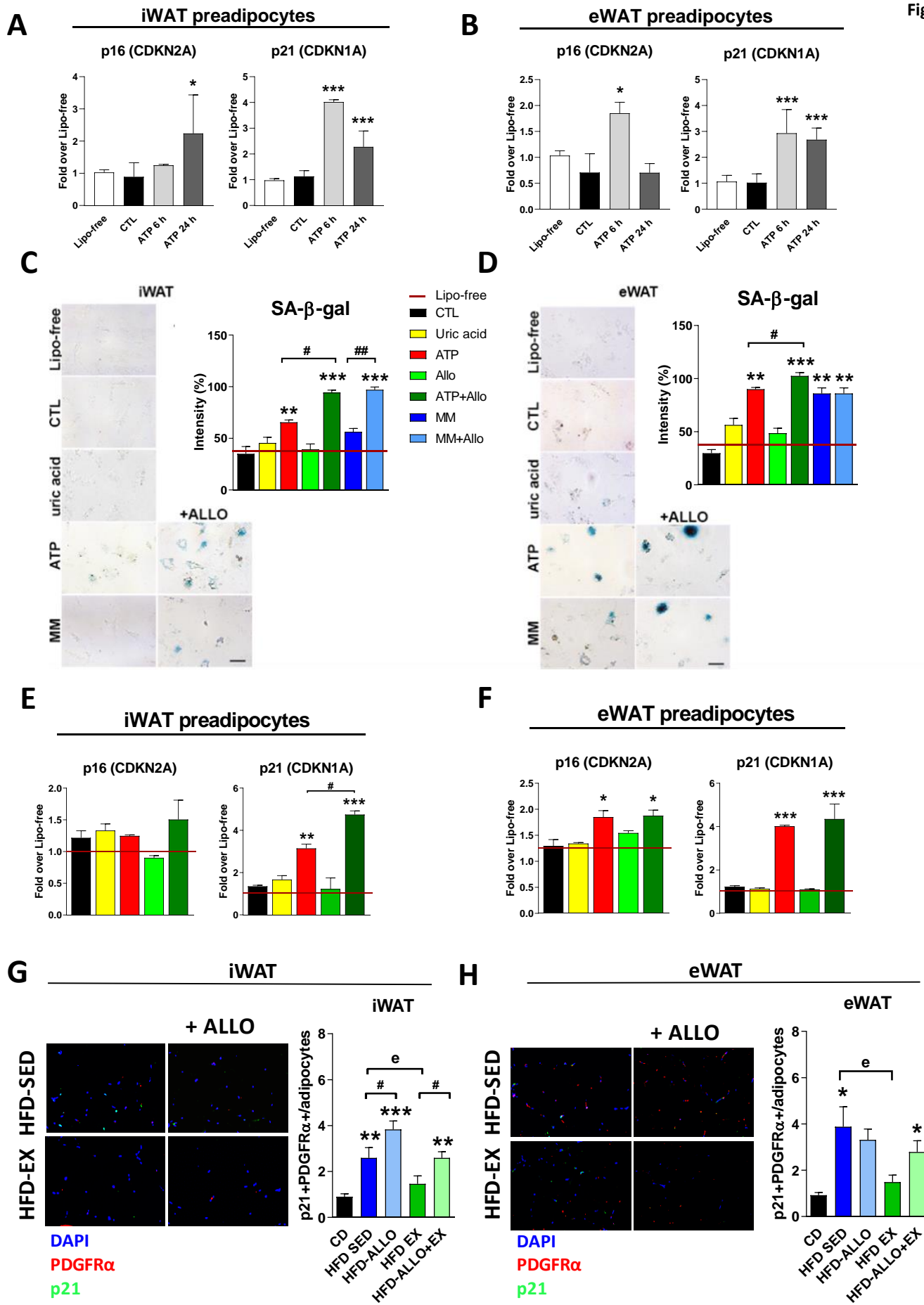


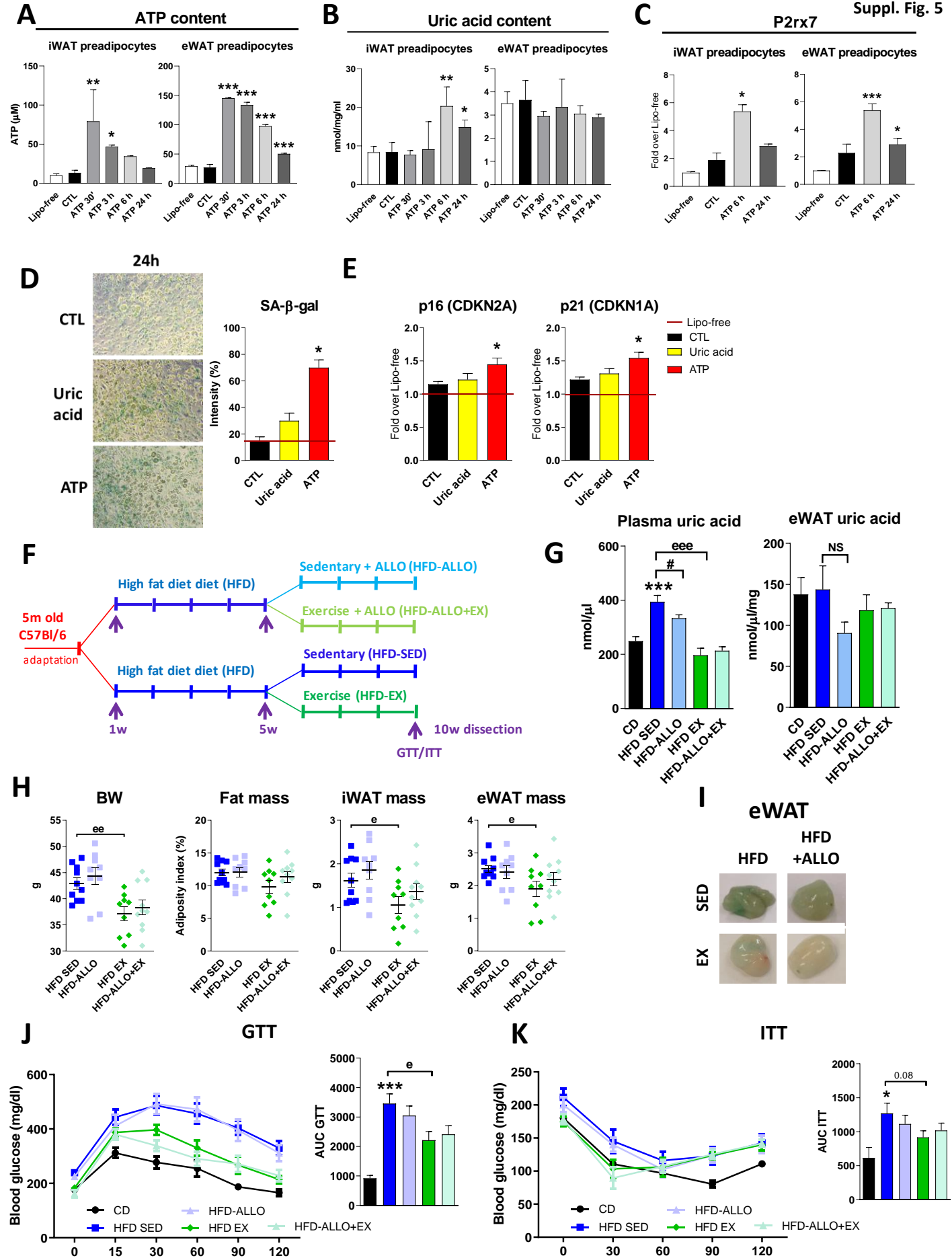


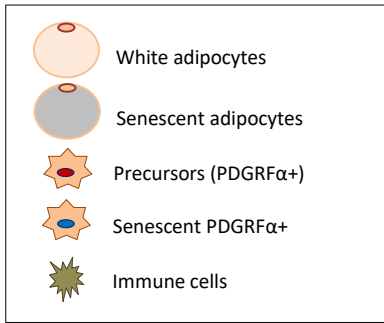








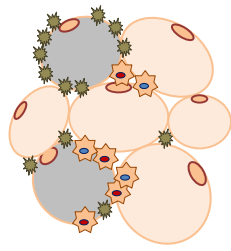




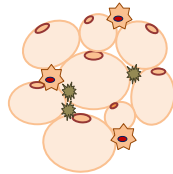
Chow diet



HFD



HFD + Exercise



↑ Senescence (β -gal, p16, p21)
 ↑ Glycolysis
 ↑ ATP content

↓ Senescence (β -gal, p16, p21)
 ↓ Glycolysis
 ↓ ATP content

STUDY 4

ETUDE 4

Résumé

Le vieillissement cardiaque est caractérisé par un remodelage du myocarde avec une hypertrophie des cardiomyocytes et le développement d'une fibrose interstitielle, ainsi qu'un dysfonctionnement diastolique et systolique. Des études récentes de métabolomique ont mis en évidence le rôle des acides aminés dans le vieillissement. Notre travail a pour but d'étudier et de comprendre comment le vieillissement conduit à une augmentation du taux plasmatique de la phénylalanine (Phe), un acide aminé essentiel, et comment la Phe induit le dysfonctionnement cardiaque observé avec le vieillissement.

Afin de répondre à ces questions, des modèles murins (jeunes et âgés, sauvages et mutants : délétés pour le gène p21, un inhibiteur du cycle cellulaire et marqueur de sénescence, donc des souris protégées contre le vieillissement cellulaire) et cellulaires (cellules musculaires C2C12) ont ainsi été utilisés et différents traitements ont été administrés (traitement avec de la Phe, avec du tetrahydrobiopterin (BH4), cofacteur essentiel de l'enzyme phénylalanine hydroxydase (Pah), ou encore avec Nutlin3a, activateur de p53 et inducteur de sénescence).

Les résultats obtenus ont démontré une augmentation avec l'âge du taux plasmatique de Phe qui concorde avec les altérations cardiaques observées avec le vieillissement, tandis qu'en l'absence de p21, ces changements ne se manifestent pas. De plus, des souris jeunes traitées avec Phe montrent un phénotype cardiaque similaire à celui de souris âgées, tandis que des souris âgées traitées avec BH4 montrent des taux plasmatiques réduits de Phe ainsi qu'un phénotype cardiaque rajeuni. Pour finir, des observations faites sur des échantillons plasmatiques humains et murins indiquent un rôle essentiel du catabolisme hépatique de Phe et de son dysfonctionnement dans l'augmentation du taux sanguin de cet acide aminé et des conséquences cardiaques observées.

Toutes ces données apportent la preuve de l'effet délétère et pathogène de l'augmentation des taux plasmatiques de Phe sur le cœur et offrent de nouvelles cibles thérapeutiques pour le traitement des altérations cardiaques associées au vieillissement.

1 **Dysregulated phenylalanine catabolism is a defining characteristic of cardiac aging**

2
3 Gabor Czibik, MD, PhD,^{1,*§} Zaineb Mezdari, MSc,^{1*} Dogus Murat Altintas, PhD,^{1*} Juliette Bréhat,
4 MSc,¹ Maria Pini, PhD,¹ Elisabeth Riant, MD,^{1,2} Costin Radu, MD,^{1,3} Thomas d'Humières, MD,^{1,2}
5 Marielle Breau, PhD,¹ Hao Liang, MSc,¹ Cecile Martin, PhD,¹ Azania Abatan, BSc,¹ Rizwan Sarwar,
6 MRCP, PhD,⁴ Ophélie Marion, MSc,¹ Suzain Naushad, MD,¹ Yanyan Zhang, MD, PhD,¹ Maissa
7 Halfaoui, MSc,¹ Nadine Suffee, PhD,^{5,6} Didier Morin, PhD,¹ Serge Adnot, MD, PhD,^{1,8}, Stéphane
8 Hatem, MD, PhD,^{5,6,9} Arash Yavari, MRCP, DPhil,^{4,7} Daigo Sawaki, MD, PhD,^{1,‡} Geneviève
9 Derumeaux, MD, PhD^{1,8,‡§}

10
11
12 ¹INSERM U955, Université Paris-Est Créteil (UPEC), Créteil, France

13 ²AP-HP, Department of Cardiology, Henri Mondor Hospital, DHU-ATVB, Créteil, France

14 ³AP-HP, Department of Cardiac Surgery, Henri Mondor Hospital, DHU-ATVB, Créteil, France

15 ⁴Experimental Therapeutics, Radcliffe Department of Medicine (RDM) University of Oxford, Oxford,
16 United Kingdom

17 ⁵Sorbonne universités, INSERM UMR_S1166, Faculté de médecine UPMC, Paris, France

18 ⁶Institute of Cardiometabolism and Nutrition, ICAN, Paris, France

19 ⁷Wellcome Centre for Human Genetics, University of Oxford, Oxford, United Kingdom

20 ⁸AP-HP, Department of Physiology, Henri Mondor Hospital, DHU-ATVB, Créteil, France

21 ⁹Department of Cardiology, Assistance Publique - Hôpitaux de Paris, Pitié-Salpêtrière Hospital, Paris,
22 France

23
24
25 *Authors equally contributed to the work

26 ‡These authors served as senior authors

27 § Corresponding authors: gabor.czibik@inserm.fr & genevieve.derumeaux@inserm.fr

28
29 Word count of abstract: 325

30 Word count of main text: 4763

32 **Background:** Aging myocardium undergoes progressive cardiac hypertrophy and interstitial fibrosis
33 with diastolic and systolic dysfunction. Recent metabolomics studies shed light on amino acids in aging.
34 The present study aims to dissect how aging leads to elevated plasma levels of the essential amino acid
35 phenylalanine (Phe) and how Phe may promote age-related cardiac dysfunction.

36 **Methods:** We studied cardiac structure and function, together with Phe catabolism in WT and p21^{-/-}
37 mice aged between 2 and 24 months, the latter known to be protected from cellular senescence. To
38 explore Phe's effects on cellular senescence and ectopic Phe catabolism we treated primary adult rat or
39 human AC-16 cardiomyocytes with Phe. To establish a role for Phe in driving cardiac aging, wild-type
40 (WT) male mice were treated twice a day with Phe (200 mg/kg) for a month. Finally, we treated aged
41 WT mice with tetrahydrobiopterin (BH4; 10 mg/kg), the essential cofactor for Phe-degrading enzyme
42 phenylalanine hydroxylase (Pah) or restricted dietary Phe intake. The impact of aging on liver Phe
43 catabolism was explored *in vitro* in AML-12 hepatocytes subjected to Phe or Nutlin3a (a p53 activator)-
44 induced senescence with or without p21 siRNA or BH4, with Pah protein and tyrosine levels
45 determined.

46 **Results:** Natural aging induced progressive increase in plasma Phe levels concomitant with cardiac
47 dysfunction, whilst p21 deletion delayed these changes. Phe treatment induced cardiac deterioration in
48 young WT mice, strikingly similar to that occurring with age, whilst it triggered cellular senescence,
49 redox and epigenetic changes *in vitro*. Pharmacological restoration of Phe catabolism with BH4 or
50 dietary Phe restriction abrogated the rise in plasma Phe and reversed senescent cardiac alterations in
51 aged WT mice to a great extent. Our findings obtained from aged mice and human samples indicated a
52 key role for hepatic Phe catabolic decline in elevated plasma Phe levels compromising cardiac integrity.

53 **Conclusions:** Our findings establish a pathogenic role for increased Phe levels in cardiac aging and
54 highlight Phe/PAH modulation as a potential therapeutic target for age-associated cardiac impairment.

55 Aging leads to increased cellular senescence in organs, thus disrupting tissue structure and function
56 through a senescence-associated secretory phenotype consisting of pro-inflammatory cytokines,
57 extracellular matrix-degrading proteins and profibrotic factors.¹ Aging is therefore a major risk factor
58 for many life-threatening disorders including cardiovascular diseases, mainly heart failure.² A recent
59 report has shown that during aging cardiomyocytes acquire a senescent-like phenotype that contributes
60 to the age-related myocardial dysfunction.³ Indeed, aging myocardium undergoes adverse structural
61 alterations characterized by progressive cardiomyocyte hypertrophy, interstitial fibrosis and
62 inflammation, ultimately leading to diastolic and systolic dysfunction.^{4,6} Apart from traditional
63 cardiovascular risk factors (e.g. hyperlipidaemia, systemic hypertension and obesity), recognized to
64 accelerate cardiac aging,⁷ specific mechanisms have been explored,⁸ among others mitochondrial
65 oxidative stress,^{3,9} and myocardial activation of phosphoinositide 3-kinase (PI3K).¹⁰ In addition, our
66 group has recently pointed out that cardiac aging is a multisystem disease resulting from complex and
67 intertwined interactions with other organs, in particular visceral adipose tissue that exerts remote
68 adverse effects by releasing profibrotic factors, such as osteopontin and TGF β .⁶

69 In parallel, metabolomics shed light on the link between amino acids and aging/heart failure. In
70 particular, plasma levels of phenylalanine (Phe) in human subjects increase with age,¹¹⁻¹⁴ and inversely
71 correlate with leukocyte telomere length,¹⁵ a marker of aging.¹⁶ In addition, increased serum Phe levels
72 have been proposed as one of the metabolic fingerprints of heart failure.^{17, 18} Collectively, these findings
73 suggest that Phe may induce systemic senescence and cardiac dysfunction. Levels of Phe, an essential
74 amino acid, are regulated through degradation into tyrosine catalyzed by the tetrahydrobiopterin (BH4)-
75 dependent rate-limiting enzyme phenylalanine hydroxylase (Pah) physiologically restricted to liver and
76 kidney.¹⁹ Tyrosine (Tyr) is the precursor of catecholamines, which have been shown to be increased in
77 the aging process²⁰ and in heart failure. How aging leads to elevated Phe levels and how abnormal Phe
78 catabolism promotes cardiac senescence are currently unknown.

79 In the present study we demonstrate that Phe administration induced firstly a remarkable age-mimicking
80 cardiac deterioration in young mice and secondly cellular senescence *in vitro*. Hepatic Phe catabolism
81 declined with age in a p21-dependent manner, whilst p21 deficiency prevented age-related cardiac
82 dysfunction. Substantiating a role for impaired Phe catabolism in cardiac aging, the Pah cofactor BH4
83 or dietary Phe restriction abrogated the age-related rise in plasma Phe and reversed age-associated
84 cardiac alterations. Here we identify Phe/PAH modulation as a potential therapeutic strategy for
85 promoting cardiac health and preventing age-related cardiomyopathy.

86 **Methods**

87 The data, analytic methods, and study materials are available to other researchers, on reasonable request,
88 for the purpose of reproducing the results or replicating the procedures presented here.

89 **Animal husbandry**

90 All animal work was approved by the Institutional Animal Care and Use Committee of the French
91 National Institute of Health and Medical Research (INSERM)-Unit 955, Créteil, France (ComEth 15-
92 001). Global p21^{-/-} mice backcrossed to C57BL/6 background for at least 10 generations (Jackson
93 Laboratory, USA) as well as wild-type (WT) littermates or C57BL/6 mice of indicated ages (Janvier
94 Labs, France) were kept in individually ventilated cages in a high-health facility with 12-hour light-
95 dark cycle, controlled temperature (20-22°C) and humidity. Water and chow were provided *ad libitum*.

96 **Cardiac phenotyping**

97 WT and p21^{-/-} male mice were followed from the age of 2 to 24 months of age. These mice were
98 sequentially evaluated for myocardial structure and function (conscious echocardiography & *in vivo*
99 hemodynamic measurements). Animals were euthanized and tissues harvested for histology, molecular
100 biology or metabolic readouts (at ages 2, 6, 10 15 and 24 months). Other WT mice received *in vivo* Phe
101 (as subcutaneous injections in a dose of 200 mg/kg 2x/die or 1x PBS as vehicle) or BH4 (as
102 intraperitoneal injections in a dose of 10 mg/kg/die 2x/die or vehicle consisting of 1x PBS with 10 mM
103 sodium ascorbate and citric acid to pH4.5) treatment. Dietary Phe restriction was achieved using a
104 custom-designed Phe-deficient diet (composition: Supplementary Table 1) supplemented with 20-25%
105 Phe of control diet in the drinking water. General state of the mice (body weight & wellbeing) was
106 closely monitored. All treatments were completed as scheduled without incidents.

107 **Data analysis and statistics**

108 Mice were randomly assigned to experimental groups and data were acquired and analyzed blind to
109 genotype, age or treatment. Statistical analyses were performed using GraphPad Prism Software
110 (version 6). Unpaired, two-tailed *t*-test was used to compare two groups, whilst more than two groups
111 were compared using one-way analysis of variance (ANOVA), with Bonferroni post-hoc test for
112 multiple comparisons. Two-way ANOVA was used to compare groups with time-dependent evolution
113 of readouts, with Bonferroni post-hoc test for more than two groups. Data are presented as mean ±
114 standard error of the mean or individual values. Annotations used: **p* < 0.05, ***p* < 0.01, ****p* < 0.001
115 compared to groups indicated. A *p* value of < 0.05 was considered significant.

116 **Details of standard molecular biology, cell culture, histology, biochemistry and *in vivo***
117 **experiments are described in the Supplementary Methods.**

118 **Results**

119 **p21 deficiency delays cardiac aging**

120 As a molecular signature of aging first we explored senescence in aging hearts, using common markers
121 of senescence in C57BL6 (WT) male mice between 2 and 24 months of age. We found that whilst p53
122 was not expressed before 2 years of age and p16 (cyclin-dependent kinase inhibitor 2a) not at all, p21
123 (cyclin-dependent kinase inhibitor 1a) was progressively expressed from 10 months of age (Fig.1A-C).
124 These results encouraged us to study p21^{-/-} mice with age-matched WT littermates as controls. Genomic
125 instability did not manifest in hearts of either genotype before 2 years of age (8-oxo-guanine, but not
126 phosphorylated γ -H2A.X; Supplementary Fig.1A). 4-hydroxynonenal (4-HNE), a marker of oxidative
127 stress, was increasingly expressed with age in WT hearts, which was considerably delayed in p21^{-/-} mice
128 (Supplementary Fig.1B).

129 Structurally, heart weight to tibia length (HW/TL) was increased at 10 and 15 months of age,^{5, 6} but
130 returned to young levels at 24 months of age in WT mice. Interestingly, HW/TL in p21^{-/-} mice did not
131 significantly change over the observation period and was smaller than in WT mice at 10-15 months of
132 age (Fig.1D). Myocardial interstitial fibrosis and vimentin-positive area (cardiac fibroblasts)
133 progressively increased with age in WT mice, which was significantly retarded in hearts of p21^{-/-} mice,
134 with the first increase occurring at 24 months of age (Fig.1E-F & Supplementary Fig.1C). We found no
135 evidence for cardiac amyloidosis in aged WT hearts (Supplementary Fig.1D).

136 WT mice exhibited hallmarks of myocardial functional aging, including progressive reductions in
137 relaxation (dP/dt_{min}) and contractility (dP/dt_{max}, systolic strain rate) recorded at comparable heart rates
138 (Supplementary Fig.1E-F), which was significantly delayed by p21 deficiency (Fig.1G-I). Left
139 ventricular ejection fraction was preserved during the observation period in both genotypes. (Fig.1J).⁵
140 Finally, urged by the widely reported observations of age-dependent increase in blood Phe levels in
141 humans¹¹⁻¹⁴ we measured plasma Phe levels. Consistent with human studies, we found an age-dependent
142 increase in WT animals (at 15 and 24 months), again significantly delayed in p21^{-/-} mice (first increased
143 at 24 months; Fig.1K). Collectively, p21 deficiency delayed age-related structural and functional
144 myocardial damage together with a postponed rise in plasma Phe levels.

145

146 **Ectopic Phe catabolism in the aging myocardium is delayed with p21 deficiency.**

147 The constellation of myocardial structural/functional decline and increase in plasma Phe concentrations
148 delayed in p21^{-/-} mice compared to age-matched WT littermates motivated us to explore Phe-related
149 effects in aged hearts. First, we studied myocardial expression of Phe transporters. At 15 months of
150 age – the last age in our series when p21 deficiency allowed full protection against age-related structural
151 and functional decline (Fig.1) – transcript levels of Slc43a2 alone showed an age-dependent
152 upregulation in WT hearts, which was prevented in hearts of p21^{-/-} mice (Fig.2A). At this age, however,

153 almost all Phe transporters showed higher myocardial expression in WT mice compared to hearts of
154 p21^{-/-} mice (Fig.2A). Given that Pah is the rate-limiting enzyme of Phe catabolism possibly leading to
155 fumarate and the non-enzymatic, irreversible, fumarate-induced posttranslational modification known
156 as succination^{21, 22} we explored ectopic Phe catabolism in the myocardium (Fig.2B). Intriguingly, we
157 found an age-dependent myocardial induction of Pah, fumarate and 2-SC (2-succinylcysteine, the
158 structural basis for succination; Fig.2C-D), delayed by p21 deficiency. In line with the local demand to
159 supply BH4 for Pah activity, GTP cyclohydrolase 1 (Gch1), the rate-limiting enzyme in *de novo* BH4
160 biosynthesis (Fig.2B), was upregulated in WT hearts at 15 months of age but not in hearts of p21^{-/-} mice.
161 The succination-sensitive Nrf2-antioxidant pathway²¹ followed this pattern (Supplementary Fig.3H-I).
162 Consistent with Pah-mediated production of fumarate, Pah and 2-SC co-localized in elderly murine and
163 human hearts alike (Fig.2E-F). In light of fumarate's energetic role as a Krebs-cycle intermediate,
164 importantly we found no sign for compromised energetics up to 15 months of age; by contrast,
165 mitochondrial complex V activity was impaired at 24 months of age in both genotypes (Fig.2G, data
166 not shown and Supplementary Fig.2E). In search of further downstream consequences of ectopic Phe
167 catabolism in the aging heart, we studied levels of H3K9me3, a recently proposed senescence marker.²³
168 Levels of this transcriptionally repressive histone code are regulated by KDM4 histone demethylases,
169 whose cofactor 2-oxoglutarate (2-OG) is subject to competitive inhibition by increased fumarate levels
170 (Fig.2H).²⁴ Accordingly, H3K9me3 was increasingly expressed in WT myocardium starting at 10
171 months of age and this was delayed in hearts of p21^{-/-} mice (first induced at 24 months of age; Fig.2I).
172 Taken together, our data demonstrate an age-associated induction of myocardial Phe catabolism with
173 redox and epigenetic consequences, which was delayed by p21 deficiency.

174

175 ***In vitro* phenylalanine treatment mimics changes characteristic of cardiac aging.**

176 To identify affected cells within the myocardium, first we stained hearts of 24-month-old WT mice with
177 p21 against cell type-specific markers. p21 co-localized with troponin I (cardiomyocytes) and vimentin
178 (cardiac fibroblasts), but not CD31 (endothelial cells; Fig.3A). To establish a role for Phe in cellular
179 senescence *in vitro*, we treated primary adult rat cardiomyocytes with Phe. Phe mimicked *in vivo*
180 findings in aged WT hearts in two important aspects: it selectively induced p21 (but not p16 and
181 phospho-p53 or p-p53; Fig.3B) and p21 expression was extranuclear (Fig.3C). BH4 antagonized Phe-
182 dependent p21 induction, suggesting that it may catalyze Phe catabolism (Fig.3B). In support, we found
183 that Phe treatment greatly elevated intracellular Phe levels (by ~35-fold), partially reversed by co-
184 treatment with BH4 (Fig.3D). Moreover, Phe treatment alone increased levels of Phe end-catabolite
185 fumarate, whose levels BH4 did not further increase (Fig.3E), probably due to the reactive nature of
186 fumarate. These results establish cardiomyocytes as a powerful Phe-buffer when challenged with
187 elevated Phe levels.

188 With regard to the p53-independent p21 induction by Phe, we hypothesized that Phe interferes with p21
189 protein degradation, another important way of p21 regulation.²⁵ To address this, we treated primary
190 adult rat cardiomyocytes with Phe or vehicle without or with proteasome inhibitor MG132. Notably,
191 Phe not only induced p21 protein, but also inversely reduced levels of a ~55 kDa unidentified band
192 (Fig.3F). MG132 alone increased the density of both bands (especially at ~55 kDa), but adding Phe
193 enhanced band intensity only at 21 kDa, whilst reducing it at ~55 kDa (Fig.3F). These findings
194 suggested Phe inhibiting p21 ubiquitination, where the ~55 kDa band may correspond to an
195 ubiquitinated form of p21 (one ubiquitin unit is 8.6 kDa, so native p21 with the maximal 4 lysil-ubiquitin
196 units equals to 55.4, which is in close vicinity of the size of the unidentified band). To explore this, we
197 immunoprecipitated p21 in MG132-treated human AC-16 cardiomyocytes and indeed found its
198 ubiquitination prevented by Phe to a great extent (Fig.3G).

199 Moreover, in Phe-treated cardiomyocytes there were increased cytosolic superoxide and suppressed
200 reduced glutathione levels (GSH) rescued by the addition of BH4, with no changes in mitochondrial
201 superoxide levels (Fig.3H & Supplementary Fig.3A-B). Notably, in Phe-treated cardiomyocytes BH4
202 greatly induced succination and succination-sensitive Nrf2 signaling (Fig.3H-I & Supplementary
203 Fig.3C). Moreover, GSH levels after Phe/BH4 co-administration were dependent on the pentose
204 phosphate pathway (PPP), as the PPP inhibitor dehydroepiandrosterone (DHEA) impaired the rescue
205 (Supplementary Fig.3D). This is consistent with the Phe/BH4-dependent upregulation of Nrf2 target
206 G6pd, the rate-limiting enzyme of PPP (Fig.3I). Apart from redox signaling Phe induced H3K9me3
207 expression, which was further enhanced by BH4 (Supplementary Fig.3C).

208 Next, we explored Pah induction. In hearts of 24-month-old WT mice Pah was expressed by
209 cardiomyocytes, cardiac fibroblasts and endothelial cells alike, however, the predominant expression
210 came from cardiomyocytes (Supplementary Fig.3E). For this reason we explored Pah expression in
211 cardiomyocytes. Phe alone or in combination with BH4 failed to induce Pah protein (Supplementary
212 Fig.3F). Substances such as H₂O₂ (known to induce Pah in melanocytes)²⁶ or HDAC inhibitor sodium
213 butyrate (to facilitate open chromatin and Pah transcription as reported for cardiac aging)²⁷ alone did
214 not induce Pah levels in cultured cardiomyocytes, only if they were combined with Phe (Supplementary
215 Fig.3G-H).

216 Finally, since both p21 and Pah were expressed in vimentin+ cardiac fibroblasts of 24-month-old WT
217 hearts mice, we treated murine neonatal cardiac fibroblasts with Phe. We found that Phe treatment
218 induced Acta2, a marker of fibroblast activation, as well as p21, Mmp9, Gdf15 and Tgfb2, the latter
219 two found induced in cardiac fibroblasts of 30-month-old WT mice³ (Fig.3J & Supplementary Fig.3I).

220 Taken together, *in vitro* Phe treatment recapitulated multiple aspects of cardiac aging, including
221 induction of senescence, ectopic Phe catabolism, succination, epigenetic and redox changes.

222

223 **Experimental hyperphenylalaninemia promotes cardiac aging *in vivo*.**

224 To replicate human age-related hyperphenylalaninemia¹¹⁻¹⁴ experimentally, we treated WT mice with
225 Phe vs. vehicle (VEH). Capitalizing on our observations in the time-course experiments (Fig.1-2) we
226 subjected two groups of mice to a 1-month treatment, corresponding to the absence (5-month-old) or
227 presence (11-month-old) of age-related myocardial structural, functional and molecular alterations
228 (Fig.4A).

229 Mice tolerated Phe treatment well without significant weight loss (Supplementary Fig.4A). Plasma Phe
230 levels increased with both age and Phe treatment, suggesting limited Phe catabolic reserve (Fig.4B).
231 Phe treatment in young mice mimicked myocardial structural changes observed in vehicle-treated old
232 mice, i.e. cardiac hypertrophy and interstitial fibrosis (Fig.4C-G), but no amyloid depositions
233 (Supplementary Fig.4B). Phe administration to young mice strikingly recapitulated age-associated
234 cardiac dysfunction, with impaired relaxation (dP/dt_{min}) and contractility (dP/dt_{max} & systolic strain rate)
235 but preserved LV ejection fraction (Fig.4H-K & Supplementary Fig.4C-D).^{5,6} Age and Phe comparably
236 upregulated myocardial p21, Pah, Gch1, 2-SC, H3K9me3 and 4-HNE without altering myocardial
237 energetics (Fig.4L & Supplementary Fig.4E-K). Like in natural aging p21 and Pah were expressed by
238 both cardiomyocytes and cardiac fibroblasts with *in vivo* Phe treatment (Supplementary Fig.4L-M).
239 Collectively, *in vivo* Phe treatment is sufficient to induce cardiac aging in young mice, whilst its failure
240 to aggravate adverse myocardial changes in elderly mice suggests Phe's involvement in cardiac aging.

241

242 **BH4 treatment rescues age-related cardiac dysfunction.**

243 Since Phe induces cardiac aging, we hypothesized that augmenting Phe catabolism could improve
244 cardiac function in older mice. To address this, we administered BH4 to 11-month-old WT mice for 6
245 weeks to enhance Pah activity and thereby reduce plasma Phe levels (Fig.5A & Supplementary Fig.5A).
246 BH4 neither influenced arterial pressures nor myocardial nitric oxide synthase (NOS) activity, a group
247 of enzymes using BH4 as a cofactor (Fig.5B-C).^{26, 27} By contrast, BH4 treatment suppressed age-
248 associated myocardial expression of p21, Pah, Gch1 & 2-SC (Fig.5D & Supplementary Fig.5B) and
249 robustly reduced interstitial fibrosis and cardiac hypertrophy (Fig.5E-H). *In vivo* BH4 treatment restored
250 myocardial relaxation and contractility towards that of young mice (Fig.5I-K). Thus, BH4
251 administration can rejuvenate aged myocardium.

252

253 **BH4 rescues age-related hepatic Pah decline.**

254 Had BH4 acted in the heart directly, we would have expected increased myocardial NOS activity and
255 Phe catabolism. In the absence of such changes, we investigated the contribution of tissues

256 physiologically expressing Pah, namely the kidney and liver. Whilst aging had no impact on renal Pah
257 or Gch1 expression, we found markedly reduced hepatic Pah and Gch1 protein levels in old WT mice,
258 the latter prevented by p21 deficiency (Supplementary Fig.6A-B & Fig.6A). From here we proceeded
259 to determine levels of Phe transporters. Interestingly, quantitative RT-PCR analysis identified three
260 distinct expression patterns amongst Phe transporters: 1. Expression declined in an age-dependent
261 manner, independent of p21 (Slc7a5 & Slc16a10); 2. No change occurred with age and loss of p21
262 (Slc43a2) and 3. Age-dependent upregulation in WT livers was prevented by p21 deficiency (Slc1a5 &
263 Slc7a8; Fig.6B). Subsequently, we confirmed protein induction of Slc7a8 in 15-month-old WT livers
264 absent in age-matched p21^{-/-} livers (Fig.6C). Collectively, these findings indicate that livers from p21-
265 ^{-/-} mice were immune to some Phe-related changes occurring with age.

266 Based on Slc7a8's higher affinity for Phe than its paralogue Slc7a5's,²⁸ we hypothesized that an age-
267 related Phe transporter shift may increase hepatic uptake of Phe with functional consequences. To
268 obtain direct evidence *in vivo*, first we stained livers of vehicle- or Phe-treated WT mice, finding
269 induction of Slc7a8, which associated with suppressed Pah expression (Fig.6D). With Phe transport
270 increased and Phe catabolism impaired, we reasoned that there should be more Phe in the liver. Indeed,
271 we found that compared to 6-month-old vehicle-treated mice, Phe treatment substantially increased
272 hepatic Phe content, comparable to that observed in older mice in 12-month-old WT mice untreated
273 with Phe (Fig.6E). These results indicate that Phe treatment and age both increase hepatic Phe content.

274 Next we explored if this excess Phe induces p21. We found an age-dependent induction of hepatic p21
275 expression (but not p-p53 and p16; Fig.6F & Supplementary Fig.6C). To address this further we treated
276 murine AML-12 hepatocytes with Phe and found a dose-dependent p21 induction (Fig.6G), whilst Pah
277 expression declined (Fig.6H).

278 Since aging induced liver senescence, we hypothesized that senescence undermines hepatic Phe
279 catabolism. We therefore treated AML-12 cells with the p53 activator Nutlin3a to indirectly induce p21.
280 Nutlin3a induced hepatocyte senescence, downregulated Pah and lowered tyrosine production, changes
281 reversed by siRNA-mediated p21 knockdown (Fig.6I-J & Supplementary Fig.6D-F). Moreover, BH4
282 administration rescued Pah and tyrosine levels from Nutlin3a-induced reduction *in vitro*
283 (Supplementary Fig.6G-I) and resulted in re-expression of hepatic Pah with reduced liver Phe content
284 and increased hepatic Pah activity *in vivo* (Fig.6K-M).^{29, 30} Finally, we found that in murine livers Pah
285 was not only expressed at orders of magnitude greater levels than other BH4-dependent enzymes, but
286 was also the only one that showed an age-dependent downregulation (Supplementary Fig.6J). Analysis
287 of a transcriptomic dataset from non-diseased human liver biopsies confirmed a progressive reduction
288 in *PAH* expression with age (Fig.6N). Taken together, advanced age undermines hepatic Phe catabolism
289 that is reversible with BH4 treatment.

290

291 **Dietary Phe restriction rejuvenates old hearts.**

292 To reinforce that lowering Phe levels rejuvenates the aged myocardium, we designed a diet deficient of
293 Phe differing only in the absence of Phe from its control diet (Supplementary Table 1). A pilot study
294 showed that mice on Phe-deficient diet lost weight compared to either Phe-containing control diet or
295 chow, probably due to interference with protein turnover. To circumvent this confounding effect, we
296 re-supplemented 20-25% Phe of control diet in drinking water that stopped weight loss. Then we
297 subjected 23-month-old WT mice to Phe-deficient diet with 20-25% Phe supplementation (Phe-) or
298 control diet (Phe+) for 4 weeks and evaluated effects.

299 Food intake, body weight, adiposity index and glucose tolerance was not influenced by Phe- diet
300 (Supplementary Fig.7A-D). At the end of Phe- diet plasma Phe levels were reduced towards values
301 observed around 2-6 months of age or 12.5 months with BH4 treatment (Fig.7A vs. Fig.1K, Fig.4B &
302 Fig.5A). Importantly, myocardial p21 expression and readouts of ectopic Phe catabolism were reversed
303 to a great extent by Phe- diet (Fig.7B). Moreover, hearts of Phe- mice displayed substantially reduced
304 interstitial fibrosis (Sirius red: by ~65%, vimentin+ area: by ~50%; Fig.7C-E) and improvement of
305 contractility and relaxation (dP/dt_{max} and dP/dt_{min} by ~30%, strain rate in conscious mice by 60%;
306 Fig.7G-I) at comparable heart rates and LV ejection fraction (Supplementary Fig.7E-G). The strength
307 of dietary Phe limitation is further illustrated by rendering 2-year-old hearts functionally and
308 structurally comparable to much younger mice (Supplementary Fig.7H-K). These results demonstrate
309 that elevated Phe levels represent an important determinant in cardiac aging, which is reversible by
310 therapeutic interventions.

311

312 **Discussion**

313 Our study provides new mechanistic insights into cardiac aging with important implications. Firstly, we
314 demonstrate that aging increases plasma Phe levels and that elevated plasma Phe levels induce cardiac
315 senescence and dysfunction, a phenotype inducible with Phe treatment in young mice. Secondly, we
316 show that age-related increase in p21 suppresses hepatic Pah function, the latter crucial in controlling
317 systemic Phe levels. Thirdly, p21 deficiency delays structural, functional and molecular alterations in
318 the aging myocardium whilst Pah cofactor BH4 or dietary Phe restriction reverses them. Collectively,
319 our findings may provide diagnostic clues for cardiac aging and open new therapeutic avenues to
320 rejuvenate aged myocardium, an important challenge in the face of high cardiovascular burden in the
321 growing population of elderly individuals.³¹

322 **Hyperphenylalaninemia promotes cardiac aging**

323 Notably, our murine experiments recapitulated elevated plasma Phe levels observed in elderly human
324 subjects.¹¹⁻¹⁴ Subsequently, we found that Phe excess induced myocardial p21, hence cardiac
325 senescence. Furthermore, increased plasma levels of the essential amino acid Phe pointed to its impaired
326 global catabolism, an observation particularly interesting in light of myocardial induction of Pah, Gch1
327 and 2-SC that we found in aged hearts confirming progressive induction of myocardial Pah transcripts
328 by aging.^{10, 27} This strongly suggests that in hyperphenylalaninemia myocardium acts to maintain Phe
329 homeostasis through induction of its catabolic machinery. In the course of this adaptation, however,
330 cardiac Phe catabolism may itself promote myocardial aging through altered intracellular signaling by
331 protein succination,²² as we have demonstrated in aging human and murine myocardium. Equally, but
332 not exclusively, increased Phe uptake with limited myocardial Phe catabolic capacity may result in the
333 accumulation of toxic metabolites, such as phenylpyruvate, phenyllactate and phenylacetate.³²
334 Moreover, increased ectopic Phe catabolism into tyrosine may fuel catecholamine biosynthesis in
335 tyrosine hydroxylase-expressing cells, such as certain neurons and chromaffin cells of the adrenal
336 medulla.²⁰ Thus, elevated Phe levels have an adverse impact on cardiac health, as evidenced by
337 structural and functional myocardial impairment with a signature of senescence and Phe catabolism.

338 **BH4 treatment rejuvenates the aging myocardium by restoring hepatic Pah activity**

339 Our findings support a paradigm of age-related hepatic hypocatabolism of Phe underlying age-related
340 rise in plasma Phe and driving cardiac aging. This is in line with downregulation of *Pah*, one of the six
341 BH4-dependent enzymes with the highest hepatic expression. *Pah*'s vital dependence on its natural
342 cofactor, BH4, is illustrated by hyperphenylalaninemia being a prominent feature of enzymatic
343 deficiencies in *de novo* BH4 biosynthesis or the recycling pathway.³³

344 Importantly, we restored healthy cardiac structure and function in naturally aged mice through
345 normalizing plasma Phe levels by BH4, consistent with revived hepatic *Pah* activity.^{29, 30} In line with

346 this, we found reduced Pah and tyrosine levels in AML12 hepatocytes with pharmacologically
347 stimulated senescence that could be rescued by both p21 knockdown and BH4. In theory, other BH4-
348 dependent enzymes, i.e. nitric oxide synthases (NOS) could play a role in the cardiac improvement
349 observed with BH4 treatment. Improved vascular NOS coupling and subsequently reduced left
350 ventricular afterload³⁴⁻³⁶ is unlikely since systemic blood pressure remained unaltered by intraperitoneal
351 BH4 delivery. Moreover, BH4 treatment did not increase myocardial NOS activity. Lack of such
352 changes is consistent with the reported failure of exogenously delivered BH4 to reach efficient systemic
353 concentrations³⁴ due to predicted BH4 uptake of natural Phe-expressing organs: the liver and kidney.³⁷
354 Restored indices of myocardial Phe catabolism by BH4 correspond to BH4 uptake by the liver fuelling
355 its Pah activity taking the burden of Phe catabolism off the heart. This is consistent with the lack of
356 reduction in cardiac damage induced by pressure overload in cardiomyocyte-restricted Gch1 transgenic
357 mice³⁸ as opposed to oral BH4 administration.³⁹ Finally, the salubrious myocardial effects of dietary
358 Phe restriction underscores the importance of lowering systemic Phe levels to rejuvenate old hearts.

359 Collectively our data show that pharmacological restoration of hepatic *Pah* activity by BH4 may
360 rejuvenate age-associated cardiac changes and have potential application in age-related cardiac disease,
361 such as heart failure.

362 **Age-dependent p21 compromises hepatic *Pah* activity**

363 Whilst Phe induced p21 in hepatocytes and cardiomyocytes *in vitro*, aging upregulated p21 expression
364 in both liver and heart, hallmarking senescence of these organs. Moreover, we uncover the absence of
365 age-related rise in plasma Phe levels and cardiac decline in p21^{-/-} mice indicating that there are particular
366 age-related gain-of-function(s) attributable to p21. Accordingly, in cultured hepatocytes we established
367 a Phe-dependent p21 induction; experimental p21 induction on the other hand was sufficient to
368 compromise Pah expression and activity in hepatocytes, which could be rescued by BH4 co-treatment.
369 This constitutes a vicious cycle: Phe induces hepatic p21, p21 compromises hepatic Pah
370 expression/activity, which raises systemic Phe levels and the cycle starts all over again. Interestingly,
371 neither Phe- nor p21-mediated life-shortening is unprecedented; whilst dietary addition of Phe reduces
372 lifespan in *C. elegans*⁴⁰ and ants,⁴¹ p21 deficiency increases it in mice.⁴² As for our findings, we
373 identified one novel function for p21, which is the suppression of hepatic *Pah* expression/activity,
374 through which p21 is a key node for the rise in plasma Phe levels with age.

375 **Cardiac aging: a quiescent organ and cellular senescence?**

376 Cellular senescence of the heart is intriguing due to the postmitotic status of cardiomyocytes (~30% of
377 all heart cells occupying 80% of the heart's volume)⁴³ that do not fall under Hayflick's concept of
378 senescence, the proliferative inability in otherwise division-competent cells.⁴⁴ Aged cardiomyocytes
379 acquire a senescent-like phenotype characterised by persistent DNA damage at telomere regions that

380 occur independent of cell division and telomere length.³ This length-independent telomere damage in
381 cardiomyocytes activates senescent pathways (p21) and raises secretion of pro-fibrotic and -
382 hypertrophic factors.³ Autocrine/paracrine effects of this secretome include proliferation of cardiac
383 fibroblasts and their activation towards myofibroblasts. In addition to this intramyocardial cascade, we
384 uncovered a role for visceral adipose tissue, adding an endocrine enhancement to cardiac aging by
385 releasing a profibrotic secretome (e.g. Tgfb1, osteopontin and leptin).⁶ Therefore, cardiac aging seems
386 to result from complex interactions as part of an integrated multi-disorder state.

387 The present study extends this organism-level approach to cardiac aging by studying circulating
388 metabolic signals. Since metabolic screens showed increased plasma Phe levels occurring in both
389 natural aging and heart failure, we specifically studied the role of plasma Phe in cardiac aging.^{11, 13-15, 17,}
390 ^{18, 27} Our findings in age-related and experimentally induced hyperphenylalaninemia confirmed a causal
391 relationship between elevated plasma Phe levels and cardiac decline.

392 **A new piece in the puzzle: the natural course of cardiac aging**

393 Murine investigations into cardiac aging traditionally explore animals with at least 18 months of age.
394 These studies among others identified dysfunctional sirtuin/NAD⁺ biology,⁴⁵ mitochondrial oxidative
395 stress,⁹ abnormal PI3K/Akt signaling, misfolded proteins,¹⁰ telomere dysfunction, DNA damage³ and
396 compromised mitochondrial energetics⁴⁶ in aged hearts. Our findings synergize with the literature
397 extending our understanding of the natural history of cardiac aging. For instance, in WT hearts at 24
398 months of age we observed elevated complex III activity with suppressed ATP synthase activity
399 pointing to the former as a potential mitochondrial source of oxidative stress.⁹

400 The early onset of age-related functional decline is most evident by the time-limited competitiveness of
401 elite athletes, which typically predates heart disease. Accordingly, during our time-course we found
402 clinically detectable impairments in myocardial structure and function as early as 10 months of age. Up
403 to and including the age of 15 months we found no sign of myocardial DNA damage, impaired
404 mitochondrial complex activities, alterations in NAD⁺/NADH levels (re: energetics and sirtuins). On
405 the contrary, we observed an emergence of myocardial p21 expression, ectopic Phe catabolism with
406 increased succination, redox imbalance and epigenetic changes starting at 10 months of age. These
407 structural, functional and molecular alterations associated with elevated plasma Phe levels, were
408 inducible with Phe treatment *in vitro* and in young WT mice *in vivo*, as well as were (depending on age
409 at least partially) reversible with interventions controlling systemic Phe levels (*in vivo* BH4 treatment
410 and dietary Phe restriction). These results demonstrate that dysregulated Phe catabolism is an early-
411 onset, persistent component of cardiac aging, preceding mechanisms described to date, and importantly,
412 it is amenable to therapeutic correction.

413 **Conclusions**

414 Our findings unlock a novel approach to rejuvenate the aged myocardium by pharmacological
415 restoration of aging-induced Phe catabolic decline. The potential of targeting Phe is highlighted by
416 related abnormalities starting at middle age and persisting throughout life. Our observations may be
417 extended to other age-related disorders, such as dementia,⁴⁷ susceptibility to cancer,^{48, 49} and all-cause
418 mortality risk⁵⁰ that could benefit from a strategy of counteracting the adverse effects of a declining
419 PAH activity.

420

421

422 **Acknowledgements**

423 We are grateful to Prof. Elizabeth Blackburn, University of California, San Francisco for helpful
424 discussions and suggestions. We thank Dr. Fatima Clerc, University of Paris Est Créteil, for providing
425 AML-12 cells. Xavier Decrouy, Christelle Gandolphe, Wilfried Verbecq-Morlot of the Histology Core
426 Facility and members of EP3 platform at IMRB U955 facility are gratefully acknowledged for their
427 excellent technical support. This work was supported by the RHU-CARMMA Grant (ANR-15-RHUS-
428 0003).

429

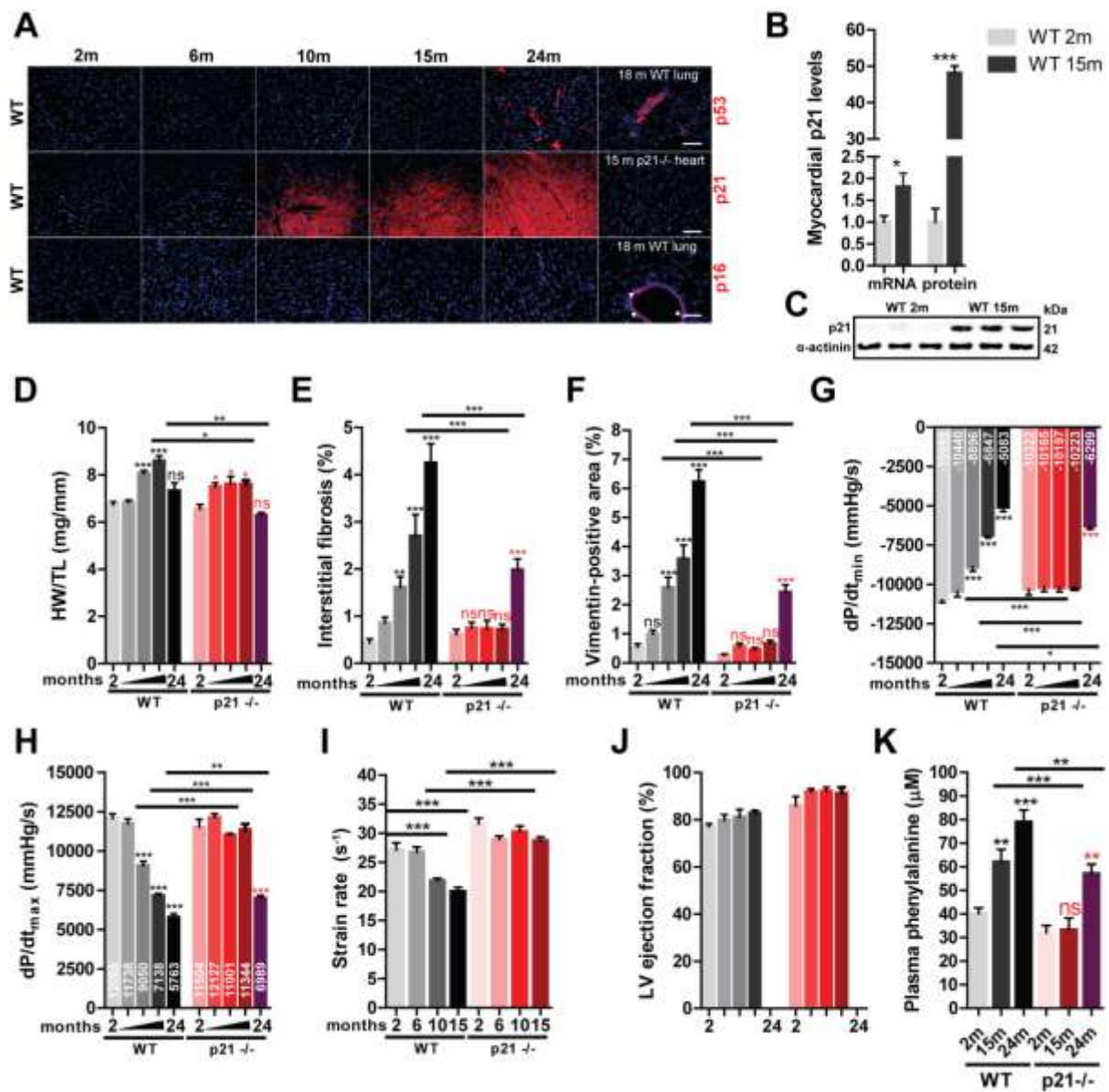
430 **Disclosures**

431 None.

432

433

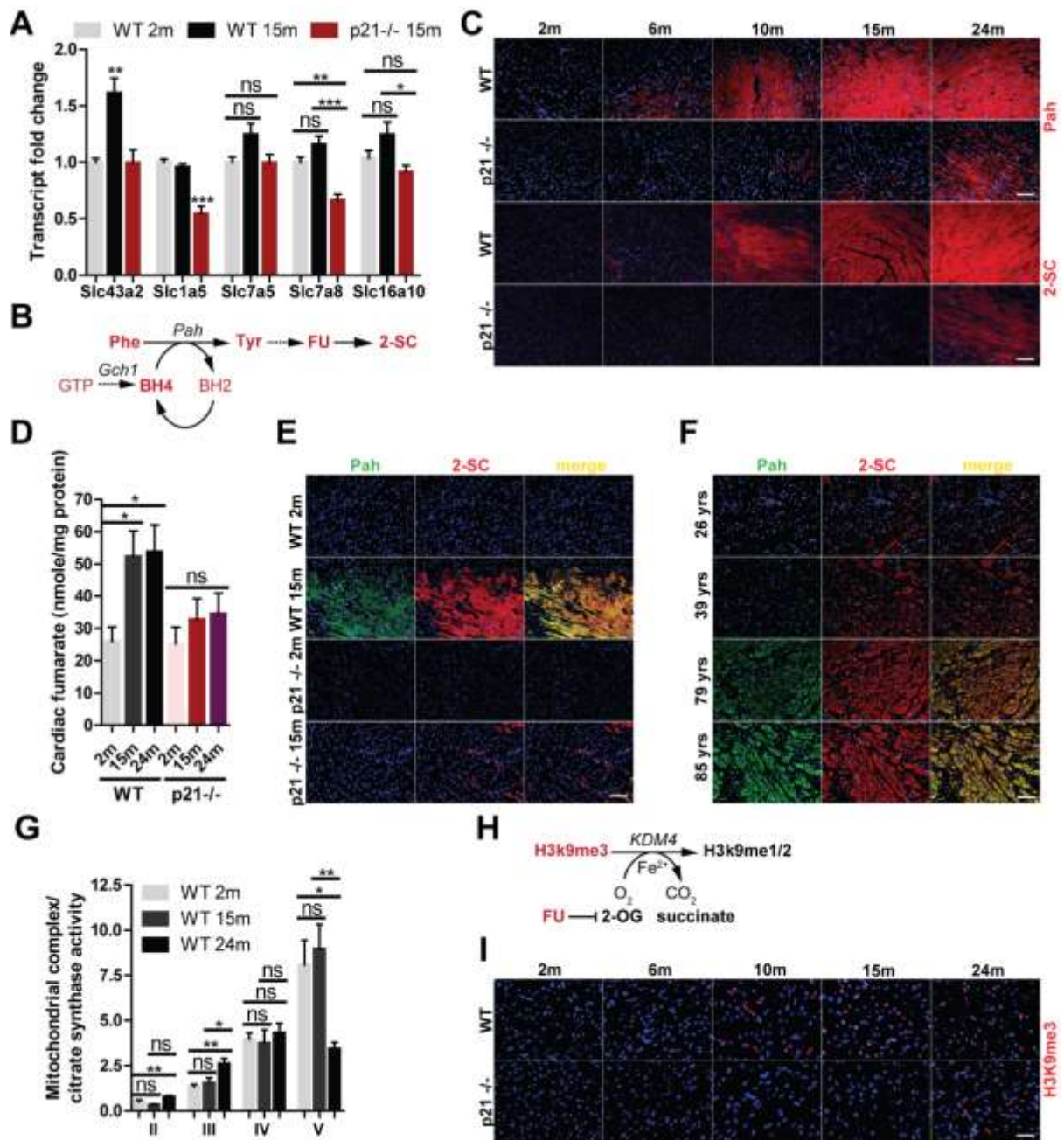
434



436

437 **Figure 1. p21 deficiency delays cardiac aging.** **A**, Expression of senescence markers in hearts of wild-
 438 type (WT) mice aged between 2 and 24 months (m; n=4/condition). **B-C**, Myocardial p21 transcript
 439 (n=7/age) and protein (n=3/age) levels in 2 and 15 month-old WT mice. Results are expressed as fold
 440 change over 2-month-old WT mice. **D**, Heart weight to tibial length (HW/TL) of WT and p21^{-/-} mice
 441 (n=8-12/condition). **E-F**, Quantification of myocardial interstitial fibrosis (**E**; Sirius red staining) and
 442 vimentin-positive areas of WT and p21^{-/-} mice at indicated ages (**F**; n=5/condition). **G-J**, dP/dt_{min} (**G**),
 443 dP/dt_{max} (**H**), systolic strain rate (**I**) & ejection fraction (**J**) of WT and p21^{-/-} mice at indicated ages (n=8-
 444 12/condition). **K**, Plasma Phe levels in 2, 15 and 24 month-old WT and p21^{-/-} mice (n=8-12/group).
 445 Shades of grey: WT, shades of color: p21^{-/-} at 2, 6, 10, 15 and 24 months with darker tones
 446 corresponding to older ages. For all microscopic images, magnification: 200x, scale-bar: 50 μm. Data
 447 are presented as original images (**A** & **C**) or mean ± SEM analyzed with Student's t-test (**B**) or one-way
 448 ANOVA with Bonferroni post-hoc test (**D-K**); ns: non-significant, **p* < 0.05, ***p* < 0.01, ****p* < 0.001.
 449 Stars above bars represent comparisons to 2 month-old of the same genotype (black: WT, red: p21^{-/-}).

450



451

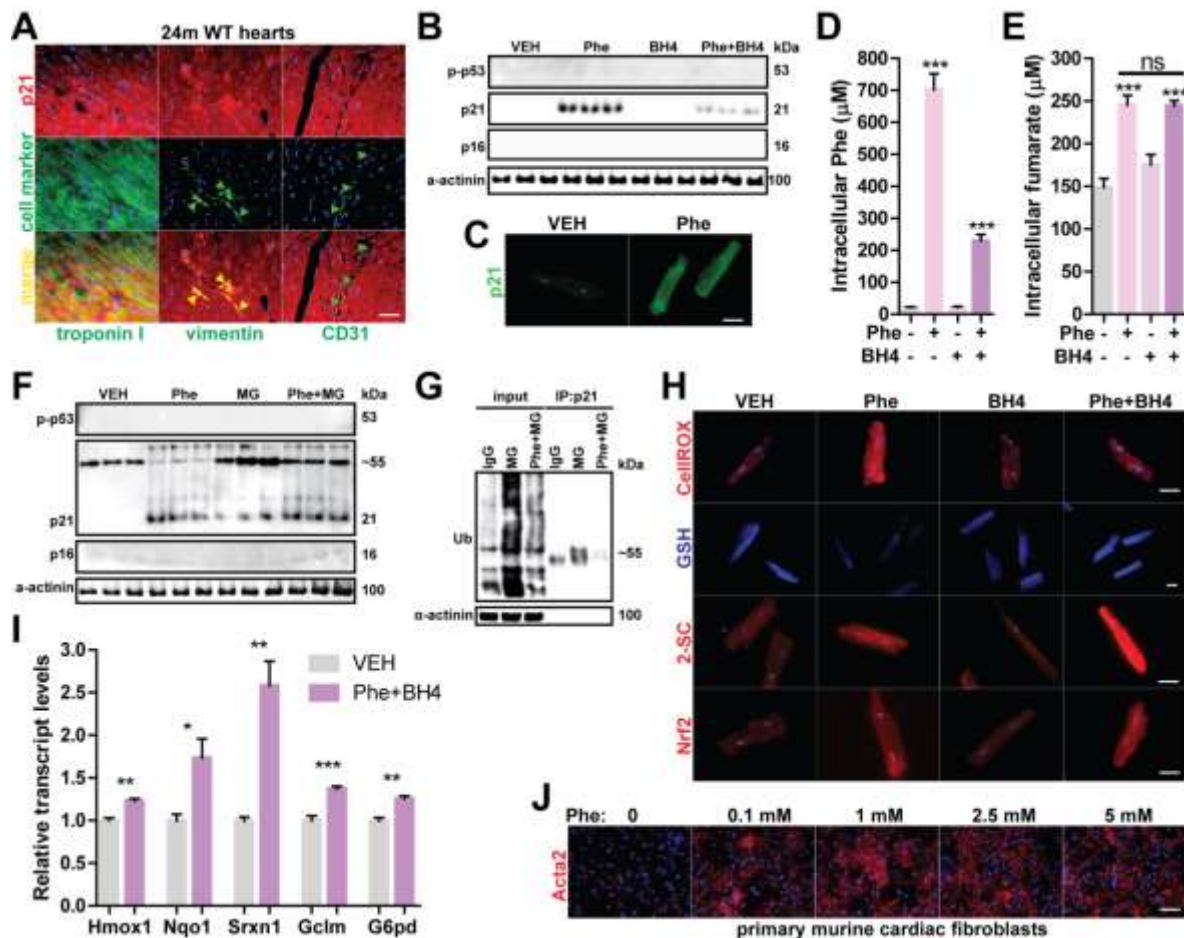
452 **Figure 2. Development of ectopic phenylalanine (Phe) catabolism in the aging myocardium and**
 453 **its delay with p21 deficiency.** **A**, Myocardial transcript levels of Phe transporters in 2 and 15 month-
 454 old WT and 15 month-old p21^{-/-} mice (n=5-8/group). **B**, Schematic to illustrate simplified Phe
 455 catabolism (phenylalanine hydroxylase: Pah; tyrosine: Tyr; fumarate: FU; 2-succinylcysteine: 2-SC;
 456 GTP cyclohydrolyase 1: Gch1; tetra/dihydrobiopterin: BH4/BH2). **C**, Myocardial immunofluorescence
 457 for Pah and 2-SC in WT and p21^{-/-} mice at indicated ages (n=4/condition). **D**, Cardiac fumarate levels
 458 in indicated conditions (n=5-10/condition) **E-F**, Representative Pah/2-SC immunofluorescent co-
 459 labeling in murine (**E**; n=3/condition) and human (**F**) hearts at indicated ages and genotypes. **G**
 460 Mitochondrial complex activities (normalized to citrate synthase activity; n=8-9/group; in hearts of 2,
 461 15 and 24 month-old WT mice). **H**, Fumarate interferes with the activity of histone demethylase 4
 462 (KDM4) resulting in higher levels of H3K9me3 (2-oxoglutarate: 2-OG). **I**, Myocardial
 463 immunofluorescence for H3K9me3 in WT and p21^{-/-} mice at indicated ages (n=4/condition). Data are
 464 presented as original images (**C**, **E-F**, magnification: 200x, scale-bar: 50 μ m; **I**, magnification: 400x,

465 scale-bar: 25 μ m) or mean \pm SEM analyzed with one-way ANOVA with Bonferroni post-hoc test (**A**,
466 **D, G**); ns: non-significant, * $p < 0.05$, ** $p < 0.01$, *** $p < 0.001$.

467

468

469

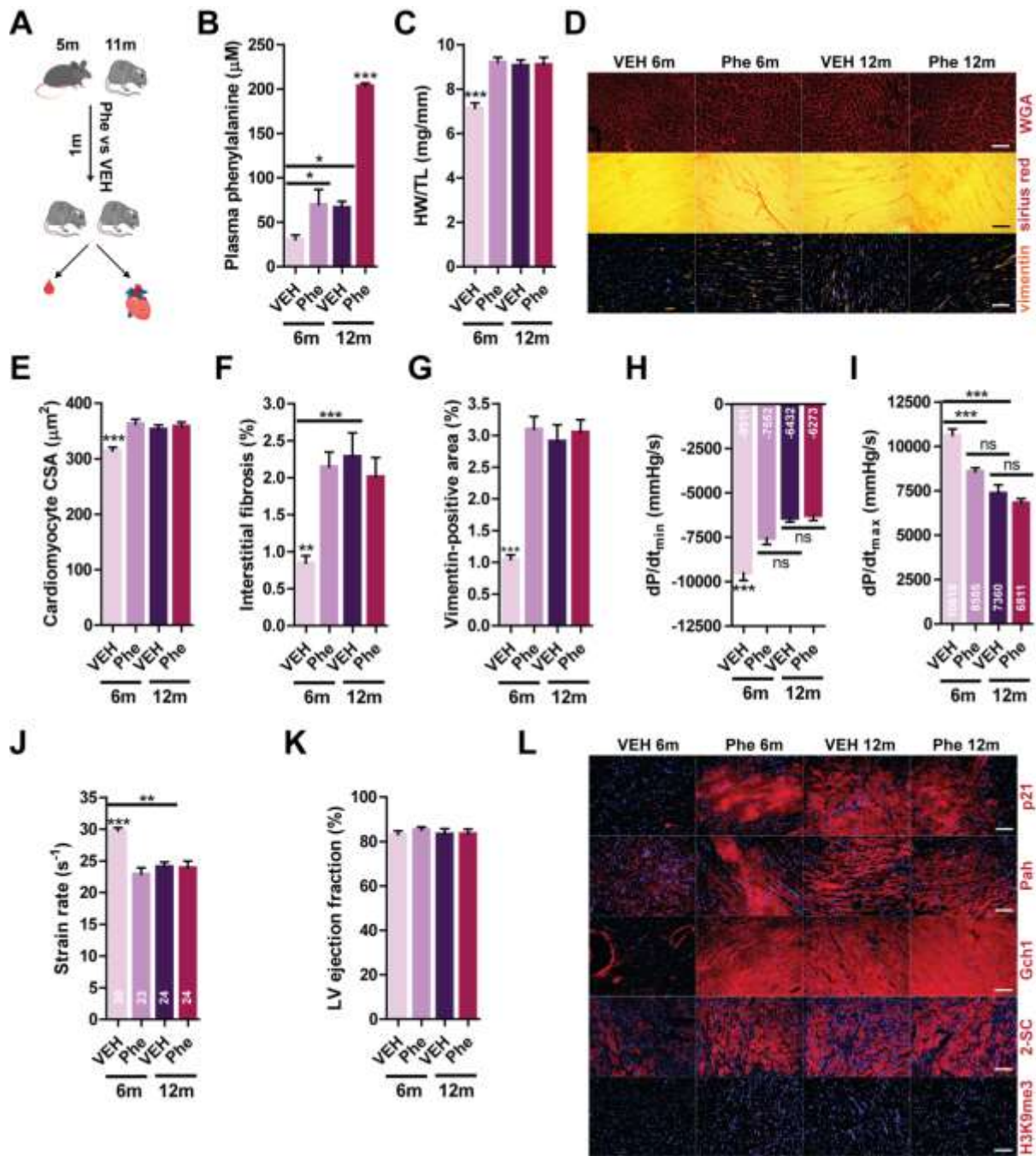


470

471 **Figure 3. Effects of phenylalanine treatment *in vitro*.** **A**, Myocardial p21 expression against markers
 472 of cardiomyocytes (troponin I), fibroblasts (vimentin) and endothelial cells (CD31) in 24-month-old
 473 WT mice. **B**, Immunoblot of indicated markers of senescence in primary adult rat cardiomyocytes
 474 treated with Phe (5 mM) and/or BH4 (10 μM ; n=3/treatment). **C**, Immunofluorescence of p21 after Phe
 475 treatment. **D-E**, Intracellular Phe (**D**) and fumarate (**E**) levels in primary adult rat cardiomyocytes
 476 treated with Phe and/or BH4 (n=6/treatment). **F**, Immunoblot of indicated markers of senescence in
 477 primary adult rat cardiomyocytes treated with Phe and/or proteasome inhibitor MG132 (MG: 10 μM ;
 478 n=3/treatment). **G**, Co-immunoprecipitation of p21 and reprobings for ubiquitin in human AC-16 cells
 479 after indicated treatments. **H**, Representative images of cytosolic superoxide (CellROX), reduced
 480 glutathione (GSH, ThiolTracker), 2-SC and Nrf2 in primary adult rat cardiomyocytes treated with Phe
 481 (5 mM) and/or BH4 (10 μM ; n=3/treatment). **I**, qRT-PCR analysis of Nrf2 target genes in vehicle and
 482 Phe+BH4 treated primary adult rat cardiomyocytes (n=4/treatment). **J**, Representative images of alpha
 483 smooth muscle actin (Acta2) expression in cardiac fibroblasts isolated from WT murine neonates
 484 treated with indicated concentrations of Phe (n=3/condition). For all microscopic images,
 485 magnification: 400x, scale-bar: 25 μm , except for GSH: magnification: 200x, scale-bar: 50 μm . Data
 486 are presented as original images (**A-C, F-H, J**) or mean \pm SEM analyzed with two-tailed unpaired t-test
 487 (**I**) or one-way ANOVA with Bonferroni post-hoc test (**D-E**); ns: non-significant, * $p < 0.05$, ** $p < 0.01$,
 488 *** $p < 0.001$ as indicated.

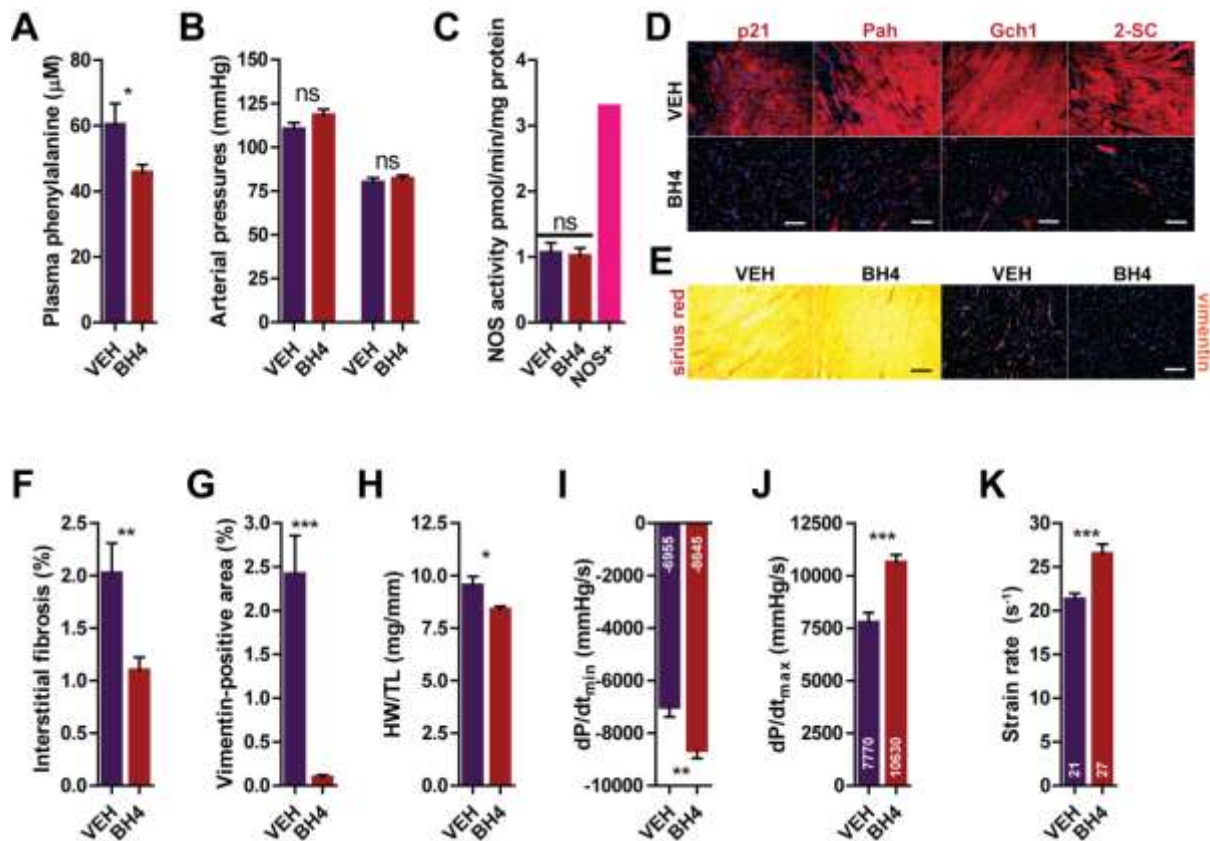
489

490



491

492 **Figure 4. Experimental hyperphenylalaninemia promotes cardiac aging *in vivo*.** A, Schematic of
 493 treatment and evaluation protocol. B, Plasma Phe levels in vehicle- or Phe-treated WT mice of 6 or 12
 494 months of age (n=8-11/group). C, Heart weight to tibial length (HW/TL) for the same groups (n=8-
 495 11/group). D, Representative images of hearts stained with wheat-germ agglutinin (WGA), sirius red
 496 or vimentin for the same groups (n=4/group). E-G, Quantification of cardiomyocyte cross-sectional
 497 area (CSA; E; n=4/group), interstitial fibrosis (Sirius red, F; n=4/group) and vimentin-positive areas
 498 (G; n=4/group) in hearts of the same animals as above. H-K, dP/dt_{min} (H), dP/dt_{max} (I), systolic strain
 499 rate (J) & LV ejection fraction (K; n=8-11/condition) in the same animals as above. L, Representative
 500 microscopic images of myocardial p21, Pah, Gch1, 2-SC & H3K9me3 immunofluorescence in the same
 501 animals as above (n=3-4/condition). For all microscopic images, magnification: 200x, scale-bar: 50 μm .
 502 Data are presented either as original images (D & L) or as mean \pm SEM analyzed with ANOVA with
 503 Bonferroni post-hoc test (B-C, E-K); ns: non-significant, * $p < 0.05$, ** $p < 0.01$, *** $p < 0.001$.



504

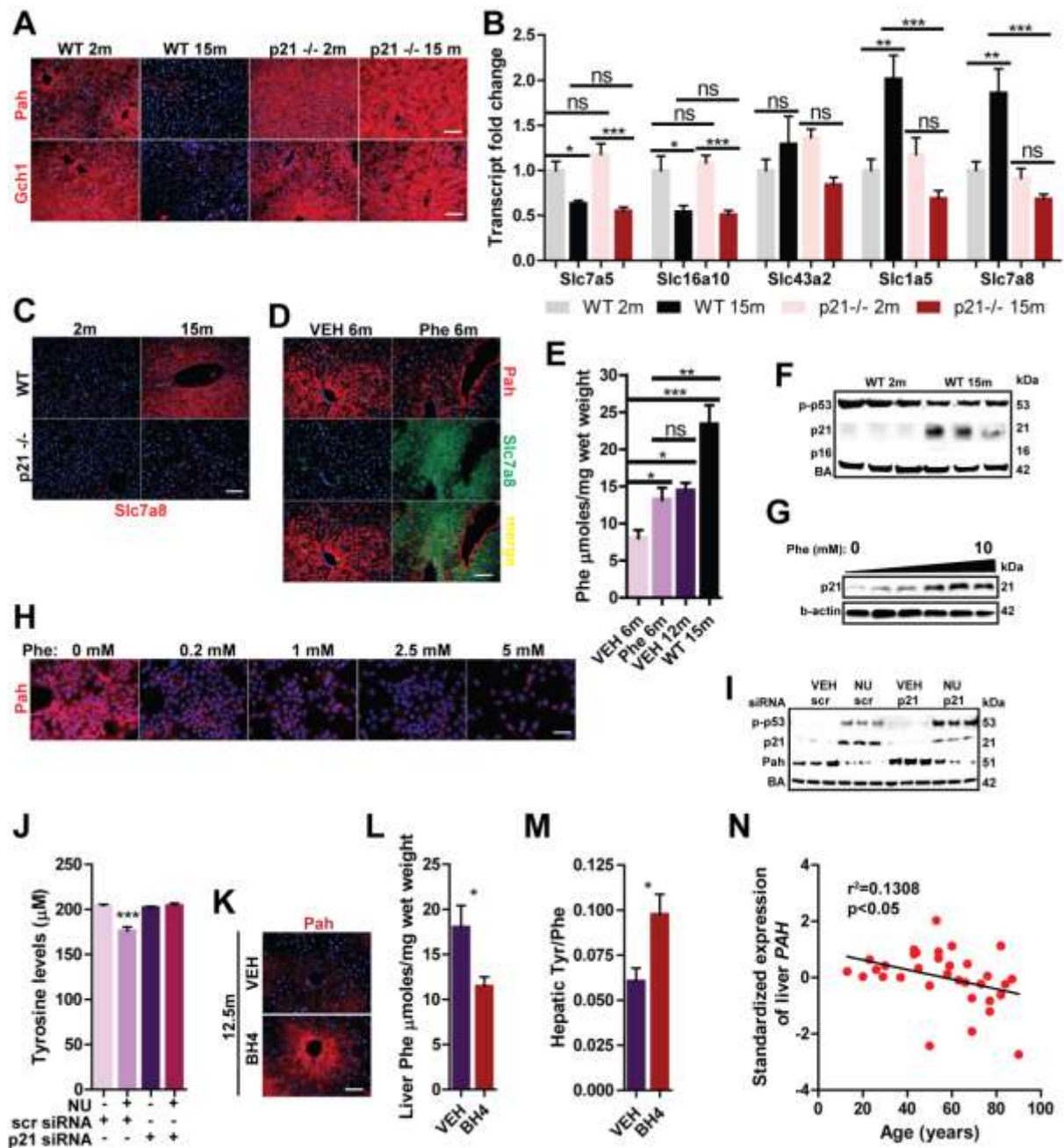
505 **Figure 5. BH4 treatment rescues age-related cardiac dysfunction.** **A**, Plasma Phe levels in 12.5
 506 month-old WT mice treated with intraperitoneal BH4 or vehicle (VEH; n=8-10/group). **B**, Systolic and
 507 diastolic arterial pressures in the same animals (n=9-10/group). **C**, Myocardial NOS activity in hearts
 508 of the same animals (n=9-10/group). **D**, Immunofluorescence of p21, Pah, Gch1 and 2-SC as above
 509 (n=4/group). **E**, Representative images of myocardial sirius red and vimentin staining with
 510 quantification (**F-G**; n=4/group). **H-K**, Heart weight to tibial length (**H**; HW/TL), dP/dt_{min} (**I**), dP/dt_{max}
 511 (**J**) & systolic strain rate (**K**; n=9-10/group) in mice treated as above. For microscopic images,
 512 magnification: 200x, scale-bar: 50 μm . Data are presented as original images (**D-E**) or mean \pm SEM
 513 and analyzed with two-tailed unpaired t-test (**A-C**, **F-K**); ns: non-significant, * $p < 0.05$, ** $p < 0.01$,
 514 *** $p < 0.001$.

515

516

517

518



519

520 **Figure 6. BH4 rescues age-related hepatic Pah decline.** A, Representative Pah and Gch1
 521 immunofluorescent images of livers in 2 and 15 month-old WT and p21^{-/-} mice (n=3/group). B, Relative
 522 transcript levels of Phe transporters in livers 2- and 15-month-old WT and p21^{-/-} mice (n=4-8/group).
 523 C, Representative immunofluorescence for Slc7a8 in livers of 2 and 15 month-old WT and p21^{-/-} mice
 524 (n=3/group). D, Representative immunofluorescent co-labeling for Slc7a8 and Pah in livers of 6-month-
 525 old vehicle- or Phe-treated WT mice (n=3/group). E, Hepatic Phe content in WT mice with indicated
 526 treatment and ages (n=7-10/group). F, Immunoblots of senescence markers 2- and 15-month-old WT
 527 as indicated (n=3/age). G-H, Expression of p21 (G) and Pah (H) in AML-12 hepatocytes as a function
 528 of Phe concentration. I-J, Immunoblots (I) of vehicle (VEH)- or Nutlin3a (NU)-treated AML-12
 529 hepatocytes transfected with p21-targeting or scrambled siRNA (n=3/condition) and tyrosine levels in
 530 media thereof (J; n=6/group). K, Representative immunofluorescence of liver Pah expression in
 531 vehicle- and BH4-treated 12.5-month-old WT mice (n=3/group). L-M, Liver Phe content (L), hepatic
 532 Tyr/Phe ratio (M) in the same groups of mice as K (n=7-10/group). N, Standardized expression of PAH

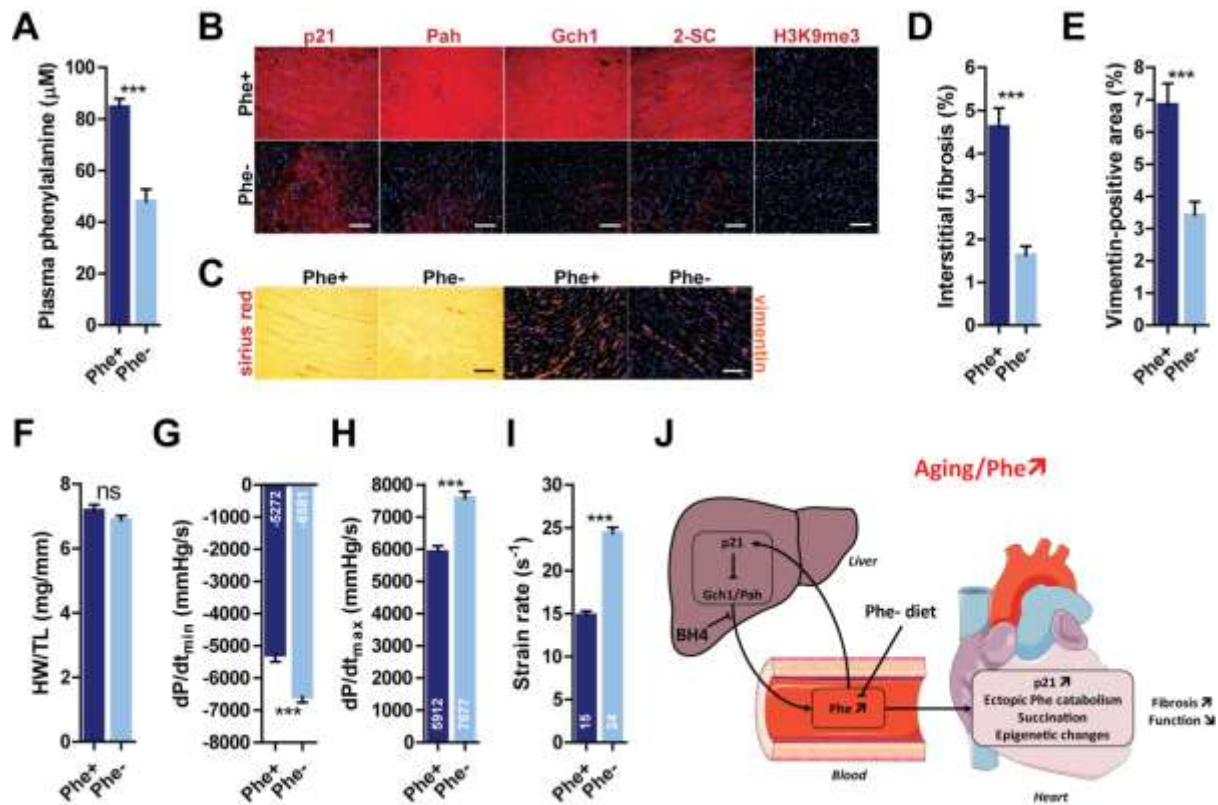
533 against age in biopsies from human liver donors (n=33). For microscopic images, magnification: 200x,
534 scale-bar: 50 μ m. Data are presented as original images (**A**, **C-D**, **F-I** & **K**) or mean \pm SEM and analyzed
535 with two-tailed unpaired t-test (**L-M**), one-way ANOVA with Bonferroni post-hoc test (**B**, **E**, **J**) or
536 linear regression analysis (**N**); ns: non-significant, * $p < 0.05$, ** $p < 0.01$, *** $p < 0.001$.

537

538

539

540



541

542 **Figure 7. Dietary Phe restriction rejuvenates old hearts.** **A**, Plasma Phe levels in 24 month-old WT
 543 mice fed Phe-deficient or control diet (Phe- and Phe+, respectively; n=10/group). **B**,
 544 Immunofluorescence of p21, Pah, Gch1, 2-SC and H3K9me3 as above (n=4/group). **C-E**, Sirius red
 545 and vimentin staining (Representative images: **C**; quantification: **D-E**; n=5/group). **F-I**, Heart weight
 546 to tibial length (HW/TL: n=11/group; **F**), dP/dt_{\min} (**G**), dP/dt_{\max} (n=9/group; **H**) & systolic strain rate
 547 (n=10-11/group; **I**) in mice treated as above. **J**, Cartoon summarizing age-dependent hepatic Phe
 548 catabolic decline, rise in blood Phe levels and ectopic Phe catabolism in the heart with potential
 549 therapeutic targets. For microscopic images, magnification: 200x, scale-bar: 50 μm . Data are presented
 550 as original images (**B-C**) or mean \pm SEM and analyzed with two-tailed unpaired t-test (**A, D-I**); ns: non-
 551 significant, * $p < 0.05$, ** $p < 0.01$, *** $p < 0.001$.

552

- 554 1. Munoz-Espin D, Serrano M. Cellular senescence: from physiology to pathology. *Nat Rev Mol*
555 *Cell Biol.*15(7):482-496.
- 556 2. Lazzarini V, Mentz RJ, Fiuzat M, Metra M, O'Connor CM. Heart failure in elderly patients:
557 distinctive features and unresolved issues. *Eur J Heart Fail.*15(7):717-723.
- 558 3. Anderson R, Lagnado A, Maggiorani D, Walaszczyk A, Dookun E, Chapman J, Birch J,
559 Salmonowicz H, Ogrodnik M, Jurk D, Proctor C, Correia-Melo C, Victorelli S, Fielder E,
560 Berlinguer-Palmini R, Owens A, Greaves LC, Kolsky KL, Parini A, Douin-Echinard V,
561 LeBrasseur NK, Arthur HM, Tual-Chalot S, Schafer MJ, Roos CM, Miller JD, Robertson N,
562 Mann J, Adams PD, Tchkonja T, Kirkland JL, Mialet-Perez J, Richardson GD, Passos JF.
563 Length-independent telomere damage drives post-mitotic cardiomyocyte senescence. *EMBO*
564 *J.*38(5).
- 565 4. Lakatta EG, Levy D. Arterial and cardiac aging: major shareholders in cardiovascular disease
566 enterprises: Part II: the aging heart in health: links to heart disease. *Circulation.*
567 2003;107(2):346-354.
- 568 5. Derumeaux G, Ichinose F, Raheer MJ, Morgan JG, Coman T, Lee C, Cuesta JM, Thibault H,
569 Bloch KD, Picard MH, Scherrer-Crosbie M. Myocardial alterations in senescent mice and
570 effect of exercise training: a strain rate imaging study. *Circ Cardiovasc Imaging.*
571 2008;1(3):227-234.
- 572 6. Sawaki D, Czibik G, Pini M, Ternacle J, Suffee N, Mercedes R, Marcelin G, Surenaud M,
573 Marcos E, Gual P, Clement K, Hue S, Adnot S, Hatem SN, Tsuchimochi I, Yoshimitsu T,
574 Henegar C, Derumeaux G. Visceral Adipose Tissue Drives Cardiac Aging Through Modulation
575 of Fibroblast Senescence by Osteopontin Production. *Circulation.*138(8):809-822.
- 576 7. Ternacle J, Wan F, Sawaki D, Surenaud M, Pini M, Mercedes R, Ernande L, Audureau E,
577 Dubois-Rande JL, Adnot S, Hue S, Czibik G, Derumeaux G. Short-term high-fat diet
578 compromises myocardial function: a radial strain rate imaging study. *Eur Heart J Cardiovasc*
579 *Imaging.* 2017.
- 580 8. Alfaras I, Di Germanio C, Bernier M, Csiszar A, Ungvari Z, Lakatta EG, de Cabo R.
581 Pharmacological Strategies to Retard Cardiovascular Aging. *Circ Res.*118(10):1626-1642.
- 582 9. Dai DF, Santana LF, Vermulst M, Tomazela DM, Emond MJ, MacCoss MJ, Gollahon K,
583 Martin GM, Loeb LA, Ladiges WC, Rabinovitch PS. Overexpression of catalase targeted to
584 mitochondria attenuates murine cardiac aging. *Circulation.* 2009;119(21):2789-2797.
- 585 10. Inuzuka Y, Okuda J, Kawashima T, Kato T, Niizuma S, Tamaki Y, Iwanaga Y, Yoshida Y,
586 Kosugi R, Watanabe-Maeda K, Machida Y, Tsuji S, Aburatani H, Izumi T, Kita T, Shioi T.
587 Suppression of phosphoinositide 3-kinase prevents cardiac aging in mice. *Circulation.*
588 2009;120(17):1695-1703.
- 589 11. Kouchiwa T, Wada K, Uchiyama M, Kasezawa N, Niisato M, Murakami H, Fukuyama K,
590 Yokogoshi H. Age-related changes in serum amino acids concentrations in healthy individuals.
591 *Clin Chem Lab Med.*50(5):861-870.
- 592 12. Bancel E, Strubel D, Bellet H, Polge A, Peray P, Magnan de Bornier B. [Effect of the age and
593 the sex on plasma concentration of amino acids]. *Ann Biol Clin (Paris).* 1994;52(9):667-670.
- 594 13. Caballero B, Gleason RE, Wurtman RJ. Plasma amino acid concentrations in healthy elderly
595 men and women. *Am J Clin Nutr.* 1991;53(5):1249-1252.
- 596 14. Cynober L, Blonde F, Nguyen Dinh F, Gerbet D, Giboudeau J. [Measurement of plasma and
597 urinary amino acids with gas chromatography in healthy subjects. Variations as a function of
598 age and sex]. *Ann Biol Clin (Paris).* 1983;41(1):33-38.
- 599 15. Eriksson JG, Guzzardi MA, Iozzo P, Kajantie E, Kautiainen H, Salonen MK. Higher serum
600 phenylalanine concentration is associated with more rapid telomere shortening in men. *Am J*
601 *Clin Nutr.*105(1):144-150.
- 602 16. Blackburn EH, Greider CW, Szostak JW. Telomeres and telomerase: the path from maize,
603 Tetrahymena and yeast to human cancer and aging. *Nat Med.* 2006;12(10):1133-1138.

- 604 17. Tenori L, Hu X, Pantaleo P, Alterini B, Castelli G, Olivotto I, Bertini I, Luchinat C, Gensini
605 GF. Metabolomic fingerprint of heart failure in humans: a nuclear magnetic resonance
606 spectroscopy analysis. *Int J Cardiol.* 168(4):e113-115.
- 607 18. Delles C, Rankin NJ, Boachie C, McConnachie A, Ford I, Kangas A, Soyninen P, Trompet S,
608 Mooijaart SP, Jukema JW, Zannad F, Ala-Korpela M, Salomaa V, Havulinna AS, Welsh P,
609 Wurtz P, Sattar N. Nuclear magnetic resonance-based metabolomics identifies phenylalanine
610 as a novel predictor of incident heart failure hospitalisation: results from PROSPER and
611 FINRISK 1997. *Eur J Heart Fail.* 2018;20(4):663-673.
- 612 19. Schuck PF, Malgarin F, Cararo JH, Cardoso F, Streck EL, Ferreira GC. Phenylketonuria
613 Pathophysiology: on the Role of Metabolic Alterations. *Aging Dis.* 2015;6(5):390-399.
- 614 20. Ziegler MG, Lake CR, Kopin IJ. Plasma noradrenaline increases with age. *Nature.*
615 1976;261(5558):333-335.
- 616 21. Ashrafian H, Czibik G, Bellahcene M, Aksentijevic D, Smith AC, Mitchell SJ, Dodd MS,
617 Kirwan J, Byrne JJ, Ludwig C, Isackson H, Yavari A, Stottrup NB, Contractor H, Cahill TJ,
618 Sahgal N, Ball DR, Birkler RI, Hargreaves I, Tennant DA, Land J, Lygate CA, Johannsen M,
619 Kharbanda RK, Neubauer S, Redwood C, de Cabo R, Ahmet I, Talan M, Gunther UL, Robinson
620 AJ, Viant MR, Pollard PJ, Tyler DJ, Watkins H. Fumarate is cardioprotective via activation of
621 the Nrf2 antioxidant pathway. *Cell Metab.* 2012;15(3):361-371.
- 622 22. Ternette N, Yang M, Laroyia M, Kitagawa M, O'Flaherty L, Wolhulter K, Igarashi K, Saito K,
623 Kato K, Fischer R, Berquand A, Kessler BM, Lappin T, Frizzell N, Soga T, Adam J, Pollard
624 PJ. Inhibition of mitochondrial aconitase by succination in fumarate hydratase deficiency. *Cell*
625 *Rep.* 3(3):689-700.
- 626 23. Di Micco R, Sulli G, Dobрева M, Liontos M, Botrugno OA, Gargiulo G, dal Zuffo R, Matti V,
627 d'Ario G, Montani E, Mercurio C, Hahn WC, Gorgoulis V, Minucci S, d'Adda di Fagagna F.
628 Interplay between oncogene-induced DNA damage response and heterochromatin in
629 senescence and cancer. *Nat Cell Biol.* 13(3):292-302.
- 630 24. Hoekstra AS, de Graaff MA, Briaire-de Bruijn IH, Ras C, Seifar RM, van Minderhout I,
631 Cornelisse CJ, Hogendoorn PC, Breuning MH, Suijker J, Korpershoek E, Kunst HP, Frizzell
632 N, Devilee P, Bayley JP, Bovee JV. Inactivation of SDH and FH cause loss of 5hmC and
633 increased H3K9me3 in paraganglioma/pheochromocytoma and smooth muscle tumors.
634 *Oncotarget.* 6(36):38777-38788.
- 635 25. Bloom J, Amador V, Bartolini F, DeMartino G, Pagano M. Proteasome-mediated degradation
636 of p21 via N-terminal ubiquitinylation. *Cell.* 2003;115(1):71-82.
- 637 26. Schallreuter KU, Wazir U, Kothari S, Gibbons NC, Moore J, Wood JM. Human phenylalanine
638 hydroxylase is activated by H₂O₂: a novel mechanism for increasing the L-tyrosine supply for
639 melanogenesis in melanocytes. *Biochem Biophys Res Commun.* 2004;322(1):88-92.
- 640 27. Park SK, Kim K, Page GP, Allison DB, Weindruch R, Prolla TA. Gene expression profiling of
641 aging in multiple mouse strains: identification of aging biomarkers and impact of dietary
642 antioxidants. *Aging Cell.* 2009;8(4):484-495.
- 643 28. Segawa H, Fukasawa Y, Miyamoto K, Takeda E, Endou H, Kanai Y. Identification and
644 functional characterization of a Na⁺-independent neutral amino acid transporter with broad
645 substrate selectivity. *J Biol Chem.* 1999;274(28):19745-19751.
- 646 29. Thony B, Ding Z, Martinez A. Tetrahydrobiopterin protects phenylalanine hydroxylase activity
647 in vivo: implications for tetrahydrobiopterin-responsive hyperphenylalaninemia. *FEBS Lett.*
648 2004;577(3):507-511.
- 649 30. Kure S, Sato K, Fujii K, Aoki Y, Suzuki Y, Kato S, Matsubara Y. Wild-type phenylalanine
650 hydroxylase activity is enhanced by tetrahydrobiopterin supplementation in vivo: an
651 implication for therapeutic basis of tetrahydrobiopterin-responsive phenylalanine hydroxylase
652 deficiency. *Mol Genet Metab.* 2004;83(1-2):150-156.
- 653 31. Prince MJ, Wu F, Guo Y, Gutierrez Robledo LM, O'Donnell M, Sullivan R, Yusuf S. The
654 burden of disease in older people and implications for health policy and practice. *Lancet.*
655 2015;385(9967):549-562.
- 656 32. Rosa AP, Jacques CE, Moraes TB, Wannmacher CM, Dutra Ade M, Dutra-Filho CS.
657 Phenylpyruvic acid decreases glucose-6-phosphate dehydrogenase activity in rat brain. *Cell*
658 *Mol Neurobiol.* 2012;32(7):1113-1118.

- 659 33. Werner ER, Blau N, Thony B. Tetrahydrobiopterin: biochemistry and pathophysiology. *Biochem J.* 2011;438(3):397-414.
- 661 34. Cunnington C, Van Assche T, Shirodaria C, Kylintireas I, Lindsay AC, Lee JM, Antoniadis C, Margaritis M, Lee R, Cerrato R, Crabtree MJ, Francis JM, Sayeed R, Ratnatunga C, Pillai R, Choudhury RP, Neubauer S, Channon KM. Systemic and vascular oxidation limits the efficacy of oral tetrahydrobiopterin treatment in patients with coronary artery disease. *Circulation.* 2012;125(11):1356-1366.
- 666 35. Antoniadis C, Cunnington C, Antonopoulos A, Neville M, Margaritis M, Demosthenous M, Bendall J, Hale A, Cerrato R, Tousoulis D, Bakogiannis C, Marinou K, Toutouza M, Vlachopoulos C, Leeson P, Stefanadis C, Karpe F, Channon KM. Induction of vascular GTP-cyclohydrolase I and endogenous tetrahydrobiopterin synthesis protect against inflammation-induced endothelial dysfunction in human atherosclerosis. *Circulation.* 2011;124(17):1860-1870.
- 672 36. Du YH, Guan YY, Alp NJ, Channon KM, Chen AF. Endothelium-specific GTP cyclohydrolase I overexpression attenuates blood pressure progression in salt-sensitive low-renin hypertension. *Circulation.* 2008;117(8):1045-1054.
- 675 37. Harding CO, Neff M, Wild K, Jones K, Elzaouk L, Thony B, Milstien S. The fate of intravenously administered tetrahydrobiopterin and its implications for heterologous gene therapy of phenylketonuria. *Mol Genet Metab.* 2004;81(1):52-57.
- 678 38. Hashimoto T, Sivakumaran V, Carnicer R, Zhu G, Hahn VS, Bedja D, Recalde A, Duglan D, Channon KM, Casadei B, Kass DA. Tetrahydrobiopterin Protects Against Hypertrophic Heart Disease Independent of Myocardial Nitric Oxide Synthase Coupling. *J Am Heart Assoc.* 2016;5(3):e003208.
- 682 39. Moens AL, Takimoto E, Tocchetti CG, Chakir K, Bedja D, Cormaci G, Ketner EA, Majmudar M, Gabrielson K, Halushka MK, Mitchell JB, Biswal S, Channon KM, Wolin MS, Alp NJ, Paolucci N, Champion HC, Kass DA. Reversal of cardiac hypertrophy and fibrosis from pressure overload by tetrahydrobiopterin: efficacy of recoupling nitric oxide synthase as a therapeutic strategy. *Circulation.* 2008;117(20):2626-2636.
- 687 40. Edwards C, Canfield J, Copes N, Brito A, Rehan M, Lipps D, Brunquell J, Westerheide SD, Bradshaw PC. Mechanisms of amino acid-mediated lifespan extension in *Caenorhabditis elegans*. *BMC Genet.* 16:8.
- 690 41. Arganda S, Bouchebti S, Bazazi S, Le Hesran S, Puga C, Latil G, Simpson SJ, Dussutour A. Parsing the life-shortening effects of dietary protein: effects of individual amino acids. *Proc Biol Sci.* 284(1846).
- 693 42. Choudhury AR, Ju Z, Djojotubroto MW, Schienke A, Lechel A, Schaetzlein S, Jiang H, Stepczynska A, Wang C, Buer J, Lee HW, von Zglinicki T, Ganser A, Schirmacher P, Nakauchi H, Rudolph KL. Cdkn1a deletion improves stem cell function and lifespan of mice with dysfunctional telomeres without accelerating cancer formation. *Nat Genet.* 2007;39(1):99-105.
- 697 43. Pinto AR, Ilinykh A, Ivey MJ, Kuwabara JT, D'Antoni ML, Debuque R, Chandran A, Wang L, Arora K, Rosenthal NA, Tallquist MD. Revisiting Cardiac Cellular Composition. *Circ Res.* 118(3):400-409.
- 700 44. Hayflick L. The Limited in Vitro Lifetime of Human Diploid Cell Strains. *Exp Cell Res.* 1965;37:614-636.
- 702 45. Alcendor RR, Gao S, Zhai P, Zablocki D, Holle E, Yu X, Tian B, Wagner T, Vatner SF, Sadoshima J. Sirt1 regulates aging and resistance to oxidative stress in the heart. *Circ Res.* 2007;100(10):1512-1521.
- 705 46. Tocchi A, Quarles EK, Basisty N, Gitari L, Rabinovitch PS. Mitochondrial dysfunction in cardiac aging. *Biochim Biophys Acta.* 1847(11):1424-1433.
- 707 47. Ravaglia G, Forti P, Maioli F, Bianchi G, Martelli M, Talerico T, Servadei L, Zoli M, Mariani E. Plasma amino acid concentrations in patients with amnesic mild cognitive impairment or Alzheimer disease. *Am J Clin Nutr.* 2004;80(2):483-488.
- 710 48. DeNicola GM, Karreth FA, Humpton TJ, Gopinathan A, Wei C, Frese K, Mangal D, Yu KH, Yeo CJ, Calhoun ES, Scrimieri F, Winter JM, Hruban RH, Iacobuzio-Donahue C, Kern SE, Blair IA, Tuveson DA. Oncogene-induced Nrf2 transcription promotes ROS detoxification and tumorigenesis. *Nature.* 2011;475(7354):106-109.
- 713

- 714 **49.** Wu LE, Gomes AP, Sinclair DA. Geroncogenesis: metabolic changes during aging as a driver
715 of tumorigenesis. *Cancer Cell*.25(1):12-19.
- 716 **50.** Deelen J, Kettunen J, Fischer K, van der Spek A, Trompet S, Kastenmuller G, Boyd A, Zierer
717 J, van den Akker EB, Ala-Korpela M, Amin N, Demirkan A, Ghanbari M, van Heemst D, Ikram
718 MA, van Klinken JB, Mooijaart SP, Peters A, Salomaa V, Sattar N, Spector TD, Tiemeier H,
719 Verhoeven A, Waldenberger M, Wurtz P, Davey Smith G, Metspalu A, Perola M, Menni C,
720 Geleijnse JM, Drenos F, Beekman M, Jukema JW, van Duijn CM, Slagboom PE. A metabolic
721 profile of all-cause mortality risk identified in an observational study of 44,168 individuals. *Nat*
722 *Commun*.10(1):3346.
- 723
- 724
- 725

Supplementary material

Dysregulated phenylalanine catabolism is a defining characteristic of cardiac aging

Gabor Czibik, MD, PhD,^{1,*§} Zaineb Mezdari, MSc,^{1*} Dogus Murat Altintas, PhD,^{1*} Juliette Bréhat, MSc,¹ Maria Pini, PhD,¹ Elisabeth Riant, MD,^{1,2} Costin Radu, MD,^{1,3} Thomas d'Humières, MD,^{1,2} Marielle Breau, PhD,¹ Hao Liang, MSc,¹ Cecile Martin, PhD,¹ Azania Abatan, BSc,¹ Rizwan Sarwar, MRCP, PhD,⁴ Ophélie Marion, MSc,¹ Suzain Naushad, MD,¹ Yanyan Zhang, MD, PhD,¹ Maissa Halfaoui, MSc,¹ Nadine Suffee, PhD,^{5,6} Didier Morin, PhD,¹ Serge Adnot, MD, PhD,^{1,8}, Stéphane Hatem, MD, PhD,^{5,6,9} Arash Yavari, MRCP, DPhil,^{4,7} Daigo Sawaki, MD, PhD,^{1‡} Geneviève Derumeaux, MD, PhD^{1,8‡§}

¹INSERM U955, Université Paris-Est Créteil (UPEC), Créteil, France

²AP-HP, Department of Cardiology, Henri Mondor Hospital, DHU-ATVB, Créteil, France

³AP-HP, Department of Cardiac Surgery, Henri Mondor Hospital, DHU-ATVB, Créteil, France

⁴Experimental Therapeutics, Radcliffe Department of Medicine (RDM) University of Oxford, Oxford, United Kingdom

⁵Sorbonne universités, INSERM UMR_S1166, Faculté de médecine UPMC, Paris, France

⁶Institute of Cardiometabolism and Nutrition, ICAN, Paris, France

⁷Wellcome Centre for Human Genetics, University of Oxford, Oxford, United Kingdom

⁸AP-HP, Department of Physiology, Henri Mondor Hospital, DHU-ATVB, Créteil, France

⁹Department of Cardiology, Assistance Publique - Hôpitaux de Paris, Pitié-Salpêtrière Hospital, Paris, France

*Authors equally contributed to the work

‡ These authors served as senior authors

§ Corresponding authors: gabor.czibik@inserm.fr & genevieve.derumeaux@inserm.fr

Methods

The data, analytic methods, and study materials are available to other researchers, on reasonable request, for the purpose of reproducing the results or replicating the procedures presented here.

Animal husbandry

Procedures involving animals were approved by the Institutional Animal Care and Use Committee of the French National Institute of Health and Medical Research (INSERM)-Unit 955, Créteil, France (ComEth 15-001). Global p21^{-/-} mice backcrossed to C57BL/6 background for at least 10 generations (Jackson Laboratory, USA) as well as wild-type (WT) littermates were kept in individually ventilated cages in a high-health facility with 12-hour light-dark cycle, controlled temperature (20-22°C) and humidity. Water and chow were provided *ad libitum*.

Cardiac phenotyping

Male WT and p21^{-/-} mice were followed from the age of 2 to 24 months of age. These mice were sequentially evaluated for myocardial structure and function as detailed later. Animals were euthanized and tissues harvested for histology and molecular biology (at ages 2, 6, 10 15 and 24 months).

***In vivo* drug treatment and phenylalanine-deficient diet**

Phe in a dose of 200 mg/kg twice a day or vehicle (1x PBS) was subcutaneously administered to 11 month-old WT mice (Janvier Labs, France) for one month. BH4 in a dose of 10 mg/kg/die 2x/die or vehicle (1x PBS with 10 mM sodium ascorbate and citric acid to pH4.5) was intraperitoneally administered to 11 month-old WT mice over six weeks. General state of the mice (body weight & wellbeing) was closely monitored. In both cases drug treatment was completed as scheduled without incidents.

As an alternative approach to limit Phe levels in 24-month--old WT mice, we designed a special diet differing only in the absence of Phe from the corresponding control diet (composition of this diet is detailed in Supplementary Table 1). During a pilot study we observed that mice on Phe-deficient diet tended to lose weight compared to either Phe-containing control diet or chow, which presumably occurred due to Phe insufficiency-related impairment of protein synthesis. To circumvent this problem, using calculations based on food intake of control diet mice and water intake of mice on Phe-deficient diet we re-supplemented 20-25% Phe of control diet mice in drinking water that stopped weight loss.

Then we subjected 23-month-old WT mice to Phe-deficient diet with 20-25% Phe supplementation (Phe-) or control diet (Phe+) for 4 weeks and evaluated plasma Phe levels and myocardial effects.

Echocardiography in conscious mice

Mice were trained to be grasped for transthoracic echocardiography that was performed in non-sedated mice to avoid the cardiac depressant effect of anesthetic agents, as previously reported.¹ Heart rates were typically above 600 beats per minute (bpm). Data acquisition for a single cohort was performed by a single operator (ER). Images were acquired from a parasternal position at the level of the papillary muscles using a 13-MHz linear-array transducer with a digital ultrasound system (Vivid 7, GE Medical System, Horton, Norway). Left ventricular dimensions and ejection fraction, anterior and posterior wall thicknesses were serially obtained from M-mode acquisition. Relative LV wall thickness (RWT) was defined as the sum of septal and posterior wall thickness over LV end-diastolic diameter, and LV mass was determined using the uncorrected cube assumption formula ($LV\ mass = 1.05 \times ((AWTd + LVEDD + PWTd)^3 - (LVEDD)^3)$). Peak systolic values of radial strain rate of the anterior and posterior wall were obtained using Tissue Doppler Imaging (TDI) as previously described.² TDI loops were acquired from parasternal view with a careful alignment with the radial component of the deformation³ at a mean frame rate of 514 fps and a depth of 1 cm. The Nyquist velocity limit was set at 12cm/s. Radial strain rate analysis was performed offline using the EchoPac Software (GE Medical Systems) blindly by a single operator (GD). Peak systolic of radial strain rate was computed from a region of interest positioned in the mid anterior wall and was measured over an axial distance of 0.6 mm. The temporal smoothing filters were turned off for all measurements. Because of the inevitable respiratory variability, we averaged peak systolic of radial strain rate on 8 consecutive cardiac cycles.

Invasive *in vivo* hemodynamic assessment of left ventricular function

In vivo hemodynamic measurements were performed just before mice of indicated ages were sacrificed.¹ Hemodynamic evaluation was performed in mice placed on a homeothermic operating table in supine position under 1.5% isoflurane anesthesia with spontaneous breathing. A 1.4-Fr microcatheter (Millar Instruments, Houston, USA) was calibrated manually before each experiment, inserted via the right carotid artery into the aorta and subsequently advanced to the left ventricle. Data were collected after at least 10 min of baseline, using the lowest isoflurane concentration tolerated to ensure minimal cardiodepression during measurement of peak rates of isovolumetric pressure development (dP/dt_{max}) and pressure decay (dP/dt_{min}). The microcatheter was then withdrawn to the aorta for measurement of systolic and diastolic pressure. Data were analyzed using the IOX software (EMKA, France).

Glucose Tolerance Test (GTT)

24-month-old WT mice on Phe-, Phe+ and chow diets were fasted for 7 hours and intraperitoneally injected with a glucose solution at a dose of 1.5 g/kg body weight. Blood samples were obtained from tail vein at baseline, 15, 30, 60, 90, 120 minutes after injection, and glucose concentration was measured with an automated glucometer (Accu-Chek Performa, Roche, Germany).

Tissue harvesting and processing

All mice were weighed, euthanized by cervical dislocation, followed by rapid excision of the organs of interest. The heart was cannulated through the aorta for perfusion with ice-cold 1x PBS, then blotted and weighed. The heart was cut in half perpendicular to its axis: the apical two-third was snap-frozen in liquid nitrogen, whilst the basic one-third was recannulated through the aorta, perfused with 10% formalin for histology. Hearts were kept in formalin at 4°C for at least 24-48 hours before embedding. Snap-frozen tissues were kept at -80 °C, until they were powdered using a mortar and pestle cooled with liquid nitrogen and collected as aliquots. Livers and kidneys were processed in a similar manner.

Human heart biopsies

Human heart biopsies (right atrial appendage) were obtained from patients undergoing elective coronary artery bypass grafting. Biopsies were obtained after approval of the ethical committee (Comité de Protection des Personnes Ile-de France VI) of Pitié-Salpêtrière Hospital, Paris and informed consent was acquired from each patient prior to the procedure.⁴

Human liver data

The available human liver transcriptomic data was generated in 33 non-diseased, beating heart liver donors with Affymetrix GeneChip Human Genome U133 Plus 2.0 Arrays.⁵ The annotations and normalized data were downloaded from NCBI Gene Expression Omnibus (accession number GSE107039). BioMart¹⁹ was used to map the microarray probesets to the human assembly in Ensembl release 96, revealing that there were 3 probesets that mapped to *PAH*. Although expression of only one probeset significantly correlated negatively with age, the expression of the other two demonstrated a similar trend. The data from these 3 probesets was reduced to a single variable by performing principal components analysis with IBM SPSS Statistics v25. The first principal component, which had a mean

of 0 and standard deviation of 1, was regressed as a dependent variable against donor age in GraphPad Prism v8.

RNA work and quantitative RT-PCR

Total RNA from cells or powdered tissue was extracted using the RNeasy mini kit or RNeasy mini fibrous tissue kit (QIAGEN), respectively, as previously described.⁷ RNA yield was measured with Nanodrop ND-1000, a >1.9 260/280 ratio was accepted. For reverse transcription the High Capacity cDNA kit was used according to the manufacturer's instructions (Applied Biosystems). Quantitative reverse transcriptase–polymerase chain reaction was used to quantify relative levels of genes of interest. Briefly, amplification reactions were carried out using Fast Universal Master Mix on a StepOnePlus system (Applied Biosystems) in a multiplexed design (FAM: gene of interest; VIC: β -actin as endogenous control) in a reaction volume of 10 μ l. All Taqman oligos used were inventoried Taqman-MGB oligos from Applied Biosystems. Relative expression was quantified using the ΔC_T method with the formula $RQ=2^{-\Delta\Delta C_T}$ (User Bulletin #2; Applied Biosystems).⁷

Protein extraction and Western blotting

Cells were washed briefly with ice-cold 1x PBS, scraped in 400 μ L T-PER lysis buffer (ThermoFisher) supplemented with 0.1 mM phenylmethylsulphonyl fluoride (PMSF) and protease/phosphatase inhibitor cocktail tablet (ThermoFisher). Pulverised tissue samples (20-30 mg) were lysed in the same buffer accelerated by sonication and passing through a 21 G needle. To pellet any debris, lysates were centrifuged at 13,000 g for 10 minutes at 4°C, with the supernatant transferred to fresh tubes. Protein concentrations were determined with Bradford assay (Biorad) and lysates were diluted to equal concentration with lysis buffer. Protein lysates were then mixed with Laemmli buffer, vortexed and heated to 95°C for 5 min. Equal amounts of protein lysates in parallel with protein molecular weight marker (ThermoFisher) were loaded onto pre-cast polyacrylamide gels (Nupage 10 or 12% Bis Tris gel, Novex, Invitrogen) and separated by electrophoresis at 200V for 1 hour. Proteins were transferred onto polyvinylidene difluoride (PVDF) membrane (Invitrogen) using an electrophoretic transfer cell (Mini Trans-Blot, Bio-Rad) in ice-cold transfer buffer (48 mM Tris base, 390 mM glycine, 0.1% SDS, 20% methanol (v/v)) at 300 mA for 2 hours. Membranes were blocked in 1x skimmed milk (ThermoFisher) for 1 hour at room temperature, followed by overnight incubation with primary antibody diluted in blocking buffer at 4°C. The antibodies and concentrations used are shown in Supplementary Table 1. Next day membranes were washed, followed by 60 minutes incubation in the corresponding horseradish peroxidase (HRP)-conjugated secondary antibody diluted 1:2000-10000 in blocking buffer (all Abcam). Blots were developed using enhanced chemiluminescence (ECL) reagents (normal, Prime & Select)

and digital images were acquired using an imaging system (Azure Biosystems). Membranes were usually stripped of antibodies and re-probed with an antibody targeting a protein serving as loading control (α -actinin for hearts & β -actin for all others). For this procedure, membranes were placed in Guanidine-HCl-based stripping solution (6M Guanidine-HCl, 0.2% Nonidet P-40, 0.1M β -mercaptoethanol, 20mM Tris-HCl, pH7.5 and 100 mM 2-mercaptoethanol) and incubated for 10 minutes at room temperature with gentle agitation, followed by extensive washing and re-blocking.⁸

Co-immunoprecipitation

Ten million human AC-16 cardiomyocytes (see later) per condition were used for co-immunoprecipitation experiments. Cells were scraped in ice-cold 1x PBS, collected and pelleted for 5 minutes at 1000g. Pellets were resuspended in DA150 buffer (20mM HEPES pH 7.9, 150mM NaCl, 20% glycerol, 0,2mM EDTA and one Roche protease/phosphatase inhibitor tablet per 10 ml) and lysed for 30 minutes at 4°C. Lysates were cleared by centrifugation at 15000g for 15 minutes. 1% v/v of the supernatant was put aside for input fraction, whilst an IP-grade rabbit monoclonal antibody raised against p21 (Abcam: ab188224) was added to the rest of the supernatants at the concentration recommended by the manufacturer (1:30; or IgG as control). Subsequently, 20 μ l of magnetic beads were added. Samples were incubated overnight at 4°C under constant agitation. Next day beads were washed 3 times in DA300 buffer (20 mM HEPES pH 7.9, 300 mM NaCl, 20% glycerol, 0,2 mM EDTA, 1 mM DTT and one Roche protease/phosphatase inhibitor tablet per 10 ml). Protein complexes were eluted at denaturing condition by heating the beads at 95°C for 10 minutes. Eluates were loaded onto a 12% Nupage gel for re-probing with an anti-ubiquitin antibody (Abcam, ab7254).

Histology

Formalin-fixed organs were embedded in paraffin. Cross-sections were cut into 7 μ m thickness using a rotary microtome (Leica). To assess cardiac fibrosis, Sirius red staining was performed, followed by dehydration and mounting with Eukitt quick-hardening mounting medium (Sigma). To visualize cardiomyocyte hypertrophy, sections were incubated in 2 μ g/mL Texas red-conjugated wheat germ agglutinin (WGA; Invitrogen) in 1x PBS at room temperature for 45 minutes. Slides were then mounted with fluorescent mounting media (Abcam). Images were acquired using a Zeiss fluorescent microscope.

Immunohistochemistry/immunofluorescence

Whenever a dispersed pattern was expected, immunohistochemistry was performed on paraffin-embedded sections. Briefly, after rehydration, citrate buffer-assisted, heat-mediated antigen retrieval

and blocking, sections were incubated overnight at +4 °C with primary antibodies raised against the following targets: 4-HNE (Millipore; goat, 1:200), Pah (Abcam; rabbit, 1:200) or 2-SC (Cambridge Biosciences; rabbit, 1:100; also see Supplementary Table 1). Next day sections were washed, then incubated with the corresponding HRP-conjugated secondary antibodies (Abcam; 1:200) for 30 minutes at room temperature, washed again, followed by incubation with 3,3'-diaminobenzidine (DAB; Sigma) under visual observation until the signal appeared. Then slides were either counterstained with haematoxylin or not, dehydrated and mounted.

Immunofluorescence was used for higher sensitivity and co-localization of proteins of interest. Briefly, paraffin-embedded sections were rehydrated, followed by antigen retrieval with citrate-assisted heat. Sections were then blocked with 30% goat serum (using antibody dilution solution with background reducing components; Dako) or Bloxall™ artificial blocking agent (Dako) and incubated overnight at +4 °C with primary antibodies raised against target proteins (see Supplementary Table 1 for details). The following day sections were washed in 1x TBST, incubated with a mixture of the corresponding Alexa Fluor 555-labelled secondary antibodies (Invitrogen) and Alexa-488-conjugated Phalloidin (to counterstain cardiomyocytes) for 30 minutes at room temperature, and washed again. In case of co-labeling Alexa Fluor 555-labelled and Alexa Fluor 647-labelled secondary antibodies were used (Invitrogen), occasionally in combination with the avidin/biotin enhancement system (Dako). Specific protocols are available upon request. Slides were mounted with fluorescent mounting media with DAPI (4',6-diamidino-2-phenylindole; Abcam).

Isolation and culture of primary cells

Left ventricular cardiomyocytes were isolated from male Sprague Dawley rats (9 weeks, 300-350g) as described previously.⁹ Briefly, rats were anesthetized with ketamine and xylazine (100 and 10 mg/kg, respectively) and received heparin (100 IU/kg). Hearts were excised and retrogradely perfused with an oxygenated (95% CO₂, 5% O₂) perfusion buffer (NaCl 113 mM, KCl 4.7 mM, KH₂PO₄ 0.6 mM, Na₂HPO₄ 0.6 mM, MgSO₄-7H₂O 1,2 mM, NaHCO₃ 12 mM, KHCO₃ 10 mM, HEPES 10 mM, Taurine 30 mM, phenol red 0.032 mM, D-glucose 5.5 mM, 2,3-butanedionemonoxime 10 mM, pH 7.4) for 2 minutes to wash out the blood from the coronary arteries. Then, hearts were perfused with digestion buffer (perfusion buffer supplemented with 0.1 mg/mL liberase, 0.14 mg/mL trypsin-EDTA and 12.5 μM Ca²⁺) for 10-12 minutes. The hearts were then placed in stopping buffer (perfusion buffer supplemented with 10% New Born Calf Serum (NBCS) and 12.5 μM Ca²⁺). Atria and the right ventricle were removed. The left ventricle was dissected into small fragments, then submitted to successive aspiration-reflux with a pipette. Digested ventricles were filtered through a 250 μm cell filter. After a 10-minute incubation at 37°C, supernatants were discarded and cells were resuspended with

calcium buffer (perfusion buffer supplemented with 5% NBCS and 12.5 μM Ca^{2+}). Subsequently, extracellular calcium was added incrementally up to 1 mM. Finally, cells were suspended in culture medium M199 (supplemented with 1% Insulin Transferrin Selenium - ITS) and seeded onto wells pre-coated with 10 $\mu\text{g}/\text{mL}$ laminin (for immunoblotting, intracellular Phe or fumarate measurements: 2×10^5 cells in 6-well plates; for RNA/qRT-PCR: 10^5 cells in 12-well plates; for fluorescence: 2×10^4 cells in 8-well Labtek II chamber slides, ThermoFisher). Cells were allowed to attach for 2 hours before starting any treatment. Duration of treatments was 4 hours at a final concentration of L-phenylalanine: 5 mM;¹⁰ BH4: 10 μM ; MG132: 1 μM . At the end of treatments the majority of cells were rod-shaped, had cross-striations and no visible vesicles on their surface, whilst for microscopic detection all cells studied were such. Treatments were performed in the M199 1% ITS media.

Primary cardiac fibroblasts were isolated from mouse neonates as described previously.⁴ Briefly, neonatal C57BL6J mice (Janvier) were euthanized by decapitation, and ventricles were minced in ice-cold balanced salt solution. Subsequently, minced ventricles were incubated in a balanced salt solution containing trypsin for 24 hours at 4°C, and then further digested with 300 U/mL of collagenase type 2 for 30 to 45 minutes at 37°C with gentle agitation. Cell suspensions were filtered with a 70 μm pore-size mesh and passed onto dishes with Medium 199 (ThermoFisher), supplemented with 10% fetal calf serum. Thirty minutes later, floating cells were removed, and the attached cardiac fibroblasts were maintained in culture until passage 3. For Phe treatment cells were seeded onto LabTek II chamber slides at a density of 70% of confluence. Having allowed to attach, cells were treated with 0.1, 0.5, 1, 2.5 and 5 mM Phe or vehicle (1x PBS) for 24 hours.

Culture of cell-lines

AC-16 cardiomyocytes (immortalized human ventricular myocytes) were maintained in DMEM/F12 (supplemented with 12.5% foetal bovine serum (FBS) and 100 U/mL penicillin/streptomycin) in a humidified incubator at 37 °C with 5% CO_2 .¹¹ Treatments were performed in 1x PBS Mg^+/Ca^+ (supplemented with 17,5 mM glucose and 0,5 mM pyruvate) for 24 hours (with a final concentration of L-phenylalanine: 5 mM; BH4: 10 μM ; MG132: 1 μM ; dehydroepiandrosterone (DHEA): 10 μM ; H_2O_2 : 10 μM ; sodium butyrate (SB): 5 μM as indicated). For microscopic evaluation, 10^4 cells were seeded onto 8-well LabTek II chamber slides. At the end of treatment cells were fixed with 4% paraformaldehyde at 37 °C for 10 minutes before permeabilization (0.1% Triton-X100 in 1x PBS for 1m minutes), blocking and primary antibody. For evaluation of redox status, 4×10^4 cells were seeded onto 24-well plates, received treatment as indicated and were processed for fluorescent probes as instructed (see later in further detail). Processing of AC-16 cells for co-immunoprecipitation experiments is described under a separate subchapter above.

AML-12 cells (ATCC® CRL-2254™) were maintained in DMEM/F-12 (1:1) culture media supplemented with 10% FBS, 10 µg/ml insulin, 5.5 µg/ml transferrin, 5 ng/ml selenium, 40 ng/ml dexamethasone and 1% penicillin/streptomycin. Cells were sub-cultivated from subconfluent flasks with a ratio from 1:4 to 1:8. For WB analysis, cells were plated on 6-well plates and harvested at 80-90% of confluence. AML-12 cells were treated with Nutlin3a (10 µM) against vehicle (DMSO) and transfected with indicated siRNA (Supplementary Table 2) at 80% confluence using Lipofectamine RNAiMAX Transfection Reagent (ThermoFischer Scientific 13778030) following the manufacturer's instructions. Transfection efficiency was constantly checked using BLOCK-IT Alexa Fluor Red Fluorescent Control (ThermoFischer Scientific 14750100). In other experiments AML-12 cells were treated with Nutlin3a without or with BH4 (10 µM). Cells were lysed for protein extraction, whilst conditioned media was used to determine tyrosine concentration.

All cell culture experiments were performed in biological triplicates at the least.

Myocardial nitric oxide synthase (NOS) activity

Myocardial tissue was probed for NOS activity using a commercial NOS activity kit according to the manufacturer's instructions (BioVision). Briefly, myocardial tissue aliquots were lysed in ice-cold NOS Assay Buffer supplemented with Pierce protease/phosphatase inhibitor cocktail and centrifuged to clear the protein lysates from insoluble cell debris. Protein lysates were then incubated with a reaction mix containing NOS cofactors, NOS substrate and nitrite reductase at 37 °C for 60 minutes, followed by addition of NOS Assay Buffer. This was followed by three 10-minute incubations at room temperature with enhancer, probe and NaOH added, respectively. Fluorometric measurements took place with excitation at 360 nm and emission at 450 nm. NOS recombined protein acted as positive control. Sample values were determined against a standard curve and normalized to protein concentration (Bradford assay).

Mitochondrial complex and citrate synthase activity

Mitochondrial enzymatic activities were measured real-time in 96-well microplates by spectrofluorimetry (Tecan Spark) and normalized to protein concentration (BCA assay).

Briefly, pulverized heart samples were homogenized in Extraction Buffer (20 mM Tris-HCl, 250 mM sucrose, 2 mM EGTA, 40 mM KCl and 1 mg/mL BSA, pH 7.2) with 1 % Percoll and 100 µg/mL digitonin. After centrifugation at 10 000 g at 4 °C, pellets were washed in Extraction Buffer, dried and kept at -80°C until further analysis. Complex II/succinate dehydrogenase activity was measured in 10 mM KH₂PO₄ buffer (pH 7.2) with addition of 0.2 mM lauryl maltoside, 5 mM succinate, 25 µM

oxidized decylubiquinone and 40 μM DCPIP (Dichloroindophenol sodium) at OD 600 nm with malonate (5 mM) as reference inhibitor. Complex III/coenzyme Q – cytochrome c reductase activity was determined in 10 mM KH_2PO_4 buffer (pH 7.2) after addition of 0.2 mM lauryl maltoside, 60 μM oxidized cytochrome c, 300 μM KCN and 12.5 μM reduced decylubiquinone at OD 550 nm with antimycin A (1 μM) as reference inhibitor. Complex IV/cytochrome c oxidase activity was measured in 10 mM KH_2PO_4 (pH 7.2) after addition of 0.2 mM lauryl maltoside, 60 μM reduced cytochrome c at OD 550 nm) with KCN (300 μM) as reference inhibitor. Complex V/ATP synthase activity was determined at OD 340 nm in a reaction buffer (25 mM KH_2PO_4 (pH 8) with 0.2 mM lauryl maltoside, 2 mM ATP, 25 mM phosphoenolpyruvate, 7.5 U pyruvate kinase, 12.5 U lactate dehydrogenase, 500 μM NADH, 1 μM antimycin A 250 mM sucrose, 30 mM KCl, 0.2 mM EGTA, 5 mM MgCl_2 , 2 μM P1,P5-Di(adenosine-5') pentaphosphate pentasodium salt (Ap5A), 0.1% BSA added, with oligomycin A (10 μM) as reference inhibitor. Citrate synthase activity was measured at OD 415 nm in a reaction mix containing 10 mM Tris, (pH 8). 150 μM 5,5'-Dithio-bis 2-nitrobenzoic acid, 300 μM acetyl-coA and 1 mM oxaloacetate. All reagents were purchased from Sigma Aldrich (France).

Determination of superoxide and metabolite levels

Levels of reduced glutathione (GSH; ThermoFisher), cytosolic (CellROX; ThermoFisher) and mitochondrial (MitoSOX; ThermoFisher) superoxide, phenylalanine (BioVision), tyrosine (BioVision) and fumarate (BioVision) levels as well as NAD^+/NADH ratios were evaluated in cells, hearts, livers or plasma, with respective agents/kits following the manufacturer's recommendations. Specifically, cellular GSH levels were estimated with the aid of ThiolTracker™ Violet fluorescent probe (final concentration: 20 μM ; ThermoFisher), whilst cytosolic and mitochondrial superoxide levels with CellROX and MitoSOX probes, respectively (CellROX final concentration: 5 μM ; MitoSOX final concentration: 2 μM). Plasma, liver or cardiomyocyte phenylalanine levels were determined using an enzyme-coupled, fluorometric method (BioVision). Briefly, samples were deproteinized via trichloroacetate precipitation, neutralized, tyrosinase-treated (to remove tyrosine that may interfere) and diluted to fit in the standard curve. Fluorescence reading took place at 587 nm after excitation at 535 nm. Levels of tyrosine in liver, or conditioned media from treated cells were determined after deproteinization using 10 kDa cut-off columns with an enzyme-coupled, colorimetric method with reading at 491 nm (BioVision). Cellular and myocardial fumarate levels were determined using an enzyme-coupled colorimetric kit with reading at 450 nm (BioVision). Myocardial NAD^+/NADH ratios were calculated based on direct measurements of NAD^+ and NADH levels of the same samples using an enzyme-coupled colorimetric kit with reading at 450 nm (BioVision).

Data analysis and statistics

Mice were randomly assigned to experimental groups and data were acquired and analyzed blind to genotype, age or treatment. Statistical analyses were performed using GraphPad Prism Software (version 6). In all cases n numbers were raised to obtain Gaussian distribution and parametric tests were used. Accordingly, unpaired, two-tailed t -test was used to compare two groups, whilst more than two groups were compared using one-way analysis of variance (ANOVA), with Bonferroni post-hoc test for multiple comparisons. Two-way ANOVA was used to compare groups with time-dependent evolution of readouts, with Bonferroni post-hoc test for more than two groups. Data are presented as mean \pm standard error of the mean or individual values. Annotations used: * $p < 0.05$, ** $p < 0.01$, *** $p < 0.001$ compared to groups indicated. A p value of < 0.05 was considered significant.

Supplementary Table 1. Composition of the custom-designed Phe-deficient and control diets.

Product #	A19011401	A19011402
	10 g/kg Phe	No Phe
Ingredient (g)		
L-Arginine	10	10
L-Histidine-HCl-H ₂ O	6	6
L-Isoleucine	8	8
L-Leucine	12	12
L-Lysine-HCl	14	14
L-Methionine	6	6
L-Phenylalanine	10	0
L-Threonine	8	8
L-Tryptophan	2	2
L-Valine	8	8
L-Alanine	10	10
L-Asparagine-H ₂ O	5	5
L-Aspartate	10	10
L-Cystine	4	4
L-Glutamic Acid	30	30
L-Glutamine	5	5
Glycine	10	10
L-Proline	5	5
L-Serine	5	5
L-Tyrosine	4	4
<i>Total L-Amino Acids</i>	<i>172</i>	<i>162</i>
Corn Starch	502.1	512.1
Maltodextrin 10	125	125
Sucrose	46.4	46.4
Cellulose	50	50

Corn Oil	50	50
Coconut Oil	0	0
Mineral Mix S10001	35	35
Sodium Bicarbonate	7.5	7.5
Vitamin Mix V10001	10	10
Choline Bitrartrate	2	2
Red Dye, FD&C #40	0	0.05
Blue Dye, FD&C #1	0.05	0
Total	1000.05	1000.05
Protein	172	162
Carbohydrate	686	696
Sucrose	46.40	46.40
Fat	50	50
Fiber	50	50
g%		
Protein	17	16
Carbohydrate	69	70
Sucrose	4.64	4.64
Fat	5	5
Fiber	5	5
kcal		
Protein	688	648
Carbohydrate	2742	2782
Fat	450	450
Total	3880	3880
kcal%		
Protein	18	17

Carbohydrate	71	72
Fat	12	12
Total	100	100
kcal/g	3.9	3.9

Supplementary Table 2. Primary antibodies used in the study. IHC: immunohistochemistry, IF: immunofluorescence, WB: Western blot.

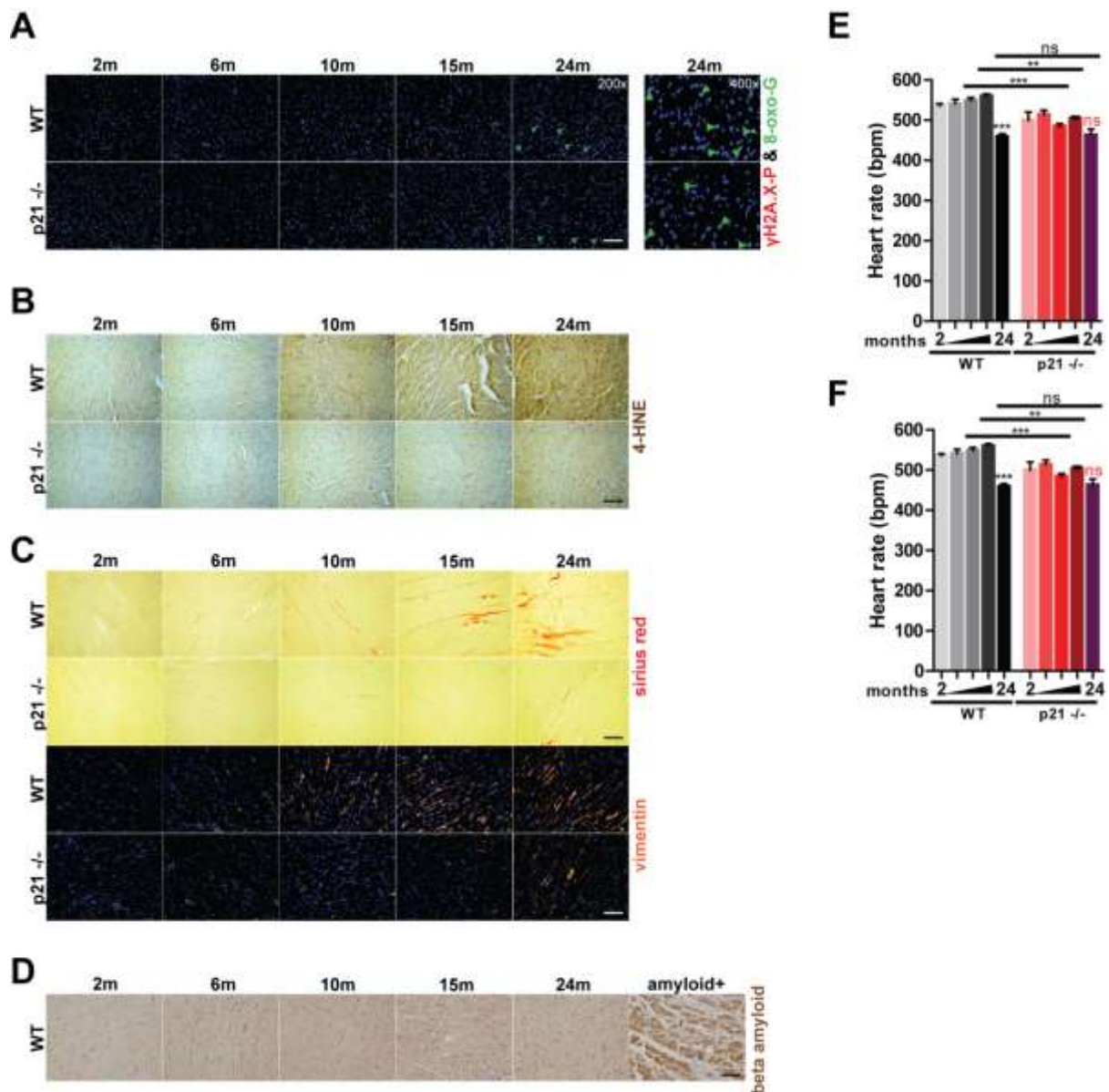
Target protein	Producer/Cat#	Species	Application/concentration
p21	Abcam: ab188224	rabbit	WB:1:1000
p21	Santa Cruz: sc-397	rabbit or goat	IF: 1:50
p-p53	Cell Signaling: 9284S	rabbit	WB: 1:1000
p53	Cell Signaling: 2524S	mouse	IF: 1:200
p16	Abbiotec: 250804	rabbit	IF: 1:100, WB: 1:100
β -actin	Abcam: ab49900	mouse-HRP	WB: 1:10000
Pah	Sigma: SAB250434	goat	IF: 100, WB: 1:200
Pah	Abcam: ab148430	rabbit	IHC: 1:200, IF: 1:100, WB: 1:300
Pah	ThermoFisher Scientific: PA5-79780	rabbit	WB: 1:1000
Gch1	Bioss antibodies: bs-0136R	rabbit	IF: 100, WB: 1:200-1000
2-SC	Cambridge BioSciences: crb2005017e	rabbit	IHC/IF: 1:100, WB:1:200
Nrf2	Genetex: GTX103322	rabbit	WB: 1:500, IF: 1:500
Cardiac troponin I	Abcam: ab47003	rabbit	IF: 1:200
CD31	Santa Cruz: sc-1506	goat	IF: 1:100
Acta2	Sigma: A2547	mouse	IF: 1:200
8-oxo-guanine	Abcam: ab206461	mouse	IF: 1:50
γ H2A.X-P	Abcam: ab81299	rabbit	IF: 1:200
H3K9me3	Abcam: ab176916	rabbit	IF: 1:200
Beta amyloid	Invitrogen: 51-2700	rabbit	IHC: 1:250
Ubiquitin	Abcam, ab7254	mouse	WB: 1:500
4-HNE	Millipore: AB5605	goat	IHC: 1:200

vimentin	Abcam: ab92547	rabbit	IF: 1:200
α -actinin	Abcam: ab68167	rabbit	WB: 1:5000

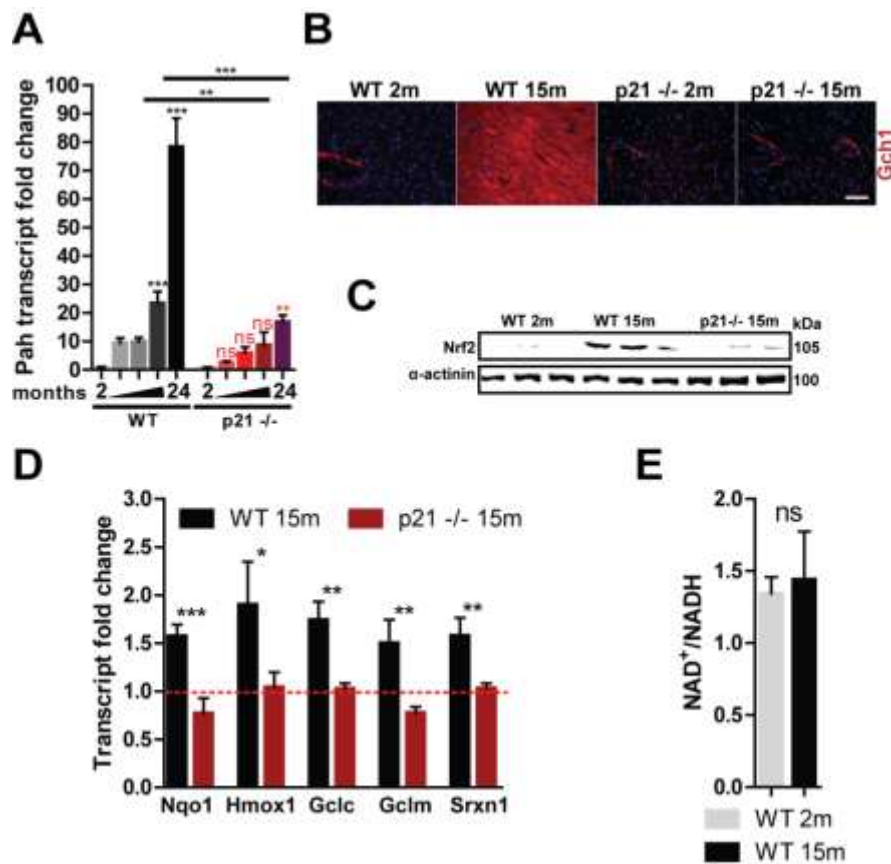
Supplementary Table 3. siRNA used for transfection experiments.

Target mRNA	Producer/Cat#
Cdkn1a (p21)	ThermoFischer Scientific: 60538
Scrambled	ThermoFischer Scientific: 12935112

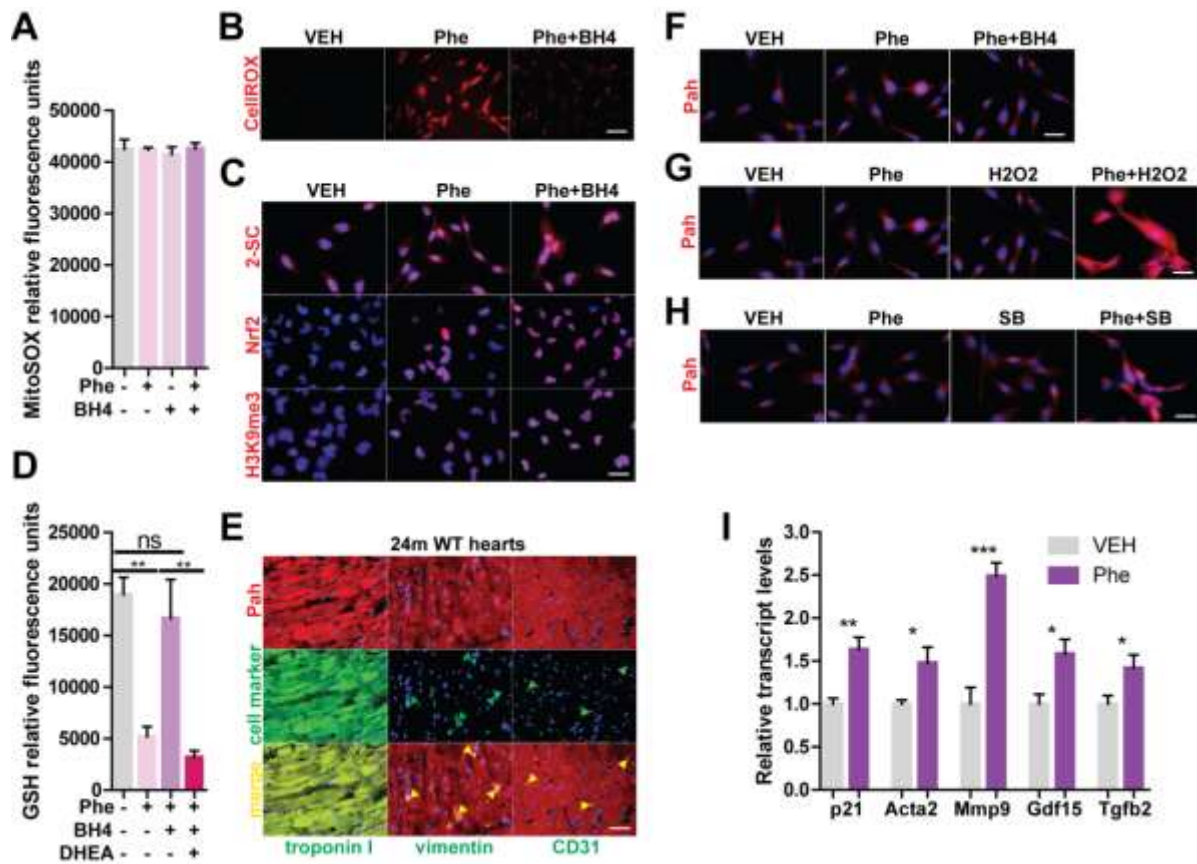
Supplementary Figures & Legends



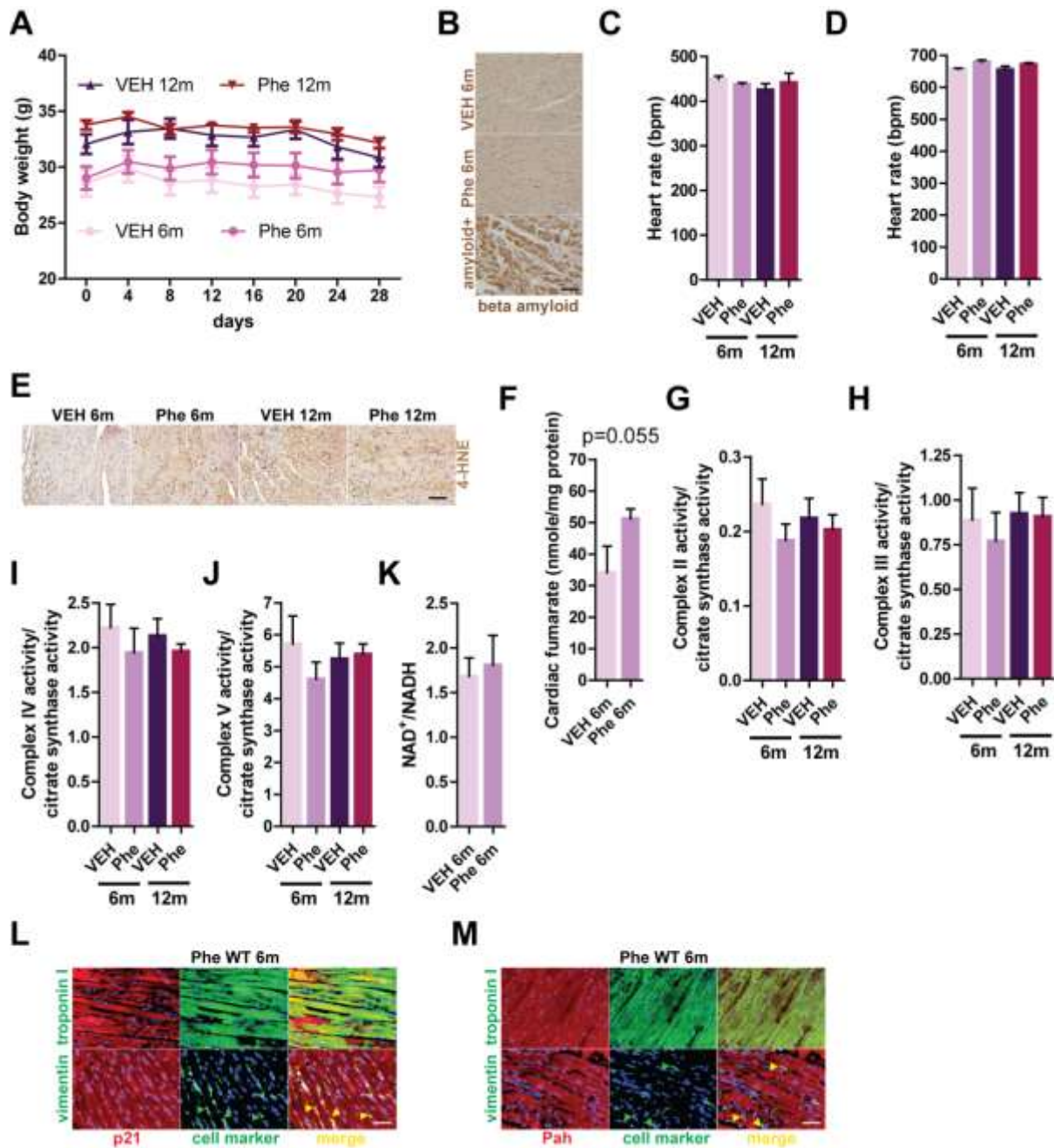
Supplementary Figure 1. p21 deficiency delays cardiac aging. **A**, DNA damage markers (8-oxo-G & γ H2A.X-P) in hearts of WT and p21^{-/-} mice aged between 2 and 24 months as indicated (n=3-4/condition). **B**, Representative immunohistochemical images of 4-hydroxynonenal (4-HNE) in hearts of WT & p21^{-/-} mice aged between 2 and 24 months as indicated (n=5/condition). **C**, Representative images of myocardial Sirius red and vimentin staining in WT and p21^{-/-} mice aged between 2 and 24 months as indicated (n=5/condition). **D**, Representative images of myocardial beta amyloid immunohistochemistry with hematoxylin counterstaining in WT mice aged between 2 and 24 months as indicated (n=5/condition). **E-F**, Heart rate during *in vivo* hemodynamic measurements (**E**) and conscious echocardiography (**F**) in WT & p21^{-/-} mice aged between 2 and 24 months (n=8-12/condition). Shades of grey: WT, shades of color: p21^{-/-} at 2, 6, 10, 15 and 24 months with darker tones corresponding to older ages. For microscopic images, magnification: 200x, scale-bar: 50 μ m unless indicated otherwise. Data are presented as original images (**A-D**) or mean \pm SEM and analyzed with one-way ANOVA with Bonferroni post-hoc test (**E-F**); ns: non-significant, * $p < 0.05$, ** $p < 0.01$, *** $p < 0.001$.



Supplementary Figure 2. Development of ectopic phenylalanine (Phe) catabolism in the aging myocardium and its delay with p21 deficiency. **A**, Relative transcript levels in hearts of WT & p21^{-/-} mice aged between 2 and 24 months as indicated (n=7-8/condition). Shades of grey: WT, shades of color: p21^{-/-} at 2, 6, 10, 15 and 24 months with darker tones corresponding to older ages. **B**, Representative myocardial Gch1 immunofluorescence in WT & p21^{-/-} mice at indicated ages (n=3/condition). **C**, Immunoblot of Nrf2 in hearts of WT and p21^{-/-} mice as indicated (n=3/condition). **D**, Quantitative RT-PCR analysis of Nrf2 target genes in hearts of 15-month-old WT and p21^{-/-} mice (n=4-10/group; dashed line: mean expression level of WT at 2 months of age based on the average of n=8 hearts). **E**, NAD⁺/NADH ratio in hearts of WT mice at 2 and 15 months of age (n=4-10/group). For microscopic images, magnification: 200x, scale-bar: 50 μm. Data are presented as original images (**B-C**) or mean ± SEM and analyzed with one-way ANOVA with Bonferroni post-hoc test (**A**) or with two-tailed unpaired t-test (**D-E**); ns: non-significant, **p* < 0.05, ***p* < 0.01, ****p* < 0.001. Stars above bars in panel **A** represent comparisons to 2 month-old of the same genotype (black: WT, red: p21^{-/-}).

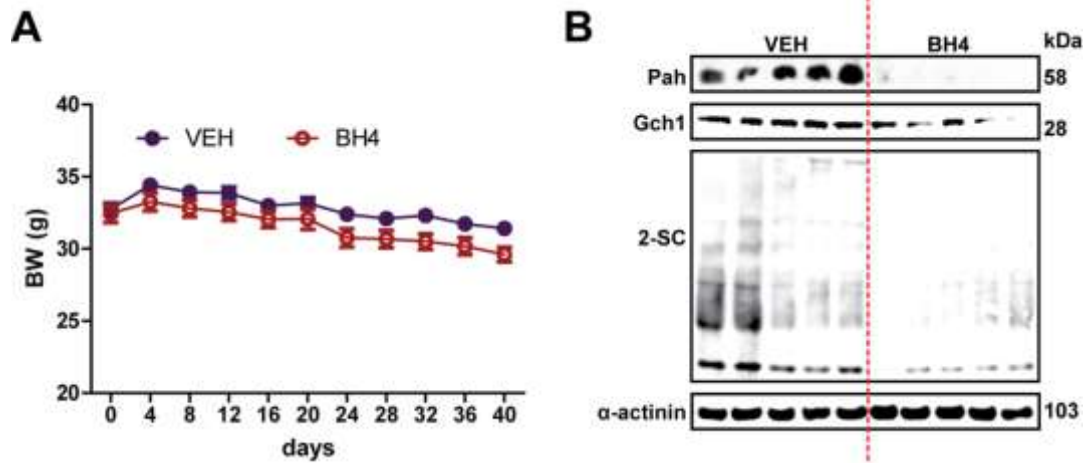


Supplementary Figure 3. Cellular effects of phenylalanine (Phe) treatment *in vitro*. **A**, Mitochondrial superoxide levels (MitoSOX) in human AC-16 cardiomyocytes treated with Phe (5 mM) and/or BH4 (10 μ M; n=5-6/condition). **B**, Representative images of cytosolic superoxide levels (CellROX) in human AC-16 cardiomyocytes treated with Phe (5 mM) without or with BH4 (10 μ M; n=3/condition). **C**, Representative images of 2-SC, Nrf2 and H3k9me3 in human AC-16 cardiomyocytes treated with Phe without or with BH4 (n=3/condition). **D**, Reduced glutathione (GSH by ThiolTracker) levels in human AC-16 cardiomyocytes treated with Phe without or with BH4 and the pentose phosphate pathway inhibitor dehydroepiandrosterone (DHEA; n=6/condition). **E**, Myocardial Pah expression against markers of cardiomyocytes (troponin I), fibroblasts (vimentin) and endothelial cells (CD31) in 24-month-old WT mice. **F-H**, Representative images of Pah immunofluorescence in human AC-16 cardiomyocytes treated with Phe alone or in combination with BH4 (**F**), H₂O₂ (**G**) and sodium butyrate (SB; **H**; n=3/condition/series). **I**, Quantitative RT-PCR analysis of genes encoding for fibroblast function and senescence in primary murine neonatal cardiac fibroblasts treated with vehicle (VEH) or Phe (n=6/condition). For all microscopic images, magnification: 400x, scale-bar: 25 μ m, except for CellROX (**B**): magnification: 200x, scale-bar: 50 μ m. Data are presented as original images (**B-C**, **E-G**) and mean \pm SEM analyzed with one-way ANOVA with Bonferroni post-hoc test (**A** & **D**) or two-tailed unpaired t-test (**I**); ns: non-significant, * p < 0.05, ** p < 0.01, *** p < 0.001 as indicated.

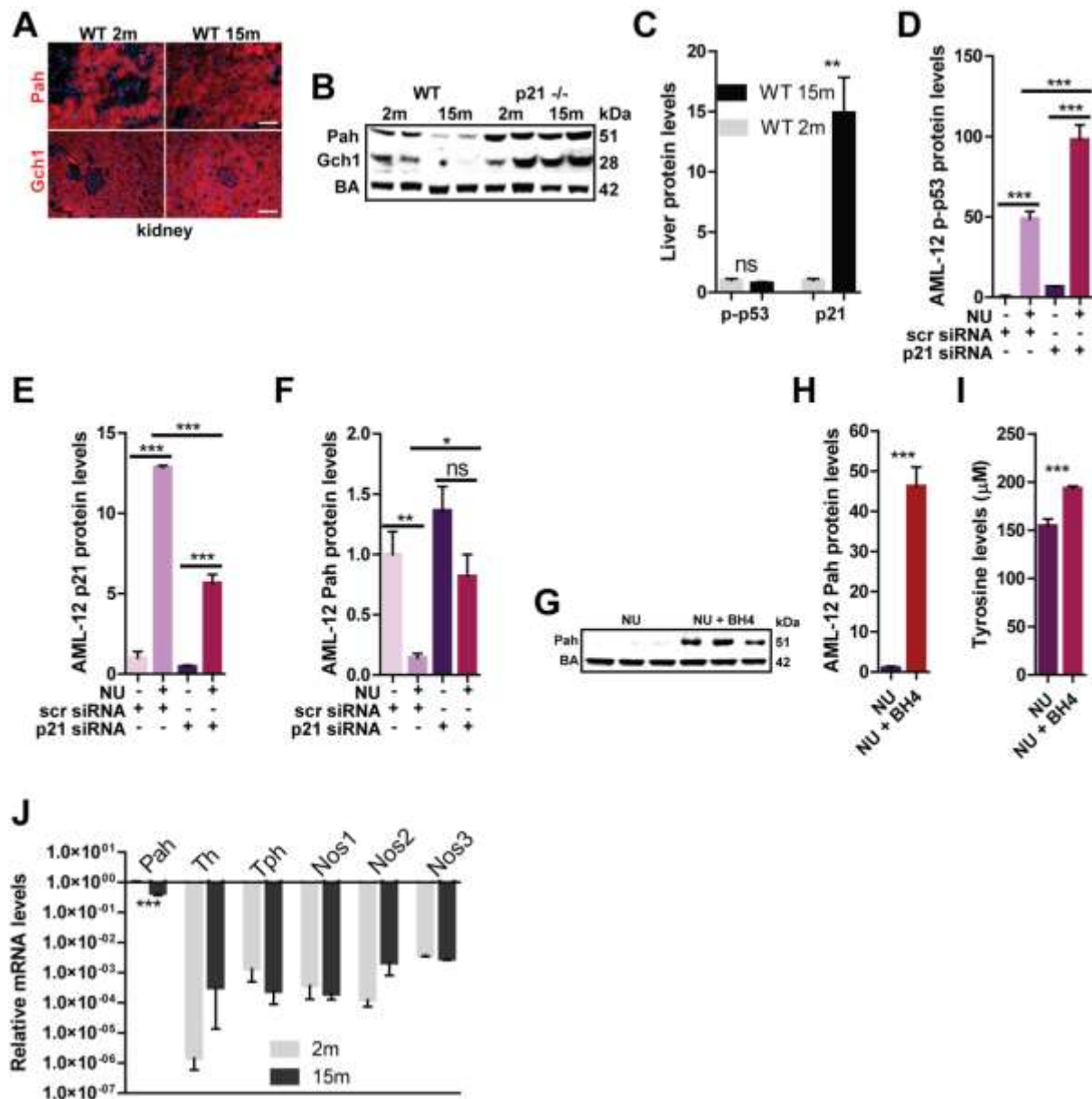


Supplementary Figure 4. Experimental hyperphenylalaninemia promotes cardiac aging *in vivo*. **A**, Body weight of 6- and 12 month-old WT mice in the course of Phe (vs. vehicle: VEH) treatment *in vivo* (n=8-11/group). **B**, Representative images of myocardial beta amyloid immunohistochemistry with hematoxylin counterstaining in 6 month-old WT mice aged treated as indicated (n=4/condition). **C-D**, Heart rate during *in vivo* hemodynamic measurements (**C**) and conscious echocardiography (**D**) in WT mice treated with Phe as indicated (n=8-11/condition). **E**, Representative microscopic images of myocardial 4-HNE immunohistochemistry in the same animals as above (n=4/condition). **F-K**, Cardiac fumarate levels (n=5-7/group; **F**), Complex II (**G**), III (**H**), IV (**I**), V (**J**; n=6-11/group for all complexes) and NAD⁺/NADH (n=7-9/group; **K**) as indicated. **L-M**, Myocardial p21 (**K**) and Pah (**L**) expression counterstained against markers of cardiomyocytes (troponin I), fibroblasts (vimentin) in 6-month-old WT mice treated with Phe. **M**, For microscopic images in panels **B** & **E**, magnification: 200x, scale-bar: 50 μ m; for images in panels **L-M**, magnification: 400x, scale-bar: 25 μ m. Data are presented either as original images (**B**, **E** & **L-M**) or as mean \pm SEM analyzed with two-way ANOVA (**A**), one-way

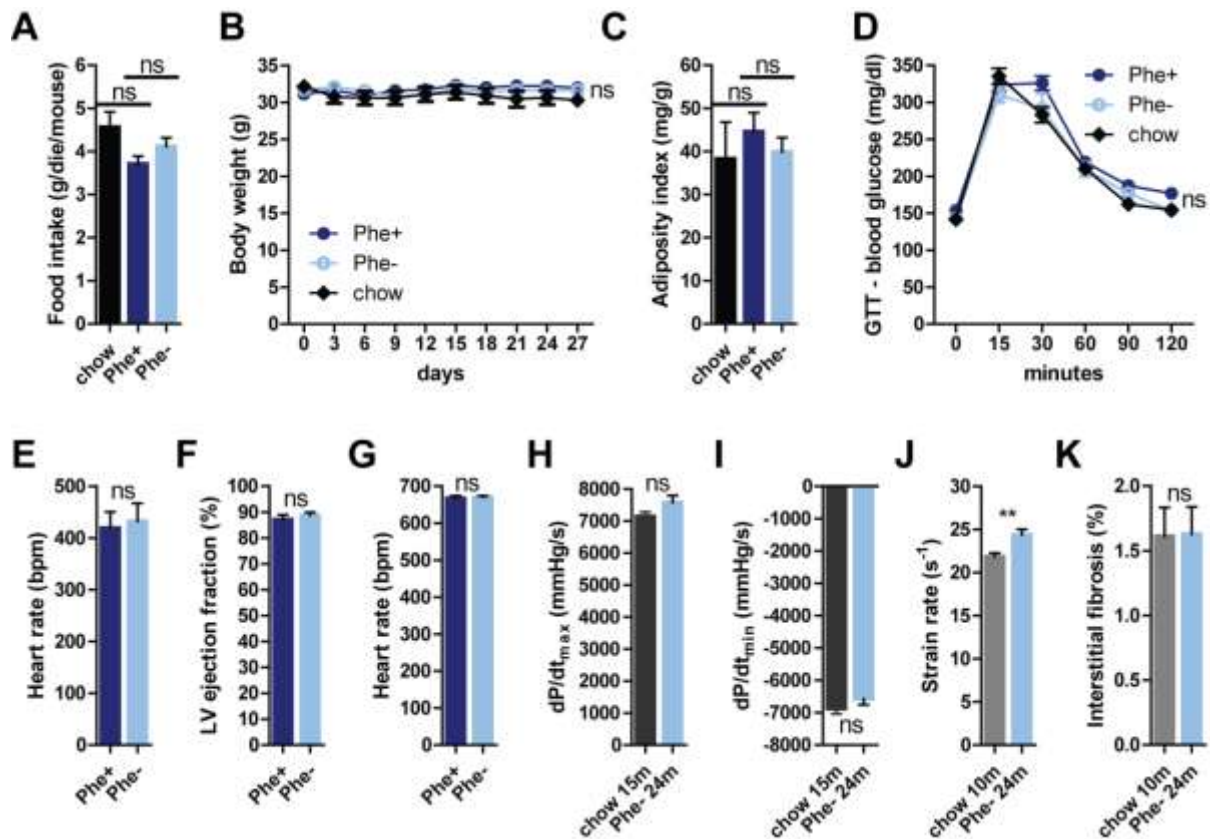
ANOVA with Bonferroni post-hoc test (**C-D** & **G-J**) or two-tailed unpaired t-test (**F** & **K**); ns: non-significant, * $p < 0.05$, ** $p < 0.01$, *** $p < 0.001$.



Supplementary Figure 5. BH4 rescues age-related cardiac dysfunction. **A**, Body weight of WT mice in the course of BH4 (vs. vehicle: VEH) treatment *in vivo* (n=9-10/group). **B**, Myocardial expression of Pah, Gch1, 2-SC with alpha-actinin as loading control in VEH- and BH4-treated 12.5 month-old WT mice (n=5/group). Data are presented as original images (**B**) or mean \pm SEM and analyzed with two-way ANOVA (**A**); ns: non-significant, * $p < 0.05$, ** $p < 0.01$, *** $p < 0.001$.



Supplementary Figure 6. BH4 rescues age-related hepatic Pah decline. **A**, Representative immunofluorescent images of Pah & Gch1 in kidneys of 2- and 15-month-old WT mice (n=3/age). **B**, Immunoblot analysis of Pah and Gch1 in livers of 2- and 15-month-old WT and p21^{-/-} mice (n=2/condition). **C**, Quantification of phospho-p53 (p-p53) and p21 immunoblots in livers of 2- and 15-month-old WT mice (n=3/group). **D-F**, Quantification of immunoblot of p-p53 (**D**) & p21 (**E**) & Pah (**F**) in AML-12 hepatocytes treated with Nutlin3a (NU) or vehicle (VEH) and knockdown with p21 or scrambled (scr) siRNA (n=3/group). **G-H**, Pah immunoblot in AML-12 hepatocytes treated with Nutlin3a (NU) without or with BH4 (**G**) and quantification (**H**; n=3/group). **I**, Extracellular tyrosine levels measured in conditioned media of AML-12 hepatocytes treated with Nutlin3a (NU) without or with BH4 (n=6/group). **J**, Relative transcript levels of BH4-dependent enzymes in livers of 2- and 15-month-old WT mice (n=7-8/group). For microscopic images, magnification: 200x, scale-bar: 50 μm. Data are presented as original images (**A-B** & **G**) or mean ± SEM and analyzed with unpaired, two-tailed t-test (**C** & **H-J**) or with one-way ANOVA with Bonferroni post-hoc test (**D-F**); ns: non-significant, **p* < 0.05, ***p* < 0.01, ****p* < 0.001.



Supplementary Figure 7. Dietary Phe restriction rejuvenates old hearts. A-D, Food intake (A), body weight (B), adiposity index (C) and glucose tolerance (D) in 24 month-old WT mice fed chow, Phe-deficient with 20-25% Phe supplementation or control diet (Phe- and Phe+, respectively; n=10-11/group). E-G, Heart rate during *in vivo* hemodynamic measurements (n=9/diet; E), ejection fraction (F) and heart rate during conscious echocardiography (n=11/diet; G) in 24 month-old WT mice fed Phe- and Phe+ diets. H-K, dP/dt_{max} (H) & dP/dt_{min} (I) in 15 month-old chow-fed WT mice vs. 24 month-old WT mice fed Phe- diet (n=9-10/group) as well as systolic strain rate (J ;n=9-10/group) and myocardial interstitial fibrosis (K; n=5/group) in 10 month-old chow-fed WT mice vs. 24 month-old WT mice fed Phe- diet. Data are presented as mean ± SEM and analyzed with one-way ANOVA with Bonferroni post-hoc test (A, C), with two-way ANOVA (B, D) or two-tailed unpaired t-test (E-K); ns: non-significant, **p* < 0.05, ***p* < 0.01, ****p* < 0.001.

References

1. Ternacle J, Wan F, Sawaki D, Surenaud M, Pini M, Mercedes R, Ernande L, Audureau E, Dubois-Rande JL, Adnot S, Hue S, Czibik G, Derumeaux G. Short-term high-fat diet compromises myocardial function: a radial strain rate imaging study. *Eur Heart J Cardiovasc Imaging*. 2017.
2. Derumeaux G, Ichinose F, Raheer MJ, Morgan JG, Coman T, Lee C, Cuesta JM, Thibault H, Bloch KD, Picard MH, Scherrer-Crosbie M. Myocardial alterations in senescent mice and effect of exercise training: a strain rate imaging study. *Circulation. Cardiovascular imaging*. 2008;1(3):227-234.
3. Sebag IA, Handschumacher MD, Ichinose F, Morgan JG, Hataishi R, Rodrigues AC, Guerrero JL, Steudel W, Raheer MJ, Halpern EF, Derumeaux G, Bloch KD, Picard MH, Scherrer-Crosbie M. Quantitative assessment of regional myocardial function in mice by tissue Doppler imaging: comparison with hemodynamics and sonomicrometry. *Circulation*. 2005;111(20):2611-2616.
4. Sawaki D, Czibik G, Pini M, Ternacle J, Suffee N, Mercedes R, Marcelin G, Surenaud M, Marcos E, Gual P, Clement K, Hue S, Adnot S, Hatem SN, Tsuchimochi I, Yoshimitsu T, Henegar C, Derumeaux G. Visceral Adipose Tissue Drives Cardiac Aging Through Modulation of Fibroblast Senescence by Osteopontin Production. *Circulation*. 138(8):809-822.
5. Bacalini MG, Franceschi C, Gentilini D, Ravaioli F, Zhou X, Remondini D, Pirazzini C, Giuliani C, Marasco E, Gensous N, Di Blasio AM, Ellis E, Gramignoli R, Castellani G, Capri M, Strom S, Nardini C, Cescon M, Grazi GL, Garagnani P. Molecular Aging of Human Liver: An Epigenetic/Transcriptomic Signature. *J Gerontol A Biol Sci Med Sci*. 74(1):1-8.
6. Kasprzyk A, Keefe D, Smedley D, London D, Spooner W, Melsopp C, Hammond M, Rocca-Serra P, Cox T, Birney E. EnsMart: a generic system for fast and flexible access to biological data. *Genome Res*. 2004;14(1):160-169.
7. Ashrafian H, Czibik G, Bellahcene M, Aksentijevic D, Smith AC, Mitchell SJ, Dodd MS, Kirwan J, Byrne JJ, Ludwig C, Isackson H, Yavari A, Stottrup NB, Contractor H, Cahill TJ, Sahgal N, Ball DR, Birkler RI, Hargreaves I, Tennant DA, Land J, Lygate CA, Johannsen M, Kharbanda RK, Neubauer S, Redwood C, de Cabo R, Ahmet I, Talan M, Gunther UL, Robinson AJ, Viant MR, Pollard PJ, Tyler DJ, Watkins H. Fumarate is cardioprotective via activation of the Nrf2 antioxidant pathway. *Cell Metab*. 2012;15(3):361-371.
8. Yeung YG, Stanley ER. A solution for stripping antibodies from polyvinylidene fluoride immunoblots for multiple reprobing. *Anal Biochem*. 2009;389(1):89-91.
9. Obame FN, Plin-Mercier C, Assaly R, Zini R, Dubois-Rande JL, Berdeaux A, Morin D. Cardioprotective effect of morphine and a blocker of glycogen synthase kinase 3 beta, SB216763 [3-(2,4-dichlorophenyl)-4(1-methyl-1H-indol-3-yl)-1H-pyrrole-2,5-dione], via inhibition of the mitochondrial permeability transition pore. *J Pharmacol Exp Ther*. 2008;326(1):252-258.
10. Sanayama Y, Matsumoto A, Shimojo N, Kohno Y, Nakaya H. Phenylalanine sensitive K562-D cells for the analysis of the biochemical impact of excess amino acid. *Sci Rep*. 4:6941.
11. Davidson MM, Nesti C, Palenzuela L, Walker WF, Hernandez E, Protas L, Hirano M, Isaac ND. Novel cell lines derived from adult human ventricular cardiomyocytes. *J Mol Cell Cardiol*. 2005;39(1):133-147.

DISCUSSION

Discussion

My PhD thesis involved four studies with senescence as a common denominator. The studies 1 to 3 investigated the adipose tissue premature senescence induced in *in vivo* and *in vitro* models of caloric overload (Studies 1 and 3) and in the context of chronological aging (Study 2). Study 4 explored naturally occurring cardiac senescence in chronological aging.

Specifically, Study 1 was tasked to evaluate time-dependent early changes in adipose tissue in HFD-fed mice, finding ATM to undergo senescence and associated dysfunction as the earliest detectable abnormality reflected in impaired systemic glucose homeostasis and cardiac dysfunction. Study 2 aimed to dissect how VAT senescence in natural aging emerges, identifying ATM senescence to compromise functional integrity of adjacent adipose tissue and systemic glucose homeostasis. The main focus of Study 3 was to explore how experimental caloric overload may induce adipose tissue and preadipocyte senescence, pointing to excessive ATP levels as the immediate inducer of premature senescence. Study 4 was based on the observation that there is an age-dependent increase in blood Phe levels and from here experimentation established Phe-related adverse cardiac effects in natural aging and impaired hepatic Pah activity as an underlying cause.

Thus, our aim is to dissect the respective role of two senescence “stressors” on visceral adipose tissue, i.e. increase in nutrients and aging, together with their combination. Indeed we demonstrate the time course of senescence cells affecting specifically different adipose tissue cells with impact on the SASP and the remote effects on target organs such as the heart. This work is still in progress and has major implications in the prevention of deleterious consequences of adipose tissue senescence, requiring tailored “senolytic” therapy before translation to the clinical setting.

These observations are summarized in supplemental table 2 with comparison of metabolic parameters, adipose tissue remodeling, circulating cytokines and impact on heart between the 3 groups of age (2, 5 and 12 months old animals). For instance, the respective occurrence of cellular senescence as assessed by staining of senescence markers (p16 & p21) on the different cell types in visceral adipose tissue show a different profile according to the age, as it is shown bellow, for example, for preadipocytes.

	PREADIPOCYTES			
	CD	2w HFD	5w HFD	10w HFD
2				
5				
12		in progress	in progress	in progress



➤ VAT senescence in natural aging

In 2018, our team identified that age-related cardiac decline was fuelled by a VAT-derived profibrotic secretome.^{319,320} During my PhD thesis I participated in experiments aiming to extend our previous findings in natural aging by identifying age-related VAT remodeling and dysfunction as a consequence of adipose tissue macrophages (ATM) senescence. Senescence-associated impairment of ATM function emerged as matricellular protein OPN-dependent macrophage dysfunction, such as efferocytosis.

First, we phenotyped VAT derived from elderly WT mice (12 months old) and established VAT aging as one characterized by structural remodeling (i.e. enlargement of adipocytes, fibrotic deposition) and senescence (SA- β -Gal activity and p16/p21/p53) with an altered secretome (i.e. profibrotic cytokines and adipokines)³²⁰ and associated metabolic dysfunction (i.e. impaired glucose tolerance, insulin sensitivity). Notably, we observed that VAT aging in mice began at middle age, as evident by signs as early as 12 months of age, which is much sooner than previous reports suggest in the literature.³²¹ Whether VAT remodeling/dysfunction occurring with natural aging is related to cellular senescence has been unknown.

In search of clues, we found that induction of matricellular proteins (i.e., OPN and galactin3) and senescence markers was more discriminative than proinflammatory genes (which have been proposed to be a source of harmful effects under stress such as caloric overload resulting in a chronic, low-grade proinflammatory state)³²² to drive VAT aging. These results associated with a marked downregulation of efferocytosis-related genes. Whilst a role for various matricellular proteins including OPN has been shown in VAT remodeling in obesity,³²³⁻³²⁶ we previously established VAT as the major source of OPN secretion in natural aging.³²⁰ Moreover, we found that OPN increasingly and overwhelmingly colocalised with markers of

senescence (especially p16) and macrophage marker F4/80 in VAT of aged WT mice. Since OPN's is known to impact on macrophage polarisation and function,³²⁷ we explored the relationship among OPN, ATM and VAT senescence further.

➤ **Importance of macrophage senescence in VAT aging**

First, to dissect the interplay between OPN and ATM senescence, we explored how OPN may induce senescence in naïve WT BMDM. As expected, recombinant OPN induced a senescent-like phenotype in naïve macrophages with reduced phagocytic activity. Interestingly, recent reports suggest that ATM's endocytotic dysfunction may be one of the primary events to mediate VAT dysfunction in both aging and obesity.^{328,329}

Next, we speculated that OPN-inducible ATM senescence may compromise inherent macrophage functions and spread senescence to the adjacent tissue. Accordingly, we found that genetic deletion and pharmacological inhibition of OPN reduced both VAT and ATM senescence, whilst restoring efferocytosis, as shown by *in vitro* and *in vivo* assays.

In addition to ameliorated macrophage function, an interesting collateral finding was that genetic OPN deletion resulted in significantly larger adipocytes and gross VAT mass. Intriguingly, OPN/senescence-free adiposity associated with better metabolic function, lending support to the concept that VAT quality is both critical and improvable.

Even though genetic deletion and pharmacological inhibition of OPN prevented or reversed functional ATM and VAT senescence, we used a secondary approach to specifically target macrophages. In the absence of available conditional OPN knockout mice, we chose to eliminate macrophages by clodronate-liposome treatment (an approach we also used in diet-induced obesity in Study 3). By deleting senescent and dysfunctional ATM (lessened p16+CD68+ cells) in elderly mice clodronate-liposome treatment ameliorated VAT structural remodeling (i.e., adipocyte hypertrophy), and more broadly, metabolic function (i.e. glucose tolerance and adipokine secretion profile). These findings strongly indicate that ATM is a major contributor to age-related VAT and systemic metabolic dysfunction.

Next, we dug further into the OPN-dependent senescence-associated impairment of ATM function. In particular, we studied efferocytosis (a key macrophage function found

downregulated as a function of age by our discriminative gene expression analysis) both *in vivo* and *in vitro*. Efferocytosis is crucial in maintaining AT homeostasis by removing apoptotic cells and cell debris. Whilst aging was associated with an increase in TUNEL+ cells in WT and OPN^{-/-} VAT alike, only aged OPN^{-/-} mice manifested efficient efferocytosis evidenced by higher rate of engulfed TUNEL+ or cleaved-caspase 3+ cells. *In vitro* functional assay further supported healthier efferocytosis by OPN deficiency: compared to age-matched WT BMDM, aged OPN^{-/-} BMDM exerted preserved phagocytic activity with higher expression levels of key efferocytosis-related genes such as *Mertk*.^{330,331} The importance of our findings is underscored by recent studies finding tissue microenvironment to be the most important determinant for macrophage functionality,³³² whilst changes in apoptotic signals program tissue macrophages differently for efferocytosis.³³³⁻³³⁵ In aging adipose tissue extracellular OPN seems to direct recruited or naïve tissue macrophages to senescent reprogramming at the cost of phagocytic function.

Several recent publications observed favourable effects by systemic elimination of senescent cells with senolytic drugs.^{267,336-338} On the other hand, induction of senescence in some cell types responsible for damage is beneficial during aging and repair processes,^{280,320,339,340} not to mention in preventing cancer. Here we have identified OPN as a novel target for ameliorating cellular senescence in specific cell types such as adipose tissue macrophages, complementing our previous observations in cardiac fibroblasts.³²⁰ Collectively, our results demonstrated that elimination of senescent ATM ameliorated AT remodeling and dysfunction. These observations suggest that macrophage-specific and senescence-targeted therapeutics (such as macrophage-directed pharmacological OPN inhibition) could be a viable strategy to control AT senescence with altered secretome and systemic metabolic decline in aging.

➤ **Role of macrophages identified by studying time-dependent effects of HFD in young WT mice**

In caloric overload, the capacity of WAT's energy storage reaches a threshold that turns on a cascade ultimately resulting in pathological consequences, including systemic inflammation, increased insulin resistance and remote organ damage.^{204,272,341} Whilst most research groups

use long-term HFD, we limited its duration of HFD to 10 weeks to observe earlier changes without secondary confounders. We challenged wild type mice of different ages (2, 5 and 12 months of age) with HFD.

The first focus was to explore early cell type-specific changes induced by HFD in young mice (2 months old) and test if experimental interference will reverse relevant HFD-induced abnormalities. Accordingly, major findings of this study can be summarised as follows:

1. Macrophage senescence is the first pathology preceding inflammation and major tissue remodeling.
2. *In vivo* pharmacological clearance of macrophages restored normal cardiometabolic status in mice fed a HFD for two weeks.

Visceral adiposity is a profound risk for T2DM and heart disease.^{318,342,343} With caloric overload, experimentally realised by HFD, the majority of high-energy nutrients find their way into adipose tissue for storage. This happens at an expense of gradual remodeling and altered function. Intriguingly, early processes within the VAT that may later escalate are unknown. In the course of the present study, we explored this initial phase and found that VAT alterations confined to adipocyte hypertrophy and macrophage senescence, without signs of inflammation, change in macrophage number or fibrotic remodeling. Early HFD-induced WAT senescence is consistent with findings identified in Study 3 where the mice were slightly older (5 months old vs 2 months old).

Intriguingly, an increase in CLS count characteristic of caloric overload was absent before 10 weeks of HFD. Moreover, whether the unaltered macrophage number and position reflect the resistance of resident macrophages to HFD-inflicted injury or their balanced but accelerated replacement from local pools,³⁴⁴ peritoneal cavity³⁴⁵ or bone marrow^{288,346} remains to be explored. At any rate, despite subtle microscopic findings in VAT, at the organism level even 2 weeks of HFD was sufficient to impair glucose homeostasis and cardiac function.

Long-term HFD induces macrophage M1 polarisation, recruitment from bone marrow and AT fibrosis, all attributed an important role in the ensuing dysmetabolic state.³⁴⁷⁻³⁴⁹ In contrast with these widely accepted abnormalities associated with long-term HFD regimen, we found no evidence for them up to 5-10 weeks of HFD. This led us to hypothesize that a senescence-associated dysfunction of adipose tissue macrophages is a critical priming event. To directly

address the possibility of macrophage involvement we fed mice HFD for 2 weeks and treated them with clodronate-liposome, as we did in old mice (Study 3). These liposomes are known to be selectively phagocytosed by macrophages and internalised clodronate subsequently induces apoptosis.³⁵⁰ Most importantly, we observed that clearance of macrophages restored normoglycemia. Although the intricate nature of macrophage dysfunction remains a matter of debate, these findings are consistent with the reversal of dysmetabolic state either with clodronate-mediated removal of macrophages^{351,352} or genetically induced apoptosis of senescent cells in p16-ATTAC mice³⁵³ on long-term HFD (>12 weeks). More importantly, these results may inform about impaired glucose homeostasis critically depending on the state of macrophages *per se*. The nonessential nature of chronic low-grade inflammation^{349,354} or fibrotic remodeling of VAT³⁴⁸ at this early stage may be reconciled by altered immune cells unable to preserve functional tissue, possibly rendering VAT (as well as probably other organs) to further injury when persistently challenged.

In the past years, several studies converged to the concept that accumulation of senescent cells during aging or after metabolic challenge such as diabetes or obesity contributes to the overall decline in organ function and lifespan. Previous studies using p16INKATTAC mice and senolytic drugs proved the merits of removal of all senescent cells to improve organ function and longevity. Thus, these observations prompted us to test the association of Dasatinib plus Quercetin to prevent HFD-related cardiac and metabolic disorders. Interestingly senolytic treatment was not efficient to prevent the cardiac functional alteration induced by HFD, despite a moderate improvement in metabolic function as assessed by GTT and ITT. Such an observation is in line with our previous data demonstrating that cellular senescence is not only harmful but has beneficial roles in cardiac aging since the senescence induction in cardiac fibroblasts is pivotal in blunting fibrosis during aging and in improving therefore cardiac function. These data provide therefore arguments to develop cell type-specific senolytic approaches with the hypothesis that eliminating selectively pathogenic senescent cells will benefit cardiac and metabolic function.

Indeed, cardiac integrity is known to be negatively affected by HFD.³⁵⁵ In hearts of HFD-fed mice we observed a slight, nonetheless significant time-dependent increase (i.e. not before 10 weeks of HFD) in cardiomyocyte cross-sectional area, but no increase in myocardial interstitial fibrosis. HFD compromised contractility prior to any detectable structural changes.

Importantly, the deficit in contractility by HFD was undone via clodronate-mediated clearance of macrophages. These observations support a vital role for macrophage dysfunction in early, HFD-induced cardiac impairment.

Despite the spectacular rescue effect achieved with pharmacological clearance of macrophages, global macrophage depletion cannot be a therapeutic aim, as life without macrophages would have dramatic effects. In an attempt to develop potentially translatable therapeutic options, first it is important to characterize these senescent macrophages deeper to understand the intricate mechanisms that shifted them into a senescent state. In addition to determining how they become senescent, it is imperative to learn how they induce metabolic and cardiac alterations.

Answers to the first question will set the course for the pathways involved that could be specifically targeted by carefully chosen senolytic or senostatic agents. The viability of this approach is suggested by recent studies showing distinct molecular vulnerabilities of senescent cells.^{270,275-278} Our data pave the way to adapt the strategy to screen potential senolytic drug candidates targeting specifically senescent tissue macrophages in order to increase the therapeutic efficiency with minimised side-effects as opposed to a global senolytic approach used in our present study. Specific delivery to target cells, i.e., macrophages may also be improved by encapsulating chosen senolytics into liposomes to be selectively phagocytosed by macrophages or even ATMs should the targeting strategy allows it.

Deciphering the mechanisms by which senescent macrophages induce metabolic and cardiac alterations need to be based on extensive analysis of the secretome of these cells. This ongoing work that I aim to contribute, will involve proteomic/metabolomic/lipidomics screening of local secretomes and plasma representing systemic circulation that reaches remote organs affected. Besides, a future area of interest is to identify circulating extracellular vesicles recently implicated in obesity.³⁵⁶ Paracrine effects will be explored using co-culturing of macrophages with potentially affected cells (preadipocytes, fibroblasts, etc).^{134,169-171}

In conclusion, our findings allow the speculation that macrophage senescence by HFD is one of the first pathological events, occurring well before local or systemic inflammation as well as major tissue remodeling take place. Its key pathogenic role is underscored by restored

cardiometabolic status after *in vivo* pharmacological clearance of macrophages. Exploratory studies will shed further light on early macrophage senescence and dysfunction in VAT and possibly other organs that may take us a step closer to improved therapeutic targets in T2DM.

➤ **Adipose tissue senescence is mediated by increased ATP content after a short-term high fat diet exposure**

After the identification of the early and key role of macrophages in adipose tissue senescence, we aimed to explore mechanisms potentially underlying the accumulation of senescent cells within both visceral and subcutaneous WAT in response to experimental caloric overload. Here we found that induction of senescence in either WAT depots was a very early event occurring two weeks after HFD initiation in parallel with metabolic alterations but independent of systemic inflammation or WAT fibrosis. Furthermore, we identified HFD-induced excessive ATP production by increased glycolysis and oxidative phosphorylation, as a putative mechanism underlying WAT senescence. Forced exercise in the form of daily swimming restored impaired systemic glucose homeostasis irrespective of reductions in body weight and adiposity. With regard to WAT senescence, we found that exercise disproportionately affected various fat pads, ameliorating senescence in subcutaneous AT but not in visceral AT. These fat-specific differences seemed to be inherent as demonstrated in tissues and primary preadipocytes derived from subcutaneous and visceral AT and were related to xanthine oxidase-mediated ATP disposal.

At the end of 10 weeks of HFD starting in male WT mice of 5 months of age, we did not observe WAT fibrosis, nor local or systemic inflammation, but glucose intolerance, insulin resistance and leptin production manifested consistent with increased fat mass and adipocyte hypertrophy along with organization of immune cells into crown-like structures.³⁵⁷

Specifically, we found unaltered tissue levels of classical pro-inflammatory SASP factors (CCL2, TNF α , IL6, IL10, PAI1)^{181,222,358} as opposed to longer (i.e. 30 vs. 10 weeks in our model) HFD exposure in older (12-13 vs. 7 months) animals.²⁸³ Instead, we observed an upregulation of several SASP-related chemokines (Mcp1) and profibrotic cytokines (Tgfb1, Fn1, Timp1) in eWAT but not iWAT. Interestingly, of the affected factors MCP-1 is secreted by senescent cells and has recently been correlated with biological age in mammals,³⁵⁹ whilst TGF β promotes matrix remodeling in remote organs³⁶⁰. Our recent observations^{341,360} lend support to the

ability of senescent WAT to secrete great quantities of profibrotic cytokines that alter tissue homeostasis prior to the development of a pro-inflammatory secretome. This profibrotic secretome has been shown to contribute to organ remodeling, dysfunction, and premature aging.^{181,188,360} Accordingly, we observed that cellular senescence as one of the earliest events occurring in WAT, two weeks after the initiation of HFD as demonstrated by increase in SA- β -gal activity, and expression of senescence markers p16 and p21.

Increased ATP content initiates WAT senescence

Caloric overload is buffered by the ability of WAT to store surplus energy as fat. For a long time, WAT has been considered as a passive storage unit as a result of anabolic metabolism, whilst little is known about catabolic processes during excessive energy intake. As evidence for increased catabolism occurring in concert with enhanced anabolism in HFD-challenged adipocytes, we found elevated ATP levels in both subcutaneous and visceral adipose tissue - derived preadipocytes, which was normalized by exercise only in subcutaneous WAT. This is consistent with marginally increased mitochondrial ROS production in WAT of HFD-fed mice, probably as a by-product of exaggerated oxidative phosphorylation.

As adipocytes are prototypic low-maintenance cells in terms of energy utilization, it is curious what happens to excess ATP and what changes it may induce. Firstly, there is a feedback inhibition by ATP and NADH at multiple upstream levels, which would slow down and eventually stop further catabolism. Secondly, we reasoned that should the adipocytes be able to turn on mechanisms to reduce ATP levels, they would be expected to do so. One such possibility is to enhance purine catabolism as a means to dispose excessive ATP. In parallel with increased responsiveness of subcutaneous WAT to exercise-induced ATP reduction, we observed substantially higher expression of xanthine oxidase (XO) – the rate-limiting enzyme controlling purine degradation –, in subcutaneous than in visceral WAT. Moreover, XO uses molecular O₂ as an essential cofactor, which is provided by exercise hyperaemia that improves blood flow in the neighbouring subcutaneous WAT. The combination of high XO expression, HFD-derived increased substrate supply for purine degradation and O₂ cofactor is consistent with the difference between subcutaneous and visceral WAT in exercise preventing/reversing senescence. We further demonstrated that ATP, but not uric acid-loaded liposomes induced senescence in primary preadipocytes derived from subcutaneous WAT and this was

dependent on XO activity, as its inhibitor allopurinol provoked senescence when cells were challenged with ATP-loaded liposomes or increased glucose/fatty acid content in the media.

➤ **Exercise exerts a “senostatic” action preventing WAT senescence during HFD**

Our findings confirm previous reports of exercise preventing adipose tissue senescence in HFD²⁸³ and add mechanistic clues to a triggering role for ATP. The significance of our present results is further highlighted by the lack of confounding factors known to interfere with senescence, such as age³⁶⁰ and weight loss,³⁶¹ in our study design.

Exercise promotes mitochondrial biogenesis and improves function in multiple organs including the heart.³⁶² Curiously, we found that exercise reduced global WAT respiration, mitochondrial ATP-linked oxygen consumption and glycolysis, ultimately resulting in reduced ATP accumulation in subcutaneous but not in visceral WAT. These observations extend our findings about increased purine degradation in calorically challenged subcutaneous WAT-derived preadipocytes and suggest that subcutaneous WAT is able to limit ATP production and activate ATP disposal in times of caloric overload, whilst visceral WAT cannot. Moreover, exercise improved insulin sensitivity in obesity in concert with modulating the excessive energy generation. These findings are in line with the normalization of HFD-induced increase in mitochondrial mass, a pattern closely reflecting that observed in other models of senescence.^{363,364} As ATP acts as a danger signal on immune cells,³⁶⁵ our data show that exercise-related ATP reductions moderate p16 and p21 expression in WAT macrophages, which may improve the clearance of senescent cells. Our data are in line with a recent observation showing that restraining mitochondrial ATP synthesis with a relatively weak respiratory chain complex IV inhibitor may alleviate age-associated disorders.³⁶⁶

Clinical impact

Given the worldwide obesity epidemics, there is an increasing interest in public health programs encouraging healthy eating behaviour and physical activity. Aerobic training has a beneficial impact at different life stages on several aspects of human health, such as cognitive function, cardiovascular, endocrine, and immune responses. Importantly, the benefit of exercise has been demonstrated in pathological conditions, including diabetes, cancer, and cardiovascular disorders³⁶⁷. Here we add mechanistic insights to the role of exercise in

preventing both cellular senescence and impaired glucose homeostasis in diet-induced obesity, reinforcing the concept that adipose tissue dysfunction affects glucose homeostasis.³⁶⁸ As such, exercise ameliorates WAT cellular senescence, adipokine dysregulation and adipocyte bioenergetics independent of weight loss, favouring the recovery of glucose homeostasis in obesity. Therefore, exercise through the control of local ATP seems an interesting approach to prevent the induction of cellular senescence and its potential deleterious consequences. In summary, exercise is an excellent “senostatic” strategy for preventing obesity-associated senescence in WAT devoid of side effects together with mitigating cardiac-associated abnormalities.

Since my team is interested in studying the cross-talk between the adipose tissue and the heart in different settings mimicking clinical situations of aging (obesity, chronological aging), all our murine models are phenotyped on both metabolic and myocardial changes.

Therefore, I have participated in a study aiming to decipher mechanisms leading to cardiac aging during chronological aging.

Dysregulated Phe catabolism in natural aging

This study followed our interest in finding extracardiac cues to cardiac deterioration associated with natural aging (coined henceforth as “cardiac aging”). Results provide new mechanistic insights into cardiac aging with important clinical implications. Firstly, we demonstrate that aging increases plasma Phe levels in mice and that elevated plasma Phe levels induce cardiac senescence and dysfunction, a phenotype inducible with Phe treatment in WT young mice. Secondly, we show that age-related increase in p21 suppresses hepatic Pah function, the latter crucial in controlling systemic Phe levels. Thirdly, p21 deficiency delays structural, functional, and molecular alterations in the aging myocardium whilst Pah cofactor BH4 or dietary Phe restriction reverses them. Collectively, our findings may provide diagnostic clues for cardiac aging and open new therapeutic avenues to rejuvenate aged myocardium, an important challenge in the face of high cardiovascular burden in the growing population of elderly individuals.³⁶⁹

Hyperphenylalaninemia promotes cardiac aging

Notably, our murine experiments recapitulated elevated plasma Phe levels observed in elderly human subjects.³⁷⁰⁻³⁷³ Subsequently, we found that Phe excess induced myocardial p21, hence cardiac senescence. Furthermore, increased plasma levels of the essential amino acid Phe pointed to its impaired global catabolism, an observation particularly interesting in light of myocardial induction of Pah, Gch1 and 2-SC that we found in aged hearts, confirming progressive induction of myocardial Pah transcripts by aging.^{374,375} This strongly suggests that in hyperphenylalaninemia myocardium acts to maintain Phe homeostasis through induction of its catabolic machinery. In the course of this adaptation, however, cardiac Phe catabolism may itself promote myocardial aging through altered intracellular signalling by protein succination,³⁷⁶ as we have demonstrated in aging human and murine myocardium. Equally, but not exclusively, increased Phe uptake with limited myocardial Phe catabolic capacity may result in the accumulation of toxic metabolites, such as phenylpyruvate, phenyllactate and phenylacetate.³⁷⁷ Moreover, increased ectopic Phe catabolism into tyrosine may fuel catecholamine biosynthesis in tyrosine hydroxylase-expressing cells, such as certain neurons and chromaffin cells of the adrenal medulla.³⁷⁸ Thus, elevated Phe levels have an adverse impact on cardiac health, as evidenced by structural and functional myocardial impairment with a signature of senescence and Phe catabolism.

BH4 treatment rejuvenates the aging myocardium by restoring hepatic Pah activity

Our findings support a paradigm of age-related hepatic hypocatabolism of Phe underlying age-related rise in plasma Phe and driving cardiac aging. This is in line with downregulation of *Pah*, one of the six BH4-dependent enzymes with the highest hepatic expression. *Pah*'s vital dependence on its natural cofactor, BH4, is illustrated by hyperphenylalaninemia being a prominent feature of enzymatic deficiencies in *de novo* BH4 biosynthesis or the recycling pathway.³⁷⁹

Importantly, we restored healthy cardiac structure and function in naturally aged mice through normalizing plasma Phe levels by BH4, consistent with revived hepatic *Pah* activity.^{380,381} In line with this, we found reduced Pah and tyrosine levels in AML12 hepatocytes with pharmacologically stimulated senescence that could be rescued by both p21 knockdown and BH4. In theory, other BH4-dependent enzymes, i.e., nitric oxide synthases (NOS) could

play a role in the cardiac improvement observed with BH4 treatment. Improved vascular NOS coupling and subsequently reduced left ventricular afterload³⁸²⁻³⁸⁴ is unlikely, however, since systemic blood pressure remained unaltered by intraperitoneal BH4 delivery. Moreover, BH4 treatment did not increase myocardial NOS activity. Lack of such changes is consistent with the reported failure of exogenously delivered BH4 to reach efficient systemic concentrations³⁸² due to predicted BH4 uptake of natural Phe-expressing organs: the liver and kidney.³⁸⁵ Restored indices of myocardial Phe catabolism by BH4 correspond to BH4 uptake by the liver fuelling its local Pah activity taking the burden of Phe catabolism off the heart. This is consistent with the lack of reduction in cardiac damage induced by pressure overload in cardiomyocyte-restricted Gch1 transgenic mice³⁸⁶ as opposed to oral BH4 administration.³⁸⁷ Finally, the salubrious myocardial effects of dietary Phe restriction underscores the importance of lowering systemic Phe levels to rejuvenate old hearts.

Collectively our data show that pharmacological restoration of hepatic *Pah* activity by BH4 may rejuvenate age-associated cardiac changes and have potential application in age-related cardiac disease, such as heart failure.

Age-dependent p21 compromises hepatic *Pah* activity

Whilst Phe induced p21 in hepatocytes and cardiomyocytes *in vitro*, aging upregulated p21 expression in both liver and heart, hallmarking senescence of these organs. Moreover, we uncovered a significant delay in age-related rise in plasma Phe levels and cardiac decline in p21^{-/-} mice indicating that there are particular age-related gain-of-function(s) attributable to p21. Accordingly, in cultured hepatocytes we established a Phe-dependent p21 induction; experimental p21 induction on the other hand was sufficient to compromise Pah expression and activity in hepatocytes, which could be rescued by BH4 co-treatment. This constitutes a vicious cycle: Phe induces hepatic p21, p21 compromises hepatic Pah expression/activity, which raises systemic Phe levels and the cycle starts all over again. Interestingly, neither Phe- nor p21-mediated life-shortening is unprecedented; whilst dietary addition of Phe reduces lifespan in *C. elegans*³⁸⁸ and ants,³⁸⁹ p21 deficiency increases it in mice.³⁹⁰ As for our findings, we identified one novel function for p21, which is the suppression of hepatic *Pah* expression/activity, through which p21 is a key node for the rise in plasma Phe levels with age.

Cardiac aging: a quiescent organ and cellular senescence?

Cellular senescence of the heart is intriguing due to the postmitotic status of cardiomyocytes (~30% of all heart cells occupying 80% of the heart's volume)³⁹¹ that do not fall under Leonard Hayflick's concept of senescence, the proliferative inability in otherwise division-competent cells.¹⁷⁹ Aged cardiomyocytes acquire a senescent-like phenotype characterised by persistent DNA damage at telomere regions that occur independent of cell division and telomere length.³⁹² This length-independent telomere damage in cardiomyocytes activates senescent pathways (p21) and raises secretion of pro-fibrotic and -hypertrophic factors.³⁹² Autocrine/paracrine effects of this secretome include proliferation of cardiac fibroblasts and their activation towards myofibroblasts. In addition to this intramyocardial cascade, we uncovered a role for visceral adipose tissue, adding an endocrine enhancement to cardiac aging by releasing a profibrotic secretome (e.g., Tgfb1, osteopontin and leptin).³²⁰ Therefore, cardiac aging seems to result from complex interactions as part of an integrated multi-disorder state.

The present study extends this organism-level approach to cardiac aging by studying circulating metabolic signals. Since metabolic screens showed increased plasma Phe levels occurring in both natural aging and heart failure, we specifically studied the role of plasma Phe in cardiac aging.^{371-373,375,393-395} Our findings in age-related and experimentally induced hyperphenylalaninemia confirmed a causal relationship between elevated plasma Phe levels and cardiac decline.

A new piece in the puzzle: the natural course of cardiac aging

Murine investigations into cardiac aging traditionally explore animals with at least 18 months of age. These studies among others identified dysfunctional sirtuin/NAD⁺ biology,³⁹⁶ mitochondrial oxidative stress,³⁹⁷ abnormal PI3K/Akt signaling, misfolded proteins,³⁷⁴ telomere dysfunction, DNA damage³⁹² and compromised mitochondrial energetics³⁹⁸ in aged hearts. Our findings synergize with the literature extending our understanding of the natural history of cardiac aging. For instance, in WT hearts at 24 months of age we observed elevated complex III activity with suppressed ATP synthase activity pointing to the former as a potential mitochondrial source of oxidative stress.³⁹⁷

The early onset of age-related functional decline is most evident by the time-limited competitiveness of elite athletes, which typically predates heart disease. Accordingly, during our time-course we found clinically detectable impairments in myocardial structure and function as early as 10 months of age. Up to and including the age of 15 months we found no sign of myocardial DNA damage, impaired mitochondrial complex activities, alterations in NAD⁺/NADH levels (re: energetics and sirtuins). On the contrary, we observed an emergence of myocardial p21 expression, ectopic Phe catabolism with increased succination, redox imbalance and epigenetic changes starting at 10 months of age. These structural, functional and molecular alterations associated with elevated plasma Phe levels, were inducible with Phe treatment *in vitro* and in young WT mice *in vivo*, as well as were (depending on age at least partially) reversible with interventions controlling systemic Phe levels (*in vivo* BH4 treatment and dietary Phe restriction). These results demonstrate that dysregulated Phe catabolism is an early-onset persistent component of cardiac aging, preceding mechanisms described to date, and importantly, it is amenable to therapeutic correction.

Conclusions

Our findings unlock a novel approach to rejuvenate the aged myocardium by pharmacological restoration of aging-induced Phe catabolic decline. The potential of targeting Phe is highlighted by related abnormalities starting at middle age and persisting throughout life. Our observations may be extended to other age-related disorders, such as dementia,³⁹⁹ susceptibility to cancer,^{400,401} and all-cause mortality risk⁴⁰² that could benefit from a strategy of counteracting the adverse effects of a declining PAH activity.

CONCLUSION

&

PERSPECTIVES

Conclusion - Perspectives

My PhD thesis involved studies investigating the adipose tissue senescence induced in *in vivo* and *in vitro* models of caloric overload or chronological aging together with exploring the remote effects on cardiometabolic parameters.

Specifically, Study 1 was tasked to evaluate time-dependent early changes in adipose tissue in HFD-fed mice, finding ATM to undergo senescence and associated dysfunction as the earliest detectable abnormality, occurring well before local or systemic inflammation as well as major tissue remodeling take place. Its key pathogenic role was underscored by restored glucose homeostasis and cardiac function after *in vivo* pharmacological clearance of macrophages. Hence, it seems important to characterize these senescent macrophages deeper to understand the intricate mechanisms that shifted them into a senescent state and to learn how they induce metabolic and cardiac alterations. These exploratory studies will shed further light on early macrophage senescence and dysfunction in VAT and possibly other organs that may take us a step closer to improved therapeutic targets in T2DM.

In 2018, our team identified that age-related cardiac decline was fuelled by a VAT-derived profibrotic secretome. During my PhD thesis I participated in experiments aiming to extend our previous findings in natural aging by identifying age-related VAT remodeling and dysfunction as a consequence of adipose tissue macrophages (ATM) senescence (Study 2). Senescence-associated impairment of ATM function emerged as matricellular protein OPN-dependent macrophage dysfunction, such as efferocytosis. This study identified ATM senescence to compromise not only functional integrity of adjacent adipose tissue but also systemic glucose homeostasis. These observations suggest that macrophage-specific and senescence-targeted therapeutics (such as macrophage-directed pharmacological OPN inhibition) could be a viable strategy to control AT senescence with altered secretome and systemic metabolic decline in aging.

After the identification of the early and key role of macrophages in adipose tissue senescence, we aimed to explore other mechanisms potentially underlying the accumulation of senescent cells in AT. Thus, the main focus of Study 3 was to explore how experimental caloric overload may induce adipose tissue and preadipocyte senescence, pointing to excessive ATP levels as the immediate inducer of premature senescence. In this context, exercise, by controlling local

ATP production turned out to be a good strategy for preventing obesity-associated senescence in AT and cardiac-associated abnormalities.

Since my team is interested in studying the cross-talk between the adipose tissue and the heart in different settings mimicking clinical situations of aging (obesity, chronological aging), all our murine models are phenotyped on both metabolic and myocardial changes.

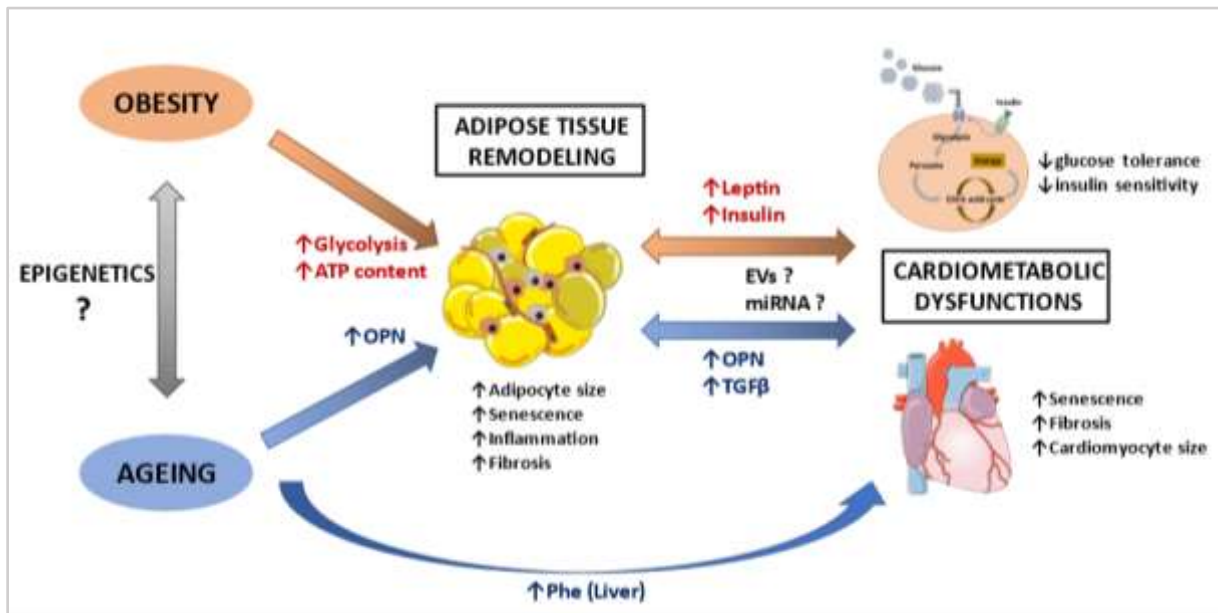
Therefore, I have participated in a study aiming to decipher mechanisms leading to cardiac aging during chronological aging (Study 4). This study followed our interest in finding extracardiac cues to cardiac deterioration associated with natural aging (coined henceforth as “cardiac aging”) and was based on the observation that there is an age-dependent increase in blood Phe levels. From here experimentation established Phe-related adverse cardiac effects in natural aging and impaired hepatic PAH activity as an underlying cause.

These findings unlock a novel approach to rejuvenate the aged myocardium by pharmacological restoration of age-induced Phe catabolic decline and may also be extended to other age-related disorders, such as dementia, susceptibility to cancer, and all-cause mortality risk that could benefit from a strategy of counteracting the adverse effects of a declining PAH activity.

Altogether our data indicate the noxious impact of high fat diet on adipose tissue that may act as a toxic organ releasing profibrotic and proinflammatory cytokines spreading senescence to remote organs with remodeling and dysfunction consequences as evidenced in the heart.

This PhD study underlines the need to integrate environmental factors in order to target the complex intertwined conditions participating to the organism aging and the related obesity- and age-diseasome. Indeed, the accumulation of senescent cells leads to premature loss of tissue renewal, inducing tissue remodeling and organ dysfunction. Premature aging may be the consequence of the senescent cell accumulation but is also driven by interconnected biological mechanisms such as epigenetic alterations, genomic instability, telomere attrition, deregulated nutrient sensing, mitochondrial dysfunction, stem cell exhaustion, and altered intercellular communication.

Our data suggest that epigenetic mechanisms are of importance in the control of “inflammaging” and deserve additional work that we aim to contribute in the next future. Indeed, epigenetic pathways are known to sense the environment and to reprogram the cell identity including endothelial and immune cells that may contribute to age-related organ dysfunction.



Graphical abstract: Adipose Tissue Remodeling as a central player in cardiometabolic disorders in the context of high-fat diet-induced obesity and aging.

SUPPLEMENTAL TABLES

SUPPLEMENTAL TABLE 1

Study 1: Supplemental tables

Used Taqman-MGB probes for qRT-PCR analysis

Target gene	Taqman assay ID
<i>Adipoq</i>	Mm00456425_m1
<i>Ccl2</i>	Mm00441242_m1
<i>Ccl5</i>	Mm01302427_m1
<i>CD68</i>	Mm03047343_m1
<i>Cdkn1a</i>	Mm04205640_g1
<i>Cdkn2a</i>	Mm00494449_m1
<i>Igf1</i>	Mm00439560_m1
<i>Lep</i>	Mm00434759_m1
<i>Slc2a4</i>	Mm00436615_m1
<i>Tnf</i>	Mm00443258_m1

Used antibodies for immunohistochemistry (IF) analysis

Target protein	Clone/product number	Company	Application/concentration
p16	2D9A12/ab54210	abcam	IF: 200 ⁻¹
p16	polyclonal/250804	Abbotec	IF: 200 ⁻¹
p21	HUGO291	EuroMabNet	IF: 200 ⁻¹
P21	monoclonal/ab80633	abcam	IF: 200 ⁻¹
Mac-3	monoclonal/ 550292	BD Biosciences	IF: 200 ⁻¹
CD68	polyclonal/ab125212	abcam	IF: 200 ⁻¹
CD3	polyclonal/ab5690	abcam	IF: 200 ⁻¹
PDGFR alpha	monoclonal/ ab203491	abcam	IF: 200 ⁻¹
GammaH2A.X(phosphoS140)	MA1-2022	Invitrogen	IF: 200 ⁻¹
Wheat germ agglutinin	W11261	Invitrogen	IF: 200 ⁻¹
BODIPY® 558/568 C12	D3835	Invitrogen	IF: 1000 ⁻¹
Isolectin GS-IB4	I21411	Invitrogen	IF: 100 ⁻¹
TO-PRO®-3	T3605	Invitrogen	IF: 1000 ⁻¹

Study 2: Supplemental tables

Used Taqman-MGB probes for qRT-PCR analysis

Target gene	Taqman assay ID	Target gene	Taqman assay ID
<i>Cdkn2a</i>	Mm00494449_m1	<i>Acaca</i>	Mm01304257_m1
<i>Cdkn1a</i>	Mm04205640_g1	<i>Pparg</i>	Mm00440940_m1
<i>Tp53</i>	Mm01731290_g1	<i>Pnpla2</i>	Mm00503040_m1
<i>Mfge8</i>	Mm00500549_m1	<i>Adipoq</i>	Mm00456425_m1
<i>Timd4</i>	Mm00724709_m1	<i>Il6</i>	Mm00446190_m1
<i>Mertk</i>	Mm00434920_m1	<i>Tnf</i>	Mm00443258_m1
<i>Mrc1</i>	Mm01329362_m1	<i>Mif</i>	Mm01611157-g1
<i>Spp1</i>	Mm00436767_m1	<i>Serpine1</i>	Mm00435858_m1
<i>Thbs1</i>	Mm01335418_m1	<i>Vegfa</i>	Mm01283063_m1
<i>Sparc</i>	Mm00486332_m1	<i>Il12b</i>	Mm01288989
<i>Lgals3</i>	Mm00802901_m1	<i>Cxcl2</i>	Mm00436450_m1
<i>Tnc</i>	Mm00495662_m1	<i>Ccl2</i>	Mm00441242_m1
<i>Postn</i>	Mm00450111_m1	<i>Cxcl1</i>	Mm04207460_m1
<i>Pdgfra</i>	Mm01205760_m1	<i>Ihnb</i>	Mm03023992_m1
<i>Lep</i>	Mm00434759_m1	<i>Tgfb1</i>	Mm01178820_m1
<i>Cd36</i>	Mm00432403_m1	<i>Il12a</i>	Mm00434169_m1
<i>Slc2a1</i>	Mm00441480	<i>Cxcl5</i>	Mm00436451_g1
<i>Ucp1</i>	Mm01244861_m1	<i>Csf2</i>	Mm01290062
<i>Pgc1a</i>	Mm01208835_m1	<i>Csf1</i>	Mm00432686
<i>Slc2a4</i>	Mm00436615_m1	<i>Il1b</i>	Mm00434228_m1
<i>Plin1</i>	Mm00558672_m1	<i>Infg</i>	Mm01168134_m1
<i>Fasn</i>	Mm00662319_m1	<i>Actb</i>	Mm02619580_g1
<i>Lipe</i>	Mm00495359_m1	<i>Axl</i>	Mm00437221_m1

Used antibodies for immunohistochemistry (IF) and western-blot (WB) analysis

Target protein	Clone/product number	Company	Application/concentration
p16	2D9A12/ab54210	abcam	IF: 200 ⁻¹
p16	polyclonal/250804	Abbiotec	IF: 200 ⁻¹ , WB: 200 ⁻¹
p21	HUGO291	EuroMabNet	IF: 200 ⁻¹ , WB: 500 ⁻¹
p53	polyclonal/ab31333	abcam	IF: 200 ⁻¹ , WB: 500 ⁻¹
phospho-p53 (Ser15)	polyclonal/9284	Cell Signaling	WB: 1000 ⁻¹
Osteopontin	polyclonal/ab8448	abcam	IF: 200 ⁻¹ , WB: 500 ⁻¹
F4/80	A3-1/MCA497GA	Serotec	IF: 200 ⁻¹
β-actin	AC-15/ab49900	abcam	WB: 5000 ⁻¹
Wheat germ agglutinin	W11261	Invitrogen	IF: 200 ⁻¹
CD68	polyclonal/ab125212	abcam	IF: 200 ⁻¹
CD3	polyclonal/ab5690	abcam	IF: 200 ⁻¹
CD45	30-F11/550539	BD Pharmingen	IF: 200 ⁻¹
GammaH2A.X(phosphoS140)	3F2/ab22551	abcam	IF: 200 ⁻¹
Cleaved caspase3	5A1E/9664	Cell Signaling	IF: 200 ⁻¹

Antibodies and reagents used for flow-cytometry

Antibodies or Reagents	Clone	Isotype	Source	Identifier
Brilliant Violet 605™ anti-mouse CD45	30-F11	Rat IgG2b, k	Biologend	103155
APC/Cyanine7 anti-mouse CD45.2	104	Mouse IgG2a, κ	Biologend	109823
Brilliant Violet 605™ anti-mouse CD45.1	A20	Mouse IgG2a, κ	Biologend	110737
PE/Cy7 anti-mouse/human CD11b	M1/70	Rat IgG2b, k	Biologend	101216
PE anti-mouse F4/80	BM8	Rat IgG2a, k	Biologend	123110
Alexa Fluor® 700 anti-mouse Ly-6G	1A8	Rat IgG2a, k	Biologend	127622
APC anti-mouse I-Ab	AF6-120.1	Rat IgG2a, k	Biologend	116418
Brilliant Violet 421™ anti-mouse Ly-6C	HK1.4	Rat IgG2c, k	Biologend	128031
FITC anti-mouse CD206	MR5D3	Rat IgG2a, k	Thermofisher Scientific	MA5-16870
Brilliant Violet 650™ anti-mouse CD206 (MMR)	C068C2	Rat IgG2a, k	Biologend	141723
APC/Cyanine7 anti-mouse CD3	17A2	Rat IgG2b, k	Biologend	100222
FITC anti-mouse CD3 ε	145-2C11	A. Hamster IgG	Biologend	100305
Alexa Fluor® 700 anti-mouse CD4	RM4-4	Rat IgG2b, k	Biologend	116021
Brilliant Violet 421™ anti-mouse CD8a	53-6.7	Rat IgG2a, k	Biologend	100737
APC anti-mouse/human CD45R/B220	RA3-6B2	Rat IgG2a, k	Biologend	103212
PE anti-mouse NK-1.1	PK136	Rat IgG2a, k	Biologend	108707
PE Rat IgG1, κ Isotype Ctrl	RTK2071		Biologend	400408
PE/Cy7 Rat IgG2b, κ Isotype Ctrl	RTK4530		Biologend	400617
FITC Rat IgG2a, κ Isotype Ctrl	RTK2758		Biologend	400505
APC Rat IgG2b, κ Isotype Ctrl	RTK4530		Biologend	400611
APC/Cy7 Rat IgG2a, κ Isotype Ctrl	RTK2758		Biologend	400523
Brilliant Violet 421™ Isotype Ctrl	TRK2758	Rat IgG2a, κ	Biologend	400535
Brilliant Violet 605™ Isotype Ctrl	RTK4530	Rat IgG2b, κ	Biologend	400649
Brilliant violet 650 isotype control	RTK2758	Rat IgG2a, k	Biologend	400541
Rat IgG2B Alexa Fluor® 700-conjugated	141945		R&D	IC013N

Study 3: Supplemental tables

Used Taqman-MGB probes for qRT-PCR analysis

Target gene	Taqman assay ID
<i>Adipoq</i>	Mm00456425_m1
<i>Adrb3</i>	Mm02601819_g1
<i>ATP5a1</i>	Mm00431960_m1
<i>Cdkn1a</i>	Mm04205640_g1
<i>Cdkn2a</i>	Mm00494449_m1
<i>Col1a</i>	Mm00801666_g1
<i>Cox5b (Gm11273)</i>	Mm01229713_g1
<i>Ctgf</i>	Mm01192933_g1
<i>Cycs</i>	Mm01621048_s1
<i>Fasn</i>	Mm00662319_m1
<i>Fn1</i>	Mm01256744_m1
<i>Glb1</i>	Mm00515342_m1
<i>Hif1a</i>	Mm00468869_m1
<i>Igf1</i>	Mm00439560_m1
<i>Il6</i>	Mm00446190_m1
<i>Lep</i>	Mm00434759_m1
<i>Lipe/Hsl</i>	Mm00495359_m1
<i>Lox</i>	Mm00495386_m1
<i>Mcp1/Ccl2</i>	Mm00441242_m1
<i>Mfn2</i>	Mm00500120_m1
<i>Nrf1</i>	Mm01135606_m1
<i>Pai1/Serpine1</i>	Mm00435858_m1
<i>PdgfRa</i>	Mm00440701_m1
<i>Plin1</i>	Mm00558672_m1
<i>Pnpla2</i>	Mm00503040_m1
<i>Ppara</i>	Mm00440939_m1
<i>Ppargc1a</i>	Mm01208835_m1
<i>Prdm16</i>	Mm00712556_m1
<i>P2rx7</i>	Mm01199500_m1
<i>Slc2a4</i>	Mm00436615_m1
<i>Tgfb1</i>	Mm01178820_m1
<i>Timp1</i>	Mm01341361_m1
<i>Tnf</i>	Mm00443258_m1
<i>Trp53</i>	Mm01731290_g1
<i>Ucp1</i>	Mm01244861_m1

Used antibodies for immunohistochemistry analysis

Target protein	Clone/product number	company
p16	2D9A12/ab54210	Abcam, UK
p21	EPR18021/ab188224	Abcam, UK
p21	C-19/sc-397-G	Santa Cruz, U.S.A.
PDGFR α	BAF1062	R&D System, U.S.A.
PDGFR α	EPR22059-270/ab203491	Abcam, UK
Mac3	CD107b/ab550292	BD Biosciences
CD3	ab5690	Abcam, UK
CD68	ab125212	Abcam, UK
CD45	AB550539	BD Pharmingen
Anti-gamma H2A.X (phospho S139)	EP854(2)Y/ab81299	Abcam, UK
Oxoguanine 8	2Q2311/ ab206461	Abcam, UK
Perilipin	k-13/ sc-47320	Santa Cruz, U.S.A.
Tom20	FL-145/sc-11415	Santa Cruz, U.S.A.
Xanthine Oxidase	EPR4605/ab109235	Abcam, UK

Study 4: Supplemental tables

Used antibodies for immunohistochemistry (IHC, IF) and western-blot (WB) analysis.

Target protein	Producer/Cat#	Species	Application/concentration
p21	Abcam: ab188224	rabbit	WB:1:1000
p21	Santa Cruz: sc-397	rabbit or goat	IF: 1:50
p-p53	Cell Signaling: 9284S	rabbit	WB: 1:1000
p53	Cell Signaling: 2524S	mouse	IF: 1:200
p16	Abbiotec: 250804	rabbit	IF: 1:100, WB: 1:100
β -actin	Abcam: ab49900	mouse-HRP	WB: 1:10000
Pah	Sigma: SAB250434	goat	IF: 100, WB: 1:200
Pah	Abcam: ab148430	rabbit	IHC: 1:200, IF: 1:100, WB: 1:300
Pah	ThermoFisher Scientific: PA5-79780	rabbit	WB: 1:1000
Gch1	Bioss antibodies: bs-0136R	rabbit	IF: 100, WB: 1:200-1000
2-SC	Cambridge BioSciences: crb2005017e	rabbit	IHC/IF: 1:100, WB:1:200
Nrf2	Genetex: GTX103322	rabbit	WB: 1:500, IF: 1:500
Cardiac troponin I	Abcam: ab47003	rabbit	IF: 1:200
CD31	Santa Cruz: sc-1506	goat	IF: 1:100
Acta2	Sigma: A2547	mouse	IF: 1:200
8-oxo-guanine	Abcam: ab206461	mouse	IF: 1:50
γ H2A.X-P	Abcam: ab81299	rabbit	IF: 1:200
H3K9me3	Abcam: ab176916	rabbit	IF: 1:200
Beta amyloid	Invitrogen: 51-2700	rabbit	IHC: 1:250
Ubiquitin	Abcam, ab7254	mouse	WB: 1:500
4-HNE	Millipore: AB5605	goat	IHC: 1:200
vimentin	Abcam: ab92547	rabbit	IF: 1:200
α -actinin	Abcam: ab68167	rabbit	WB: 1:5000

SUPPLEMENTAL TABLE 2

Summary of the findings in obesity and aging: Metabolic parameters in 2-, 5- and 12-month-old mice fed CD or HFD.

BODY WEIGHT & GLUCOSE METABOLISM					
Age	CD	2w HFD	5w HFD	10w HFD	20w HFD
2m	Normal BW Normal glucose tolerance Normal insulin sensitivity	Normal BW ↓glucose tolerance ↓insulin sensitivity	↑BW ↓glucose tolerance ↓insulin sensitivity	↑BW ↓glucose tolerance ↓insulin sensitivity	↑BW ↓glucose tolerance ↓insulin sensitivity
5m	Normal BW Normal glucose tolerance Normal insulin sensitivity	↑BW ↓glucose tolerance ↓insulin sensitivity	↑BW ↓glucose tolerance ↓insulin sensitivity	↑BW ↓glucose tolerance ↓insulin sensitivity	↑BW ↓glucose tolerance ↓insulin sensitivity
12m	↑BW ↓glucose tolerance ↓insulin sensitivity	Ongoing analysis	↑BW ↓glucose tolerance ↓insulin sensitivity	Ongoing analysis	↑BW ↓glucose tolerance ↓insulin sensitivity

Summary of the findings in obesity and aging: Adipose tissue phenotype in 2-, 5- and 12-month-old mice fed CD or HFD. Mac: macrophages, Lymph: lymphocytes, Pread: preadipocytes, CLS: crown like structures.

Age	VAT				
	CD	2w HFD	5w HFD	10w HFD	20w HFD
2m	Normal adipocyte size No CLS No immune cell infiltration No senescence No fibrosis Basal apoptosis	↑ adipocyte size ↑ senescence (Mac) No CLS No immune cell infiltration No fibrosis Apoptosis to be checked	↑ adipocyte size ↑ CLS number ↑ senescence (Mac, Lymph) No immune cell infiltration No fibrosis Apoptosis to be checked	↑ adipocyte size ↑ CLS number ↑ immune cell infiltration ↑ senescence (Mac, Lymph, Pread) No fibrosis Apoptosis to be checked	↑ adipocyte size ↑ CLS number ↑ immune cell infiltration ↑ senescence (Mac -others to be checked-) Fibrosis to be checked Apoptosis to be checked
5m	Normal adipocyte size No CLS No immune cell infiltration No senescence No fibrosis Basal apoptosis	↑ adipocyte size ↑ senescence (Pread -others to be checked-) Other parameters to be checked	↑ adipocyte size ↑ CLS number ↑ senescence (Pread -others to be checked-) Other parameters to be checked	↑ adipocyte size ↑ CLS number ↑ immune cell infiltration ↑ senescence (Mac, Lymph, Pread) No fibrosis Apoptosis to be checked	↑ adipocyte size ↑ CLS number Other parameters to be checked
12m	↑ adipocyte size ↑ immune cell infiltration ↑ senescence (Mac, Lymph) ↑ fibrosis ↑ apoptosis	Ongoing analysis	Ongoing analysis	Ongoing analysis	Ongoing analysis

Summary of the findings in obesity and aging: Plasma levels of cytokines in 2-, 5- and 12-month-old mice fed CD or HFD.

Age	PLASMA				
	CD	2w HFD	5w HFD	10w HFD	20w HFD
2m	Normal levels of adipokines and cytokines	<p>↑Leptin ↑Insulin ↑Activin A</p> <p>No increase in IL-6, CCL-2, TNFα</p> <p>No increase in MMP2, MMP9, TIMP-1, THBS-4</p>	<p>↑Leptin ↑Insulin ↑THBS-4 ↑Adiponectin</p> <p>No increase in IL-6, CCL-2, TNFα</p> <p>No increase in MMP2, MMP9, TIMP-1</p>	<p>↑Leptin ↑Insulin ↑IL-10</p> <p>No increase in IL-6, CCL-2, TNFα</p> <p>No increase in MMP2, MMP9, TIMP-1, THBS-4</p>	Ongoing analysis
5m	Normal levels of adipokines and cytokines	Ongoing analysis	<p>↑Leptin ↑Adiponectin ↑TGFβ</p>	<p>↑Leptin ↑Adiponectin ↑Insulin ↑IGF-1 ↑FGF-21 ↑PAI-1</p> <p>No increase in OPN, Activin A, TGFβ</p>	<p>↑Leptin ↓Adiponectin ↑CRP</p> <p>No increase in TGFβ</p>
12m	<p>↑Leptin ↑Adiponectin ↑TGFβ ↑IL-10 ↑OPN ↑Phe</p>	Ongoing analysis	Ongoing analysis	Ongoing analysis	Ongoing analysis

Summary of the findings in obesity and aging: Cardiac phenotype in 2-, 5- and 12-month-old mice fed CD or HFD. Systolic SR: systolic strain rate.

	HEART				
Age	CD	2w HFD	5w HFD	10w HFD	20w HFD
2m	Normal systolic SR Normal cardiomyocyte size No fibrosis No senescence Inflammation to be checked	↓ Systolic SR Normal cardiomyocyte size No fibrosis Senescence to be checked Inflammation to be checked	↓ Systolic SR Normal cardiomyocyte size No fibrosis Senescence to be checked Inflammation to be checked	↓ Systolic SR ↑ cardiomyocyte size ↑ (slight) fibrosis Senescence to be checked Inflammation to be checked	Ongoing analysis
5m	Normal systolic SR Normal cardiomyocyte size No fibrosis No senescence Inflammation to be checked		↓ Systolic SR ↑ cardiomyocyte size ↑ fibrosis Senescence to be checked Inflammation to be checked	↓ Systolic SR ↑ cardiomyocyte size ↑ fibrosis Senescence to be checked Inflammation to be checked	↓ Systolic SR ↑ cardiomyocyte size ↑ fibrosis Senescence to be checked Inflammation to be checked
12m	↓ Systolic SR ↑ cardiomyocyte size ↑ fibrosis ↑ senescence Inflammation to be checked	Ongoing analysis	Ongoing analysis	Ongoing analysis	Ongoing analysis

BIBLIOGRAPHY

References

- 1 Piche, M. E., Poirier, P., Lemieux, I. & Despres, J. P. Overview of Epidemiology and Contribution of Obesity and Body Fat Distribution to Cardiovascular Disease: An Update. *Prog Cardiovasc Dis* **61**, 103-113, doi:10.1016/j.pcad.2018.06.004 (2018).
- 2 Flegal, K. M., Kit, B. K., Orpana, H. & Graubard, B. I. Association of all-cause mortality with overweight and obesity using standard body mass index categories: a systematic review and meta-analysis. *JAMA* **309**, 71-82, doi:10.1001/jama.2012.113905 (2013).
- 3 *International Diabetes Federation. IDF Diabetes Atlas — 7th Edition. DiabetesAtlas* (2015).
- 4 Zheng, Y., Ley, S. H. & Hu, F. B. Global aetiology and epidemiology of type 2 diabetes mellitus and its complications. *Nat Rev Endocrinol* **14**, 88-98, doi:10.1038/nrendo.2017.151 (2018).
- 5 Global, regional, and national age-sex specific all-cause and cause-specific mortality for 240 causes of death, 1990-2013: a systematic analysis for the Global Burden of Disease Study 2013. *Lancet* **385**, 117-171, doi:10.1016/s0140-6736(14)61682-2 (2015).
- 6 Roglic, G. & Unwin, N. Mortality attributable to diabetes: estimates for the year 2010. *Diabetes Res Clin Pract* **87**, 15-19, doi:10.1016/j.diabres.2009.10.006 (2010).
- 7 Schellenberg, E. S., Dryden, D. M., Vandermeer, B., Ha, C. & Korownyk, C. Lifestyle interventions for patients with and at risk for type 2 diabetes: a systematic review and meta-analysis. *Ann Intern Med* **159**, 543-551, doi:10.7326/0003-4819-159-8-201310150-00007 (2013).
- 8 Hu, F. B. *et al.* Diet, lifestyle, and the risk of type 2 diabetes mellitus in women. *N Engl J Med* **345**, 790-797, doi:10.1056/NEJMoa010492 (2001).
- 9 Knowler, W. C. *et al.* Reduction in the incidence of type 2 diabetes with lifestyle intervention or metformin. *N Engl J Med* **346**, 393-403, doi:10.1056/NEJMoa012512 (2002).
- 10 Guglielmi, V. & Sbraccia, P. Obesity phenotypes: depot-differences in adipose tissue and their clinical implications. *Eat Weight Disord* **23**, 3-14, doi:10.1007/s40519-017-0467-9 (2018).
- 11 Després, J. P. Body fat distribution and risk of cardiovascular disease: an update. *Circulation* **126**, 1301-1313, doi:10.1161/circulationaha.111.067264 (2012).
- 12 Geer, E. B. & Shen, W. Gender differences in insulin resistance, body composition, and energy balance. *Gen Med* **6 Suppl 1**, 60-75, doi:10.1016/j.genm.2009.02.002 (2009).
- 13 Lee, M. J., Wu, Y. & Fried, S. K. Adipose tissue heterogeneity: implication of depot differences in adipose tissue for obesity complications. *Mol Aspects Med* **34**, 1-11, doi:10.1016/j.mam.2012.10.001 (2013).
- 14 Anand, S. S. *et al.* Adipocyte hypertrophy, fatty liver and metabolic risk factors in South Asians: the Molecular Study of Health and Risk in Ethnic Groups (mol-SHARE). *PLoS One* **6**, e22112, doi:10.1371/journal.pone.0022112 (2011).
- 15 Guglielmi, V. *et al.* Age-related different relationships between ectopic adipose tissues and measures of central obesity in sedentary subjects. *PLoS One* **9**, e103381, doi:10.1371/journal.pone.0103381 (2014).
- 16 Blüher, M. Metabolically Healthy Obesity. *Endocrine Reviews* **41**, 405-420, doi:10.1210/endrev/bnaa004 (2020).
- 17 Lemos, T. & Gallagher, D. Current body composition measurement techniques. *Curr Opin Endocrinol Diabetes Obes* **24**, 310-314, doi:10.1097/med.0000000000000360 (2017).
- 18 Gaborit, B. *et al.* Ectopic fat storage in the pancreas using 1H-MRS: importance of diabetic status and modulation with bariatric surgery-induced weight loss. *Int J Obes (Lond)* **39**, 480-487, doi:10.1038/ijo.2014.126 (2015).

- 19 Dutour, A. *et al.* Exenatide decreases liver fat content and epicardial adipose tissue in patients with obesity and type 2 diabetes: a prospective randomized clinical trial using magnetic resonance imaging and spectroscopy. *Diabetes Obes Metab* **18**, 882-891, doi:10.1111/dom.12680 (2016).
- 20 Sun, K., Tordjman, J., Clement, K. & Scherer, P. E. Fibrosis and adipose tissue dysfunction. *Cell Metab* **18**, 470-477, doi:10.1016/j.cmet.2013.06.016 (2013).
- 21 Datta, R., Podolsky, M. J. & Atabai, K. Fat fibrosis: friend or foe? *JCI Insight* **3**, doi:10.1172/jci.insight.122289 (2018).
- 22 Barabási, A. L. Network medicine--from obesity to the "diseasome". *N Engl J Med* **357**, 404-407, doi:10.1056/NEJMe078114 (2007).
- 23 Rende, D., Baysal, N. & Kirdar, B. Complex disease interventions from a network model for type 2 diabetes. *PLoS One* **8**, e65854, doi:10.1371/journal.pone.0065854 (2013).
- 24 Venteclef, N. *et al.* Human epicardial adipose tissue induces fibrosis of the atrial myocardium through the secretion of adipo-fibrokinases. *Eur Heart J* **36**, 795-805a, doi:10.1093/eurheartj/ehf099 (2015).
- 25 Ternacle, J. *et al.* Short-term high-fat diet compromises myocardial function: a radial strain rate imaging study. *Eur Heart J Cardiovasc Imaging* **18**, 1283-1291, doi:10.1093/ehjci/jew316 (2017).
- 26 Sawaki, D. *et al.* Visceral Adipose Tissue Drives Cardiac Aging Through Modulation of Fibroblast Senescence by Osteopontin Production. *Circulation* **138**, 809-822, doi:10.1161/circulationaha.117.031358 (2018).
- 27 <Animal models are essential to biological research, issues and perspectives_Futura Science.pdf>.
- 28 Rosenfeld, L. Insulin: discovery and controversy. *Clin Chem* **48**, 2270-2288 (2002).
- 29 van der Worp, H. B. *et al.* Can animal models of disease reliably inform human studies? *PLoS Med* **7**, e1000245, doi:10.1371/journal.pmed.1000245 (2010).
- 30 Chu, D. T., Malinowska, E., Jura, M. & Kozak, L. P. C57BL/6J mice as a polygenic developmental model of diet-induced obesity. *Physiol Rep* **5**, doi:10.14814/phy2.13093 (2017).
- 31 Brockmann, G. A. & Bevova, M. R. Using mouse models to dissect the genetics of obesity. *Trends Genet* **18**, 367-376, doi:10.1016/s0168-9525(02)02703-8 (2002).
- 32 Sacks, H. & Symonds, M. E. Anatomical locations of human brown adipose tissue: functional relevance and implications in obesity and type 2 diabetes. *Diabetes* **62**, 1783-1790, doi:10.2337/db12-1430 (2013).
- 33 Mo, Q. *et al.* Identification and characterization of a supraclavicular brown adipose tissue in mice. *JCI Insight* **2**, doi:10.1172/jci.insight.93166 (2017).
- 34 Cinti, S. UCP1 protein: The molecular hub of adipose organ plasticity. *Biochimie* **134**, 71-76, doi:10.1016/j.biochi.2016.09.008 (2017).
- 35 Vijgen, G. H. *et al.* Brown adipose tissue in morbidly obese subjects. *PLoS One* **6**, e17247, doi:10.1371/journal.pone.0017247 (2011).
- 36 Bartelt, A. & Heeren, J. Adipose tissue browning and metabolic health. *Nat Rev Endocrinol* **10**, 24-36, doi:10.1038/nrendo.2013.204 (2014).
- 37 Finlin, B. S. *et al.* Human adipose beiging in response to cold and mirabegron. *JCI Insight* **3**, doi:10.1172/jci.insight.121510 (2018).
- 38 Sakellariou, P. *et al.* Chronic l-menthol-induced browning of white adipose tissue hypothesis: A putative therapeutic regime for combating obesity and improving metabolic health. *Med Hypotheses* **93**, 21-26, doi:10.1016/j.mehy.2016.05.006 (2016).
- 39 <Subcutaneous and visceral adipose tissue, their relation to the metabolic syndrome, Wajchenberg, Endocrine reviews 2000.pdf>.
- 40 Kwok, K. H., Lam, K. S. & Xu, A. Heterogeneity of white adipose tissue: molecular basis and clinical implications. *Exp Mol Med* **48**, e215, doi:10.1038/emm.2016.5 (2016).

- 41 Tran, T. T., Yamamoto, Y., Gesta, S. & Kahn, C. R. Beneficial effects of subcutaneous fat transplantation on metabolism. *Cell Metab* **7**, 410-420, doi:10.1016/j.cmet.2008.04.004 (2008).
- 42 Shuster, A., Patlas, M., Pinthus, J. H. & Mourtzakis, M. The clinical importance of visceral adiposity: a critical review of methods for visceral adipose tissue analysis. *Br J Radiol* **85**, 1-10, doi:10.1259/bjr/38447238 (2012).
- 43 Kruglikov, I. L. & Scherer, P. E. Dermal Adipocytes: From Irrelevance to Metabolic Targets? *Trends Endocrinol Metab* **27**, 1-10, doi:10.1016/j.tem.2015.11.002 (2016).
- 44 Tchkonina, T. *et al.* Mechanisms and metabolic implications of regional differences among fat depots. *Cell Metab* **17**, 644-656, doi:10.1016/j.cmet.2013.03.008 (2013).
- 45 Zechner, R. *et al.* FAT SIGNALS--lipases and lipolysis in lipid metabolism and signaling. *Cell Metab* **15**, 279-291, doi:10.1016/j.cmet.2011.12.018 (2012).
- 46 Unger, R. H., Clark, G. O., Scherer, P. E. & Orci, L. Lipid homeostasis, lipotoxicity and the metabolic syndrome. *Biochim Biophys Acta* **1801**, 209-214, doi:10.1016/j.bbali.2009.10.006 (2010).
- 47 Bodis, K. & Roden, M. Energy metabolism of white adipose tissue and insulin resistance in humans. *Eur J Clin Invest* **48**, e13017, doi:10.1111/eci.13017 (2018).
- 48 Zhang, Y. *et al.* Positional cloning of the mouse obese gene and its human homologue. *Nature* **372**, 425-432, doi:10.1038/372425a0 (1994).
- 49 Scherer, P. E., Williams, S., Fogliano, M., Baldini, G. & Lodish, H. F. A novel serum protein similar to C1q, produced exclusively in adipocytes. *J Biol Chem* **270**, 26746-26749, doi:10.1074/jbc.270.45.26746 (1995).
- 50 Kershaw, E. E. & Flier, J. S. Adipose tissue as an endocrine organ. *J Clin Endocrinol Metab* **89**, 2548-2556, doi:10.1210/jc.2004-0395 (2004).
- 51 Smitka, K. & Maresova, D. Adipose Tissue as an Endocrine Organ: An Update on Pro-inflammatory and Anti-inflammatory Microenvironment. *Prague Med Rep* **116**, 87-111, doi:10.14712/23362936.2015.49 (2015).
- 52 Campfield, L. A., Smith, F. J., Guisez, Y., Devos, R. & Burn, P. Recombinant mouse OB protein: evidence for a peripheral signal linking adiposity and central neural networks. *Science* **269**, 546-549, doi:10.1126/science.7624778 (1995).
- 53 Farooqi, I. S. *et al.* Effects of recombinant leptin therapy in a child with congenital leptin deficiency. *N Engl J Med* **341**, 879-884, doi:10.1056/nejm199909163411204 (1999).
- 54 Petersen, K. F. *et al.* Leptin reverses insulin resistance and hepatic steatosis in patients with severe lipodystrophy. *J Clin Invest* **109**, 1345-1350, doi:10.1172/jci15001 (2002).
- 55 Wang, M. Y. *et al.* Leptin therapy in insulin-deficient type I diabetes. *Proc Natl Acad Sci U S A* **107**, 4813-4819, doi:10.1073/pnas.0909422107 (2010).
- 56 Perry, R. J. *et al.* Leptin reverses diabetes by suppression of the hypothalamic-pituitary-adrenal axis. *Nat Med* **20**, 759-763, doi:10.1038/nm.3579 (2014).
- 57 Margetic, S., Gazzola, C., Pegg, G. G. & Hill, R. A. Leptin: a review of its peripheral actions and interactions. *Int J Obes Relat Metab Disord* **26**, 1407-1433, doi:10.1038/sj.ijo.0802142 (2002).
- 58 Yang, W. S. *et al.* Weight reduction increases plasma levels of an adipose-derived anti-inflammatory protein, adiponectin. *J Clin Endocrinol Metab* **86**, 3815-3819, doi:10.1210/jcem.86.8.7741 (2001).
- 59 Hotta, K. *et al.* Circulating concentrations of the adipocyte protein adiponectin are decreased in parallel with reduced insulin sensitivity during the progression to type 2 diabetes in rhesus monkeys. *Diabetes* **50**, 1126-1133, doi:10.2337/diabetes.50.5.1126 (2001).
- 60 Yamauchi, T. & Kadowaki, T. Physiological and pathophysiological roles of adiponectin and adiponectin receptors in the integrated regulation of metabolic and cardiovascular diseases. *Int J Obes (Lond)* **32 Suppl 7**, S13-18, doi:10.1038/ijo.2008.233 (2008).
- 61 Martínez, M. C. & Andriantsitohaina, R. Extracellular Vesicles in Metabolic Syndrome. *Circ Res* **120**, 1674-1686, doi:10.1161/circresaha.117.309419 (2017).

- 62 Koeck, E. S. *et al.* Adipocyte exosomes induce transforming growth factor beta pathway dysregulation in hepatocytes: a novel paradigm for obesity-related liver disease. *J Surg Res* **192**, 268-275, doi:10.1016/j.jss.2014.06.050 (2014).
- 63 Deng, Z. B. *et al.* Adipose tissue exosome-like vesicles mediate activation of macrophage-induced insulin resistance. *Diabetes* **58**, 2498-2505, doi:10.2337/db09-0216 (2009).
- 64 Sarantopoulos, C. N. *et al.* Elucidating the Preadipocyte and Its Role in Adipocyte Formation: a Comprehensive Review. *Stem Cell Rev Rep* **14**, 27-42, doi:10.1007/s12015-017-9774-9 (2018).
- 65 Cawthorn, W. P., Scheller, E. L. & MacDougald, O. A. Adipose tissue stem cells meet preadipocyte commitment: going back to the future. *J Lipid Res* **53**, 227-246, doi:10.1194/jlr.R021089 (2012).
- 66 Takada, I., Kouzmenko, A. P. & Kato, S. Wnt and PPARgamma signaling in osteoblastogenesis and adipogenesis. *Nat Rev Rheumatol* **5**, 442-447, doi:10.1038/nrrheum.2009.137 (2009).
- 67 Kanazawa, A. *et al.* Wnt5b partially inhibits canonical Wnt/beta-catenin signaling pathway and promotes adipogenesis in 3T3-L1 preadipocytes. *Biochem Biophys Res Commun* **330**, 505-510, doi:10.1016/j.bbrc.2005.03.007 (2005).
- 68 Choy, L., Skillington, J. & Derynck, R. Roles of autocrine TGF-beta receptor and Smad signaling in adipocyte differentiation. *J Cell Biol* **149**, 667-682, doi:10.1083/jcb.149.3.667 (2000).
- 69 Traustadottir, G. A., Kosmina, R., Sheikh, S. P., Jensen, C. H. & Andersen, D. C. Preadipocytes proliferate and differentiate under the guidance of Delta-like 1 homolog (DLK1). *Adipocyte* **2**, 272-275, doi:10.4161/adip.24994 (2013).
- 70 Tang, Q. Q., Otto, T. C. & Lane, M. D. Commitment of C3H10T1/2 pluripotent stem cells to the adipocyte lineage. *Proc Natl Acad Sci U S A* **101**, 9607-9611, doi:10.1073/pnas.0403100101 (2004).
- 71 Suenaga, M., Matsui, T. & Funaba, M. BMP Inhibition with dorsomorphin limits adipogenic potential of preadipocytes. *J Vet Med Sci* **72**, 373-377, doi:10.1292/jvms.09-0442 (2010).
- 72 Mori, S., Kiuchi, S., Ouchi, A., Hase, T. & Murase, T. Characteristic expression of extracellular matrix in subcutaneous adipose tissue development and adipogenesis; comparison with visceral adipose tissue. *Int J Biol Sci* **10**, 825-833, doi:10.7150/ijbs.8672 (2014).
- 73 Chazenbalk, G. *et al.* Novel pathway of adipogenesis through cross-talk between adipose tissue macrophages, adipose stem cells and adipocytes: evidence of cell plasticity. *PLoS One* **6**, e17834, doi:10.1371/journal.pone.0017834 (2011).
- 74 Sakamoto, H. *et al.* Sequential changes in genome-wide DNA methylation status during adipocyte differentiation. *Biochem Biophys Res Commun* **366**, 360-366, doi:10.1016/j.bbrc.2007.11.137 (2008).
- 75 Ortega, F. J. *et al.* MiRNA expression profile of human subcutaneous adipose and during adipocyte differentiation. *PLoS One* **5**, e9022, doi:10.1371/journal.pone.0009022 (2010).
- 76 Chazenbalk, G. *et al.* Androgens inhibit adipogenesis during human adipose stem cell commitment to preadipocyte formation. *Steroids* **78**, 920-926, doi:10.1016/j.steroids.2013.05.001 (2013).
- 77 Tchkonina, T. *et al.* Abundance of two human preadipocyte subtypes with distinct capacities for replication, adipogenesis, and apoptosis varies among fat depots. *Am J Physiol Endocrinol Metab* **288**, E267-277, doi:10.1152/ajpendo.00265.2004 (2005).
- 78 Lee, Y. H., Petkova, A. P. & Granneman, J. G. Identification of an adipogenic niche for adipose tissue remodeling and restoration. *Cell Metab* **18**, 355-367, doi:10.1016/j.cmet.2013.08.003 (2013).
- 79 Lee, Y. H., Petkova, A. P., Mottillo, E. P. & Granneman, J. G. In vivo identification of bipotential adipocyte progenitors recruited by beta3-adrenoceptor activation and high-fat feeding. *Cell Metab* **15**, 480-491, doi:10.1016/j.cmet.2012.03.009 (2012).
- 80 Rosen, E. D. & Spiegelman, B. M. What we talk about when we talk about fat. *Cell* **156**, 20-44, doi:10.1016/j.cell.2013.12.012 (2014).
- 81 Charriere, G. *et al.* Preadipocyte conversion to macrophage. Evidence of plasticity. *J Biol Chem* **278**, 9850-9855, doi:10.1074/jbc.M210811200 (2003).

- 82 Nguyen, A. *et al.* Stromal vascular fraction: A regenerative reality? Part 1: Current concepts and review of the literature. *J Plast Reconstr Aesthet Surg* **69**, 170-179, doi:10.1016/j.bjps.2015.10.015 (2016).
- 83 Guo, J. *et al.* Stromal vascular fraction: A regenerative reality? Part 2: Mechanisms of regenerative action. *J Plast Reconstr Aesthet Surg* **69**, 180-188, doi:10.1016/j.bjps.2015.10.014 (2016).
- 84 Planat-Benard, V. *et al.* Plasticity of human adipose lineage cells toward endothelial cells: physiological and therapeutic perspectives. *Circulation* **109**, 656-663, doi:10.1161/01.Cir.0000114522.38265.61 (2004).
- 85 Prunet-Marcassus, B. *et al.* From heterogeneity to plasticity in adipose tissues: site-specific differences. *Exp Cell Res* **312**, 727-736, doi:10.1016/j.yexcr.2005.11.021 (2006).
- 86 Zuk, P. A. *et al.* Human adipose tissue is a source of multipotent stem cells. *Mol Biol Cell* **13**, 4279-4295, doi:10.1091/mbc.e02-02-0105 (2002).
- 87 Panina, Y. A. *et al.* Plasticity of Adipose Tissue-Derived Stem Cells and Regulation of Angiogenesis. *Front Physiol* **9**, 1656, doi:10.3389/fphys.2018.01656 (2018).
- 88 Sun, Y., Chen, S., Zhang, X. & Pei, M. Significance of Cellular Cross-Talk in Stromal Vascular Fraction of Adipose Tissue in Neovascularization. *Arterioscler Thromb Vasc Biol* **39**, 1034-1044, doi:10.1161/ATVBAHA.119.312425 (2019).
- 89 Klar, A. S. *et al.* Characterization of vasculogenic potential of human adipose-derived endothelial cells in a three-dimensional vascularized skin substitute. *Pediatr Surg Int* **32**, 17-27, doi:10.1007/s00383-015-3808-7 (2016).
- 90 Ferrante, A. W., Jr. The immune cells in adipose tissue. *Diabetes Obes Metab* **15 Suppl 3**, 34-38, doi:10.1111/dom.12154 (2013).
- 91 Bharath, L. P., Ip, B. C. & Nikolajczyk, B. S. Adaptive Immunity and Metabolic Health: Harmony Becomes Dissonant in Obesity and Aging. *Compr Physiol* **7**, 1307-1337, doi:10.1002/cphy.c160042 (2017).
- 92 Russo, L. & Lumeng, C. N. Properties and functions of adipose tissue macrophages in obesity. *Immunology* **155**, 407-417, doi:10.1111/imm.13002 (2018).
- 93 Gordon, S. Alternative activation of macrophages. *Nat Rev Immunol* **3**, 23-35, doi:10.1038/nri978 (2003).
- 94 Kratz, M. *et al.* Metabolic dysfunction drives a mechanistically distinct proinflammatory phenotype in adipose tissue macrophages. *Cell Metab* **20**, 614-625, doi:10.1016/j.cmet.2014.08.010 (2014).
- 95 Ni, Y. *et al.* Adipose Tissue Macrophage Phenotypes and Characteristics: The Key to Insulin Resistance in Obesity and Metabolic Disorders. *Obesity (Silver Spring)* **28**, 225-234, doi:10.1002/oby.22674 (2020).
- 96 Vergadi, E., Ieronymaki, E., Lyroni, K., Vaporidi, K. & Tsatsanis, C. Akt Signaling Pathway in Macrophage Activation and M1/M2 Polarization. *J Immunol* **198**, 1006-1014, doi:10.4049/jimmunol.1601515 (2017).
- 97 Frayn, K. N. Adipose tissue and the insulin resistance syndrome. *Proc Nutr Soc* **60**, 375-380, doi:10.1079/pns200195 (2001).
- 98 Jo, J. *et al.* Hypertrophy and/or Hyperplasia: Dynamics of Adipose Tissue Growth. *PLoS Comput Biol* **5**, e1000324, doi:10.1371/journal.pcbi.1000324 (2009).
- 99 Haghiaci, M. *et al.* Increased death of adipose cells, a path to release cell-free DNA into systemic circulation of obese women. *Obesity (Silver Spring)* **20**, 2213-2219, doi:10.1038/oby.2012.138 (2012).
- 100 Cinti, S. *et al.* Adipocyte death defines macrophage localization and function in adipose tissue of obese mice and humans. *J Lipid Res* **46**, 2347-2355, doi:10.1194/jlr.M500294-JLR200 (2005).
- 101 Gautheron, J. *et al.* The necroptosis-inducing kinase RIPK3 dampens adipose tissue inflammation and glucose intolerance. *Nat Commun* **7**, 11869, doi:10.1038/ncomms11869 (2016).

- 102 Petersen, M. C. & Shulman, G. I. Mechanisms of Insulin Action and Insulin Resistance. *Physiol Rev* **98**, 2133-2223, doi:10.1152/physrev.00063.2017 (2018).
- 103 Leto, D. & Saltiel, A. R. Regulation of glucose transport by insulin: traffic control of GLUT4. *Nat Rev Mol Cell Biol* **13**, 383-396, doi:10.1038/nrm3351 (2012).
- 104 Shulman, G. I. *et al.* Quantitation of muscle glycogen synthesis in normal subjects and subjects with non-insulin-dependent diabetes by ¹³C nuclear magnetic resonance spectroscopy. *N Engl J Med* **322**, 223-228, doi:10.1056/nejm199001253220403 (1990).
- 105 Kruszynska, Y. T., Home, P. D. & Alberti, K. G. In vivo regulation of liver and skeletal muscle glycogen synthase activity by glucose and insulin. *Diabetes* **35**, 662-667, doi:10.2337/diab.35.6.662 (1986).
- 106 Leavens, K. F. & Birnbaum, M. J. Insulin signaling to hepatic lipid metabolism in health and disease. *Crit Rev Biochem Mol Biol* **46**, 200-215, doi:10.3109/10409238.2011.562481 (2011).
- 107 Lin, H. V. & Accili, D. Hormonal regulation of hepatic glucose production in health and disease. *Cell Metab* **14**, 9-19, doi:10.1016/j.cmet.2011.06.003 (2011).
- 108 Roden, M. *et al.* The roles of insulin and glucagon in the regulation of hepatic glycogen synthesis and turnover in humans. *J Clin Invest* **97**, 642-648, doi:10.1172/jci118460 (1996).
- 109 Brady, M. J. IRS2 takes center stage in the development of type 2 diabetes. *The Journal of Clinical Investigation* **114**, 886-888, doi:10.1172/JCI23108 (2004).
- 110 Rieusset, J. *et al.* Insulin acutely regulates the expression of the peroxisome proliferator-activated receptor-gamma in human adipocytes. *Diabetes* **48**, 699-705, doi:10.2337/diabetes.48.4.699 (1999).
- 111 Kraegen, E. W., James, D. E., Jenkins, A. B. & Chisholm, D. J. Dose-response curves for in vivo insulin sensitivity in individual tissues in rats. *Am J Physiol* **248**, E353-362, doi:10.1152/ajpendo.1985.248.3.E353 (1985).
- 112 Farese, R. V., Jr., Yost, T. J. & Eckel, R. H. Tissue-specific regulation of lipoprotein lipase activity by insulin/glucose in normal-weight humans. *Metabolism* **40**, 214-216, doi:10.1016/0026-0495(91)90178-y (1991).
- 113 Goldberg, I. J., Eckel, R. H. & Abumrad, N. A. Regulation of fatty acid uptake into tissues: lipoprotein lipase- and CD36-mediated pathways. *J Lipid Res* **50 Suppl**, S86-90, doi:10.1194/jlr.R800085-JLR200 (2009).
- 114 Ader, M. & Bergman, R. N. Peripheral effects of insulin dominate suppression of fasting hepatic glucose production. *Am J Physiol* **258**, E1020-1032, doi:10.1152/ajpendo.1990.258.6.E1020 (1990).
- 115 Cherrington, A. D., Edgerton, D. & Sindelar, D. K. The direct and indirect effects of insulin on hepatic glucose production in vivo. *Diabetologia* **41**, 987-996, doi:10.1007/s001250051021 (1998).
- 116 Freidenberg, G. R., Henry, R. R., Klein, H. H., Reichart, D. R. & Olefsky, J. M. Decreased kinase activity of insulin receptors from adipocytes of non-insulin-dependent diabetic subjects. *J Clin Invest* **79**, 240-250, doi:10.1172/jci112789 (1987).
- 117 Freidenberg, G. R., Reichart, D., Olefsky, J. M. & Henry, R. R. Reversibility of defective adipocyte insulin receptor kinase activity in non-insulin-dependent diabetes mellitus. Effect of weight loss. *J Clin Invest* **82**, 1398-1406, doi:10.1172/jci113744 (1988).
- 118 Jackson, R. A., Roshania, R. D., Hawa, M. I., Sim, B. M. & DiSilvio, L. Impact of glucose ingestion on hepatic and peripheral glucose metabolism in man: an analysis based on simultaneous use of the forearm and double isotope techniques. *J Clin Endocrinol Metab* **63**, 541-549, doi:10.1210/jcem-63-3-541 (1986).
- 119 Kowalski, G. M. & Bruce, C. R. The regulation of glucose metabolism: implications and considerations for the assessment of glucose homeostasis in rodents. *Am J Physiol Endocrinol Metab* **307**, E859-871, doi:10.1152/ajpendo.00165.2014 (2014).
- 120 Abel, E. D. *et al.* Adipose-selective targeting of the GLUT4 gene impairs insulin action in muscle and liver. *Nature* **409**, 729-733, doi:10.1038/35055575 (2001).

- 121 Kraus, D. *et al.* Nicotinamide N-methyltransferase knockdown protects against diet-induced obesity. *Nature* **508**, 258-262, doi:10.1038/nature13198 (2014).
- 122 Yang, Q. *et al.* Serum retinol binding protein 4 contributes to insulin resistance in obesity and type 2 diabetes. *Nature* **436**, 356-362, doi:10.1038/nature03711 (2005).
- 123 Chen, Y. D., Golay, A., Swislocki, A. L. & Reaven, G. M. Resistance to insulin suppression of plasma free fatty acid concentrations and insulin stimulation of glucose uptake in noninsulin-dependent diabetes mellitus. *J Clin Endocrinol Metab* **64**, 17-21, doi:10.1210/jcem-64-1-17 (1987).
- 124 Frazee, E. *et al.* Ambient plasma free fatty acid concentrations in noninsulin-dependent diabetes mellitus: evidence for insulin resistance. *J Clin Endocrinol Metab* **61**, 807-811, doi:10.1210/jcem-61-5-807 (1985).
- 125 Golay, A., Swislocki, A. L., Chen, Y. D. & Reaven, G. M. Relationships between plasma-free fatty acid concentration, endogenous glucose production, and fasting hyperglycemia in normal and non-insulin-dependent diabetic individuals. *Metabolism* **36**, 692-696, doi:10.1016/0026-0495(87)90156-9 (1987).
- 126 Pereira, M. J. *et al.* Impaired adipose tissue lipid storage, but not altered lipolysis, contributes to elevated levels of NEFA in type 2 diabetes. Degree of hyperglycemia and adiposity are important factors. *Metabolism* **65**, 1768-1780, doi:10.1016/j.metabol.2016.09.008 (2016).
- 127 Riemens, S. C., Sluiter, W. J. & Dullaart, R. P. Enhanced escape of non-esterified fatty acids from tissue uptake: its role in impaired insulin-induced lowering of total rate of appearance in obesity and Type II diabetes mellitus. *Diabetologia* **43**, 416-426, doi:10.1007/s001250051324 (2000).
- 128 Arner, P. The adipocyte in insulin resistance: key molecules and the impact of the thiazolidinediones. *Trends Endocrinol Metab* **14**, 137-145, doi:10.1016/s1043-2760(03)00024-9 (2003).
- 129 Guilherme, A., Virbasius, J. V., Puri, V. & Czech, M. P. Adipocyte dysfunctions linking obesity to insulin resistance and type 2 diabetes. *Nat Rev Mol Cell Biol* **9**, 367-377, doi:10.1038/nrm2391 (2008).
- 130 Hotamisligil, G. S. *et al.* IRS-1-mediated inhibition of insulin receptor tyrosine kinase activity in TNF- α - and obesity-induced insulin resistance. *Science* **271**, 665-668, doi:10.1126/science.271.5249.665 (1996).
- 131 Lee, Y. S. *et al.* Inflammation is necessary for long-term but not short-term high-fat diet-induced insulin resistance. *Diabetes* **60**, 2474-2483, doi:10.2337/db11-0194 (2011).
- 132 Samuel, V. T. *et al.* Inhibition of protein kinase C ϵ prevents hepatic insulin resistance in nonalcoholic fatty liver disease. *J Clin Invest* **117**, 739-745, doi:10.1172/jci30400 (2007).
- 133 Chen, G. Y. & Nunez, G. Sterile inflammation: sensing and reacting to damage. *Nat Rev Immunol* **10**, 826-837, doi:10.1038/nri2873 (2010).
- 134 Rogero, M. M. & Calder, P. C. Obesity, Inflammation, Toll-Like Receptor 4 and Fatty Acids. *Nutrients* **10**, doi:10.3390/nu10040432 (2018).
- 135 Hotamisligil, G. S., Shargill, N. S. & Spiegelman, B. M. Adipose expression of tumor necrosis factor- α : direct role in obesity-linked insulin resistance. *Science* **259**, 87-91, doi:10.1126/science.7678183 (1993).
- 136 Hwang, D. H., Kim, J. A. & Lee, J. Y. Mechanisms for the activation of Toll-like receptor 2/4 by saturated fatty acids and inhibition by docosahexaenoic acid. *Eur J Pharmacol* **785**, 24-35, doi:10.1016/j.ejphar.2016.04.024 (2016).
- 137 Ertunc, M. E. & Hotamisligil, G. S. Lipid signaling and lipotoxicity in metaflammation: indications for metabolic disease pathogenesis and treatment. *J Lipid Res* **57**, 2099-2114, doi:10.1194/jlr.R066514 (2016).
- 138 Fried, S. K., Bunkin, D. A. & Greenberg, A. S. Omental and subcutaneous adipose tissues of obese subjects release interleukin-6: depot difference and regulation by glucocorticoid. *J Clin Endocrinol Metab* **83**, 847-850, doi:10.1210/jcem.83.3.4660 (1998).

- 139 Kanda, H. *et al.* MCP-1 contributes to macrophage infiltration into adipose tissue, insulin resistance, and hepatic steatosis in obesity. *J Clin Invest* **116**, 1494-1505, doi:10.1172/jci26498 (2006).
- 140 Guo, S. Insulin signaling, resistance, and the metabolic syndrome: insights from mouse models into disease mechanisms. *J Endocrinol* **220**, T1-t23, doi:10.1530/joe-13-0327 (2014).
- 141 Hotamisligil, G. S. & Davis, R. J. Cell Signaling and Stress Responses. *Cold Spring Harb Perspect Biol* **8**, doi:10.1101/cshperspect.a006072 (2016).
- 142 Exley, M. A., Hand, L., O'Shea, D. & Lynch, L. Interplay between the immune system and adipose tissue in obesity. *J Endocrinol* **223**, R41-48, doi:10.1530/joe-13-0516 (2014).
- 143 Martyniak, K. & Masternak, M. M. Changes in adipose tissue cellular composition during obesity and aging as a cause of metabolic dysregulation. *Exp Gerontol* **94**, 59-63, doi:10.1016/j.exger.2016.12.007 (2017).
- 144 Balagopal, P. *et al.* Reduction of elevated serum retinol binding protein in obese children by lifestyle intervention: association with subclinical inflammation. *J Clin Endocrinol Metab* **92**, 1971-1974, doi:10.1210/jc.2006-2712 (2007).
- 145 Lumeng, C. N., Bodzin, J. L. & Saltiel, A. R. Obesity induces a phenotypic switch in adipose tissue macrophage polarization. *J Clin Invest* **117**, 175-184, doi:10.1172/jci29881 (2007).
- 146 Canello, R. *et al.* Increased infiltration of macrophages in omental adipose tissue is associated with marked hepatic lesions in morbid human obesity. *Diabetes* **55**, 1554-1561, doi:10.2337/db06-0133 (2006).
- 147 Lumeng, C. N., Deyoung, S. M., Bodzin, J. L. & Saltiel, A. R. Increased inflammatory properties of adipose tissue macrophages recruited during diet-induced obesity. *Diabetes* **56**, 16-23, doi:10.2337/db06-1076 (2007).
- 148 Dalmas, E. *et al.* T cell-derived IL-22 amplifies IL-1 β -driven inflammation in human adipose tissue: relevance to obesity and type 2 diabetes. *Diabetes* **63**, 1966-1977, doi:10.2337/db13-1511 (2014).
- 149 Dalmas, E. *et al.* Irf5 deficiency in macrophages promotes beneficial adipose tissue expansion and insulin sensitivity during obesity. *Nat Med* **21**, 610-618, doi:10.1038/nm.3829 (2015).
- 150 Nishimura, S. *et al.* Adipogenesis in obesity requires close interplay between differentiating adipocytes, stromal cells, and blood vessels. *Diabetes* **56**, 1517-1526, doi:10.2337/db06-1749 (2007).
- 151 Bertola, A. *et al.* Identification of adipose tissue dendritic cells correlated with obesity-associated insulin-resistance and inducing Th17 responses in mice and patients. *Diabetes* **61**, 2238-2247, doi:10.2337/db11-1274 (2012).
- 152 Talukdar, S. *et al.* Neutrophils mediate insulin resistance in mice fed a high-fat diet through secreted elastase. *Nat Med* **18**, 1407-1412, doi:10.1038/nm.2885 (2012).
- 153 Liu, J. *et al.* Genetic deficiency and pharmacological stabilization of mast cells reduce diet-induced obesity and diabetes in mice. *Nat Med* **15**, 940-945, doi:10.1038/nm.1994 (2009).
- 154 Wolf, A. M., Wolf, D., Rumpold, H., Enrich, B. & Tilg, H. Adiponectin induces the anti-inflammatory cytokines IL-10 and IL-1RA in human leukocytes. *Biochem Biophys Res Commun* **323**, 630-635, doi:10.1016/j.bbrc.2004.08.145 (2004).
- 155 Wu, D. *et al.* Eosinophils sustain adipose alternatively activated macrophages associated with glucose homeostasis. *Science* **332**, 243-247, doi:10.1126/science.1201475 (2011).
- 156 Feuerer, M. *et al.* Lean, but not obese, fat is enriched for a unique population of regulatory T cells that affect metabolic parameters. *Nat Med* **15**, 930-939, doi:10.1038/nm.2002 (2009).
- 157 Cipolletta, D. Adipose tissue-resident regulatory T cells: phenotypic specialization, functions and therapeutic potential. *Immunology* **142**, 517-525, doi:10.1111/imm.12262 (2014).
- 158 Cipolletta, D., Kolodin, D., Benoist, C. & Mathis, D. Tissue-resident T(regs): a unique population of adipose-tissue-resident Foxp3+CD4+ T cells that impacts organismal metabolism. *Semin Immunol* **23**, 431-437, doi:10.1016/j.smim.2011.06.002 (2011).
- 159 Winer, D. A. *et al.* B cells promote insulin resistance through modulation of T cells and production of pathogenic IgG antibodies. *Nat Med* **17**, 610-617, doi:10.1038/nm.2353 (2011).

- 160 Nishimura, S. *et al.* CD8⁺ effector T cells contribute to macrophage recruitment and adipose
tissue inflammation in obesity. *Nat Med* **15**, 914-920, doi:10.1038/nm.1964 (2009).
- 161 Sun, K., Kusminski, C. M. & Scherer, P. E. Adipose tissue remodeling and obesity. *J Clin Invest*
121, 2094-2101, doi:10.1172/jci45887 (2011).
- 162 Khan, T. *et al.* Metabolic dysregulation and adipose tissue fibrosis: role of collagen VI. *Mol Cell*
Biol **29**, 1575-1591, doi:10.1128/mcb.01300-08 (2009).
- 163 <How does high fat diet induce adipose tissue fibrosis_Kwon_J Investig Med 2012.pdf>.
doi:10.231/JIM.0b013e318271fdb9.
- 164 Halberg, N. *et al.* Hypoxia-inducible factor 1 α induces fibrosis and insulin resistance in
white adipose tissue. *Mol Cell Biol* **29**, 4467-4483, doi:10.1128/mcb.00192-09 (2009).
- 165 Buechler, C., Krautbauer, S. & Eisinger, K. Adipose tissue fibrosis. *World J Diabetes* **6**, 548-553,
doi:10.4239/wjd.v6.i4.548 (2015).
- 166 Sun, K., Halberg, N., Khan, M., Magalang, U. J. & Scherer, P. E. Selective inhibition of hypoxia-
inducible factor 1 α ameliorates adipose tissue dysfunction. *Mol Cell Biol* **33**, 904-917,
doi:10.1128/mcb.00951-12 (2013).
- 167 Kim, K. H., Song, M. J., Chung, J., Park, H. & Kim, J. B. Hypoxia inhibits adipocyte differentiation
in a HDAC-independent manner. *Biochem Biophys Res Commun* **333**, 1178-1184,
doi:10.1016/j.bbrc.2005.06.023 (2005).
- 168 Tan, J. T. *et al.* Connective tissue growth factor inhibits adipocyte differentiation. *Am J Physiol*
Cell Physiol **295**, C740-751, doi:10.1152/ajpcell.00333.2007 (2008).
- 169 Keophiphath, M. *et al.* Macrophage-secreted factors promote a profibrotic phenotype in
human preadipocytes. *Mol Endocrinol* **23**, 11-24, doi:10.1210/me.2008-0183 (2009).
- 170 Wynn, T. A. & Vannella, K. M. Macrophages in Tissue Repair, Regeneration, and Fibrosis.
Immunity **44**, 450-462, doi:10.1016/j.immuni.2016.02.015 (2016).
- 171 Lacasa, D., Taleb, S., Keophiphath, M., Miranville, A. & Clement, K. Macrophage-secreted
factors impair human adipogenesis: involvement of proinflammatory state in preadipocytes.
Endocrinology **148**, 868-877, doi:10.1210/en.2006-0687 (2007).
- 172 Marcelin, G. *et al.* A PDGFR α -Mediated Switch toward CD9(high) Adipocyte Progenitors
Controls Obesity-Induced Adipose Tissue Fibrosis. *Cell Metab* **25**, 673-685,
doi:10.1016/j.cmet.2017.01.010 (2017).
- 173 Song, E. *et al.* Influence of alternatively and classically activated macrophages on fibrogenic
activities of human fibroblasts. *Cell Immunol* **204**, 19-28, doi:10.1006/cimm.2000.1687 (2000).
- 174 Meneghin, A. & Hogaboam, C. M. Infectious disease, the innate immune response, and fibrosis.
J Clin Invest **117**, 530-538, doi:10.1172/jci30595 (2007).
- 175 Wynn, T. A. Fibrotic disease and the T(H)1/T(H)2 paradigm. *Nat Rev Immunol* **4**, 583-594,
doi:10.1038/nri1412 (2004).
- 176 Burton, D. G. A. & Faragher, R. G. A. Obesity and type-2 diabetes as inducers of premature
cellular senescence and ageing. *Biogerontology* **19**, 447-459, doi:10.1007/s10522-018-9763-7
(2018).
- 177 Liu, Z., Wu, K. K. L., Jiang, X., Xu, A. & Cheng, K. K. Y. The role of adipose tissue senescence in
obesity- and ageing-related metabolic disorders. *Clin Sci (Lond)* **134**, 315-330,
doi:10.1042/CS20190966 (2020).
- 178 Tchkonja, T. *et al.* Fat tissue, aging, and cellular senescence. *Aging Cell* **9**, 667-684,
doi:10.1111/j.1474-9726.2010.00608.x (2010).
- 179 Hayflick, L. THE LIMITED IN VITRO LIFETIME OF HUMAN DIPLOID CELL STRAINS. *Exp Cell Res*
37, 614-636, doi:10.1016/0014-4827(65)90211-9 (1965).
- 180 Shay, J. W. & Wright, W. E. Hayflick, his limit, and cellular ageing. *Nat Rev Mol Cell Biol* **1**, 72-
76, doi:10.1038/35036093 (2000).
- 181 Muñoz-Espín, D. & Serrano, M. Cellular senescence: from physiology to pathology. *Nat Rev*
Mol Cell Biol **15**, 482-496, doi:10.1038/nrm3823 (2014).
- 182 Campisi, J. & d'Adda di Fagagna, F. Cellular senescence: when bad things happen to good cells.
Nat Rev Mol Cell Biol **8**, 729-740, doi:10.1038/nrm2233 (2007).

- 183 Harley, C. B., Futcher, A. B. & Greider, C. W. Telomeres shorten during ageing of human fibroblasts. *Nature* **345**, 458-460, doi:10.1038/345458a0 (1990).
- 184 Kuilman, T., Michaloglou, C., Mooi, W. J. & Peeper, D. S. The essence of senescence. *Genes Dev* **24**, 2463-2479, doi:10.1101/gad.1971610 (2010).
- 185 Toussaint, O., Medrano, E. E. & von Zglinicki, T. Cellular and molecular mechanisms of stress-induced premature senescence (SIPS) of human diploid fibroblasts and melanocytes. *Exp Gerontol* **35**, 927-945, doi:10.1016/s0531-5565(00)00180-7 (2000).
- 186 Collado, M., Blasco, M. A. & Serrano, M. Cellular senescence in cancer and aging. *Cell* **130**, 223-233, doi:10.1016/j.cell.2007.07.003 (2007).
- 187 Coppé, J. P., Desprez, P. Y., Krtolica, A. & Campisi, J. The senescence-associated secretory phenotype: the dark side of tumor suppression. *Annu Rev Pathol* **5**, 99-118, doi:10.1146/annurev-pathol-121808-102144 (2010).
- 188 van Deursen, J. M. The role of senescent cells in ageing. *Nature* **509**, 439-446, doi:10.1038/nature13193 (2014).
- 189 Greider, C. W. & Blackburn, E. H. Telomeres, telomerase and cancer. *Sci Am* **274**, 92-97, doi:10.1038/scientificamerican0296-92 (1996).
- 190 Blackburn, E. H. Telomeres. *Trends Biochem Sci* **16**, 378-381, doi:10.1016/0968-0004(91)90155-o (1991).
- 191 Campisi, J. Senescent cells, tumor suppression, and organismal aging: good citizens, bad neighbors. *Cell* **120**, 513-522, doi:10.1016/j.cell.2005.02.003 (2005).
- 192 Cesare, A. J. & Karlseder, J. A three-state model of telomere control over human proliferative boundaries. *Curr Opin Cell Biol* **24**, 731-738, doi:10.1016/j.ceb.2012.08.007 (2012).
- 193 Rouault, C. *et al.* Senescence-associated β -galactosidase in subcutaneous adipose tissue associates with altered glycaemic status and truncal fat in severe obesity. *Diabetologia*, doi:10.1007/s00125-020-05307-0 (2020).
- 194 Blackburn, E. H., Epel, E. S. & Lin, J. Human telomere biology: A contributory and interactive factor in aging, disease risks, and protection. *Science* **350**, 1193-1198, doi:10.1126/science.aab3389 (2015).
- 195 Salama, R., Sadaie, M., Hoare, M. & Narita, M. Cellular senescence and its effector programs. *Genes Dev* **28**, 99-114, doi:10.1101/gad.235184.113 (2014).
- 196 Serrano, M., Lin, A. W., McCurrach, M. E., Beach, D. & Lowe, S. W. Oncogenic ras provokes premature cell senescence associated with accumulation of p53 and p16INK4a. *Cell* **88**, 593-602, doi:10.1016/s0092-8674(00)81902-9 (1997).
- 197 Lin, A. W. *et al.* Premature senescence involving p53 and p16 is activated in response to constitutive MEK/MAPK mitogenic signaling. *Genes Dev* **12**, 3008-3019, doi:10.1101/gad.12.19.3008 (1998).
- 198 d'Adda di Fagagna, F. Living on a break: cellular senescence as a DNA-damage response. *Nat Rev Cancer* **8**, 512-522, doi:10.1038/nrc2440 (2008).
- 199 Bartkova, J. *et al.* Oncogene-induced senescence is part of the tumorigenesis barrier imposed by DNA damage checkpoints. *Nature* **444**, 633-637, doi:10.1038/nature05268 (2006).
- 200 Di Micco, R. *et al.* Oncogene-induced senescence is a DNA damage response triggered by DNA hyper-replication. *Nature* **444**, 638-642, doi:10.1038/nature05327 (2006).
- 201 Balin, A. K., Fisher, A. J. & Carter, D. M. Oxygen modulates growth of human cells at physiologic partial pressures. *J Exp Med* **160**, 152-166, doi:10.1084/jem.160.1.152 (1984).
- 202 Horikoshi, T., Balin, A. K. & Carter, D. M. Effect of oxygen on the growth of human epidermal keratinocytes. *J Invest Dermatol* **86**, 424-427, doi:10.1111/1523-1747.ep12285695 (1986).
- 203 Michiels, C., Toussaint, O. & Remacle, J. Comparative study of oxygen toxicity in human fibroblasts and endothelial cells. *J Cell Physiol* **144**, 295-302, doi:10.1002/jcp.1041440216 (1990).
- 204 Minamino, T. *et al.* A crucial role for adipose tissue p53 in the regulation of insulin resistance. *Nat Med* **15**, 1082-1087, doi:10.1038/nm.2014 (2009).

- 205 Zhong, W., Zou, G., Gu, J. & Zhang, J. L-arginine attenuates high glucose-accelerated senescence in human umbilical vein endothelial cells. *Diabetes Res Clin Pract* **89**, 38-45, doi:10.1016/j.diabres.2010.03.013 (2010).
- 206 Kitada, K. *et al.* Hyperglycemia causes cellular senescence via a SGLT2- and p21-dependent pathway in proximal tubules in the early stage of diabetic nephropathy. *J Diabetes Complications* **28**, 604-611, doi:10.1016/j.jdiacomp.2014.05.010 (2014).
- 207 Takahashi, A., Ohtani, N. & Hara, E. Irreversibility of cellular senescence: dual roles of p16INK4a/Rb-pathway in cell cycle control. *Cell Div* **2**, 10, doi:10.1186/1747-1028-2-10 (2007).
- 208 Shimi, T. *et al.* The role of nuclear lamin B1 in cell proliferation and senescence. *Genes Dev* **25**, 2579-2593, doi:10.1101/gad.179515.111 (2011).
- 209 Freund, A., Laberge, R. M., Demaria, M. & Campisi, J. Lamin B1 loss is a senescence-associated biomarker. *Mol Biol Cell* **23**, 2066-2075, doi:10.1091/mbc.E11-10-0884 (2012).
- 210 Gallage, S. & Gil, J. Mitochondrial Dysfunction Meets Senescence. *Trends Biochem Sci* **41**, 207-209, doi:10.1016/j.tibs.2016.01.005 (2016).
- 211 Dimri, G. P. *et al.* A biomarker that identifies senescent human cells in culture and in aging skin in vivo. *Proc Natl Acad Sci U S A* **92**, 9363-9367, doi:10.1073/pnas.92.20.9363 (1995).
- 212 Rai, T. S. & Adams, P. D. Lessons from senescence: Chromatin maintenance in non-proliferating cells. *Biochim Biophys Acta* **1819**, 322-331, doi:10.1016/j.bbagr.2011.07.014 (2012).
- 213 Narita, M. *et al.* Rb-mediated heterochromatin formation and silencing of E2F target genes during cellular senescence. *Cell* **113**, 703-716, doi:10.1016/s0092-8674(03)00401-x (2003).
- 214 Zhang, R. *et al.* Formation of MacroH2A-containing senescence-associated heterochromatin foci and senescence driven by ASF1a and HIRA. *Dev Cell* **8**, 19-30, doi:10.1016/j.devcel.2004.10.019 (2005).
- 215 Duarte, L. F. *et al.* Histone H3.3 and its proteolytically processed form drive a cellular senescence programme. *Nat Commun* **5**, 5210, doi:10.1038/ncomms6210 (2014).
- 216 Chen, H. *et al.* MacroH2A1 and ATM Play Opposing Roles in Paracrine Senescence and the Senescence-Associated Secretory Phenotype. *Mol Cell* **59**, 719-731, doi:10.1016/j.molcel.2015.07.011 (2015).
- 217 Capell, B. C. *et al.* MLL1 is essential for the senescence-associated secretory phenotype. *Genes Dev* **30**, 321-336, doi:10.1101/gad.271882.115 (2016).
- 218 Contrepois, K. *et al.* Histone variant H2A.J accumulates in senescent cells and promotes inflammatory gene expression. *Nat Commun* **8**, 14995, doi:10.1038/ncomms14995 (2017).
- 219 Lee, S. & Schmitt, C. A. The dynamic nature of senescence in cancer. *Nat Cell Biol* **21**, 94-101, doi:10.1038/s41556-018-0249-2 (2019).
- 220 Kuo, L. J. & Yang, L. X. Gamma-H2AX - a novel biomarker for DNA double-strand breaks. *In Vivo* **22**, 305-309 (2008).
- 221 Kuilman, T. & Peeper, D. S. Senescence-messaging secretome: SMS-ing cellular stress. *Nat Rev Cancer* **9**, 81-94, doi:10.1038/nrc2560 (2009).
- 222 Coppé, J. P. *et al.* Senescence-associated secretory phenotypes reveal cell-nonautonomous functions of oncogenic RAS and the p53 tumor suppressor. *PLoS Biol* **6**, 2853-2868, doi:10.1371/journal.pbio.0060301 (2008).
- 223 Serrano, M. Cancer: final act of senescence. *Nature* **479**, 481-482, doi:10.1038/479481a (2011).
- 224 Hoenicke, L. & Zender, L. Immune surveillance of senescent cells--biological significance in cancer- and non-cancer pathologies. *Carcinogenesis* **33**, 1123-1126, doi:10.1093/carcin/bgs124 (2012).
- 225 Rodier, F. *et al.* Persistent DNA damage signalling triggers senescence-associated inflammatory cytokine secretion. *Nat Cell Biol* **11**, 973-979, doi:10.1038/ncb1909 (2009).
- 226 Freund, A., Patil, C. K. & Campisi, J. p38MAPK is a novel DNA damage response-independent regulator of the senescence-associated secretory phenotype. *Embo j* **30**, 1536-1548, doi:10.1038/emboj.2011.69 (2011).

- 227 Herranz, N. & Gil, J. Mechanisms and functions of cellular senescence. *J Clin Invest* **128**, 1238-1246, doi:10.1172/jci95148 (2018).
- 228 Prieur, A., Besnard, E., Babled, A. & Lemaître, J. M. p53 and p16(INK4A) independent induction of senescence by chromatin-dependent alteration of S-phase progression. *Nat Commun* **2**, 473, doi:10.1038/ncomms1473 (2011).
- 229 Yamada, T., Kamiya, M., Higuchi, M. & Nakanishi, N. Fat depot-specific differences of macrophage infiltration and cellular senescence in obese bovine adipose tissues. *J Vet Med Sci* **80**, 1495-1503, doi:10.1292/jvms.18-0324 (2018).
- 230 Grundy, S. M., Pasternak, R., Greenland, P., Smith, S., Jr. & Fuster, V. Assessment of cardiovascular risk by use of multiple-risk-factor assessment equations: a statement for healthcare professionals from the American Heart Association and the American College of Cardiology. *Circulation* **100**, 1481-1492, doi:10.1161/01.cir.100.13.1481 (1999).
- 231 Reidy, K., Kang, H. M., Hostetter, T. & Susztak, K. Molecular mechanisms of diabetic kidney disease. *J Clin Invest* **124**, 2333-2340, doi:10.1172/jci72271 (2014).
- 232 Bonomini, F., Rodella, L. F. & Rezzani, R. Metabolic syndrome, aging and involvement of oxidative stress. *Aging Dis* **6**, 109-120, doi:10.14336/ad.2014.0305 (2015).
- 233 Horvath, S. *et al.* Obesity accelerates epigenetic aging of human liver. *Proc Natl Acad Sci U S A* **111**, 15538-15543, doi:10.1073/pnas.1412759111 (2014).
- 234 Mooradian, A. D. Tissue specificity of premature aging in diabetes mellitus. The role of cellular replicative capacity. *J Am Geriatr Soc* **36**, 831-839, doi:10.1111/j.1532-5415.1988.tb04269.x (1988).
- 235 Ronan, L. *et al.* Obesity associated with increased brain age from midlife. *Neurobiol Aging* **47**, 63-70, doi:10.1016/j.neurobiolaging.2016.07.010 (2016).
- 236 Yang, H. *et al.* Obesity accelerates thymic aging. *Blood* **114**, 3803-3812, doi:10.1182/blood-2009-03-213595 (2009).
- 237 Xu, M. *et al.* Targeting senescent cells enhances adipogenesis and metabolic function in old age. *Elife* **4**, e12997, doi:10.7554/eLife.12997 (2015).
- 238 Grant, R. W. & Dixit, V. D. Adipose tissue as an immunological organ. *Obesity (Silver Spring)* **23**, 512-518, doi:10.1002/oby.21003 (2015).
- 239 Wu, D. *et al.* Aging up-regulates expression of inflammatory mediators in mouse adipose tissue. *J Immunol* **179**, 4829-4839, doi:10.4049/jimmunol.179.7.4829 (2007).
- 240 Baker, D. J. *et al.* Clearance of p16Ink4a-positive senescent cells delays ageing-associated disorders. *Nature* **479**, 232-236, doi:10.1038/nature10600 (2011).
- 241 Youm, Y. H. *et al.* Canonical Nlrp3 inflammasome links systemic low-grade inflammation to functional decline in aging. *Cell Metab* **18**, 519-532, doi:10.1016/j.cmet.2013.09.010 (2013).
- 242 Kursawe, R. *et al.* A Role of the Inflammasome in the Low Storage Capacity of the Abdominal Subcutaneous Adipose Tissue in Obese Adolescents. *Diabetes* **65**, 610-618, doi:10.2337/db15-1478 (2016).
- 243 Vergoni, B. *et al.* DNA Damage and the Activation of the p53 Pathway Mediate Alterations in Metabolic and Secretory Functions of Adipocytes. *Diabetes* **65**, 3062-3074, doi:10.2337/db16-0014 (2016).
- 244 Ye, J. Mechanisms of insulin resistance in obesity. *Front Med* **7**, 14-24, doi:10.1007/s11684-013-0262-6 (2013).
- 245 Pérez, L. M. *et al.* 'Adipaging': ageing and obesity share biological hallmarks related to a dysfunctional adipose tissue. *J Physiol* **594**, 3187-3207, doi:10.1113/jp271691 (2016).
- 246 van Olden, C. *et al.* Adipose Tissue Senescence Is Associated With Insulin Resistance In Obese Individuals. *Atherosclerosis* **287**, e73, doi:<https://doi.org/10.1016/j.atherosclerosis.2019.06.210> (2019).
- 247 Inoue, N. *et al.* Cyclin-dependent kinase inhibitor, p21WAF1/CIP1, is involved in adipocyte differentiation and hypertrophy, linking to obesity, and insulin resistance. *J Biol Chem* **283**, 21220-21229, doi:10.1074/jbc.M801824200 (2008).

- 248 Liu, Z. *et al.* The Dysfunctional MDM2-p53 Axis in Adipocytes Contributes to Aging-Related Metabolic Complications by Induction of Lipodystrophy. *Diabetes* **67**, 2397-2409, doi:10.2337/db18-0684 (2018).
- 249 Yahagi, N. *et al.* p53 Activation in adipocytes of obese mice. *J Biol Chem* **278**, 25395-25400, doi:10.1074/jbc.M302364200 (2003).
- 250 Tyner, S. D. *et al.* p53 mutant mice that display early ageing-associated phenotypes. *Nature* **415**, 45-53, doi:10.1038/415045a (2002).
- 251 Fu, W., Liu, Y., Sun, C. & Yin, H. Transient p53 inhibition sensitizes aged white adipose tissue for beige adipocyte recruitment by blocking mitophagy. *Faseb j* **33**, 844-856, doi:10.1096/fj.201800577R (2019).
- 252 Chen, Y. W., Harris, R. A., Hatahet, Z. & Chou, K. M. Ablation of XP-V gene causes adipose tissue senescence and metabolic abnormalities. *Proc Natl Acad Sci U S A* **112**, E4556-4564, doi:10.1073/pnas.1506954112 (2015).
- 253 Gustafson, B., Nerstedt, A. & Smith, U. Reduced subcutaneous adipogenesis in human hypertrophic obesity is linked to senescent precursor cells. *Nat Commun* **10**, 2757, doi:10.1038/s41467-019-10688-x (2019).
- 254 Mitterberger, M. C., Lechner, S., Mattesich, M. & Zwerschke, W. Adipogenic differentiation is impaired in replicative senescent human subcutaneous adipose-derived stromal/progenitor cells. *J Gerontol A Biol Sci Med Sci* **69**, 13-24, doi:10.1093/gerona/glt043 (2014).
- 255 Tchkonja, T. *et al.* Increased TNF α and CCAAT/enhancer-binding protein homologous protein with aging predispose preadipocytes to resist adipogenesis. *Am J Physiol Endocrinol Metab* **293**, E1810-1819, doi:10.1152/ajpendo.00295.2007 (2007).
- 256 Zauberman, A., Oren, M. & Zipori, D. Involvement of p21(WAF1/Cip1), CDK4 and Rb in activin A mediated signaling leading to hepatoma cell growth inhibition. *Oncogene* **15**, 1705-1711, doi:10.1038/sj.onc.1201348 (1997).
- 257 Wouters, K. *et al.* The tumour suppressor CDKN2A/p16(INK4a) regulates adipogenesis and bone marrow-dependent development of perivascular adipose tissue. *Diab Vasc Dis Res* **14**, 516-524, doi:10.1177/1479164117728012 (2017).
- 258 Cao, Y. Angiogenesis modulates adipogenesis and obesity. *J Clin Invest* **117**, 2362-2368, doi:10.1172/jci32239 (2007).
- 259 Roberts, A. C. & Porter, K. E. Cellular and molecular mechanisms of endothelial dysfunction in diabetes. *Diab Vasc Dis Res* **10**, 472-482, doi:10.1177/1479164113500680 (2013).
- 260 Villaret, A. *et al.* Adipose tissue endothelial cells from obese human subjects: differences among depots in angiogenic, metabolic, and inflammatory gene expression and cellular senescence. *Diabetes* **59**, 2755-2763, doi:10.2337/db10-0398 (2010).
- 261 Briot, A. *et al.* Senescence Alters PPAR γ (Peroxisome Proliferator-Activated Receptor Gamma)-Dependent Fatty Acid Handling in Human Adipose Tissue Microvascular Endothelial Cells and Favors Inflammation. *Arterioscler Thromb Vasc Biol* **38**, 1134-1146, doi:10.1161/atvbaha.118.310797 (2018).
- 262 Shirakawa, K. *et al.* Obesity accelerates T cell senescence in murine visceral adipose tissue. *J Clin Invest* **126**, 4626-4639, doi:10.1172/jci88606 (2016).
- 263 Lee, Y. H. *et al.* Senescent T Cells Predict the Development of Hyperglycemia in Humans. *Diabetes* **68**, 156-162, doi:10.2337/db17-1218 (2019).
- 264 Tardelli, M. *et al.* Osteopontin is a key player for local adipose tissue macrophage proliferation in obesity. *Mol Metab* **5**, 1131-1137, doi:10.1016/j.molmet.2016.09.003 (2016).
- 265 Hall, B. M. *et al.* Aging of mice is associated with p16(Ink4a)- and β -galactosidase-positive macrophage accumulation that can be induced in young mice by senescent cells. *Aging (Albany NY)* **8**, 1294-1315, doi:10.18632/aging.100991 (2016).
- 266 Camell, C. D. *et al.* Inflammasome-driven catecholamine catabolism in macrophages blunts lipolysis during ageing. *Nature* **550**, 119-123, doi:10.1038/nature24022 (2017).
- 267 Baker, D. J. *et al.* Naturally occurring p16(Ink4a)-positive cells shorten healthy lifespan. *Nature* **530**, 184-189, doi:10.1038/nature16932 (2016).

- 268 Ogrodnik, M. *et al.* Cellular senescence drives age-dependent hepatic steatosis. *Nat Commun* **8**, 15691, doi:10.1038/ncomms15691 (2017).
- 269 Farr, J. N. *et al.* Independent Roles of Estrogen Deficiency and Cellular Senescence in the Pathogenesis of Osteoporosis: Evidence in Young Adult Mice and Older Humans. *J Bone Miner Res* **34**, 1407-1418, doi:10.1002/jbmr.3729 (2019).
- 270 Zhu, Y. *et al.* The Achilles' heel of senescent cells: from transcriptome to senolytic drugs. *Aging Cell* **14**, 644-658, doi:10.1111/accel.12344 (2015).
- 271 Xu, M. *et al.* Senolytics improve physical function and increase lifespan in old age. *Nat Med* **24**, 1246-1256, doi:10.1038/s41591-018-0092-9 (2018).
- 272 Palmer, A. K. *et al.* Targeting senescent cells alleviates obesity-induced metabolic dysfunction. *Aging Cell* **18**, e12950, doi:10.1111/accel.12950 (2019).
- 273 Hickson, L. J. *et al.* Senolytics decrease senescent cells in humans: Preliminary report from a clinical trial of Dasatinib plus Quercetin in individuals with diabetic kidney disease. *EBioMedicine* **47**, 446-456, doi:10.1016/j.ebiom.2019.08.069 (2019).
- 274 Justice, J. N. *et al.* Senolytics in idiopathic pulmonary fibrosis: Results from a first-in-human, open-label, pilot study. *EBioMedicine* **40**, 554-563, doi:10.1016/j.ebiom.2018.12.052 (2019).
- 275 Zhu, Y. *et al.* New agents that target senescent cells: the flavone, fisetin, and the BCL-X(L) inhibitors, A1331852 and A1155463. *Aging (Albany NY)* **9**, 955-963, doi:10.18632/aging.101202 (2017).
- 276 Yousefzadeh, M. J. *et al.* Fisetin is a senotherapeutic that extends health and lifespan. *EBioMedicine* **36**, 18-28, doi:10.1016/j.ebiom.2018.09.015 (2018).
- 277 Chang, J. *et al.* Clearance of senescent cells by ABT263 rejuvenates aged hematopoietic stem cells in mice. *Nat Med* **22**, 78-83, doi:10.1038/nm.4010 (2016).
- 278 Fuhrmann-Stroissnigg, H. *et al.* Identification of HSP90 inhibitors as a novel class of senolytics. *Nat Commun* **8**, 422, doi:10.1038/s41467-017-00314-z (2017).
- 279 Xu, M. *et al.* JAK inhibition alleviates the cellular senescence-associated secretory phenotype and frailty in old age. *Proc Natl Acad Sci U S A* **112**, E6301-6310, doi:10.1073/pnas.1515386112 (2015).
- 280 Xue, W. *et al.* Senescence and tumour clearance is triggered by p53 restoration in murine liver carcinomas. *Nature* **445**, 656-660, doi:10.1038/nature05529 (2007).
- 281 Krimpenfort, P., Quon, K. C., Mooi, W. J., Loonstra, A. & Berns, A. Loss of p16Ink4a confers susceptibility to metastatic melanoma in mice. *Nature* **413**, 83-86, doi:10.1038/35092584 (2001).
- 282 Wang, C. *et al.* Adult-onset, short-term dietary restriction reduces cell senescence in mice. *Aging (Albany NY)* **2**, 555-566, doi:10.18632/aging.100196 (2010).
- 283 Schafer, M. J. *et al.* Exercise Prevents Diet-Induced Cellular Senescence in Adipose Tissue. *Diabetes* **65**, 1606-1615, doi:10.2337/db15-0291 (2016).
- 284 Stanford, K. I., Middelbeek, R. J. & Goodyear, L. J. Exercise Effects on White Adipose Tissue: Beiging and Metabolic Adaptations. *Diabetes* **64**, 2361-2368, doi:10.2337/db15-0227 (2015).
- 285 Justice, J. N. *et al.* Cellular Senescence Biomarker p16INK4a+ Cell Burden in Thigh Adipose is Associated With Poor Physical Function in Older Women. *J Gerontol A Biol Sci Med Sci* **73**, 939-945, doi:10.1093/gerona/glx134 (2018).
- 286 Rönn, T. *et al.* A six months exercise intervention influences the genome-wide DNA methylation pattern in human adipose tissue. *PLoS Genet* **9**, e1003572, doi:10.1371/journal.pgen.1003572 (2013).
- 287 Horowitz, J. F. Fatty acid mobilization from adipose tissue during exercise. *Trends Endocrinol Metab* **14**, 386-392, doi:10.1016/s1043-2760(03)00143-7 (2003).
- 288 Weisberg, S. P. *et al.* Obesity is associated with macrophage accumulation in adipose tissue. *J Clin Invest* **112**, 1796-1808, doi:10.1172/JCI19246
112/12/1796 [pii] (2003).

- 289 Mezzanotte, L., van 't Root, M., Karatas, H., Goun, E. A. & Löwik, C. In Vivo Molecular Bioluminescence Imaging: New Tools and Applications. *Trends Biotechnol* **35**, 640-652, doi:10.1016/j.tibtech.2017.03.012 (2017).
- 290 Ternacle, J. *et al.* Short-term high-fat diet compromises myocardial function: a radial strain rate imaging study. *Eur Heart J Cardiovasc Imaging*, doi:jew316 [pii] 10.1093/ehjci/jew316 (2017).
- 291 van Rooijen, N. & Hendriks, E. Liposomes for specific depletion of macrophages from organs and tissues. *Methods Mol Biol* **605**, 189-203, doi:10.1007/978-1-60327-360-2_13 (2010).
- 292 Westwell-Roper, C. Y., Ehses, J. A. & Verchere, C. B. Resident macrophages mediate islet amyloid polypeptide-induced islet IL-1 β production and β -cell dysfunction. *Diabetes* **63**, 1698-1711, doi:10.2337/db13-0863 (2014).
- 293 Derumeaux, G. *et al.* Myocardial alterations in senescent mice and effect of exercise training: a strain rate imaging study. *Circ Cardiovasc Imaging* **1**, 227-234, doi:10.1161/circimaging.107.745919 (2008).
- 294 Manni, I., de Latouliere, L., Gurtner, A. & Piaggio, G. Transgenic Animal Models to Visualize Cancer-Related Cellular Processes by Bioluminescence Imaging. *Front Pharmacol* **10**, 235, doi:10.3389/fphar.2019.00235 (2019).
- 295 Sorrentino, J. A. *et al.* p16INK4a reporter mice reveal age-promoting effects of environmental toxicants. *J Clin Invest* **124**, 169-173, doi:10.1172/jci70960 (2014).
- 296 Dey, P. in *Basic and Advanced Laboratory Techniques in Histopathology and Cytology* 171-183 (Springer Singapore, 2018).
- 297 Frolova, E. G. *et al.* Thrombospondin-4 regulates vascular inflammation and atherogenesis. *Circ Res* **107**, 1313-1325, doi:10.1161/circresaha.110.232371 (2010).
- 298 Nishi, C., Toda, S., Segawa, K. & Nagata, S. Tim4- and MerTK-mediated engulfment of apoptotic cells by mouse resident peritoneal macrophages. *Mol Cell Biol* **34**, 1512-1520, doi:10.1128/mcb.01394-13 (2014).
- 299 Foresti, R. *et al.* Nrf2 activators modulate oxidative stress responses and bioenergetic profiles of human retinal epithelial cells cultured in normal or high glucose conditions. *Pharmacol Res* **99**, 296-307, doi:10.1016/j.phrs.2015.07.006 (2015).
- 300 Braud, L. *et al.* Carbon monoxide-induced metabolic switch in adipocytes improves insulin resistance in obese mice. *JCI Insight* **3**, doi:10.1172/jci.insight.123485 (2018).
- 301 Yeung, Y. G. & Stanley, E. R. A solution for stripping antibodies from polyvinylidene fluoride immunoblots for multiple reprobing. *Anal Biochem* **389**, 89-91, doi:10.1016/j.ab.2009.03.017 (2009).
- 302 Odegaard, J. I. & Chawla, A. Pleiotropic actions of insulin resistance and inflammation in metabolic homeostasis. *Science* **339**, 172-177, doi:10.1126/science.1230721 (2013).
- 303 Lemonnier, D., Suquet, J. P., Aubert, R., De Gasquet, P. & Pequignot, E. Metabolism of the mouse made obese by a high-fat diet. *Diabete Metab* **1**, 77-85 (1975).
- 304 Björntorp, P. Obesity and adipose tissue distribution as risk factors for the development of disease. A review. *Infusionstherapie* **17**, 24-27, doi:10.1159/000222436 (1990).
- 305 Fox, C. S. *et al.* Abdominal visceral and subcutaneous adipose tissue compartments: association with metabolic risk factors in the Framingham Heart Study. *Circulation* **116**, 39-48, doi:10.1161/circulationaha.106.675355 (2007).
- 306 Visser, M., Bouter, L. M., McQuillan, G. M., Wener, M. H. & Harris, T. B. Elevated C-reactive protein levels in overweight and obese adults. *Jama* **282**, 2131-2135, doi:10.1001/jama.282.22.2131 (1999).
- 307 Shah, N. R. & Braverman, E. R. Measuring adiposity in patients: the utility of body mass index (BMI), percent body fat, and leptin. *PLoS One* **7**, e33308, doi:10.1371/journal.pone.0033308 (2012).

- 308 van der Heijden, R. A. *et al.* High-fat diet induced obesity primes inflammation in adipose tissue prior to liver in C57BL/6j mice. *Aging (Albany NY)* **7**, 256-268, doi:10.18632/aging.100738 (2015).
- 309 Xu, H. *et al.* Chronic inflammation in fat plays a crucial role in the development of obesity-related insulin resistance. *J Clin Invest* **112**, 1821-1830, doi:10.1172/jci19451 (2003).
- 310 Krishnan, J. *et al.* Dietary obesity-associated Hif1 α activation in adipocytes restricts fatty acid oxidation and energy expenditure via suppression of the Sirt2-NAD⁺ system. *Genes Dev* **26**, 259-270, doi:10.1101/gad.180406.111 (2012).
- 311 Lee, Y. S. *et al.* Increased adipocyte O₂ consumption triggers HIF-1 α , causing inflammation and insulin resistance in obesity. *Cell* **157**, 1339-1352, doi:10.1016/j.cell.2014.05.012 (2014).
- 312 Aguayo-Mazzucato, C. *et al.* Acceleration of β Cell Aging Determines Diabetes and Senolysis Improves Disease Outcomes. *Cell Metab* **30**, 129-142.e124, doi:10.1016/j.cmet.2019.05.006 (2019).
- 313 Akagiri, S. *et al.* A Mouse Model of Metabolic Syndrome; Increase in Visceral Adipose Tissue Precedes the Development of Fatty Liver and Insulin Resistance in High-Fat Diet-Fed Male KK/Ta Mice. *J Clin Biochem Nutr* **42**, 150-157, doi:10.3164/jcbn.2008022 (2008).
- 314 Chen, W., Wilson, J. L., Khaksari, M., Cowley, M. A. & Enriori, P. J. Abdominal fat analyzed by DEXA scan reflects visceral body fat and improves the phenotype description and the assessment of metabolic risk in mice. *Am J Physiol Endocrinol Metab* **303**, E635-643, doi:10.1152/ajpendo.00078.2012 (2012).
- 315 Fischer, I. P. *et al.* A history of obesity leaves an inflammatory fingerprint in liver and adipose tissue. *Int J Obes (Lond)* **42**, 507-517, doi:10.1038/ijo.2017.224 (2018).
- 316 Neeland, I. J. *et al.* Dysfunctional adiposity and the risk of prediabetes and type 2 diabetes in obese adults. *Jama* **308**, 1150-1159, doi:10.1001/2012.jama.11132 (2012).
- 317 Packer, M. Leptin-Aldosterone-Nephrilysin Axis: Identification of Its Distinctive Role in the Pathogenesis of the Three Phenotypes of Heart Failure in People With Obesity. *Circulation* **137**, 1614-1631, doi:10.1161/circulationaha.117.032474 (2018).
- 318 Rosito, G. A. *et al.* Pericardial fat, visceral abdominal fat, cardiovascular disease risk factors, and vascular calcification in a community-based sample: the Framingham Heart Study. *Circulation* **117**, 605-613, doi:10.1161/circulationaha.107.743062 (2008).
- 319 Sawaki, D. *et al.* Response by Sawaki *et al.* to Letter Regarding Article, "Visceral Adipose Tissue Drives Cardiac Aging Through Modulation of Fibroblast Senescence by Osteopontin Production". *Circulation* **139**, 845-846, doi:10.1161/CIRCULATIONAHA.118.038482.
- 320 Sawaki, D. *et al.* Visceral Adipose Tissue Drives Cardiac Aging Through Modulation of Fibroblast Senescence by Osteopontin Production. *Circulation* **138**, 809-822, doi:CIRCULATIONAHA.117.031358 [pii]
10.1161/CIRCULATIONAHA.117.031358.
- 321 Burd, C. E. *et al.* Monitoring tumorigenesis and senescence in vivo with a p16(INK4a)-luciferase model. *Cell* **152**, 340-351, doi:S0092-8674(12)01497-3 [pii]
10.1016/j.cell.2012.12.010.
- 322 McNelis, J. C. & Olefsky, J. M. Macrophages, immunity, and metabolic disease. *Immunity* **41**, 36-48, doi:S1074-7613(14)00190-3 [pii]
10.1016/j.immuni.2014.05.010.
- 323 Nomiya, T. *et al.* Osteopontin mediates obesity-induced adipose tissue macrophage infiltration and insulin resistance in mice. *J Clin Invest* **117**, 2877-2888, doi:10.1172/JCI31986 (2007).
- 324 Kos, K. & Wilding, J. P. SPARC: a key player in the pathologies associated with obesity and diabetes. *Nat Rev Endocrinol* **6**, 225-235, doi:nrendo.2010.18 [pii]
10.1038/nrendo.2010.18.

- 325 Kong, P. *et al.* Thrombospondin-1 regulates adiposity and metabolic dysfunction in diet-induced obesity enhancing adipose inflammation and stimulating adipocyte proliferation. *Am J Physiol Endocrinol Metab* **305**, E439-450, doi:ajpendo.00006.2013 [pii]
10.1152/ajpendo.00006.2013.
- 326 Pejnovic, N. N. *et al.* Galectin-3 deficiency accelerates high-fat diet-induced obesity and amplifies inflammation in adipose tissue and pancreatic islets. *Diabetes* **62**, 1932-1944, doi:db12-0222 [pii]
10.2337/db12-0222.
- 327 Shirakawa, K. *et al.* IL (Interleukin)-10-STAT3-Galectin-3 Axis Is Essential for Osteopontin-Producing Reparative Macrophage Polarization After Myocardial Infarction. *Circulation* **138**, 2021-2035, doi:CIRCULATIONAHA.118.035047 [pii]
10.1161/CIRCULATIONAHA.118.035047.
- 328 Jaitin, D. A. *et al.* Lipid-Associated Macrophages Control Metabolic Homeostasis in a Trem2-Dependent Manner. *Cell* **178**, 686-698 e614, doi:S0092-8674(19)30625-7 [pii]
10.1016/j.cell.2019.05.054.
- 329 Silva, H. M. *et al.* Vasculature-associated fat macrophages readily adapt to inflammatory and metabolic challenges. *J Exp Med* **216**, 786-806, doi:jem.20181049 [pii]
10.1084/jem.20181049.
- 330 Zagorska, A., Traves, P. G., Lew, E. D., Dransfield, I. & Lemke, G. Diversification of TAM receptor tyrosine kinase function. *Nat Immunol* **15**, 920-928, doi:ni.2986 [pii]
10.1038/ni.2986.
- 331 Watanabe, S., Alexander, M., Misharin, A. V. & Budinger, G. R. S. The role of macrophages in the resolution of inflammation. *J Clin Invest* **129**, 2619-2628, doi:124615 [pii]
10.1172/JCI124615.
- 332 Lavin, Y. *et al.* Tissue-resident macrophage enhancer landscapes are shaped by the local microenvironment. *Cell* **159**, 1312-1326, doi:S0092-8674(14)01449-4 [pii]
10.1016/j.cell.2014.11.018.
- 333 Cummings, R. J. *et al.* Different tissue phagocytes sample apoptotic cells to direct distinct homeostasis programs. *Nature* **539**, 565-569, doi:nature20138 [pii]
10.1038/nature20138.
- 334 Hashimoto, D. *et al.* Tissue-resident macrophages self-maintain locally throughout adult life with minimal contribution from circulating monocytes. *Immunity* **38**, 792-804, doi:S1074-7613(13)00157-X [pii]
10.1016/j.immuni.2013.04.004.
- 335 Roberts, A. W. *et al.* Tissue-Resident Macrophages Are Locally Programmed for Silent Clearance of Apoptotic Cells. *Immunity* **47**, 913-927 e916, doi:S1074-7613(17)30437-5 [pii]
10.1016/j.immuni.2017.10.006.
- 336 Baker, D. J. *et al.* Clearance of p16Ink4a-positive senescent cells delays ageing-associated disorders. *Nature* **479**, 232-236, doi:nature10600 [pii]
10.1038/nature10600.
- 337 Xu, M. *et al.* Senolytics improve physical function and increase lifespan in old age. *Nat Med* **24**, 1246-1256, doi:10.1038/s41591-018-0092-9
10.1038/s41591-018-0092-9 [pii].

- 338 Palmer, A. K. *et al.* Targeting senescent cells alleviates obesity-induced metabolic dysfunction. *Aging Cell* **18**, e12950, doi:10.1111/accel.12950.
- 339 Krizhanovsky, V. *et al.* Senescence of activated stellate cells limits liver fibrosis. *Cell* **134**, 657-667, doi:S0092-8674(08)00836-2 [pii]
- 10.1016/j.cell.2008.06.049 (2008).
- 340 He, S. & Sharpless, N. E. Senescence in Health and Disease. *Cell* **169**, 1000-1011, doi:S0092-8674(17)30546-9 [pii]
- 10.1016/j.cell.2017.05.015.
- 341 Ternacle, J. *et al.* Short-term high-fat diet compromises myocardial function: a radial strain rate imaging study. *Eur Heart J Cardiovasc Imaging* **18**, 1283-1291, doi:10.1093/ehjci/jew316 (2017).
- 342 Neeland, I. J. *et al.* Dysfunctional adiposity and the risk of prediabetes and type 2 diabetes in obese adults. *JAMA* **308**, 1150-1159, doi:1360863 [pii]
- 10.1001/2012.jama.11132.
- 343 Packer, M. Leptin-Aldosterone-Nepriylsin Axis: Identification of Its Distinctive Role in the Pathogenesis of the Three Phenotypes of Heart Failure in People With Obesity. *Circulation* **137**, 1614-1631, doi:CIRCULATIONAHA.117.032474 [pii]
- 10.1161/CIRCULATIONAHA.117.032474.
- 344 Amano, S. U. *et al.* Local proliferation of macrophages contributes to obesity-associated adipose tissue inflammation. *Cell Metab* **19**, 162-171, doi:10.1016/j.cmet.2013.11.017.
- 345 Wang, J. & Kubes, P. A Reservoir of Mature Cavity Macrophages that Can Rapidly Invade Visceral Organs to Affect Tissue Repair. *Cell* **165**, 668-678, doi:S0092-8674(16)30265-3 [pii]
- 10.1016/j.cell.2016.03.009.
- 346 Hill, D. A. *et al.* Distinct macrophage populations direct inflammatory versus physiological changes in adipose tissue. *Proc Natl Acad Sci U S A* **115**, E5096-E5105, doi:1802611115 [pii]
- 10.1073/pnas.1802611115.
- 347 Chawla, A., Nguyen, K. D. & Goh, Y. P. Macrophage-mediated inflammation in metabolic disease. *Nat Rev Immunol* **11**, 738-749, doi:nri3071 [pii]
- 10.1038/nri3071.
- 348 Marcelin, G. *et al.* A PDGFRalpha-Mediated Switch toward CD9(high) Adipocyte Progenitors Controls Obesity-Induced Adipose Tissue Fibrosis. *Cell Metab* **25**, 673-685, doi:S1550-4131(17)30045-1 [pii]
- 10.1016/j.cmet.2017.01.010.
- 349 Weisberg, S. P. *et al.* CCR2 modulates inflammatory and metabolic effects of high-fat feeding. *J Clin Invest* **116**, 115-124, doi:10.1172/JCI24335 (2006).
- 350 Bakker, E. N. *et al.* Flow-dependent remodeling of small arteries in mice deficient for tissue-type transglutaminase: possible compensation by macrophage-derived factor XIII. *Circ Res* **99**, 86-92, doi:01.RES.0000229657.83816.a7 [pii]
- 10.1161/01.RES.0000229657.83816.a7 (2006).
- 351 Feng, B. *et al.* Clodronate liposomes improve metabolic profile and reduce visceral adipose macrophage content in diet-induced obese mice. *PLoS One* **6**, e24358, doi:10.1371/journal.pone.0024358
- PONE-D-11-09806 [pii].
- 352 Kumar, D. *et al.* Temporal immunometabolic profiling of adipose tissue in HFD-induced obesity: manifestations of mast cells in fibrosis and senescence. *Int J Obes (Lond)* **43**, 1281-1294, doi:10.1038/s41366-018-0228-5

10.1038/s41366-018-0228-5 [pii].

353 Aguayo-Mazzucato, C. *et al.* Acceleration of beta Cell Aging Determines Diabetes and Senolysis Improves Disease Outcomes. *Cell Metab*, doi:S1550-4131(19)30246-3 [pii]

10.1016/j.cmet.2019.05.006.

354 Duncan, B. B. *et al.* Low-grade systemic inflammation and the development of type 2 diabetes: the atherosclerosis risk in communities study. *Diabetes* **52**, 1799-1805, doi:10.2337/diabetes.52.7.1799 (2003).

355 Ternacle, J. *et al.* Short-term high-fat diet compromises myocardial function: a radial strain rate imaging study. *Eur Heart J Cardiovasc Imaging* **18**, 1283-1291, doi:jew316 [pii]

10.1093/ehjci/jew316.

356 Amosse, J. *et al.* Phenotyping of circulating extracellular vesicles (EVs) in obesity identifies large EVs as functional conveyors of Macrophage Migration Inhibitory Factor. *Mol Metab* **18**, 134-142, doi:10.1016/j.molmet.2018.10.001 (2018).

357 Murano, I. *et al.* Dead adipocytes, detected as crown-like structures, are prevalent in visceral fat depots of genetically obese mice. *Journal of lipid research* **49**, 1562-1568, doi:10.1194/jlr.M800019-JLR200 (2008).

358 Saker, M. *et al.* Osteopontin, a Key Mediator Expressed by Senescent Pulmonary Vascular Cells in Pulmonary Hypertension. *Arteriosclerosis, thrombosis, and vascular biology* **36**, 1879-1890, doi:10.1161/atvbaha.116.307839 (2016).

359 Yousefzadeh, M. J. *et al.* Circulating levels of monocyte chemoattractant protein-1 as a potential measure of biological age in mice and frailty in humans. *Aging Cell* **17**, doi:10.1111/accel.12706 (2018).

360 Sawaki, D. *et al.* Visceral Adipose Tissue Drives Cardiac Aging Through Modulation of Fibroblast Senescence by Osteopontin Production. *Circulation* **138**, 809-822, doi:10.1161/CIRCULATIONAHA.117.031358 (2018).

361 Ma, S. *et al.* Caloric Restriction Reprograms the Single-Cell Transcriptional Landscape of Rattus Norvegicus Aging. *Cell* **180**, 984-1001.e1022, doi:10.1016/j.cell.2020.02.008 (2020).

362 Judge, S. & Leeuwenburgh, C. Cardiac mitochondrial bioenergetics, oxidative stress, and aging. *Am J Physiol Cell Physiol* **292**, C1983-1992, doi:10.1152/ajpcell.00285.2006 (2007).

363 Korolchuk, V. I., Miwa, S., Carroll, B. & von Zglinicki, T. Mitochondria in Cell Senescence: Is Mitophagy the Weakest Link? *EBioMedicine* **21**, 7-13, doi:10.1016/j.ebiom.2017.03.020 (2017).

364 Stab, B. R., 2nd *et al.* Mitochondrial Functional Changes Characterization in Young and Senescent Human Adipose Derived MSCs. *Frontiers in aging neuroscience* **8**, 299, doi:10.3389/fnagi.2016.00299 (2016).

365 Faas, M. M., Saez, T. & de Vos, P. Extracellular ATP and adenosine: The Yin and Yang in immune responses? *Molecular aspects of medicine* **55**, 9-19, doi:10.1016/j.mam.2017.01.002 (2017).

366 Tavallaie, M. *et al.* Moderation of mitochondrial respiration mitigates metabolic syndrome of aging. *Proc Natl Acad Sci U S A*, doi:10.1073/pnas.1917948117 (2020).

367 Myers, J. Cardiology patient pages. Exercise and cardiovascular health. *Circulation* **107**, e2-5, doi:10.1161/01.cir.0000048890.59383.8d (2003).

368 Pini, M. *et al.* Adipose tissue adaptive response to trans-10,cis-12-conjugated linoleic acid engages alternatively activated M2 macrophages. *FASEB J* **30**, 241-251, doi:10.1096/fj.15-276675 (2016).

369 Prince, M. J. *et al.* The burden of disease in older people and implications for health policy and practice. *Lancet* **385**, 549-562, doi:S0140-6736(14)61347-7 [pii]

10.1016/S0140-6736(14)61347-7 (2015).

370 Bancel, E. *et al.* [Effect of the age and the sex on plasma concentration of amino acids]. *Ann Biol Clin (Paris)* **52**, 667-670 (1994).

- 371 Cynober, L., Blonde, F., Nguyen Dinh, F., Gerbet, D. & Giboudeau, J. [Measurement of plasma and urinary amino acids with gas chromatography in healthy subjects. Variations as a function of age and sex]. *Ann Biol Clin (Paris)* **41**, 33-38 (1983).
- 372 Kouchiwa, T. *et al.* Age-related changes in serum amino acids concentrations in healthy individuals. *Clin Chem Lab Med* **50**, 861-870, doi:10.1515/cclm-2011-0846
/j/cclm.2012.50.issue-5/cclm-2011-0846/cclm-2011-0846.xml [pii].
- 373 Caballero, B., Gleason, R. E. & Wurtman, R. J. Plasma amino acid concentrations in healthy elderly men and women. *Am J Clin Nutr* **53**, 1249-1252 (1991).
- 374 Inuzuka, Y. *et al.* Suppression of phosphoinositide 3-kinase prevents cardiac aging in mice. *Circulation* **120**, 1695-1703, doi:CIRCULATIONAHA.109.871137 [pii]
10.1161/CIRCULATIONAHA.109.871137 (2009).
- 375 Park, S. K. *et al.* Gene expression profiling of aging in multiple mouse strains: identification of aging biomarkers and impact of dietary antioxidants. *Aging Cell* **8**, 484-495, doi:ACE496 [pii]
10.1111/j.1474-9726.2009.00496.x (2009).
- 376 Ternette, N. *et al.* Inhibition of mitochondrial aconitase by succination in fumarate hydratase deficiency. *Cell Rep* **3**, 689-700, doi:S2211-1247(13)00072-7 [pii]
10.1016/j.celrep.2013.02.013.
- 377 Rosa, A. P. *et al.* Phenylpyruvic acid decreases glucose-6-phosphate dehydrogenase activity in rat brain. *Cell Mol Neurobiol* **32**, 1113-1118, doi:10.1007/s10571-012-9834-2 (2012).
- 378 Ziegler, M. G., Lake, C. R. & Kopin, I. J. Plasma noradrenaline increases with age. *Nature* **261**, 333-335 (1976).
- 379 Werner, E. R., Blau, N. & Thony, B. Tetrahydrobiopterin: biochemistry and pathophysiology. *Biochem J* **438**, 397-414, doi:BJ20110293 [pii]
10.1042/BJ20110293 (2011).
- 380 Kure, S. *et al.* Wild-type phenylalanine hydroxylase activity is enhanced by tetrahydrobiopterin supplementation in vivo: an implication for therapeutic basis of tetrahydrobiopterin-responsive phenylalanine hydroxylase deficiency. *Mol Genet Metab* **83**, 150-156, doi:S1096-7192(04)00171-4 [pii]
10.1016/j.ymgme.2004.06.016 (2004).
- 381 Thony, B., Ding, Z. & Martinez, A. Tetrahydrobiopterin protects phenylalanine hydroxylase activity in vivo: implications for tetrahydrobiopterin-responsive hyperphenylalaninemia. *FEBS Lett* **577**, 507-511, doi:S0014579304013109 [pii]
10.1016/j.febslet.2004.10.056 (2004).
- 382 Cunningham, C. *et al.* Systemic and vascular oxidation limits the efficacy of oral tetrahydrobiopterin treatment in patients with coronary artery disease. *Circulation* **125**, 1356-1366, doi:CIRCULATIONAHA.111.038919 [pii]
10.1161/CIRCULATIONAHA.111.038919 (2012).
- 383 Antoniadou, C. *et al.* Induction of vascular GTP-cyclohydrolase I and endogenous tetrahydrobiopterin synthesis protect against inflammation-induced endothelial dysfunction in human atherosclerosis. *Circulation* **124**, 1860-1870, doi:CIRCULATIONAHA.111.029272 [pii]
10.1161/CIRCULATIONAHA.111.029272 (2011).
- 384 Du, Y. H., Guan, Y. Y., Alp, N. J., Channon, K. M. & Chen, A. F. Endothelium-specific GTP cyclohydrolase I overexpression attenuates blood pressure progression in salt-sensitive low-renin hypertension. *Circulation* **117**, 1045-1054, doi:CIRCULATIONAHA.107.748236 [pii]
10.1161/CIRCULATIONAHA.107.748236 (2008).

- 385 Harding, C. O. *et al.* The fate of intravenously administered tetrahydrobiopterin and its implications for heterologous gene therapy of phenylketonuria. *Mol Genet Metab* **81**, 52-57, doi:S1096719203002208 [pii]
- 10.1016/j.yimgme.2003.10.002 (2004).
- 386 Hashimoto, T. *et al.* Tetrahydrobiopterin Protects Against Hypertrophic Heart Disease Independent of Myocardial Nitric Oxide Synthase Coupling. *J Am Heart Assoc* **5**, e003208, doi:JAHA.116.003208 [pii]
- 10.1161/JAHA.116.003208 (2016).
- 387 Moens, A. L. *et al.* Reversal of cardiac hypertrophy and fibrosis from pressure overload by tetrahydrobiopterin: efficacy of recoupling nitric oxide synthase as a therapeutic strategy. *Circulation* **117**, 2626-2636, doi:CIRCULATIONAHA.107.737031 [pii]
- 10.1161/CIRCULATIONAHA.107.737031 (2008).
- 388 Edwards, C. *et al.* Mechanisms of amino acid-mediated lifespan extension in *Caenorhabditis elegans*. *BMC Genet* **16**, 8, doi:10.1186/s12863-015-0167-2
- s12863-015-0167-2 [pii].
- 389 Arganda, S. *et al.* Parsing the life-shortening effects of dietary protein: effects of individual amino acids. *Proc Biol Sci* **284**, doi:rsph.2016.2052 [pii]
- 10.1098/rsph.2016.2052.
- 390 Choudhury, A. R. *et al.* Cdkn1a deletion improves stem cell function and lifespan of mice with dysfunctional telomeres without accelerating cancer formation. *Nat Genet* **39**, 99-105, doi:ng1937 [pii]
- 10.1038/ng1937 (2007).
- 391 Pinto, A. R. *et al.* Revisiting Cardiac Cellular Composition. *Circ Res* **118**, 400-409, doi:CIRCRESAHA.115.307778 [pii]
- 10.1161/CIRCRESAHA.115.307778.
- 392 Anderson, R. *et al.* Length-independent telomere damage drives post-mitotic cardiomyocyte senescence. *EMBO J* **38**, doi:embj.2018100492 [pii]
- 10.15252/embj.2018100492.
- 393 Delles, C. *et al.* Nuclear magnetic resonance-based metabolomics identifies phenylalanine as a novel predictor of incident heart failure hospitalisation: results from PROSPER and FINRISK 1997. *Eur J Heart Fail* **20**, 663-673, doi:10.1002/ejhf.1076 (2018).
- 394 Eriksson, J. G. *et al.* Higher serum phenylalanine concentration is associated with more rapid telomere shortening in men. *Am J Clin Nutr* **105**, 144-150, doi:ajcn.116.130468 [pii]
- 10.3945/ajcn.116.130468.
- 395 Tenori, L. *et al.* Metabolomic fingerprint of heart failure in humans: a nuclear magnetic resonance spectroscopy analysis. *Int J Cardiol* **168**, e113-115, doi:S0167-5273(13)01567-2 [pii]
- 10.1016/j.ijcard.2013.08.042.
- 396 Alcendor, R. R. *et al.* Sirt1 regulates aging and resistance to oxidative stress in the heart. *Circ Res* **100**, 1512-1521, doi:01.RES.0000267723.65696.4a [pii]
- 10.1161/01.RES.0000267723.65696.4a (2007).
- 397 Dai, D. F. *et al.* Overexpression of catalase targeted to mitochondria attenuates murine cardiac aging. *Circulation* **119**, 2789-2797, doi:CIRCULATIONAHA.108.822403 [pii]
- 10.1161/CIRCULATIONAHA.108.822403 (2009).

- 398 Tocchi, A., Quarles, E. K., Basisty, N., Gitari, L. & Rabinovitch, P. S. Mitochondrial dysfunction in cardiac aging. *Biochim Biophys Acta* **1847**, 1424-1433, doi:S0005-2728(15)00152-8 [pii]
10.1016/j.bbabbio.2015.07.009.
- 399 Ravaglia, G. *et al.* Plasma amino acid concentrations in patients with amnesic mild cognitive impairment or Alzheimer disease. *Am J Clin Nutr* **80**, 483-488, doi:80/2/483 [pii]
10.1093/ajcn/80.2.483 (2004).
- 400 DeNicola, G. M. *et al.* Oncogene-induced Nrf2 transcription promotes ROS detoxification and tumorigenesis. *Nature* **475**, 106-109, doi:nature10189 [pii]
10.1038/nature10189 (2011).
- 401 Wu, L. E., Gomes, A. P. & Sinclair, D. A. Geroncogenesis: metabolic changes during aging as a driver of tumorigenesis. *Cancer Cell* **25**, 12-19, doi:S1535-6108(13)00534-5 [pii]
10.1016/j.ccr.2013.12.005.
- 402 Deelen, J. *et al.* A metabolic profile of all-cause mortality risk identified in an observational study of 44,168 individuals. *Nat Commun* **10**, 3346, doi:10.1038/s41467-019-11311-9
10.1038/s41467-019-11311-9 [pii].